FINAL REPORT

A NIST Kinetic Data Base for PAH Reaction and Soot Particle Inception during Combustion

SERDP Project WP-1198

DECEMBER 2007

Wing Tsang, NIST
Samuel Manzello, NIST
Collen Stroud, NIST
Michael Donovan, NIST
Valeri Babushok, NIST
Kermit Smyth, NIST
NIOT

Charles Frayne
David Lehnert
Sean McGivern
AFRL

Scott Stouffer,
UDRI

Vishwanath R. Katta,
ISSI

REPORT DOCUMENTATION PAGE

Form Approved
OMB No. 0704-0188

PLEASE DO NOT RETURN YOUR FORM TO THE ABOVE ORGANIZATION.

1. REPORT DATE *(DD-MM-YYYY)*	2. REPORT TYPE	3. DATES COVERED *(From - To)*
17-06-2008	FINAL	01-01-2001 to 12-31-2007

4. TITLE AND SUBTITLE

A NIST Kinetic Data Base for PAH Reaction and Soot Particle Inception During Combusion

5a. CONTRACT NUMBER

5b. GRANT NUMBER

5c. PROGRAM ELEMENT NUMBER

6. AUTHOR(S)

Wing Tsang, NIST
Collen Stroud, NIST
Charles Frayne, AFRL
Sean McGivern, AFRL
Kermit Smyth, NIST
Vishwanath R. Katta, ISSI
Samuel Manzello, NIST
Michael Donovan, NIST
David Lehnert, AFRL
Valeri Babushok, NIST
Scott Stouffer, UDRI

5d. PROJECT NUMBER

WP-1198

5e. TASK NUMBER

5f. WORK UNIT NUMBER

7. PERFORMING ORGANIZATION NAME(S) AND ADDRESS(ES)

National Institute of Standards and Technology
100 Bureau Drive
Gaithersburg, MD 20899

8. PERFORMING ORGANIZATION REPORT NUMBER

9. SPONSORING/MONITORING AGENCY NAME(S) AND ADDRESS(ES)

Strategic Environmental Research and Development Program
901 N. Stuart St., Suite 303
Arlington, VA 22203

10. SPONSOR/MONITOR'S ACRONYM(S)

SERDP

11. SPONSOR/MONITOR'S REPORT NUMBER(S)

WP-1198-FR

12. DISTRIBUTION/AVAILABILITY STATEMENT

Approved for public release; distribution is unlimited

13. SUPPLEMENTARY NOTES

14. ABSTRACT

A gas-phase chemical kinetics database was developed that describes the transformation of fuel molecules to their desired end products of carbon dioxide and water, as well as to the undesired polycyclic aromatic hydrocarbons (PAH), and a quantitative soot particle inception model based on experiments was developed. Surrogate real fuel molecules studied included heptane as a representative of the aliphatic constituents of real fuel and butylbenzene as a representative of the aromatic component. Existing data was compiled, evaluated and updated using NIST CHEMRATE, a user friendly reaction rate theory program, to determine which kinetic rates would be measured. Rates for fuel cracking and reactions involving PAH with three or fewer rings using a shock tube were identified. A particle inception model was developed based on experiments performed in diffusion flames and in a well-stirred reactor.

15. SUBJECT TERMS

combustion, chemical kinetics, polycyclic aromatic hydrocarbons, soot particles, fuel, heptane

16. SECURITY CLASSIFICATION OF:			17. LIMITATION OF ABSTRACT	18. NUMBER OF PAGES	19a. NAME OF RESPONSIBLE PERSON
a. REPORT	b. ABSTRACT	c. THIS PAGE			Bruce D. Sartwell
Unclassified	Unclassified	Unclassified	UL	169	19b. TELEPHONE NUMBER *(Include area code)* 703-696-2128

Reset

Acknowledgments

The financial support of the U.S. Department of Defense Strategic Environmental Research & Development Program is hereby acknowledged.

Table of Contents

1. Summary and Conclusions

This is the final report of Project **(SERDP # 1198)** (**A NIST Kinetic Data Base for PAH Reaction and Soot Particle Inception during Combustion)** It results from an experimental and analytical program designed to improve existing chemical kinetic databases used for the simulation of heptane combustion with special emphasis on the formation of PAH and soot. This is a joint work of Building and Fire Research and Chemical Sciences and Technology Laboratory at NIST. The original principal investigators were Linda Blevins, George Mulholland and Wing Tsang. Dr Blevins has since joined the DOE. Dr. Mulholland has retired. Dr. Samuel Manzello has taken their place. The experimental studies involve studies in a heated pulse shock tube and a stirred flow-plug flow reactor especially constructed for the present studies.

The former was focussed on determining the mechanisms and rate constants for the unimolecular decomposition and isomerization of all the radicals formed as the initial heptyl radicals degrades to smaller unsaturated structures. Altogether there are 21 radicals undergoing 29 beta bond scissions and 11 reversible isomerizations or a total of 51 reactions. In addition, for completeness the decomposition of heptane and the 1-olefins from 1-hexene to 1-butene are also included. The mechanisms and rate constants for a majority of these reactions are directly determined through single pulse shock tube experiments. Others were generated from existing data. The unique features of the reactions are the relatively large size of the radicals, the low reaction thresholds and the presence of isomerization processes. These raise a number of unique problems not usually described for the simple high reaction threshold reactions found in the literature. These have been solved in the course of this work. A special feature of these high temperature reactions is the contribution of energy transfer effects leading to the presence of pressure dependences. Use have been made of a NIST program for the determination of such effects. They lead to reductions of rate constants by as much as an order of magnitude at temperatures in excess of 1000 K at pressures of 1 bar. These effects are lowered to a factor of 2 to 3 at 100 bars pressure. As a result it is not possible to express results in terms of a single rate expression for a single process. This is an extra complication and the correction factors are tabulated in extensive tables. Also included in the report are the thermodynamic properties of the 21 radicals in JANNAF format. When these processes are combined with the well established bimolecular processes involving radical attack on the stable compounds it will be possible to describe completely the pyrolytoc cracking of heptane

The integration of the database for cracking into that for heptane combustion is intended to extend the range of the database to cover increasingly rich systems. The reader is referred to http://kinetics.nist.gov/CKMech/ for a listing reactions in the database. It also contains listing of other databases and is extremely useful for making comparisons. .This is of course of vital importance for the description of PAH and soot formation, since obviously such phenomenan can only be formed as the combustion mixture becomes richer. We have thus intergrated 51 unimolecular decomposition and

isomerization reactions and 24 species processes into a heptane combustion data base consisting of 347 species and 1745 reactions. This is a small fraction of the total database needed to fit the whole range of conditions for heptane combustion. Nevertheless they represent the only set of reactions invovling a fuel such as heptane where the rate constants are directly measured as opposed to the standard methodology of deriving them from estimates established under very different conditions or used to fit global results.

Since existing heptane databases fit certain sets of experimental data on heptane combustion it is important that the inclusion of extra reactions do not significantly degrade the existing fits. Fortunately, the pyrolytic reactions do not appear to have large affects on the the original fits. This is partly due to the pyrolytic reactions being at conditions and temperatures that are different than the combustion processes. Nevertheless some changes in the rate constants in the existing databases have been made to marginally improve the fits. In additon we have also captured in the new database the reactions leading to PAH formation from small unsaturated compounds. Thus this database permits the simulation of combustion phenomenon across the entire range of stoichiomtries.

However, in the course of work it became clear that there are severe problems in the established heptane combustion databases. Some have been put together many years ago and therefore do not reflect the latest understanding of the nature of the reactions in the database. In order to match global results adjustments have ben made in other rate constants, thus compounding the error . The large size of these databases is another factor in making it extremely difficult to systematically bring these databases up to modern standards. Nevertheless there is probably no alternative. We illustrate the situation with the reaction of a fuel radical with oxygen. The consequence is a fuel peroxyl radical that is vibrationally excited. This can then undergo a whole series of isomerizaion processes leading ultimately to the production of OH. All of these are expressed as thermal rate constants in current databases. This cannot be the case for high temperature systems. Thus the postulated rate constants are probably wrong and the pressure dependence is ignored. The above deal with known reactions. In the case of the formation of aromatics it is suspected that there are pathways that has not been enumerated. Thus in present study, in an attempt to study the reactions of cyclopentadienyl radical a pathway for formation of benzene has been discovered. Probably the main problem in studying the formation of larger PAHs and soot is the unavailability of samples of precursors to possible intermediates in the reaction chain. Thus it is not possible to possible to test mechanisms in the traditional fashion used by chemical kineticists.

In order to fill in the gaps in mechanisms in the transformation of small unsaturates to PAH and soot a stirred-flow plug-flow apparatus has been constructed at NIST. The entire system has the advantage of well defined boundary conditions and removes some of the spacial ambiguities present in direct studies with flames. The facility is equiped with a nano differential mobility analyzer to determine particle size, gas samples can be extracted and analyzed with gc-ms. Solid samples are collected on filers and subjected to TEM analysis and less volatile PAHs analyzed via extractive techniques, Experiments have been carried out with ethylene as the fuel. Results on

a. the effect of equivalence ratio on the soot size distributions derived for fixed dilution ratio
b. the effect of dilution ratio on the soot size distribution for fized equivalence ratio
c. the effect of temperature on the soot size distribution for fixed equivalence ratio.

have been obtained.

They demonstrate the ability to measure highly diluted particle size distributions using a gas cooled dilution probe in a combustion environment at temperatures near 1400K and showed that soot size distributions were sensitive to equivalence ratio. The particle size distribution at an equivalence ratio of 2 was closest to the self preserving distribution for coagulation in the free molecule region.

The gas chromatographic analysis of the volatile fraction was (up to four aromatic rings) in reasonable agreement with the results of simulations using the ethylene portion of the heptane combustion database. It is also in agreement with several other existing soot models. This is fairly impressive. We have however discussed our reservations on this type of fits. Clearly there is much to be done. Ethylene is probably the unsaturated compound that is has the lowest propensity for PAH and soot formation. There is thus the need to examine the behavior of other possible precursor.

Our last set of experiments may be of some importance in establishing a more unambiguous mechanism. This involves adding small amounts of compounds that may play a key role in the formation of larger aromatic rings into the combusting ethylene mixture near the incipient soot formation regions. The two compounds that have been tested are ethylbenzene and benzene. The former has very little effect on the distribution of PAH that are formed. However the latter has dramatic effects on the yields of larger rings (up to 4 rings). Clearly this suggests the role of phenyl radicals. Much more needs to be done. The issue is whether using such molecular probes it will be possible to reduce the ambiguity in the PAH and soot formation mechanism.

B. Introduction

The recent DOE Workshop on Basic Research Needs for Clean and Efficient Combustion for 21st Century Transportation Fuels[1] identified a " single overarching grand challenge, ***The development of a validated predictive, multiscale combustion modeling capability to optimize the design and operation of evolving fuels in advanced engines for transportation applications***..... This predictive capability, if attained, will change fundamentally the process for fuel research and engine development by establishing a scientific understanding of sufficient depth and flexibility to facilitate realistic simulation of fuel combustion in existing and proposed engines."

The technical progress that makes this a realistice possibility are in the advances in Computational Fluid Dynamics (CFD) codes hat have lead to the capability of describing complex reactive flow problems and thus simulating combustion phenomenon in ever greater detail[2,3]. Increasingly, there is the opportunity of simulating the behavior of **real fuels in real devices**. It promises to bring combustion technology into the modern era. One could not design VLSI chips without simulation capabilities. Modern airplanes are largely designed on the basis of simulation before wind tunnel tests. The Montreal Protocol that limits Freon manufacturing is largely based on the results of simulations. Warnings on global warming are based on simulations. Currently, combustion technology is still based to a large extent on expensive and uncertain physical testing. This places severe constraint on innovation and optimization.

The fundamental problem in combustion simulation has always been the difficulties in bringing detailed chemistry into CFD codes. Combustion phenomena is the manifestation of the complex interaction between chemical kinetics and fluid dynamics. Thus the simulations that have been carried out have been largely based on ignoring the role of one or the other area. The present program is designed to help in providing the chemical kinetic information necessary for properly using the state of the art CFD codes.

There are a number of fundamental barriers in the development of the necessary chemical kinetic databases for simulation applications to real systems. The basic problem is that the nature of the fuel[4] and chemistry is extremely complex. The fuel that is generally used is not well specified. Without proper specification of the fuel, it is impossible to carry out the type of molecule based simulation that is the basis of the more fundamental approach. Even the detailed chemistry of the combustion of a single real fuel molecule involves hundreds of species and thousands of reactions. This will need to be expanded for fuel mixtures.

There has been much recent work aimed at selecting a set of compounds that in mixtures can serve as surrogates for real fuels [5]. This work is nearing completion and it is the consensus of combustion scientists that this is a realistic approach. Without such "standard" fuels it will be impossible to carry out reproducible experimental results that are the ultimate basis for any research program. At the same time it will permit the preparation of appropriate databases for simulations.

There exists a large number of kinetic databases for specific fuel molecules[6-10]. The general approach is to take whatever data in the literature, supplement this with the general rules that have been developed in studies that are usually based on smaller molecules and as a final step, adjusting a number of rate constants so that the simulation can match the limited set of experimental global observations.. The fact that for an organic molecule such as heptane, there are many databases is an indication of the unsatisfactory nature of this approach. This general process is nevertheless fully in line with traditional means of describing and modeling chemical processes. Combustion can be regarded as a chemical process aimed at generating energy, carbon dioxide and water without the production of undesirable side products such as NOx and soot. For chemical processing there is the sequence; from bench to pilot to full scale. Classical chemical industry methods are usually focused on a single operational systems. We also note that the scale up factor from pilot to full scale is usually not very large. This is directly related to the empiricism in such an approach. Combustion applications are large and varied. Thus a purely empirical approach based on laboratory measurements may not be sufficient.

The chemical kinetics database needed for the simulation of the breakdown of any organic fuel under all combustion conditions can be divided into four distinct and more or less independent modules. They are

(a) The decomposition and oxidation of methane and related hydrocarbons.
(b) The oxidative breakdown of larger fuel molecules
(c) The pyrolytic breakdown of large fuel molecules into small unsaturated species that are the precursors if Soot/PAH formation
(d) The reactions of the small unsaturates and their growth that ultimately lead to Soot/PAH formation.

The information for part (a) can be found in GRIMECH(11).. Most existing models for fuel combustion are in category (b). They are applicable to near stoichiometric situations. There are numerous Soot/PAH models, In general they are not as complete as the first three categories and represent a research frontier. The present work will focus on modules (c) and (d).

Module (c) represents an area that has not been emphasized in combustion modeling. Nevertheless it is a process that can be competitive with oxidation and the unsaturated compounds are the precursors to soot models. It extends the application of combustion models (b) to much richer conditions. There have been much work on module (d)[12]. They have not been altogether satisfactory. An important reason is that this is an intrinsically more difficult problem. For all of the other three modules complex molecules are broken down to simpler entities. As the reaction proceeds, the system becomes simpler. In contrast for SOOT/PAH formation, as the reaction proceeds new and more complex species are being formed. Thus the database becomes larger. Furthermore these larger and complex PAHs are extremely expensive to obtain in pure form. Thus the standard and well established methodology for determining mechanism and rate constants cannot be employed. The general procedure is therefore to begin with a small unsaturated compound, carry out experiments under rich

conditions, determine the spectra of PAHs and in some instances the nature of the soot particles and then through kinetic modeling extract rate constants that can now be used to simulate the process.

The elements of the database are single step chemical reactions. These represent fundamental properties of molecules similar to a boiling point. They are thus not adjustable parameters. However in the absence of data estimates must be made. Since the chemistry of combustion is extremely complex and for proper description there are scores of species and reactions global results such as ignition delays, flame speeds or PAH formation can always be reproduced by a certain set of reactions. The important issue is whether such sets of reactions can have predictive capabilities. This is of course the rationale for such work. The expectation is that the development of a "correct" model will lead to a design tool for innovation and optimization in combustion technology.

The non-uniqueness problems in the development chemical kinetic databases has been mentioned earlier. This is made worse by the fact that chemical kinetics is a research area. Thus new quantitative understanding is constantly being developed. The intricacies of the chemistry and the resulting fits means that it is extremely difficult to incorporate "new" details into an existing database that has already been fitted to reproduce certain sets of results. The current program thus seek to begin the process of deriving a more up to date and fundamentally sound chemical kinetics database for simulations.

Heptane has been chosen as an initial fuel compound. The various elements in the program are outlined in this report contain

Unimolecular reactions for the decomposition of heptane, heptyl radicals and all the associated compounds and radicals in the decomposition chain (CSTL)
A database for heptane combustion that partially incorporates the results from the first item (CSTL)
Experimental results dealing with cyclopentadiene type radicals (CSTL)
Description of the stirred flow-plug flow reactor that was constructed under this program (BFRL)
Measurement of particle distribution from the stirred flow-plug flow reactor (BFRL)
Analysis of volatile species and those trapped on particulates in the filter. (CSTL and BFRL)
Experimental studies on determining soot formation by Laser Induced Incandescence, (BFRL).

References

1. Basic Research Needs for Clean and Efficient Combustion of 21st Century Transportation Fuels" Report of the Basic Energy Sciences Workshop on Basic

Eesearch Needs for Clean and Efficient Combustion of 21st Century Transportation Fuels, Office of Science, US. Department of Energy, 2007
2. Kee, R. J., Coltrin, M. E. and Glarborg, P., "Chemically Reacting Flow" Theory and Practice, Wiley, Interscience, New York, 2003
3. Maas, U. and Pope, S. B., Comb. Flame 88, 2391, 1992
4. Edwards, T., Harrison, W. E. III, and Maurice, L. Q., "Properties and Usage of Air Force Fuel: JP-8", AIAA 2001-0498, 39th AIAA Aerospace Sciences Meeting and Exhibit, Jamuary 8-11, 2001 Reno. NV
5.. Colket M., Edward, C. T., Williams, S., Cernansky, N. P., Miller, D. L., Egolfopoulos, F., Lindstedt, P., Seshadri, K., Dryer F. L., Law, C. K., Friend, D., Lenhart, D. B., Pitsc, H., Sarofim, A, Smooke, M., Tsang, W., "Development of an Experimental Database and Kinetic Models for Surrogate Fuels", 45th AIAAAerospace Sciences Meeting and Exhibit, Reno, Nevada, January 9, 2007
6. Curran, H. J., Gaffuri, P., Pitz, W. J., and Westbrook, C. K.,"A Comprehensive Modeling Study of Heptane Combustion". Comb. and Flame., 114, 149, 1998
7. Lindstedt, R.P., Maurice, L.Q. Detailed Kinetic Modeling of n-Heptane Combustion Comb. Sci. Tech., 1995, 107: 317-353.
8. Bakali, A.E., Delfau, J-L., Vovelle, C., Kinetic Modeling of a Rich Atmospheric Pressure, Premixed n-Heptane/O2/N2 Flame. Combust.Flame, 1999, 118:381-389
9. Babushok, V. and Tsang, W., *J. Prop. and Pwr.* 20 (2004) 403-414.
10. . Fournet, R., Warth, V., Glaude, P.A., Battin-Leclerc, F., Scacchi, G., Come, G.M., Int.J.Chem.Kinet., 2000, 32:36-51.
11. Smith, G. P., Golden, D. M., Frenklach, M., . Moriarty, N. W., Eiteneer, B., Goldenberg, M., Bowman, C. T., Hanson, R. K., Song, S., Gardiner, W. C., Jr., Lissianski, V. V., and Qin, Z., http://www.me.berkeley.edu/gri_mech/
12. Richter H, and Howard J.B., Prog. Energ. Combust.: 4 565, 2000

C. Heptane Pyrolysis

The breakdown of heptane to form the small unsaturated precursors to soot is largely a free radical process. There are two pathways for the generation of radicals in combustion systems. The first involve the breaking a carbon-carbon bond from stable compounds and intermediates formed as a result of the decomposition process. These processes become important at higher temperatures. The compounds of interest are heptane itself and the 1-olefins, or specifically 1-hexene, 1-pentene and 1-butene, This will be one focus of the present work. There have been much experimental and theoretical work on these processes. Correlations have been established and predictions can be made. The general situation is quite satisfactory.

Radicals can also be formed from the attack of reactive radicals on the fuel itself. There has been much experimental and theoretical work on the kinetics of such processes. Correlations have been developed and rate constants can be estimated with high accuracy. The appropriate values can be found in many existing models of fuel combustion.

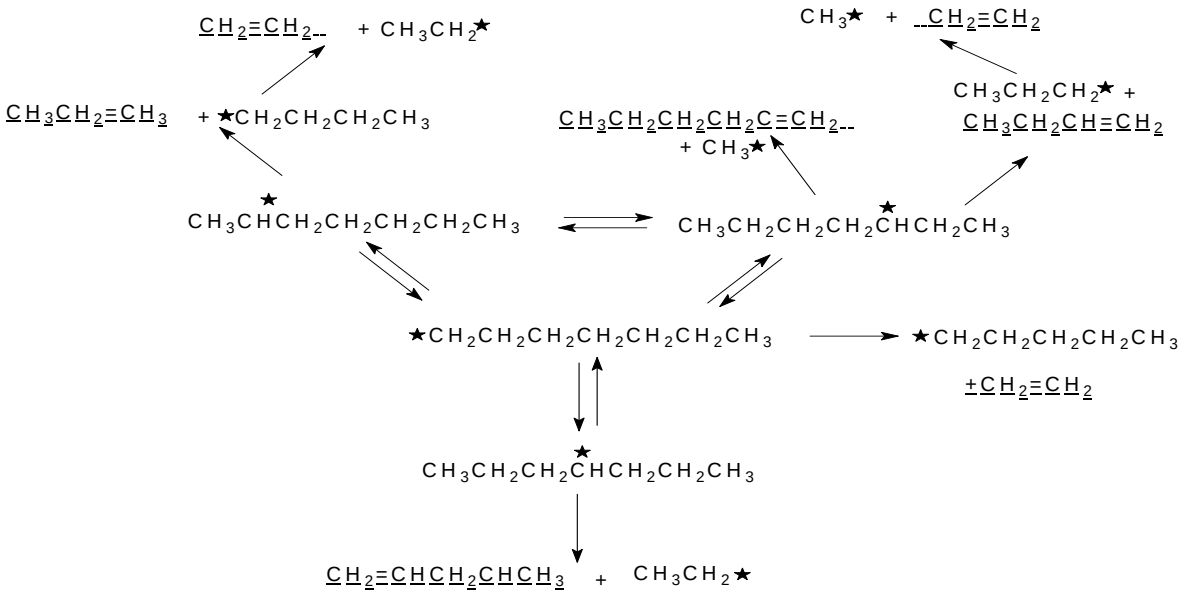

Figure 1: Mechanism for the decomposition and isomerization reactions of the four heptyl isomers

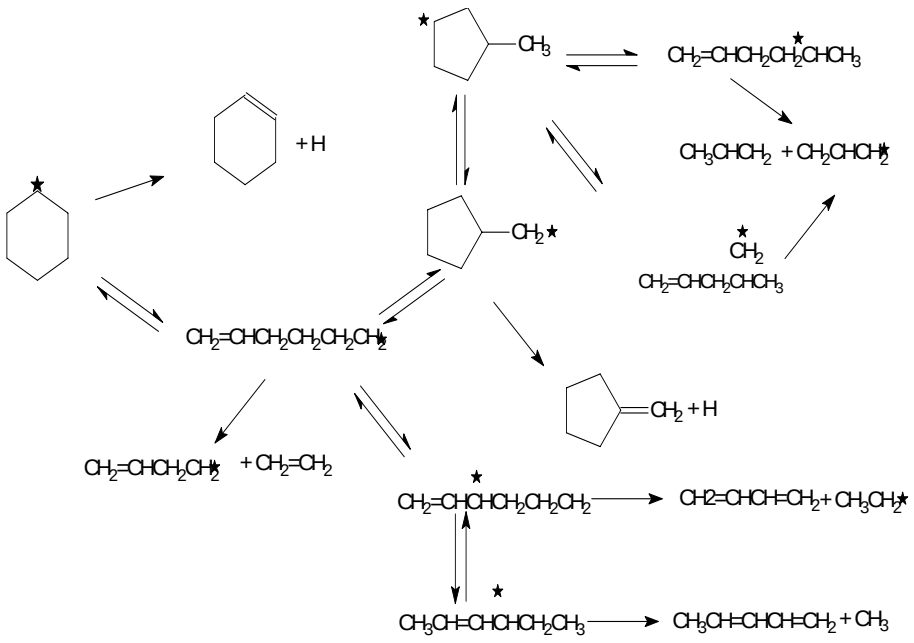

Figure 2: Mechanism for the decomposition of 1-hexenyl-6, 1-hexenyl-5, 1-hexenyl-3, and various cyclopentyl and cyclohexyl radicals. Note the absence of 1-hexenyl-4 in the reaction scheme.

Decane Decomposition $C_7H_{16} \rightarrow CH_3 + C_6H_{13}$ $C_7H_{16} \rightarrow C_2H_5 + C_5H_{11}$ $C_7H_{16} \rightarrow C_3H_7 + C_4H_9$ **Heptyl Radical Isomerization** $1\text{-}C_7H_{15} \Leftrightarrow 2\text{-}C_7H_{15}$ $1\text{-}C_7H_{15} \Leftrightarrow 3\text{-}C_7H_{15}$ $1\text{-}C_7H_{15} \Leftrightarrow 4\text{-}C_7H_{15}$ $2\text{-}C_7H_{15} \Leftrightarrow 3\text{-}C_7H_{15}$ **Heptyl Radical Decomposition** $1\text{-}C_7H_{15} \rightarrow C_2H_4 + 1\text{-}C_5H_{11}$ $2\text{-}C_7H_{15} \rightarrow C_3H_6 + 1\text{-}C_4H_9$ $3\text{-}C_7H_{15} \rightarrow 1\text{-}C_4H_8 + 1\text{-}C_3H_7$ $3\text{-}C_7H_{15} \rightarrow 1\text{-}C_6H_{12} + CH_3$ $4\text{-}C_7H_{15} \rightarrow 1\text{-}C_5H_{10} + C_2H_5$ **Pentyl Radical Isomerization** $1\text{-}C_5H_{11} \Leftrightarrow 2\text{-}C_5H_{11}$	**Pentyl Radical Decomposition** $1\text{-}C_5H_{11} \rightarrow C_2H_4 + 1\text{-}C_3H_7$ $2\text{-}C_5H_{11} \rightarrow C_3H_6 + C_2H_5$ **Olefin Decomposition** $1\text{-}C_4H_8 \rightarrow C_3H_5 + CH_3$ $1\text{-}C_5H_{10} \rightarrow C_3H_5 + C_2H_5$ $\rightarrow C_3H_6 + C_2H_4$ $1\text{-}C_6H_{12} \rightarrow C_3H_5 + 1\text{-}C_3H_7$ $\rightarrow C_3H_6 + C_3H_6$ **1-Butenyl Radical Decomposition** $1\text{-}C_4H_7\text{-}3 \rightarrow 1,3\text{-}C_4H_6 + H$ $1\text{-}C_4H_7\text{-}4 \rightarrow 1,3\text{-}C_4H_6 + H$ $\rightarrow C_2H_3 + C_2H_4$ **1-Pentenyl Radical Decomposition** $1\text{-}C_5H_9\text{-}3 \rightarrow 1,3\text{-}C_4H_6 + CH_3$	$1\text{-}C_5H_9\text{-}4 \rightarrow 1,3\text{-}C_5H_8 + H$ $\rightarrow 1,4\text{-}C_5H_8 + H$ $\rightarrow C_2H_3 + C_3H_6$ $1\text{-}C_5H_9\text{-}5 \rightarrow C_3H_5 + C_2H_4$ $1\text{-}C_5H_9\text{-}5 \Leftrightarrow c\text{-}C_5H_9$ $c\text{-}C_5H_9 \rightarrow c\text{-}C_5H_8 + H$ **1-Hexenyl Radical Decomposition** $1\text{-}C_6H_{11}\text{-}3 \rightarrow 1,3\text{-}C_4H_6 + C_2H_5$ $1\text{-}C_6H_{11}\text{-}4 \rightarrow 1,4\text{-}C_5H_8 + CH_3$ $1\text{-}C_6H_{11}\text{-}5 \rightarrow C_3H_5 + C_3H_6$ $1\text{-}C_6H_{11}\text{-}5 \Leftrightarrow 3\text{-}CH_3c\ C_5H_9$ $3\text{-}CH_3c\ C_5H_8 \Leftrightarrow CH_2c\text{-}C_5H_9$ $CH_2c\text{-}C_5H_9 \Leftrightarrow 1\text{-}C_6H_{11}\text{-}6$ $1\text{-}C_6H_{11}\text{-}6 \Leftrightarrow c\ C_6H_{11}$ $1\text{-}C_6H_{11}\text{-}6 \Leftrightarrow 1\text{-}C_6H_{11}\text{-}4$ $c\ C_6H_{11} \rightarrow c\ C_6H_{10} + H$ $1\text{-}C_6H_{11}\text{-}6 \rightarrow 1\text{-}C_4H_7\text{-}4 + C_2H_4$

Table 1. Specific reactions involved in the pyrolysis of heptane

Seven carbon	Six carbon	Five carbon	Four carbon	Three carbon
Heptyl –1 Heptyl –2 Heptyl –3 Heptyl –4	1-hexenyl-6 1-hexenyl-5 1-hexenyl-4 1-hexenyl-3 cyclohexyl cyclopentylmethylene methylcyclopentyl	Pentyl-1 Pentyl-2 1-pentenyl-5 1-pentenyl-4 1-pentenyl-3 cyclopentyl	Butyl-1 1-butenyl-4 1-butenyl-3	Propyl-1

Table 2. Radical species involved in heptane and 1-hexene pyrolysis.

The next process involves the breakdown of the large radicals that are formed. This is the focus of the present work. The mechanism for the breakdown of heptyl and 1-hexenyl and cyclohexyl radicals can be found in Figures 1 and 2. The necessity for understanding of the linear alkyl radicals are obvious. The presence of the latter is due to the conversion of some of the 1-hexenyl radicals to cyclohexyl. Examination of Figures 1 and 2 is indicative of the key role of isomerization. This is superimposed on the beta bond scission reactions that actually reduce the radical size.

Examination of the reactions and species in Tables 1 and 2 shows that for every large alkane fuel the breakdown process must include in the database those reactions that involve the breakdown of the smaller species in the reaction chain. For heptane, this involve radicals with five carbons or less Thus from heptyl radicals, pentyl, butyl and propyl radicals are formed during the decomposition process. These processes also lead to the formation of the 1-hexenyl, 1-pentenyl and 1-butenyl radicals. The decomposition of these compound leads to the formation of the dienes that are known to have high propensity for PAH/Soot formation. The mechanism for the decomposition of the smaller saturated radical fragments are much simpler than the parent. Thus for example, for 1-pentyl radical, the decomposition process is

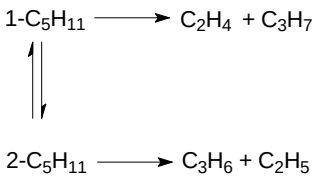

Figure 3: Mechanism for the decomposition of pentyl radicals

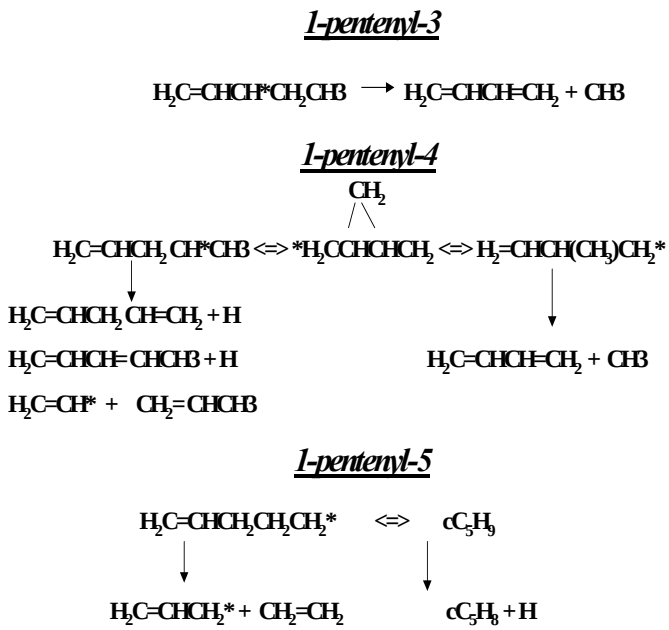

Figure 4: Mechanism for the decomposition of 1-pentenyl radicals. The absence of contributions from isomerization means that each isomer is decomposing by itself.

Reactions for the three 1-pentenyl radicals are summarized in Figure 4 In comparison to Figures 1 and 2 note the simplicity of the mechanism. For pentyl radical, there is only one possible isomerization. This is in contrast to heptyl where there are 4 isomerization processes. For 1-butyl there is only one possible reaction. In the case of 1-butenyl there are two possible isomers and they do not interconvert. Thus for real fuels, there are drastic increases in possible processes that must be considered.

All the reactions under consideration are unimolecular processes [1]. This is an active research area and there has been much progress. It is now possible to describe processes that involve species that are not equilibrated with the bath. The consequence is rate constants that have pressure dependences. This is particularly important for combustion environments since it is the large rate constants brought about by the high temperatures that distort the equilibrium distributions. These developments is however generally not reflected in the available kinetic databases. This is another rationale for the present approach. We have developed a program to treat such effects[2]. It take as input data high pressure rate expressions, that is reactions with the molecules that are equilibrated with the bath, calculates the departures from such situations and derives a pressure dependent arate constant. This will be used for the present application.

Procedures: The basic information for describing such processes are the high pressure rate expressions. This must be obtained from direct experiments. For this purpose we make use of available data in the literature or carry out studies using a single pulse shock tube. For the former we not only take advantage of direct measurements but also derive values on the basis of detailed balance from rate measurements on the reverse reactions and through various empirical correlations.

Figure 5 contains a schematic of our single pulse shock tube. This is a well established technique[3] and has the unique capability of studying the unimolecular isomerization and decomposition of the larger polyatomic molecules. .The special

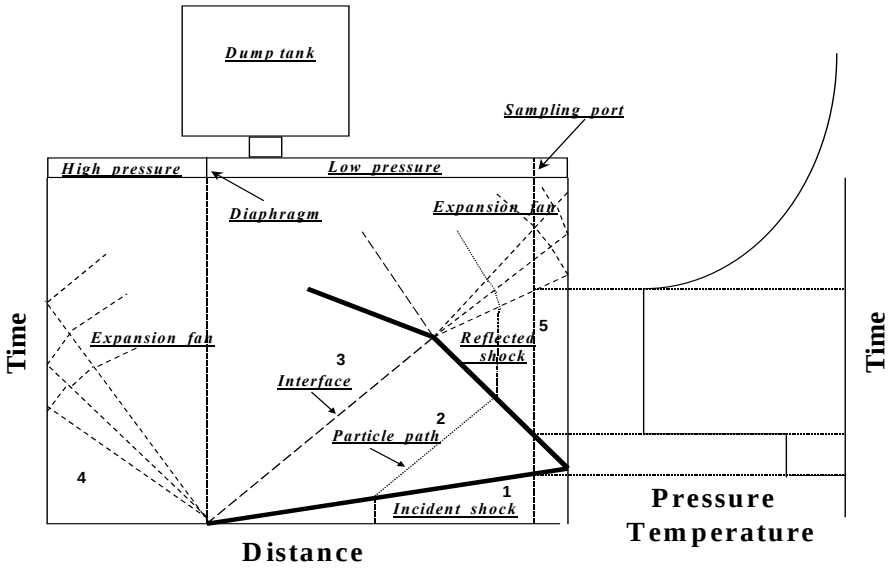

Figure 5: Schematic of single pulse shock tube and associated wave diagrams.

characteristic of single pulse shock tube experiments is the homogeneous heating by the shock wave and the short reaction time. In the present case this is of the order of 500 microsecs. When this is coupled with studies at sufficiently low concentration and the presence of radical scavengers that capture reactive radicals, the consequence is that a particular molecule is isolated in the high temperature environment and can only undergo unimolecular decompositions and isomerizations. The methodology has been used to study the decomposition of larger organic fuel molecules. Indeed the results on the decomposition of heptane and associated 1-olefins to be presented below are based on correlations derived from the earlier studies.

For larger fuel radicals such as those with six or seven carbon atoms there are no direct experimental data. Particularly important is the need to determine the branching ratios for the initial decomposition steps. The procedure is to find a suitable precursor that readily releases the radical into the high temperature environment. For the present studies we use the following compounds; n-heptyl iodide for heptyl radical and 1,8 nonadiene and tertbutylcyclohexane for 1-hexenyl-6 These radicals are very

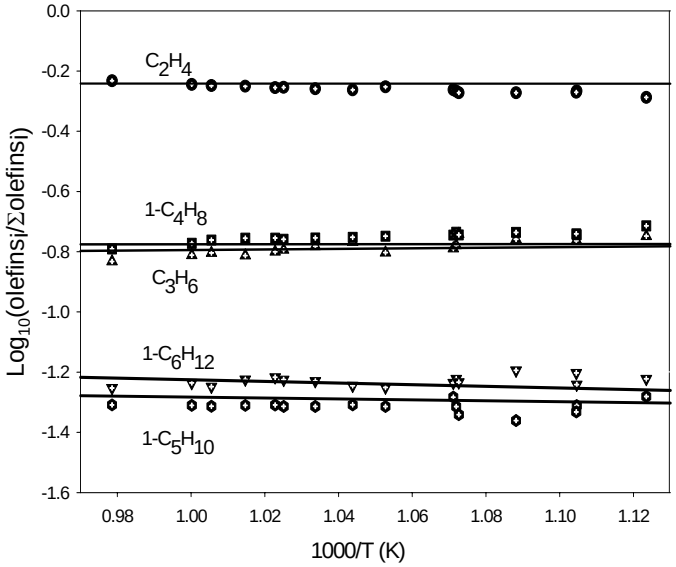

Figure 6: Branching ratio for olefin production during the decomposition of heptyl-1 [4]

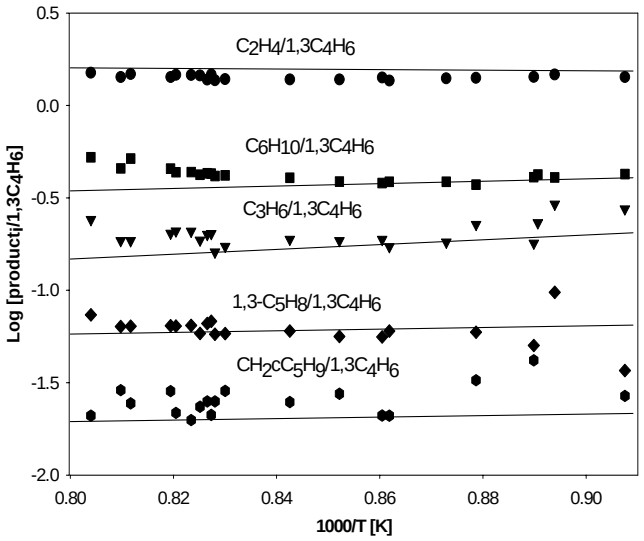

Figure 7 Branching ratios in terms of olefin to 1,3-butadiene during the decomposition of cyclohexyl radicals from tertbutyl cyclohexane

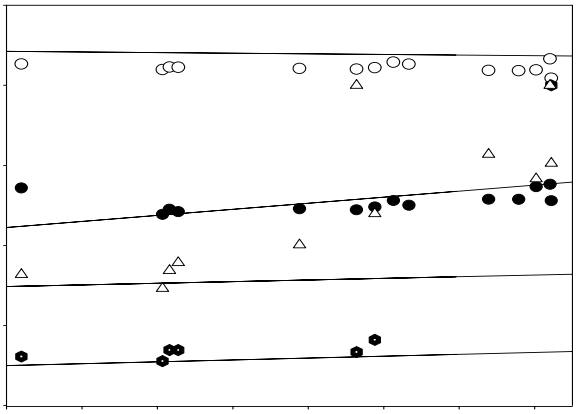

Figure 8 Branching ratios in terms of olefin to 1,3butadiene during the decomposition of 1-hexenyl-6 radicals from 1,8 nonadiene

unstable and in the shock tube environments they decompose in the microseconds or less. Absolute rate constants cannot be obtained. The experimentally determined quantities were the branching ratios for olefin production. Some typical results can be found in Figures 6-8

The present procedure is to fit the experimental observation through unimolecular rate theory using the NIST developed program to obtain high pressure rate constants. The input for this program are the molecular properties of the species and transition states. Data dealing with the radicals in question do not exist. Particularly important are the thermodynamic properties. The methodology for making accurate predictions is well established. The present treatment attempts to be consistent with the values in the API Tables[5]. . We follow the observation of Pitzer[6] on the additional vibrational frequencies needed upon insertion of a methylene group into a linear hydrocarbon molecule. We then adjust the low frequency modes so that the thermodynamic properties are the same as those given in the standard tables[5]. Radical properties are derived on the basis of the prescription of Benson[7]. Vibrational frequencies associated with the hydrogen motion (at the radical site) are eliminated and the hindered rotors adjacent to the radical site are converted into free rotors. The resulting properties of the radicals covered in the pyrolysis of heptyl radicals can be found in the table on pg.49. The bond dissociation energies for primary and secondary C-H bonds are taken to be 420 and 412 kJ/mol & the allylic resonance energy is 45 kJ/mol[3] The primary use of these properties are directly in simulations and for calculating rate constants of the decomposition process in many of the instances where rate constants of the reverse addition reaction is available. The transition state structures were chosen to reproduce the desired A-factor in the rate

expression. It is known that energy transfer effects are not particularly affected by the molecular properties of the transition state as long as the proper A-factor can be reproduced.

There are some unique issues in treating the unimolecular reaction with multiple channels including isomerization and with low reaction thresholds[8]. Probably most important is the necessity for treating the system as open in the sense of continually creating radicals. This is in contrast to the situation treated in standard texts where the thresholds are sufficiently large so that the peak of the distribution function is much smaller. In the present case for sufficiently large molecules the threshold is smaller than the peak of the distribution function. Thus the radical is inherently unstable. An open system leads to a constant distribution function and it is then possible to deduce rate constants. A necessary consequence of this effect is that as the temperature becomes sufficiently high rate constants begins to return to the high

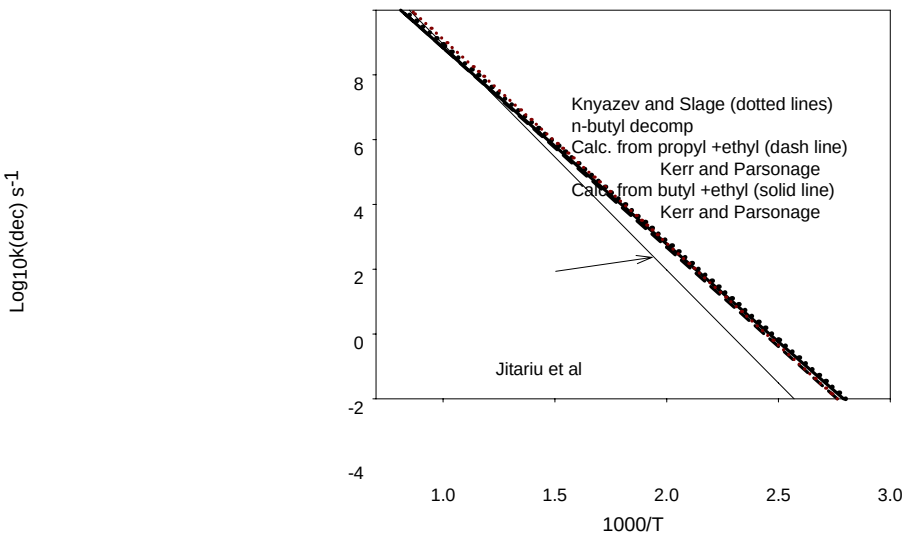

Fig 9: Rate constants as a function of temperature for the beta bond scission reaction for various 1-alkyl radical [9-11[. The results of Jitariu et al are for 1-pentyl

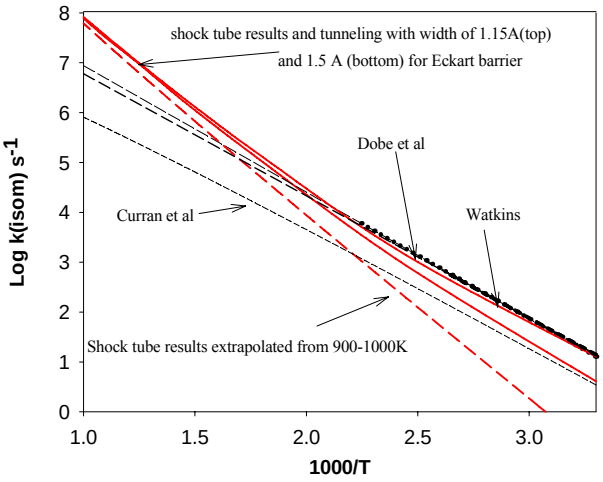

Figure 10: Rate constants for 1-5 H-transfer isomerization for 1-hexyl radical[12-14]

pressure value, since the decomposition can now occur from the original high temperature Boltzmann distribution. This leads to Arrhenius plots at constant pressure that initially show the expected negative curvature but then develops a positive curvature. This makes it virtually impossible to represent the rate expression in standard formats. The rate expressions were chosen to match the experimental results. For this purpose we begin by noting that rate constants for beta bond scission are invariant with regard to the departing alkyl group. This can be seen in Figure 9, With these values fixed we then determine rate expressions for H-transfer isomerization. The rate constants for 1-4 and 1-5 H-transfer isomerization are uniquely determined in studies on [8] 1-pentyl and 1-hexyl radicals. The experimental work on these processes has been carried several years ago.

A long standing problem was the low observed values[12-14] for the rate parameters for the isomerization processes. As a result it has not been possible to construct transition state structures. Nevertheless these are simple systems and the experimental results appear to be replicable. However our experimental results are inconsistent with linear extrapolation to the lower temperature region. We have rationalized these observations on the assumption that the observed effects are a consequence of tunneling. This is reasonable. H-atoms are being transferred and there is a considerable barrier. Using an unsymmetrical Eckart barrier with a width of 1.15 Angstroms. We are able to fit the high and low temperature results with a highly curved Arrhenius plot. The results for 1-5 H-transfer isomerization for 1-hexyl can be found in Figure 10. A somewhat similar plot can be made for 1-4 H-transfer isomerization for 1-pentyl.

For heptyl radicals we begin with the same values and make adjustments to fit the experimental observations. It appears that such variations are very small and our

tentative conclusions it that for 1-n H-transfer processses the size of the adjoining alkyl group has very little effect. For heptyl radical there is also contributions from 1-6 H-transfer isomerization. Surprisingly this is only a factor of 2 smaller that that for 1- 5 H-transfer isomerization. The general trends for the two isomerization processes described earlier suggest the role of ring strain contributing to the activation energy and decreases in the entropy of activation. If this is the case, then the rate constants for 1-6 isomerization would be much smaller than those for the 1-5 H-transfer reaction. A problem with the present procedure is that as the fuel radical gets sufficiently large the internal isomerization in the form of secondary to secondary radical isomerization can make contributions. In the present case we have assumed that the rate constant for 3 to 2 H-transfer involving a 5 member transition state is intermediate between the value for the exothermic 1-4 and endothermic 4-1 H-transfer process. In order for the 1-6 H-transfer isomerization to be much smaller than the value for 1-5 H-transfer reaction, the rate constant for the thermally neutral 3-2 isomerization process must be much larger than the exothermic 1-4 process. This seems unlikely.

Cyclohexyl and 1-hexen-6-yl are two radicals that are treated together due to their conversion into each other as a result of cyclization and decyclization processes. Cyclic radicals can be formed directly from cyclic fuels. Fuels containing cyclanes are formed from tar sands and oil shale. One can expect greater quantities of such compounds in future fuel mixtures. A natural issue is how these compounds will affect their combustion and pollution generation properties.

The data on cyclohexyl and 1-hexen-6-yl radicals were generated from the pyrolysis of tert-butylcyclohexane and 1,8-nonadiene. The cleavage of the weakest bonds in these molecules releases the desired radicals into the shock tube system. The temperatures are somewhat higher than those for the 1-iodoheptane pyrolysis. This is due to the greater thermal stability of the precursors. Results are cast in the form of ratio of products to 1,3-butadiene. This is because in 1-8 nonadiene decomposition propene can be formed from a variety of mechanisms. Therefore the yields cannot be used as a measure of the cracking pattern of interest. The experimental results are summarized in Figures 7 and 8. Figure 9 contains important experimental results on the chemically activated isomerization of cyclohexyl radicals. This will be discussed subsequently. The contribution from this program is as in the heptyl case to rationalize these results in terms of rate constants and thus provide a basis for generalizations.

These results are consistent with the mechanism as outlined in Figure 2. It is clear that the introduction of cyclization and olefinic structures leads to extra complications in comparison to a linear radical such as heptyl. The overall mechanism now involves eight radical species, seven beta bond scission and seven reversible isomerizations. Note that the only 1-hexenyl radical that is not formed is the 1-hexen-

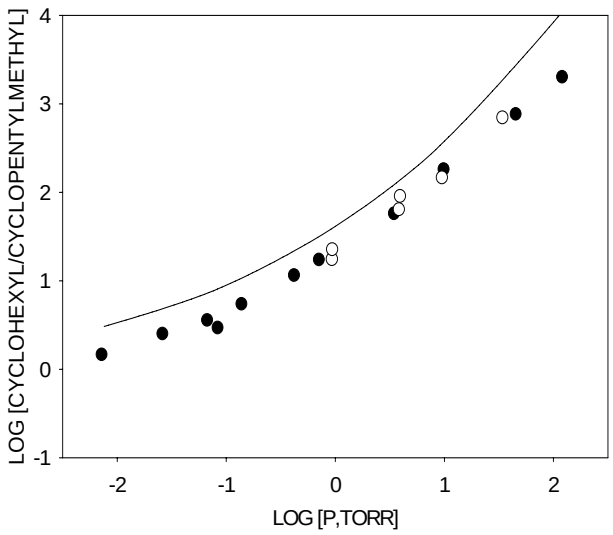

Figure 11: Cyclohexyl to cyclopentylmethyl ratios from the chemically activated decomposition of cyclohexyl radical formed from H-addition to cyclohexene. The Line is the result of using the same step size down for H_2 as in cyclopentyl radical decomposition

4-yl species. The can be compared with the much simpler situation for heptyl radicals where there are four isomers, five beta bond scissions and four reversible isomerization.

Interest in the 1-hexenyl radicals is due to the sequence of reactions

Fuel radical => smaller radical + 1-olefin => 1-olefinyl => dienes

The subsequent cyclization of the 1-hexen-6-yl radical provides a natural link between the linear and cyclic fuels.

Ethylene is once again the major product. However large quantities of 1,3-butadiene are formed. Cyclohexene is another product and is present in concentrations similar to that for propene. As the temperature is increased it is decomposed to form butadiene and ethylene. The values in Figures 7 and 8 represent the corrected numbers and takes this into account. Many minor products are also formed. The present analysis tries to account for their presence. This is not due to the intrinsic importance of these compounds in the breakdown of the molecules studied here. They yield insights into the mechanisms for the reactions of other types of molecules and thus provide the basis for making estimates.

The introduction of cyclization processes leads to processes that are different than those for the linear radicals. Nevertheless a combination of the cracking patterns derived from the shock tube studies and literature values do permit a basis for estimation. These are summarized in Table 3. Particularly important are issues bearing on the relative importance of terminal to non-terminal addition leading to cyclization. Fortunately, there exist data that bear unambiguously on this issue. This is the results of Stein and Rabinovitch[15] on the chemically activated decomposition of cyclohexyl radicals generated form the addition of H-atoms to cyclohexene. Using a step size down parameter from an earlier study on cyclopentyl radical reactions, we find that their results are consistent with the rate constants for the two processes being fairly close to each other.

The lines in Figure 7 are based on the high pressure rate expressions given in Table 3 and assuming a step size down of .3*T cm^{-1} for collisions with argon. This is the same value used in the analysis of all the cracking patterns derived from shock tube experiments. The results is that the rate constants actually determined are about 0.3 to 0.5 of the high pressure value. Figure 8 contains a plot of products to butadiene formed from the decomposition of 1-hexenyl-6. The lines are derived from the high pressure rate constants used in fitting the results from cyclohexyl radical decomposition (see Figure 7). This represents an excellent consistency check of the results. It would probably be worthwhile to carry out similar studies with other radical starting products. An interesting result is the larger yields of cyclohexene from cyclohexyl in comparison to those from 1-hexenyl-6. This may have significance in comparing sooting tendencies of cyclic to olefinic fuel components.

An interesting consequence of the present work is that the rate constants for 1-4 H-transfer isomerization of cyclopentyl methyl radical into the five membered ring is considerably smaller than those for a straight chain radical. This is understandable on a purely structural basis. It opens up the problem of defining rate constants for H-transfer isomerizations involving other ring structures. This can be a challenge. For real fuels, there is the ultimate need to estimate rate constants for processes involving methylated decalines. It may well be that theory can give some guidance on these issues. The quantitative description of this set of reactions may well be the remaining hurdle for the proper treatment for the pyrolysis of real fuels. These H-transfer isomerizations are also important in the sequence of reactions leading to oxidation.

An important issue is the uncertainties in the rate constants that have been determined. In the case of heptyl radicals the simplicity of the mechanism should minimize the uncertainties. The complications of the mechanism for the cyclohexyl system will increase the uncertainties. This will be particularly serious if a product is formed from a series of reactions or through parallel pathways. Of course the uncertainties will decrease by starting with different radicals. The results with 1-hexenyl-6 is thus reassuring.

A complete picture of departures from the high pressure values for combustion applications can only be given in tabular form as for heptyl in Table 4. As before each of the eight isomers must be described individually in terms of seven bond fission and seven reversible isomerization reactions. Except for the ring closing reactions that have extraordinarily low barriers and A-factors, the general patterns are very similar to those for the heptyl isomers described earlier.

Results: The recommended rate constants for all the processes of interest can be found in this section. The order are given from the largest (7 carbon atoms) to the smallest (4 carbon atoms). They are separated into the alkyl and 1-alkenyl radicals. The hexyl radicals are not included since they are not formed in the decomposition of heptyl radicals. The results are given in the form of high pressure rate expressions and as deviations from high pressure behavior in tabular form over the range of 0.1 to 100 bar and appropriate lower temperature up to 1900 K. The reason for the tabular form is that it has not been possible to use standard formats for pressure dependent reactions. As will be seen latter this is due to the multichannel nature of the reactions and the very low reaction threshold that can in fact be below the peak of the normal molecular distribution function. .

A: Heptyl Radicals:

A1: ***heptyl-1, heptyl-2, heptyl-3, heptyl-4*** : Due to H-transfer isomerization via 1-4, 1-5, 1-6 and 3-2 processes all the isomeric heptyl radicals are formed during the decomposition of 1-heptyl radicals. The rationale for the selection of the high pressure rate expression has been given in an earlier section. The deviations from high pressure behavior are tabulated in Tables 4a-d. For a number of the isomerization reactions k_∞/k is slightly smaller than 1. This is impossible and is a consequence of the low reaction thresholds for the isomerization reaction. It is recommended that this deficit be added the tabulated values. Effects are very small and within the estimated uncertainties.

Reaction	Log A	N	Activation energy E/R
$1\text{-}C_7H_{15} = C_2H_4 + 1\text{-}C_5H_{11}$	11.90	.33	13694
$2\text{-}C_7H_{15} = C_3H_6 + 1\text{-}C_4H_9$	11.70	.56	14138
$3\text{-}C_7H_{15} = 1\text{-}C_4H_8 + 1\text{-}C_3H_7$	12.47	.31	14221
$3\text{-}C_7H_{15} = 1\text{-}C_6H_{12} + CH_3$	11.04	.75	14797
$4\text{-}C_7H_{15} = 1\text{-}C_5H_{10} + C_2H_5$	12.77	.31	14221
$3\text{-}C_7H_{15} = 1\text{-}C_7H_{15}$	2.87	2.43	6441
$4\text{-}C_7H_{15} = 1\text{-}C_7H_{15}$	2.10	2.88	9884
$2\text{-}C_7H_{15} = 1\text{-}C_7H_{15}$	1.52	2.81	7561
$3\text{-}C_7H_{15} = 2\text{-}C_7H_{15}$	2.30	2.83	9048
$1\text{-}C_7H_{15} = 3\text{-}C_7H_{15}$	2.83	2.39	5237
$1\text{-}C_7H_{15} = 4\text{-}C_7H_{15}$	2.07	2.85	8680
$1\text{-}C_7H_{15} = 2\text{-}C_7H_{15}$	2.39	2.51	6292
$2\text{-}C_7H_{15} = 3\text{-}C_7H_{15}$	1.39	3.09	9113

Table 3: High pressure rate expressions used in fitting data in Figure 3. Rate expressions are expressed as $k=AT^n exp(-E/RT)$

	Log P	500	700	900	1100	1300	1500	1700	1900
1-C_7H_{15} = C_2H_4 + 1-C_5H_{11}	-1	0.000	0.408	1.002	1.216	1.132	0.952	0.770	0.627
	0	0.033	0.128	0.525	0.812	0.864	0.796	0.691	0.590
	1	0.008	0.024	0.175	0.411	0.556	0.592	0.567	0.518
	2	0.005	0.005	0.031	0.119	0.241	0.333	0.376	0.385
2-C_7H_{15} = C_3H_6 + 1-C_4H_9	-1	0.023	0.241	0.743	1.173	1.360	1.348	1.210	1.024
	0	0.009	0.063	0.313	0.663	0.901	0.989	0.959	0.866
	1	0.007	0.014	0.083	0.267	0.477	0.618	0.673	0.665
	2	0.007	0.006	0.016	0.062	0.161	0.278	0.368	0.417
3-C_7H_{15} = 1-C_4H_8 + 1-C_3H_7	-1	0.021	0.300	0.864	1.262	1.404	1.375	1.242	1.067
	0	0.003	0.081	0.394	0.760	0.979	1.051	1.017	0.924
	1	0.001	0.013	0.114	0.335	0.553	0.689	0.738	0.725
	2	0.001	0.002	0.019	0.088	0.210	0.336	0.426	0.472
3-C_7H_{15} = 1-C_4H_8 + 1-C_3H_7	-1	0.031	0.360	0.979	1.394	1.524	1.475	1.323	1.135
	0	0.007	0.102	0.457	0.853	1.079	1.143	1.095	0.990
	1	0.003	0.018	0.136	0.383	0.619	0.760	0.806	0.786
	2	0.003	0.003	0.024	0.104	0.239	0.377	0.472	0.518
4-C_7H_{15} = 1-C_5H_{10} + C_2H_5	-1	0.025	0.244	0.726	1.102	1.191	1.092	0.913	0.733
	0	0.004	0.066	0.315	0.635	0.805	0.824	0.753	0.649
	1	0.001	0.011	0.082	0.261	0.441	0.539	0.557	0.527
	2	0.001	0.001	0.012	0.055	0.147	0.248	0.317	0.348
3-C_7H_{15} = 1-C_7H_{15} =	-1	0.009	0.069	0.342	0.632	0.820	0.898	0.880	0.801
	0	0.009	0.019	0.146	0.368	0.553	0.663	0.697	0.675
	1	0.009	0.008	0.040	0.156	0.304	0.422	0.491	0.515
	2	0.009	0.006	0.010	0.041	0.113	0.203	0.278	0.328
4-C_7H_{15} = 1-C_7H_{15} =	-1	0.015	0.137	0.533	0.918	1.074	1.033	0.889	0.730
	0	0.011	0.040	0.231	0.529	0.723	0.776	0.732	0.647
	1	0.011	0.012	0.063	0.219	0.397	0.508	0.543	0.526
	2	0.011	0.008	0.013	0.049	0.135	0.237	0.312	0.351
2-C_7H_{15} = 1-C_7H_{15} =	-1	0.007	0.068	0.354	0.695	0.923	1.010	0.972	0.861
	0	0.006	0.017	0.140	0.384	0.599	0.722	0.751	0.714
	1	0.006	0.006	0.035	0.149	0.310	0.442	0.516	0.537
	2	0.006	0.004	0.007	0.033	0.101	0.195	0.277	0.332
3-C_7H_{15} = 2-C_7H_{15}	-1	0.013	0.145	0.567	0.949	1.154	1.201	1.131	1.001
	0	0.011	0.040	0.255	0.567	0.797	0.908	0.918	0.862
	1	0.011	0.012	0.074	0.249	0.449	0.593	0.663	0.674
	2	0.011	0.008	0.017	0.068	0.172	0.291	0.384	0.440
1-C_7H_{15} = 3-C_7H_{15}	-1	-0.021	0.085	0.418	0.616	0.640	0.588	0.503	0.447
	0	-0.022	0.011	0.226	0.403	0.459	0.464	0.435	0.413
	1	-0.022	-0.012	0.090	0.207	0.276	0.323	0.339	0.353
	2	-0.022	-0.016	0.039	0.074	0.110	0.166	0.210	0.255
1-C_7H_{15} = 4-C_7H_{15}	-1	-0.015	0.206	0.735	0.995	0.966	0.840	0.698	0.603
	0	-0.019	0.050	0.398	0.663	0.721	0.691	0.621	0.567
	1	-0.020	-0.004	0.149	0.344	0.454	0.503	0.503	0.496
	2	-0.020	-0.014	0.050	0.116	0.191	0.273	0.327	0.370
1-C_7H_{15} = 2-C_7H_{15}	-1	-0.045	0.095	0.487	0.712	0.728	0.657	0.556	0.488
	0	-0.047	0.002	0.257	0.463	0.525	0.523	0.483	0.453
	1	-0.047	-0.029	0.091	0.232	0.316	0.366	0.379	0.389
	2	-0.047	-0.033	0.027	0.074	0.122	0.187	0.236	0.282
2-C_7H_{15}= 3-C_7H_{15}	-1	0.035	0.130	0.501	0.901	1.139	1.201	1.125	0.979
	0	0.033	0.047	0.215	0.512	0.753	0.875	0.885	0.825
	1	0.033	0.027	0.066	0.211	0.402	0.548	0.621	0.633
	2	0.033	0.024	0.025	0.057	0.141	0.251	0.343	0.401

Table 4a: Log k_∞/k for reactions involved in 1-heptyl radical isomerization and decomposition.

	Log P	500	700	900	1100	1300	1500	1700	1900
1-C_7H_{15} = C_2H_4 + 1-C_5H_{11}	-1	0.029	0.293	0.829	1.282	1.456	1.424	1.268	1.067
	0	0.007	0.072	0.342	0.720	0.964	1.049	1.009	0.903
	1	0.005	0.011	0.080	0.278	0.500	0.652	0.708	0.693
	2	0.004	0.003	0.010	0.054	0.155	0.282	0.379	0.429
2-C_7H_{15} = C_3H_6 + 1-C_4H_9	-1	0.025	0.309	0.924	1.333	1.438	1.349	1.158	0.937
	0	0.009	0.089	0.446	0.838	1.033	1.055	0.967	0.830
	1	0.007	0.019	0.141	0.406	0.630	0.738	0.744	0.690
	2	0.007	0.007	0.028	0.124	0.279	0.413	0.485	0.503
3-C_7H_{15} = 1-C_4H_8 + 1-C_3H_7	-1	0.019	0.248	0.765	1.239	1.481	1.510	1.376	1.150
	0	0.003	0.064	0.321	0.692	0.966	1.083	1.059	0.943
	1	0.001	0.011	0.086	0.281	0.509	0.670	0.732	0.714
	2	0.001	0.001	0.014	0.066	0.176	0.309	0.408	0.458
3-C_7H_{15} = 1-C_4H_8 + 1-C_3H_7	-1	0.029	0.303	0.878	1.383	1.622	1.627	1.466	1.218
	0	0.006	0.083	0.377	0.784	1.072	1.182	1.142	1.009
	1	0.003	0.015	0.105	0.324	0.573	0.742	0.801	0.773
	2	0.003	0.003	0.018	0.079	0.202	0.347	0.454	0.504
4-C_7H_{15} = 1-C_5H_{10} + C_2H_5	-1	0.025	0.233	0.700	1.177	1.456	1.523	1.421	1.220
	0	0.004	0.062	0.280	0.624	0.906	1.049	1.057	0.970
	1	0.001	0.010	0.069	0.226	0.434	0.604	0.689	0.697
	2	0.001	0.001	0.010	0.043	0.121	0.233	0.334	0.397
3-C_7H_{15} = 1-C_7H_{15} =	-1	0.009	0.051	0.283	0.592	0.827	0.955	0.964	0.868
	0	0.009	0.016	0.111	0.323	0.530	0.668	0.719	0.690
	1	0.009	0.008	0.030	0.126	0.274	0.405	0.484	0.507
	2	0.009	0.006	0.009	0.031	0.093	0.183	0.264	0.318
4-C_7H_{15} = 1-C_7H_{15} =	-1	0.015	0.130	0.509	0.961	1.274	1.404	1.362	1.201
	0	0.011	0.038	0.205	0.515	0.800	0.971	1.014	0.957
	1	0.011	0.012	0.053	0.189	0.389	0.565	0.666	0.692
	2	0.011	0.008	0.013	0.040	0.111	0.222	0.328	0.400
2-C_7H_{15} = 1-C_7H_{15} =	-1	0.007	0.104	0.477	0.822	1.006	1.036	0.945	0.794
	0	0.007	0.028	0.224	0.509	0.706	0.788	0.772	0.693
	1	0.006	0.008	0.067	0.243	0.424	0.539	0.580	0.565
	2	0.006	0.005	0.014	0.072	0.185	0.297	0.372	0.405
3-C_7H_{15} = 2-C_7H_{15}	-1	0.013	0.113	0.487	0.910	1.190	1.300	1.248	1.080
	0	0.011	0.032	0.202	0.510	0.776	0.927	0.953	0.880
	1	0.011	0.011	0.056	0.207	0.410	0.574	0.657	0.664
	2	0.011	0.008	0.013	0.051	0.144	0.266	0.368	0.427
1-C_7H_{15} = 3-C_7H_{15}	-1	-0.021	0.028	0.293	0.524	0.717	0.799	0.804	0.770
	0	-0.022	-0.008	0.127	0.280	0.457	0.561	0.611	0.634
	1	-0.022	-0.015	0.048	0.094	0.225	0.330	0.410	0.475
	2	-0.022	-0.016	0.031	0.007	0.060	0.129	0.209	0.296
1-C_7H_{15} = 4-C_7H_{15}	-1	-0.017	0.117	0.572	0.943	1.178	1.222	1.149	1.038
	0	-0.020	0.013	0.248	0.524	0.772	0.886	0.905	0.879
	1	-0.020	-0.012	0.077	0.194	0.396	0.542	0.629	0.679
	2	-0.020	-0.015	0.035	0.028	0.116	0.226	0.334	0.433
1-C_7H_{15} = 2-C_7H_{15}	-1	-0.046	0.028	0.348	0.624	0.837	0.916	0.902	0.847
	0	-0.047	-0.022	0.142	0.332	0.534	0.645	0.690	0.701
	1	-0.047	-0.033	0.040	0.108	0.261	0.380	0.465	0.528
	2	-0.047	-0.034	0.017	0.001	0.064	0.146	0.237	0.328
2-C_7H_{15}= 3-C_7H_{15}	-1	0.036	0.175	0.646	1.043	1.223	1.216	1.083	0.900
	0	0.034	0.062	0.316	0.658	0.873	0.942	0.899	0.795
	1	0.033	0.029	0.108	0.325	0.535	0.657	0.689	0.659
	2	0.033	0.024	0.033	0.106	0.242	0.371	0.451	0.482

Table 4b: Log k_∞/k for reactions involved in 2-heptyl radical isomerization and decomposition.

	Log P	500	700	900	1100	1300	1500	1700	1900
1-C_7H_{15} = C_2H_4 + 1-C_5H_{11}	-1	0.032	0.349	0.936	1.360	1.484	1.439	1.291	1.104
	0	0.008	0.093	0.414	0.809	1.028	1.100	1.058	0.955
	1	0.005	0.015	0.105	0.335	0.558	0.706	0.760	0.744
	2	0.004	0.004	0.014	0.072	0.186	0.320	0.419	0.470
2-C_7H_{15} = C_3H_6 + 1-C_4H_9	-1	0.023	0.237	0.741	1.214	1.462	1.498	1.368	1.144
	0	0.009	0.061	0.304	0.670	0.946	1.069	1.051	0.938
	1	0.007	0.013	0.078	0.263	0.489	0.655	0.722	0.707
	2	0.007	0.006	0.015	0.058	0.163	0.295	0.397	0.450
3-C_7H_{15} = 1-C_4H_8 + 1-C_3H_7	-1	0.021	0.332	0.961	1.351	1.436	1.338	1.143	0.921
	0	0.004	0.097	0.481	0.872	1.051	1.061	0.966	0.824
	1	0.001	0.017	0.162	0.445	0.665	0.761	0.758	0.695
	2	0.001	0.002	0.031	0.146	0.315	0.448	0.513	0.522
3-C_7H_{15} = 1-C_4H_8 + 1-C_3H_7	-1	0.031	0.393	1.080	1.484	1.549	1.427	1.212	0.976
	0	0.007	0.119	0.548	0.970	1.149	1.145	1.034	0.879
	1	0.003	0.023	0.188	0.501	0.736	0.832	0.820	0.748
	2	0.003	0.004	0.038	0.168	0.353	0.496	0.562	0.569
4-C_7H_{15} = 1-C_5H_{10} + C_2H_5	-1	0.025	0.242	0.732	1.207	1.467	1.528	1.436	1.253
	0	0.004	0.064	0.301	0.661	0.940	1.084	1.097	1.018
	1	0.001	0.011	0.074	0.247	0.465	0.640	0.730	0.742
	2	0.001	0.001	0.011	0.048	0.133	0.254	0.361	0.429
3-C_7H_{15} = 1-C_7H_{15} =	-1	0.009	0.088	0.406	0.698	0.862	0.901	0.833	0.705
	0	0.009	0.026	0.198	0.443	0.613	0.690	0.682	0.616
	1	0.009	0.009	0.065	0.222	0.380	0.480	0.518	0.507
	2	0.009	0.007	0.015	0.073	0.178	0.277	0.342	0.371
4-C_7H_{15} = 1-C_7H_{15} =	-1	0.015	0.135	0.534	0.987	1.286	1.410	1.375	1.233
	0	0.011	0.039	0.220	0.546	0.830	1.002	1.051	1.003
	1	0.011	0.012	0.057	0.207	0.415	0.597	0.704	0.735
	2	0.011	0.008	0.013	0.043	0.123	0.242	0.355	0.432
2-C_7H_{15} = 1-C_7H_{15} =	-1	0.007	0.066	0.349	0.709	0.972	1.101	1.089	0.963
	0	0.006	0.017	0.134	0.384	0.620	0.771	0.817	0.772
	1	0.006	0.006	0.032	0.145	0.315	0.464	0.551	0.571
	2	0.006	0.004	0.007	0.031	0.101	0.205	0.298	0.357
3-C_7H_{15} = 2-C_7H_{15}	-1	0.013	0.171	0.648	1.029	1.195	1.183	1.052	0.870
	0	0.011	0.051	0.324	0.663	0.866	0.927	0.881	0.775
	1	0.011	0.014	0.110	0.340	0.546	0.661	0.687	0.651
	2	0.011	0.008	0.025	0.114	0.260	0.389	0.464	0.488
1-C_7H_{15} = 3-C_7H_{15}	-1	-0.021	0.047	0.356	0.564	0.749	0.816	0.818	0.792
	0	-0.022	-0.004	0.165	0.313	0.496	0.593	0.641	0.666
	1	-0.022	-0.015	0.064	0.109	0.256	0.362	0.441	0.508
	2	-0.022	-0.016	0.039	0.003	0.075	0.150	0.234	0.322
1-C_7H_{15} = 4-C_7H_{15}	-1	-0.016	0.154	0.666	1.001	1.211	1.238	1.169	1.072
	0	-0.020	0.025	0.309	0.583	0.828	0.931	0.948	0.926
	1	-0.020	-0.010	0.102	0.226	0.444	0.590	0.676	0.726
	2	-0.020	-0.014	0.044	0.030	0.142	0.259	0.371	0.470
1-C_7H_{15} = 2-C_7H_{15}	-1	-0.046	0.052	0.421	0.670	0.871	0.933	0.918	0.872
	0	-0.047	-0.016	0.187	0.373	0.578	0.681	0.725	0.738
	1	-0.047	-0.032	0.059	0.127	0.297	0.417	0.501	0.565
	2	-0.047	-0.034	0.026	-0.002	0.083	0.171	0.264	0.358
2-C_7H_{15}= 3-C_7H_{15}	-1	0.035	0.127	0.496	0.923	1.208	1.319	1.264	1.092
	0	0.033	0.046	0.207	0.514	0.784	0.939	0.965	0.891
	1	0.033	0.027	0.062	0.207	0.410	0.577	0.664	0.672
	2	0.033	0.024	0.024	0.054	0.142	0.265	0.369	0.431

Table 4c: Log k_∞/k for reactions involved in 3-heptyl radical isomerization and decomposition.

	Log P	500	700	900	1100	1300	1500	1700	1900
1-C_7H_{15} = C_2H_4 + 1-C_5H_{11}	-1	0.020	0.218	0.723	1.158	1.262	1.154	0.963	0.771
	0	0.004	0.025	0.266	0.640	0.847	0.875	0.798	0.684
	1	0.004	-0.006	0.033	0.229	0.445	0.567	0.591	0.555
	2	0.004	0.001	-0.005	0.027	0.130	0.251	0.333	0.366
2-C_7H_{15} = C_3H_6 + 1-C_4H_9	-1	0.022	0.204	0.663	1.146	1.436	1.512	1.414	1.215
	0	0.009	0.055	0.267	0.611	0.897	1.043	1.053	0.967
	1	0.007	0.013	0.070	0.230	0.441	0.609	0.692	0.698
	2	0.007	0.006	0.015	0.052	0.137	0.250	0.348	0.408
3-C_7H_{15} = 1-C_4H_8 + 1-C_3H_7	-1	0.017	0.213	0.709	1.195	1.465	1.528	1.437	1.254
	0	0.003	0.058	0.304	0.671	0.953	1.093	1.102	1.020
	1	0.001	0.011	0.089	0.278	0.500	0.667	0.748	0.752
	2	0.001	0.002	0.017	0.074	0.178	0.300	0.399	0.456
3-C_7H_{15} = 1-C_4H_8 + 1-C_3H_7	-1	0.025	0.263	0.818	1.338	1.608	1.651	1.536	1.332
	0	0.006	0.075	0.357	0.760	1.059	1.197	1.193	1.095
	1	0.003	0.016	0.108	0.320	0.563	0.740	0.820	0.818
	2	0.003	0.003	0.022	0.087	0.203	0.337	0.444	0.503
4-C_7H_{15} = 1-C_5H_{10} + C_2H_5	-1	0.034	0.388	1.034	1.442	1.534	1.420	1.196	0.947
	0	0.005	0.120	0.526	0.930	1.114	1.114	1.000	0.840
	1	0.001	0.022	0.183	0.480	0.704	0.795	0.781	0.706
	2	0.001	0.003	0.036	0.162	0.337	0.469	0.529	0.531
3-C_7H_{15} = 1-C_7H_{15} =	-1	0.009	0.042	0.257	0.566	0.810	0.953	0.988	0.929
	0	0.009	0.015	0.105	0.312	0.521	0.668	0.737	0.734
	1	0.009	0.008	0.032	0.126	0.269	0.401	0.489	0.528
	2	0.009	0.006	0.010	0.035	0.095	0.179	0.258	0.315
4-C_7H_{15} = 1-C_7H_{15} =	-1	0.017	0.232	0.777	1.203	1.376	1.336	1.161	0.939
	0	0.011	0.073	0.399	0.780	0.997	1.044	0.969	0.833
	1	0.011	0.019	0.141	0.406	0.632	0.746	0.756	0.702
	2	0.011	0.009	0.032	0.140	0.307	0.444	0.516	0.531
2-C_7H_{15} = 1-C_7H_{15} =	-1	0.007	0.055	0.305	0.660	0.942	1.097	1.113	1.014
	0	0.006	0.015	0.116	0.346	0.583	0.746	0.811	0.790
	1	0.006	0.006	0.029	0.126	0.282	0.430	0.524	0.559
	2	0.006	0.004	0.007	0.028	0.085	0.174	0.260	0.322
3-C_7H_{15} = 2-C_7H_{15}	-1	0.012	0.095	0.448	0.874	1.172	1.308	1.293	1.170
	0	0.011	0.030	0.191	0.493	0.764	0.932	0.985	0.947
	1	0.011	0.011	0.059	0.206	0.403	0.570	0.668	0.697
	2	0.011	0.008	0.016	0.058	0.146	0.259	0.360	0.425
1-C_7H_{15} = 3-C_7H_{15}	-1	-0.022	0.004	0.248	0.467	0.641	0.678	0.632	0.574
	0	-0.022	-0.019	0.098	0.238	0.405	0.481	0.498	0.497
	1	-0.022	-0.018	0.037	0.068	0.195	0.288	0.348	0.394
	2	-0.022	-0.016	0.033	-0.005	0.045	0.111	0.184	0.259
1-C_7H_{15} = 4-C_7H_{15}	-1	-0.019	0.069	0.497	0.851	1.038	1.006	0.882	0.762
	0	-0.020	-0.013	0.196	0.460	0.682	0.747	0.722	0.677
	1	-0.020	-0.020	0.050	0.153	0.350	0.472	0.528	0.553
	2	-0.020	-0.016	0.032	0.006	0.094	0.199	0.294	0.374
1-C_7H_{15} = 2-C_7H_{15}	-1	-0.047	-0.002	0.294	0.558	0.745	0.769	0.702	0.626
	0	-0.047	-0.036	0.106	0.283	0.471	0.549	0.558	0.545
	1	-0.047	-0.036	0.025	0.077	0.227	0.331	0.393	0.434
	2	-0.047	-0.034	0.019	-0.014	0.048	0.126	0.207	0.285
2-C_7H_{15}= 3-C_7H_{15}	-1	0.035	0.110	0.441	0.866	1.178	1.322	1.299	1.156
	0	0.033	0.043	0.182	0.467	0.741	0.913	0.964	0.916
	1	0.033	0.026	0.058	0.182	0.370	0.537	0.635	0.662
	2	0.033	0.024	0.024	0.050	0.121	0.226	0.325	0.391

Table 4d: Log k_∞/k for reactions involved in 4-heptyl radical isomerization and decomposition.

A2. Pentyl. Radicals: ***Pentyl-1 and Pentyl-2:***. There is only one isomerization process involving 1-4 H-transfer. The 3-isomer cannot be formed in the mechanism for heptyl radical decomposition.. The high pressure rate expressions can be found in Table 5 and the deviation from high pressure behavior are in Table 6 .

Reactions	Log A	N	E/R	Rationale
$1\text{-}C_5H_{11} = C_2H_4 + 1\text{-}C_3H_7$	11.88	.33	13695	Beta bond scission of primary radicals
$2\text{-}C_5H_{11} = C_3H_6 + C_2H_4$	12.60	1.11	14363	Beta bond scission of secondary radicals
$1\text{-}C_5H_{11} = 2\text{-}C_5H_{11}$	-1.104	3.058	10023	From 1-pentyl radical decomp and isomer [16],
$2\text{-}C_5H_{11} = 1\text{-}C_5H_{11}$	2.258	.2.788	8794	

Table 5: High pressure rate expressions for the decomposition and isomerization of pentyl-1 and pentyl-2

Reactions	Pressure bar	Temperature							
		600	700	800	1000	1200	1400	1600	1900
$1\text{-}C_5H_{11} = C_2H_4 + 1\text{-}C_3H_7$	0.1	0.24	0.48	0.76	1.26	1.52	1.58	1.51	1.28
	1.0	0.05	0.14	0.29	0.66	0.96	1.11	1.13	1.03
	10	0.01	0.03	0.07	0.25	0.48	0.66	0.75	0.76
	100	0.00	0.00	0.01	0.05	0.15	0.28	0.39	0.48
$2\text{-}C_5H_{11} = C_3H_6 + C_2H_4$	0.1	0.17	0.32	0.52	0.97	1.33	1.53	1.57	1.42
	1.0	0.04	0.10	0.19	0.46	0.76	0.97	1.07	1.05
	10	0.01	0.02	0.04	0.15	0.32	0.51	0.63	0.71
	100	0.00	0.00	0.01	0.03	0.08	0.17	0.27	0.38
$1\text{-}C_5H_{11} = 2\text{-}C_5H_{11}$	0.1	0.06	0.16	0.32	0.74	1.12	1.38	1.48	1.40
	1.0	0.02	0.05	0.12	0.36	0.65	0.89	1.02	1.04
	10	0.01	0.01	0.03	0.12	0.28	0.47	0.61	0.71
	100	0.01	0.01	0.01	0.02	0.07	0.16	0.27	0.39
$2\text{-}C_5H_{11} = 1\text{-}C_5H_{11}$	0.1	0.07	0.22	0.43	0.87	1.18	1.32	1.34	1.20
	1.0	0.01	0.06	0.16	0.46	0.74	0.92	0.99	0.96
	10	0.00	0.01	0.03	0.17	0.37	0.55	0.66	0.70
	100	0.00	0.00	0.00	0.03	0.12	0.24	0.34	0.44

Table 6: Deviation from high pressure behavior for the decomposition and isomerization of pentyl-1 and pentyl-2

A3: n-Butyl radical: The high pressure rate expression is based on the results of Knyazev and Slagle [9]. The deviation from the high pressure can be found in Table 7. Note presence of only one channel. Hence there is no issue regarding the nature of the products that are formed

$$k \text{ (high pressure)re} = 2.5 \times 10^{12} T^{.175} \text{rxp}(-13527/T)$$

Reaction	Pressure	Temperature [K]								
$1\text{-}C_4H_9 = C_2H_5 + C_2H_4$	bar	600	700	800	900	1000	1200	1400	1600	1900
	.1	0.25	0.47	0.74	1.02	1.27	1.61	1.76	1.77	1.60
	1.0	0.07	0.16	0.31	0.50	0.69	1.02	1.21	1.27	1.22
	10	0.01	0.04	0.08	0.17	0.28	0.52	0.71	0.82	0.86
	199	0.00	0.01	0.02	0.03	0.07	0.18	0.31	0.43	0.52

Table 7: Deviation from high pressure behavior for the decomposition and isomerization of butyl-1

A4: **n-Propyl Radical**: The high pressure rate expression is based on an earlier analysis [18]. The deviation from the high pressure values can be found in Table 8. As for butyl there is only one reaction channel, since isomerization via 1-2 H-atom transfer has a threshold that is larger than the that for beta bond scission,.

$k = 3{,}2x10^{11}T^{-.565}\exp(-15208/T)$

Reaction	Pressure	Temperature [K]								
$nC_3H_7 = C_2H_4 + CH_3$	bar	600	700	800	900	1000	1200	1400	1600	1900
		0.38	0.59	0.84	1.11	1.38	1.84	2.16	2.34	2.43
		0.12	0.23	0.37	0.56	0.77	1.16	1.46	1.66	1.79
		0.02	0.06	0.11	0.20	0.33	0.60	0.86	1.06	1.23
		0.00	0.01	0.01	0.04	0.09	0.22	0.38	0.55	0.73

Table 8: Deviation from high pressure behavior for the decomposition and isomerization of n-propyl radical

B 1-Olefinyl Radicals: 1-olefins are formed from beta bond scission reactions of alkyl radicals. The compounds that are formed starting from the heptyl radicals are 1-hexene own to propene. Radical attack will lead to the formation of 1-olefinyl radicals. These can then fragment into the smaller olefins and dienes (predominantly 1,3-butadiene).

B1: ***1-hexenyl-6, 1-hexenyl-5, 1-hexenyl-3:*** These three radicals are linked together through isomerization processes. Particularly interesting is the role of cyclohexyl and methylated cyclopentyl radicals. This demonstrates a natural linkage between linear and cyclic radicals. It represents an additional complicating feature with the introduction of a double bond into a linear radical structure. The consequence is the presence of seven isomers and a total of 7 beta bond scission reactions and 7 reversible isomerization processes leading to a total of 21 reactions. This can be compared with the five beta bond scission and eight reversible isomerizations in the .

Reactions	Log A	N	Activation energy E/R	Source for initial fits
c-C_6H_{11} = c-C_6H_{10} + H	11.524	.69	17085	From H+cyclohexene and detailed balance [10]
c-$C_5H_9CH_2$ = $CH_2C_5H_8$ + H	8.89	1.11	17421	From non-terminal H + isobutene and detailed balance [10]
1-C_6H_{11} -3 =C_4H_6(1,3-butadiene) + C_2H_5	11.53	.66	16237	From ethyl+butadiene and detailed balance [10]
1-C_6H_{11} - 6 = C_4H_7 -4 + C_2H_4	12.60	.0.12	13876	Beta C-C bond scission as in hexyl [8]
4-C_6H_{11} - 3 = 1,3C_5H_8 + CH_3	13.69	-.21	16782	From H+butadiene and detailed balance [10]
1-C_6H_{11} -5 = C_3H_6 + C_3H_5(allyl)	12.66	.13	12273	From allyl + ethylene and detailed balance[18]
2-CH_3-4-C_5H_8 - 1 = C_3H_5 (allyl) + C_3H_6	12.73	.12	12052	From allyl+ethylene and detailed balance [18]
c-C_6H_{11}= 1-C_6H_{11} – 6	12.78	.07	14083	Beta C-C bond scission from alkyl radicals [8]
1-C_6H_{11} - 6= c-C_6H_{11}	4.74	1.33	2375	Detailed balance
1-C_6H_{11} - 6= c-$C_5H_9CH_2$	8.98	.36	5387	From chemically activated cyclohexyl isomerization [15]
c-$C_5H_9CH_2$ = 1-C_6H_{11} – 6	12.72	.03	13950	From above and detailed balance
1-CH_3-c-C_5 H_8-3 =1-C_6H_{11}-5	12.88	.15	16578	Decyclization of five carbon ring. From results on decyclization of cyclopentyl radical [18]
1-C_6H_{11}-5 = 1-CH_3-c-C_5 H_8-3	7.13	.94	8369	Detailed balance
1-CH_3-c-C_5 H_8-3= 2-CH_3-4-C_5 H_8-1	12.55	.15	16308	Decyclization of five carbon ring derived from results of cyclopentyl decyclization[18]
2-CH_3-4-C_5 H_8-1= 1-CH_3-c-C_5 H_8-3	8.36	.84	7355	Detailed balance
1-C_6H_{11} – 6 = 1-C_6H_{11} – 3	2.19	2.83	7834	1-4 H-transfer isomerization including allylic resonance effects [8]
1-C_6H_{11} – 3 = 1-C_6H_{11} – 6	2.92	2.93	14726	Detailed balance
c-$C_5H_9CH_2$ = 1-CH_3c-C_5H_8-3	1.82	2.85	10610	1-4 Hydrogen transfer into 5 carbon ring. Results deduced from present results
1-CH_3c-C_5H_8-3= c-$C_5H_9CH_2$	2.85	2.61	11351	Detailed balance
1-C_6H_{11} – 3 = 4-C_6H_{11} – 3	3.97	2.38	11143	From present results
4-C_6H_{11} – 3 = 1-C_6H_{11} – 3	5.52	2.05	11423	Detailed balance

Table 9: Reactions, high pressure rate expressions and source of data for mechanism from Figure 7. The results from detailed balance on based on the thermodynamic properties and the experimental results from Ref [9] or described in table.

Reactions	Pressure bar	Temperature [K]							
		600	700	800	1000	1200	1400	1600	1900
$c\text{-}C_6H_{11} = c\text{-}C_6H_{10} + H$ 1	0.1	0.03	0.09	0.20	0.55	0.91	1.17	1.32	1.37
	1.0	0.01	0.02	0.06	0.25	0.53	0.78	0.95	1.06
	10	0.00	0.01	0.01	0.07	0.22	0.41	0.57	0.73
	100	0.00	0.00	0.00	0.01	0.05	0.13	0.24	0.39
$c\text{-}C_5H_9CH_2 = CH_2C_5H_8 + H$ 2	0.1	0.06	0.16	0.31	0.71	1.08	1.31	1.41	1.37
	1.0	0.02	0.04	0.09	0.32	0.63	0.88	1.02	1.09
	10	0.01	0.01	0.02	0.09	0.25	0.45	0.61	0.75
	100	0.01	0.01	0.01	0.02	0.05	0.14	0.24	0.39
$1\text{-}C_6H_{11}\text{-}3 = C_4H_6$(1,3-butadiene) $+ C_2H_5$ 3	0.1	0.02	0.08	0.18	0.48	0.78	0.97	1.04	0.98
	1.0	0.00	0.01	0.04	0.19	0.42	0.62	0.74	0.77
	10	0.00	0.00	0.00	0.04	0.15	0.30	0.43	0.53
	100	0.00	0.00	0.00	0.00	0.02	0.08	0.16	0.27
$1\text{-}C_6H_{11}\text{ - }6 = C_4H_7\text{ -}4 + C_2H_4$ 4	0.1	0.26	0.51	0.76	1.13	1.28	1.26	1.16	0.95
	1.0	0.07	0.17	0.31	0.65	0.89	0.97	0.95	0.83
	10	0.01	0.04	0.09	0.27	0.48	0.62	0.68	0.66
	100	0.00	0.01	0.02	0.07	0.17	0.29	0.38	0.44
$4\text{-}C_6H_{11}\text{ - }3 = 1,3C_5H_8 + CH_3$ 5	0.1	0.03	0.08	0.17	0.46	0.76	0.94	1.02	0.98
	1.0	0.01	0.02	0.05	0.18	0.39	0.58	0.70	0.75
	10	0.01	0.01	0.02	0.04	0.13	0.26	0.39	0.49
	100	0.01	0.01	0.01	0.01	0.03	0.07	0.13	0.24
$1\text{-}C_6H_{11}\text{ -}5 = C_3H_6 + C_3H_5$(allyl) 6	0.1	0.19	0.35	0.55	0.94	1.23	1.39	1.46	1.36
	1.0	0.05	0.12	0.22	0.46	0.70	0.87	0.98	0.98
	10	0.01	0.03	0.06	0.17	0.30	0.43	0.55	0.62
	100	0.00	0.00	0.01	0.04	0.09	0.15	0.22	0.30
$2\text{-}CH_3\text{-}4\text{-}C_5H_8\text{ - }1 = C_3H_5$ (allyl) $+ C_3H_6$ 7	0.1	0.18	0.35	0.54	0.93	1.22	1.38	1.43	1.34
	1.0	0.06	0.13	0.23	0.49	0.73	0.91	0.99	1.00
	10	0.02	0.04	0.08	0.20	0.34	0.48	0.58	0.65
	100	0.01	0.01	0.02	0.06	0.12	0.18	0.25	0.33
$cC_6H_{11} = 1\text{- }C_6H_{11}\text{–}6$ 8	0.1	0.02	0.04	0.10	0.32	0.60	0.83	0.98	1.07
	1.0	0.01	0.02	0.03	0.14	0.34	0.54	0.69	0.81
	10	0.01	0.01	0.01	0.04	0.14	0.27	0.41	0.54
	100	0.01	0.01	0.01	0.02	0.04	0.09	0.17	0.29
$1\text{-}C_6H_{11} – 6 =$ $c\text{- }C_6H_{11}$ 9	0.1	0.02	0.03	0.06	0.15	0.29	0.34	0.36	0.35
	1.0	0.01	0.00	0.01	0.07	0.20	0.24	0.27	0.29
	10	0.01	-0.01	-0.01	0.01	0.11	0.15	0.19	0.21
	100	0.01	-0.01	-0.01	-0.01	0.05	0.07	0.10	0.13
$1\text{-}C_6H_{11} – 6 = c\text{-}C_5H_9CH_2$ 10	0.1	0.04	0.03	0.12	0.29	0.44	0.52	0.47	0.47
	1.0	0.02	-0.03	0.03	0.15	0.29	0.38	0.35	0.39
	10	0.02	-0.04	-0.01	0.05	0.16	0.24	0.23	0.29
	100	0.02	-0.05	-0.02	0.00	0.06	0.12	0.11	0.18
$c\text{-}C_5H_9CH_2 = 1\text{-}C_6H_{11} – 6$ 11	0.1	0.01	0.04	0.11	0.36	0.64	0.86	0.98	1.02
	1.0	0.01	0.01	0.03	0.15	0.35	0.54	0.68	0.77
	10	0.01	0.01	0.01	0.04	0.13	0.26	0.38	0.51
	100	0.01	0.01	0.01	0.01	0.03	0.07	0.14	0.25
$1\text{-}CH_3\text{-}c\text{-}C_5\text{ }H_8\text{-}3 = 1\text{-}C_6H_{11}\text{-}5$ 12	0.1	0.03	0.09	0.20	0.52	0.88	1.15	1.31	1.36
	1.0	0.01	0.02	0.06	0.21	0.46	0.69	0.87	0.98
	10	0.00	0.00	0.01	0.05	0.16	0.31	0.46	0.61
	100	0.00	0.00	0.00	0.01	0.03	0.08	0.15	0.27
$1\text{-}C_6H_{11}\text{-}5 = 1\text{-}CH_3\text{-}c\text{-}C_5\text{ }H_8\text{-}3$ 13	0.1	0.07	0.18	0.26	0.50	0.80	0.99	1.04	1.10
	1.0	0.03	0.08	0.09	0.22	0.45	0.62	0.68	0.78
	10	0.02	0.05	0.02	0.05	0.19	0.31	0.36	0.49

	100	0.02	0.04	0.00	-0.02	0.05	0.11	0.12	0.23
1-CH_3-c-C_5 H_8-3= 2-CH_3-4-C_5 H_8-1 14	0.1	0.03	0.08	0.19	0.50	0.85	1.12	1.29	1.34
	1.0	0.00	0.02	0.05	0.20	0.44	0.67	0.85	0.97
	10	0.00	0.00	0.01	0.05	0.15	0.30	0.45	0.60
	100	0.00	0.00	0.00	0.01	0.03	0.08	0.15	0.27
2-CH_3-4-C_5 H_8-1= 1-CH_3-c-C_5 H_8-3 15	0.1	0.01	0.11	0.21	0.43	0.67	0.82	0.95	0.99
	1.0	-0.01	0.04	0.09	0.20	0.38	0.52	0.65	0.73
	10	-0.02	0.01	0.03	0.06	0.16	0.26	0.38	0.47
	100	-0.02	0.01	0.01	0.00	0.04	0.08	0.16	0.24
1-C_6H_{11} – 6 = 1-C_6H_{11} – 3 16	0.1	0.12	0.17	0.39	0.73	0.94	1.05	1.00	0.87
	1.0	0.06	0.03	0.15	0.42	0.64	0.80	0.81	0.75
	10	0.04	-0.02	0.04	0.18	0.34	0.52	0.58	0.60
	100	0.04	-0.04	0.01	0.05	0.12	0.26	0.32	0.40
1-C_6H_{11} – 3 = 1-C_6H_{11} – 6 17	0.1	0.02	0.08	0.20	0.54	0.87	1.08	1.14	1.07
	1.0	0.00	0.01	0.04	0.22	0.49	0.71	0.84	0.86
	10	0.00	0.00	0.00	0.05	0.18	0.36	0.50	0.61
	100	0.00	0.00	0.00	0.00	0.02	0.10	0.20	0.33
c-$C_5H_9CH_2$ = 1-CH_3c-C_5H_8-3 18	0.1	-0.02	0.09	0.12	0.31	0.65	0.87	1.04	1.08
	1.0	-0.02	0.07	0.05	0.11	0.36	0.55	0.74	0.82
	10	-0.02	0.06	0.04	0.01	0.14	0.26	0.43	0.55
	100	-0.02	0.06	0.04	-0.01	0.04	0.07	0.17	0.27
1-CH_3c-C_5H_8-3= c-$C_5H_9CH_2$	0.1	0.01	0.03	0.11	0.34	0.66	0.94	1.13	1.24
	1.0	0.01	0.01	0.04	0.14	0.34	0.56	0.74	0.89
	10	0.00	0.01	0.02	0.04	0.12	0.25	0.39	0.55
	100	0.00	0.00	0.02	0.01	0.03	0.07	0.14	0.25
1-C_6H_{11} – 3 = 4-C_6H_{11} – 320	0.1	0.00	0.08	0.05	0.25	0.58	0.71	0.81	0.81
	1.0	0.00	0.06	0.00	0.08	0.32	0.43	0.56	0.62
	10	0.00	0.06	-0.01	0.00	0.13	0.19	0.30	0.40
	100	0.00	0.06	-0.01	-0.02	0.04	0.03	0.09	0.19
4-C_6H_{11} – 3 = 1-C_6H_{11} – 3 21	0.1	0.01	0.03	0.08	0.28	0.54	0.74	0.86	0.87
	1.0	0.01	0.01	0.02	0.10	0.28	0.45	0.58	0.66
	10	0.01	0.01	0.01	0.03	0.09	0.20	0.31	0.42
	100	0.01	0.01	0.01	0.01	0.02	0.05	0.11	0.20

Table 10a: Deviation from high pressure behavior as a result of the decomposition and isomerization of 1-hexenyl-6

Reactions	Pressure bar	Temperature [K]							
		600	700	800	1000	1200	1400	1600	1900
c-C_6H_{11} = c-C_6H_{10} + H 1	0.1	-0.01	0.01	0.06	0.36	0.76	1.13	1.38	1.55
	1.0	0.00	0.00	0.02	0.14	0.40	0.70	0.94	1.15
	10	0.00	0.00	0.01	0.04	0.15	0.33	0.53	0.74
	100	0.00	0.00	0.00	0.01	0.03	0.09	0.20	0.37
c-$C_5H_9CH_2$ = $CH_2C_5H_8$ + H 2	0.1	-0.01	0.04	0.15	0.57	1.02	1.38	1.57	1.64
	1.0	0.00	0.01	0.03	0.22	0.53	0.85	1.08	1.24
	10	0.01	0.01	0.01	0.05	0.18	0.39	0.59	0.80
	100	0.01	0.01	0.01	0.01	0.03	0.10	0.21	0.38
1-C_6H_{11} -3 = C_4H_6(1,3-butadiene) + C_2H_5 3	0.1	0.07	0.19	0.40	0.98	1.45	1.71	1.78	1.66
	1.0	0.01	0.05	0.14	0.48	0.89	1.18	1.31	1.31
	10	0.00	0.01	0.03	0.17	0.43	0.69	0.87	0.96
	100	0.00	0.00	0.01	0.03	0.13	0.30	0.46	0.61
1-C_6H_{11} - 6 = C_4H_7 -4 + C_2H_4 4	0.1	-0.04	0.17	0.41	0.96	1.33	1.48	1.44	1.24
	1.0	-0.07	-0.01	0.09	0.42	0.76	1.01	1.08	1.02
	10	-0.02	-0.02	0.00	0.11	0.31	0.54	0.68	0.75
	100	0.00	0.00	0.00	0.01	0.07	0.18	0.30	0.43
4-C_6H_{11} - 3 = 1,3C_5H_8 + CH_3 5	0.1	0.06	0.15	0.30	0.76	1.18	1.48	1.60	1.55
	1.0	0.02	0.04	0.08	0.31	0.63	0.92	1.09	1.16
	10	0.01	0.01	0.02	0.08	0.24	0.45	0.62	0.77
	100	0.01	0.01	0.01	0.02	0.05	0.13	0.25	0.40
1-C_6H_{11} -5 = C_3H_6 + C_3H_5(allyl) 6	0.1	0.19	0.34	0.52	0.89	1.20	1.43	1.56	1.57
	1.0	0.05	0.12	0.22	0.44	0.67	0.87	1.01	1.09
	10	0.01	0.03	0.06	0.16	0.29	0.42	0.55	0.66
	100	0.00	0.00	0.01	0.04	0.09	0.14	0.21	0.31
2-CH_3-4-C_5H_8 - 1 = C_3H_5 (allyl) + C_3H_6 7	0.1	0.16	0.31	0.48	0.88	1.21	1.43	1.54	1.54
	1.0	0.06	0.13	0.22	0.46	0.70	0.90	1.03	1.11
	10	0.02	0.04	0.08	0.19	0.33	0.46	0.58	0.69
	100	0.01	0.01	0.02	0.06	0.12	0.18	0.24	0.33
cC_6H_{11} = 1- C_6H_{11}–6 8	0.1	0.01	0.01	0.03	0.19	0.46	0.76	0.98	1.17
	1.0	0.01	0.01	0.01	0.07	0.24	0.46	0.66	0.85
	10	0.01	0.01	0.01	0.03	0.09	0.22	0.36	0.54
	100	0.01	0.01	0.01	0.01	0.03	0.06	0.14	0.26
1-C_6H_{11} – 6 = c- C_6H_{11} 9	0.1	0.01	-0.02	0.03	0.13	0.23	0.30	0.38	0.41
	1.0	0.01	-0.01	0.02	0.06	0.13	0.19	0.27	0.31
	10	0.01	-0.01	0.02	0.04	0.06	0.09	0.16	0.21
	100	0.01	-0.01	0.02	0.03	0.02	0.02	0.07	0.11
1-C_6H_{11} – 6 = c-$C_5H_9CH_2$ 10	0.1	0.00	-0.06	0.05	0.21	0.39	0.43	0.52	0.58
	1.0	0.01	-0.06	0.02	0.09	0.22	0.26	0.35	0.45
	10	0.02	-0.05	0.03	0.03	0.10	0.11	0.20	0.31
	100	0.02	-0.05	0.03	0.02	0.05	0.01	0.07	0.17
c-$C_5H_9CH_2$ = 1-C_6H_{11} – 6 11	0.1	0.00	0.01	0.04	0.25	0.56	0.84	1.04	1.18
	1.0	0.01	0.01	0.01	0.09	0.27	0.50	0.68	0.85
	10	0.01	0.01	0.01	0.02	0.09	0.21	0.36	0.52
	100	0.01	0.01	0.01	0.01	0.02	0.05	0.12	0.24
1-CH_3-c-C_5 H_8-3 =1-C_6H_{11}-5 12	0.1	0.02	0.08	0.17	0.47	0.84	1.18	1.40	1.55
	1.0	0.01	0.02	0.05	0.19	0.42	0.68	0.90	1.08
	10	0.00	0.00	0.01	0.05	0.14	0.29	0.45	0.64
	100	0.00	0.00	0.00	0.01	0.03	0.07	0.14	0.27
1-C_6H_{11}-5 = 1-CH_3-c-C_5 H_8-3 13	0.1	0.07	0.17	0.23	0.52	0.80	1.00	1.08	1.15
	1.0	0.03	0.08	0.08	0.25	0.45	0.61	0.70	0.78
	10	0.02	0.05	0.01	0.09	0.20	0.30	0.36	0.46

	100	0.02	0.04	-0.01	0.02	0.07	0.10	0.12	0.19
1-CH_3-c-C_5 H_8-3= 2-CH_3-4-C_5 H_8-1 14	0.1	0.02	0.07	0.15	0.45	0.81	1.15	1.37	1.52
	1.0	0.00	0.02	0.05	0.18	0.40	0.67	0.87	1.06
	10	0.00	0.00	0.01	0.05	0.13	0.28	0.44	0.63
	100	0.00	0.00	0.00	0.01	0.03	0.07	0.14	0.26
2-CH_3-4-C_5 H_8-1= 1-CH_3-c-C_5 H_8-3 15	0.1	0.01	0.10	0.23	0.41	0.64	0.87	1.00	1.03
	1.0	-0.01	0.04	0.12	0.20	0.36	0.55	0.67	0.73
	10	-0.02	0.01	0.07	0.07	0.15	0.28	0.38	0.44
	100	-0.02	0.01	0.05	0.00	0.03	0.11	0.16	0.20
1-C_6H_{11} – 6 = 1-C_6H_{11} – 3 16	0.1	0.00	-0.02	0.15	0.55	0.94	1.09	1.19	1.10
	1.0	0.01	-0.06	0.02	0.23	0.56	0.73	0.88	0.90
	10	0.03	-0.05	0.00	0.06	0.25	0.38	0.56	0.65
	100	0.04	-0.04	0.00	0.01	0.08	0.12	0.25	0.37
1-C_6H_{11} – 3 = 1-C_6H_{11} – 6 17	0.1	0.06	0.20	0.43	1.06	1.59	1.87	1.94	1.80
	1.0	0.01	0.05	0.15	0.54	0.99	1.31	1.46	1.45
	10	0.00	0.01	0.03	0.19	0.49	0.79	0.98	1.09
	100	0.00	0.00	0.01	0.04	0.16	0.35	0.53	0.71
c-$C_5H_9CH_2$ = 1-CH_3c-C_5H_8-3 18	0.1	-0.02	0.06	0.04	0.25	0.54	0.90	1.11	1.19
	1.0	-0.02	0.06	0.02	0.10	0.27	0.56	0.75	0.86
	10	-0.02	0.06	0.02	0.03	0.08	0.26	0.41	0.52
	100	-0.02	0.06	0.02	0.02	0.01	0.09	0.15	0.22
1-CH_3c-C_5H_8-3= c-$C_5H_9CH_2$	0.1	0.01	0.03	0.09	0.30	0.62	0.94	1.18	1.38
	1.0	0.01	0.01	0.04	0.12	0.31	0.55	0.76	0.97
	10	0.00	0.01	0.02	0.03	0.11	0.24	0.39	0.58
	100	0.00	0.00	0.02	0.01	0.02	0.06	0.12	0.25
1-C_6H_{11} – 3 = 4-C_6H_{11} – 320	0.1	0.01	0.13	0.17	0.67	0.99	1.35	1.40	1.40
	1.0	0.00	0.08	0.04	0.34	0.60	0.93	1.01	1.08
	10	0.00	0.06	-0.01	0.14	0.27	0.56	0.65	0.77
	100	0.00	0.06	-0.02	0.06	0.06	0.25	0.33	0.47
4-C_6H_{11} – 3 = 1-C_6H_{11} – 3 21	0.1	0.02	0.05	0.14	0.47	0.85	1.15	1.31	1.36
	1.0	0.01	0.02	0.04	0.19	0.45	0.71	0.89	1.00
	10	0.01	0.01	0.01	0.05	0.17	0.34	0.50	0.66
	100	0.01	0.01	0.01	0.02	0.04	0.10	0.20	0.34

Table 10b: Deviation from high pressure behavior as a result of the decomposition and isomerization of 1-hexenyl-3

Reactions	Pressure bar	Temperature [K]							
		600	700	800	1000	1200	1400		
c-C_6H_{11} = c-C_6H_{10} + H 1	0.1	0.02	0.06	0.14	0.46	0.89	1.28	1.58	1.85
	1.0	0.01	0.02	0.04	0.19	0.47	0.77	1.03	1.28
	10	0.00	0.01	0.01	0.05	0.18	0.36	0.55	0.77
	100	0.00	0.00	0.00	0.01	0.04	0.11	0.20	0.36
c-$C_5H_9CH_2$ = $CH_2C_5H_8$ + H 2	0.1	0.05	0.14	0.28	0.72	1.19	1.53	1.68	1.57
	1.0	0.02	0.04	0.08	0.30	0.61	0.91	1.07	1.10
	10	0.01	0.01	0.02	0.07	0.21	0.40	0.56	0.69
	100	0.01	0.01	0.01	0.02	0.04	0.10	0.19	0.32
1-C_6H_{11} -3 = C_4H_6(1,3-butadiene) + C_2H_5 3	0.1	0.02	0.07	0.16	0.50	0.92	1.27	1.51	1.61
	1.0	0.00	0.01	0.03	0.17	0.43	0.72	0.94	1.11
	10	0.00	0.00	0.00	0.03	0.12	0.29	0.46	0.65
	100	0.00	0.00	0.00	0.00	0.01	0.05	0.13	0.27
1-C_6H_{11} - 6 = C_4H_7 -4 + C_2H_4 4	0.1	0.21	0.40	0.64	1.14	1.53	1.74	1.79	1.64
	1.0	0.05	0.12	0.23	0.54	0.86	1.10	1.22	1.22
	10	0.01	0.03	0.06	0.19	0.38	0.56	0.71	0.80
	100	0.00	0.01	0.01	0.05	0.12	0.21	0.31	0.41
4-C_6H_{11} - 3 = 1,3C_5H_8 + CH_3 5	0.1	0.03	0.08	0.16	0.48	0.88	1.20	1.43	1.56
	1.0	0.01	0.02	0.04	0.17	0.41	0.66	0.88	1.05
	10	0.01	0.01	0.02	0.04	0.12	0.26	0.42	0.59
	100	0.01	0.01	0.01	0.01	0.02	0.06	0.12	0.24
1-C_6H_{11} -5 = C_3H_6 + C_3H_5(allyl) 6	0.1	0.28	0.55	0.85	1.32	1.51	1.48	1.32	0.99
	1.0	0.07	0.20	0.38	0.77	1.01	1.07	1.02	0.82
	10	0.01	0.04	0.11	0.34	0.56	0.69	0.71	0.64
	100	0.00	0.01	0.02	0.09	0.22	0.34	0.41	0.44
2-CH_3-4-C_5H_8 - 1 = C_3H_5 (allyl) + C_3H_6 7	0.1	0.15	0.32	0.55	1.00	1.32	1.45	1.44	1.23
	1.0	0.06	0.12	0.23	0.52	0.79	0.96	1.02	0.95
	10	0.02	0.04	0.08	0.20	0.37	0.53	0.62	0.66
	100	0.01	0.01	0.02	0.06	0.12	0.21	0.28	0.37
cC_6H_{11} = 1- C_6H_{11}–6 8	0.1	0.01	0.03	0.06	0.25	0.56	0.86	1.12	1.37
	1.0	0.01	0.01	0.02	0.11	0.29	0.51	0.72	0.94
	10	0.01	0.01	0.01	0.03	0.11	0.23	0.38	0.56
	100	0.01	0.01	0.01	0.02	0.03	0.07	0.14	0.26
1-C_6H_{11} – 6 = c- C_6H_{11} 9	0.1	-0.01	0.04	0.01	0.11	0.28	0.37	0.44	0.50
	1.0	-0.01	0.03	-0.01	0.04	0.17	0.24	0.30	0.36
	10	-0.01	0.03	-0.02	0.00	0.08	0.13	0.17	0.22
	100	-0.01	0.03	-0.02	-0.02	0.04	0.05	0.07	0.11
1-C_6H_{11} – 6 = c-$C_5H_9CH_2$ 10	0.1	-0.05	0.06	0.07	0.23	0.44	0.58	0.61	0.72
	1.0	-0.05	0.04	0.01	0.10	0.25	0.37	0.39	0.51
	10	-0.05	0.03	-0.01	0.02	0.11	0.20	0.21	0.32
	100	-0.05	0.03	-0.01	0.00	0.04	0.09	0.07	0.17
c-$C_5H_9CH_2$ = 1-C_6H_{11} – 6 11	0.1	0.01	0.04	0.10	0.34	0.67	0.96	1.13	1.19
	1.0	0.01	0.01	0.03	0.13	0.33	0.54	0.70	0.79
	10	0.01	0.01	0.01	0.03	0.10	0.23	0.34	0.46
	100	0.01	0.01	0.01	0.01	0.02	0.05	0.11	0.20
1-CH_3-c-C_5 H_8-3 =1-C_6H_{11}-5 12	0.1	0.01	0.07	0.18	0.56	0.97	1.24	1.36	1.28
	1.0	0.00	0.01	0.04	0.23	0.52	0.77	0.91	0.94
	10	0.00	0.00	0.00	0.05	0.19	0.37	0.52	0.62
	100	0.00	0.00	0.00	0.00	0.03	0.11	0.21	0.33
1-C_6H_{11}-5 = 1-CH_3-c-C_5 H_8-3 13	0.1	0.14	0.23	0.39	0.77	1.04	1.13	1.02	0.78
	1.0	0.07	0.06	0.14	0.43	0.68	0.81	0.76	0.63
	10	0.05	0.00	0.00	0.16	0.37	0.51	0.51	0.47

	100	0.05	-0.01	-0.04	0.01	0.14	0.25	0.28	0.30
1-CH_3-c-C_5 H_8-3= 2-CH_3-4-C_5 H_8-1 14	0.1	0.01	0.06	0.17	0.54	0.94	1.21	1.33	1.26
	1.0	0.00	0.01	0.04	0.22	0.50	0.75	0.89	0.93
	10	0.00	0.00	0.00	0.05	0.19	0.36	0.51	0.61
	100	0.00	0.00	0.00	0.00	0.03	0.11	0.20	0.32
2-CH_3-4-C_5 H_8-1= 1-CH_3-c-C_5 H_8-3 15	0.1	0.03	0.14	0.17	0.46	0.72	0.87	0.98	0.89
	1.0	0.02	0.08	0.05	0.22	0.42	0.56	0.68	0.65
	10	0.01	0.06	-0.01	0.06	0.18	0.29	0.41	0.43
	100	0.01	0.05	-0.02	0.00	0.04	0.09	0.19	0.22
1-C_6H_{11} – 6 = 1-C_6H_{11} – 3 16	0.1	0.00	0.15	0.29	0.68	1.03	1.32	1.43	1.42
	1.0	-0.04	0.05	0.10	0.33	0.59	0.85	0.98	1.05
	10	-0.04	0.02	0.03	0.12	0.26	0.46	0.58	0.69
	100	-0.05	0.02	0.01	0.04	0.08	0.19	0.26	0.36
1-C_6H_{11} – 3 = 1-C_6H_{11} – 6 17	0.1	0.02	0.07	0.18	0.57	1.04	1.44	1.69	1.79
	1.0	0.00	0.01	0.04	0.20	0.51	0.83	1.08	1.26
	10	0.00	0.00	0.00	0.03	0.15	0.35	0.55	0.76
	100	0.00	0.00	0.00	0.00	0.01	0.07	0.17	0.33
c-$C_5H_9CH_2$ = 1-CH_3c-C_5H_8-3 18	0.1	0.08	0.04	0.05	0.29	0.68	0.96	1.20	1.19
	1.0	0.07	0.02	-0.01	0.10	0.34	0.56	0.76	0.79
	10	0.07	0.02	-0.02	0.00	0.12	0.23	0.39	0.45
	100	0.07	0.02	-0.02	-0.02	0.03	0.04	0.13	0.18
1-CH_3c-C_5H_8-3= c-$C_5H_9CH_2$	0.1	0.00	0.02	0.09	0.36	0.72	1.01	1.18	1.18
	1.0	0.00	0.01	0.03	0.15	0.39	0.63	0.79	0.86
	10	0.00	0.00	0.02	0.04	0.14	0.31	0.45	0.57
	100	0.00	0.00	0.01	0.01	0.03	0.09	0.18	0.30
1-C_6H_{11} – 3 = 4-C_6H_{11} – 320	0.1	0.07	0.00	0.03	0.26	0.65	0.90	1.12	1.30
	1.0	0.07	-0.02	-0.02	0.07	0.32	0.49	0.69	0.87
	10	0.07	-0.02	-0.02	-0.01	0.11	0.17	0.32	0.49
	100	0.07	-0.02	-0.02	-0.02	0.04	0.01	0.07	0.18
4-C_6H_{11} – 3 = 1-C_6H_{11} – 3 21	0.1	0.01	0.03	0.07	0.29	0.62	0.92	1.15	1.33
	1.0	0.01	0.01	0.02	0.10	0.28	0.50	0.70	0.89
	10	0.01	0.01	0.01	0.03	0.08	0.20	0.33	0.51
	100	0.01	0.01	0.01	0.01	0.02	0.04	0.10	0.20

Table 10c: Deviation from high pressure behavior as a result of the decomposition and isomerization of 1-hexenyl-5

case of the heptyl radicals described earlier. The high pressure rate constants are summarized in Table 9 Deviation from high pressure behavior can be seen in Table 10a-c

2: **1-Hexenyl-4**: There are no isomerization process that leads to the formation of this radical. It is particular interesting in that it can undergo a rapid homo-allylic rearrangement to form a primary radical. The consequence is the formation of additional 1,3-butadiene in place of the 1,3-pentadiene that is the major product from the decomposition of the secondary radical. The high pressure rate expressions can be found in Table 11 and the deviations from the high pressure values are in Table 12 .

Reaction	Log A	n	E/R	Basis for estimates
$1\text{-}C_6H_{11}\text{-}4 = 1,3\text{-}C_5H_8 + CH_3$	13.02	.172	6748	Methyl + propene and detailed balance [10]
$3\text{-}CH_2C_5H_9 = 1,3\text{-}C_4H_6 + C_3H_5$	12.69	.148	5606	Internal addition of methyl +butadiene and detailed balance
$1\text{-}C_6H_{11}\text{-}4 = 3\text{-}CH_2C_5H_9$	6.88	1.81	3245	From estimate of Carter and Tardy [19]
$3\text{-}CH_2C_5H_9 = 1\text{-}C_6H_{11}\text{-}4$	11.01	.707	3011	

Table 11: High Pressure Rate Expression for the decomposition and isomerization pg 1-Hexenyl-4

Reaction	Pressure	Temperature [K]								
	bar	600	700	800	900	1000	1200	1400	1600	1900
$1\text{-}C_6H_{11}\text{-}4 = 1,3\text{-}C_5H_8 + CH_3$	.1	0.06	0.18	0.40	0.67	0.95	1.39	1.61	1.64	1.47
	1.0	0.01	0.04	0.12	0.26	0.45	0.83	1.09	1.20	1.16
	10	0.00	0.01	0.02	0.06	0.14	0.38	0.62	0.78	0.84
	100	0.00	0.00	0.00	0.01	0.02	0.11	0.25	0.40	0.53
$3\text{-}CH_2C_5H_9 = 1,3\text{-}C_4H_6 + C_3H_5$	.1	0.04	0.13	0.31	0.54	0.79	1.18	1.37	1.40	1.23
	1.0	0.01	0.03	0.09	0.21	0.38	0.71	0.93	1.02	0.98
	10	0.00	0.01	0.02	0.05	0.12	0.33	0.54	0.67	0.72
	100	0.00	0.00	0.00	0.01	0.02	0.09	0.22	0.34	0.45
$1\text{-}C_6H_{11}\text{-}4 = 3\text{-}CH_2C_5H_9$	.1	0.00	0.02	0.08	0.20	0.35	0.63	0.85	0.98	1.01
	1.0	0.00	0.00	0.02	0.07	0.16	0.37	0.56	0.69	0.76
	10	0.00	0.00	0.00	0.02	0.05	0.17	0.32	0.44	0.54
	100	0.00	0.00	0.00	0.00	0.01	0.05	0.13	0.22	0.33
$3\text{-}CH_2C_5H_9 = 1\text{-}C_6H_{11}\text{-}4$	.1	0.00	0.02	0.08	0.19	0.31	0.55	0.71	0.83	0.82
	1.0	0.00	0.00	0.02	0.07	0.14	0.33	0.47	0.60	0.63
	10	0.00	0.00	0.01	0.02	0.04	0.15	0.26	0.39	0.46

Table 12: Deviation from high pressure behavior $\log(k_\infty/k\}$ for 1-hexenyl-4 decomposition and isomerization:

3: **1-Pentenyl Radicals**: The three isomers do not convert to each other. Thus each of these radicals undergo its own decomposition and isomerization processes.

3A. 1-Pentenyl-3. Kerr and Parsonage [10] have analyzed the available literature for the terminal addition of methyl to butadiene to form 1-penten-3-yl.. They recommend over the temperature range 353-453 the rate expression for terminal addition to be k(1,3-butadiene + methyl) $=1.34x10^{-13}exp(-2063/T)$ cm^3/molecule-s. At the low temperatures where these studies were carried out it is certainly the high pressure value, It is thus possible to calculate the high pressure rate expression for the reverse decomposition process through detailed balance**.**

$k = 5.7x10^{13}T^{-.102}exp(-18063/T)$

Table 13 summarizes results for the deviations from high pressure behavior.

Reaction	Pressure	Temperature [K]								
$1\text{-}C_5H_9\text{-}3 = 1,3\text{-}C_4H_6 + CH_3$	bar	600	700	800	900	1000	1200	1400	1600	1900
	.1	0.05	0.14	0.29	0.49	0.73	1.20	1.55	1.73	1.79
	1.0	0.01	0.03	0.08	0.18	0.31	0.65	0.96	1.17	1.31
	10	0.00	0.01	0.02	0.04	0.09	0.25	0.48	0.67	0.86
	199	0.00	0.00	0.00	0.01	0.02	0.06	0.16	0.28	0.45

Table 13: Deviation from high pressure behavior $\log(k_\infty/k\}$ for 1-pentenyl-3 decomposition and isomerization:

3B. 1-Pentenyl-4 The chemically activated decomposition of 1-penten-4-yl radical has been studied by Carter and Tardy (19) from the addition of hydrogen atoms to 1,4-pentadiene. The most interesting observation is that there is a very fast isomerization process, termed the homo-allylic rearrangement that occurs even at room temperature. An estimated maximum rate expression is $k(1\text{-}C_5H_9\text{-}4\text{-yl} => 3\text{-}CH_3\text{-}1\text{-}C_4H_7\text{-}4\text{-yl}) = 8x10^{12}exp(-7850/T)s^{-1}$. They also found that the barrier for methyl addition to the internal bond in butadiene is 13 to 17 kJ/mol higher than that for a similar reaction for terminal addition to an olefin and attribute this to the conjugation stabilization of 1,3-butadiene. We have used this through detailed balance to estimate the high pressure rate expression for the ejection of the methyl and internal hydrogen from 1-penten-4-yl (Table 14). The rate expressions for breaking the vinylic C-C bond is based on the rate constant for the addition of vinyl to ethylene and used for the decomposition of 1-butene-4-yl and that for the ejection of the external hydrogen is based on hydrogen addition to butadiene. As before, these are all high pressure values and are summarized in Table II.

Reaction	A	n	E/R
C5H9-4 ----> 1,3C5H8 + H	3.5E+08	-1.35363	-16350
C5H9-4 ----> C3H6 + C2H3	1.39E+12	-0.57976	-19022.3
C5H9-4 ----> 1,4-C5H8 + H	5.69E+09	-1.17085	-18670.1
C5H9-4 <---> 3-CH2C4H7	5.52E+08	-1.422	-7352.38
3-CH2C4H7 ----> 1,3-C4H6 + CH3	4.6E+11	-0.40671	-15729.1
3-CH2C4H7 <---> C5H9-4	3.14E+10	-1.0577	-6740.64

Table 14: High pressure rate expressions for the deomposition and isomerization of 1-pentenyl-4

Reaction	Pressure	Temperature / Log_{10} k_∞/k							
	bar	600	700	800	1000	1200	1400	1600	1900
C5H9-4 = 1,3C5H8 + H	0.1	0.03	0.10	0.24	0.70	1.23	1.66	1.94	2.11
	1.0	0.01	0.02	0.07	0.32	0.71	1.10	1.38	1.61
	10.0	0.00	0.01	0.02	0.10	0.32	0.61	0.88	1.14
	100	0.00	0.00	0.00	0.02	0.09	0.25	0.45	0.70
C5H9-4 = C3H6 + C2H3	0.1	0.08	0.19	0.38	0.94	1.53	1.96	2.21	2.31
	1.0	0.02	0.05	0.12	0.43	0.89	1.30	1.58	1.78
	10.0	0.01	0.01	0.03	0.14	0.40	0.72	1.01	1.26
	100	0.01	0.01	0.01	0.03	0.12	0.30	0.51	0.78
C5H9-4 = 1,4-C5H8 + H	0.1	0.08	0.20	0.39	0.97	1.58	2.02	2.27	2.37
	1.0	0.02	0.05	0.13	0.45	0.92	1.34	1.64	1.83
	10.0	0.01	0.01	0.03	0.15	0.42	0.75	1.05	1.31
	100	0.00	0.00	0.01	0.03	0.13	0.31	0.54	0.82
C5H9-4 =-CH2C4H7	0.1	0.00	0.01	0.02	0.13	0.34	0.56	0.74	0.95
	1.0	0.00	0.00	0.01	0.05	0.19	0.36	0.53	0.71
	10.0	0.00	0.00	0.00	0.02	0.08	0.20	0.33	0.49
	100	0.00	0.00	0.00	0.01	0.02	0.08	0.16	0.30
3-CH2C4H7 =1,3-C4H6 + CH3	0.1	0.03	0.09	0.21	0.63	1.12	1.50	1.75	1.91
	1.0	0.01	0.02	0.06	0.28	0.64	0.99	1.24	1.45
	10.0	0.00	0.01	0.01	0.09	0.28	0.55	0.78	1.02
	100	0.00	0.00	0.01	0.02	0.08	0.22	0.40	0.62
3-CH2C4H7 = C5H9-4	0.1	0.02	0.01	0.03	0.14	0.31	0.52	0.67	0.83
	1.0	0.02	0.01	0.02	0.06	0.16	0.34	0.47	0.62
	10.0	0.02	0.01	0.02	0.02	0.06	0.19	0.29	0.43
	100	0.02	0.01	0.01	0.01	0.01	0.08	0.14	0.25

Table 15: : Deviation from high pressure behavior log(k_∞/k} for 1-pentenyl-4 decomposition and isomerization:

B3-Pentenyl-5: Tsang and Walker [20] produced 1-penten-5-yl from the decomposition of 1,7-octadiene and determined the ratio of the cyclopentene and ethylene to follow the relation (cyclopentene)/ (ethylene) = 6.9×10^{-3} exp(2118/T) over the temperature range of 1050-1150 and ata pressure of 3 bar argon. Since these product are formed rapidly under the reaction conditions, they are a direct reflection of the branching ratio for 1-penten-5-yl decomposition. Handford-Styring and Walker [21] have determined the rate expression for ethylene formation during the decomposition of cyclopentyl radicals in a slowly reacting hydrogen/oxygen mixture and derived the followingto rate expression 1.4×10^{13} exp(-17260/T). Their analysis also included the earlier work of Gordon [22]. This can be

considered to be the rate determining step if ring opening reaction is not reversed. This is a fundamental problem with high temperature work. That is the possibility of contributions from the reverse reactions. Hydrogen addition to cyclohexene and cis-butene-2 have been summarized by Parsonage and Kerr [10]. The rate constants are all near $8x10^{-13}$ cm^3/molecule-s. Using an activation of 17 kJ/mol this leads to a rate expression 0f $6.6x10^{-10}exp(-2000/T)$ cm^3/molecule-s. Detailed balance then leads to a high pressure rate expression for the ejection of a hydrogen atom from cyclopentyl radical. We then adjusted the barriers to decylization of cyclopentyl radicals and the decomposition of 1-penten-5-yl to match the experimental observations This leads to the high pressure rate expressions summarized in Table 16. It appears that the experimental determination are within a factor of 2 to 3 of the high pressure limit. This has no consequence on the present conclusions since the fits are made on the basis of direct comparisons of the rate constants. Note that unlike the first two cases where the expressions were directly derived from the reverse rate expressions, for this system the existing data used in the analysus is directly concerned with the decomposition process. However the isomerization process is very important and must estimated through an iterative procedure involving directly fitting the experimental observations.

Reaction	A	n	E/R
C5H9-5 ----> C3H5 (allyl) + C2H4	12.018	-0.36984	-12644.3
c-C5H9 <---> C5H9-5	12.33285	-0.29294	-16971
c-C5H9 ----> c-C5H8 + H	11.81478	-0.54805	-16678.6
C5H9-5 <---> c-C5H9	6.29403	-1.2675	-8594.65

Table 16: High pressure rate expression for the decomposition and isomerization of 1-pentenyl-5

Reactions	Pressure	Temperature/k_∞/k							
	Bar	600	700	800	1000	1200	1400	1600	1900
C5H9-5 ----> C3H5 (allyl) + C2H4	0.1	0.05	0.15	0.31	0.72	1.05	1.23	1.27	1.17
	1.0	0.01	0.03	0.08	0.30	0.56	0.76	0.86	0.87
	10.0	0.00	0.01	0.01	0.07	0.21	0.36	0.48	0.57
	100.0	0.03	0.09	0.20	0.56	0.99	1.34	1.57	1.68
c-C5H9 <---> C5H9-5	0.1	0.02	0.03	0.06	0.24	0.54	0.83	1.06	1.21
	1.0	0.02	0.02	0.02	0.07	0.22	0.42	0.61	0.80
	10.0	0.02	0.02	0.02	0.02	0.06	0.14	0.27	0.44
	100.0	0.02	0.08	0.19	0.55	0.98	1.34	1.52	1.68
c-C5H9 ----> c-C5H8 + H	0.1	0.01	0.02	0.05	0.23	0.53	0.83	1.01	1.22
	1.0	0.01	0.01	0.01	0.06	0.21	0.42	0.56	0.80
	10.0	0.01	0.01	0.01	0.01	0.05	0.14	0.21	0.44
	100.0	0.06	0.19	0.37	0.77	1.05	1.24	1.34	1.25
C5H9-5 <---> c-C5H9	0.1	0.01	0.07	0.16	0.44	0.68	0.86	0.98	0.96
	1.0	0.00	0.03	0.05	0.18	0.36	0.53	0.65	0.70
	10.0	0.00	0.02	0.02	0.05	0.12	0.25	0.37	0.45
	100.0	0.22	0.45	0.75	1.29	1.62	1.74	1.71	1.49

Table 17: : Deviation from high pressure behavior log(k_∞/k} for 1-pentenyl-5 decomposition and isomerization

B4. 1-Butenyl: There are 2 isomeric compounds. One, 1-butenyl-3 involves a resonance stabilized compound and is much more stable than the 1-butenyl-4. There are no isomerization process that converts these compounds

B4a. **1-butenyl-3**: The high pressure rate expression was derived through detailed balance from the reverse radical addition to 1,3-butadiene[10].

$k=4.7x10^{8}\ T^{1.316}exp(-22495/T)$

Reaction	Pressure	Temperature [K]								
1-C_4H_7 –3 = 1,3-C_4H_6 + H	bar	600	700	800	900	1000	1200	1400	1600	1900
	.1	0.00	0.01	0.04	0.09	0.18	0.45	0.82	1.20	1.67
	1.0	0.00	0.00	0.01	0.02	0.04	0.16	0.37	0.65	1.06
	10	0.00	0.00	0.00	0.00	0.01	0.04	0.12	0.26	0.54
	100	0.00	0.00	0.00	0.00	0.00	0.01	0.02	0.06	0.19

Table 18: : Deviation from high pressure behavior $\log(k_\infty/k\}$ for 1-butenyl-3 decomposition and isomerization

B4b 1-Butenyl-4: This is a two channel process. The present results are based on the experimental observations of Fahr and Stein[23] and Shestov et al[24] on the kinetics of the reverse radical addition reaction and through detailed balance. Experimentally these are chemically activated processes. This has been taken into account in the present analysis.

Reaction	A	n	E/R
C4H7-4 ----> C4H6 (1,3 butadiene) + H	9.6308	-0.95993	-16086
C4H7-4 ----> C2H3 + C2H4	9.81522	-1.06742	-17747.1

Table 19: High pressure rate expressions for the decomposition and isomerization of 1-butenyl-4

Reactions	Pressure bar	Temperature							
		600	700	800	1000	1200	1400	1600	1900
C4H7-4 ----> C4H6 (1,3 butadiene) + H	.1	0.11	0.23	0.41	0.86	1.33	1.59	1.96	2.15
	1.0	0.02	0.07	0.15	0.42	0.77	0.99	1.35	1.58
	10	0.00	0.01	0.03	0.14	0.35	0.48	0.82	1.06
	100	0.00	0.00	0.00	0.03	0.10	0.12	0.39	0.60
C4H7-4 ----> C2H3 + C2H4	.1	0.24	0.41	0.64	1.18	1.70	2.09	2.32	2.45
	1.0	0.06	0.13	0.24	0.58	0.99	1.36	1.62	1.82
	10	0.01	0.03	0.06	0.21	0.46	0.74	0.99	1.23
	100	0.00	0.01	0.01	0.05	0.14	0.30	0.47	0.71

Table 20: : Deviation from high pressure behavior $\log(k_\infty/k\}$ for 1-butenyl-4 decomposition and isomerization

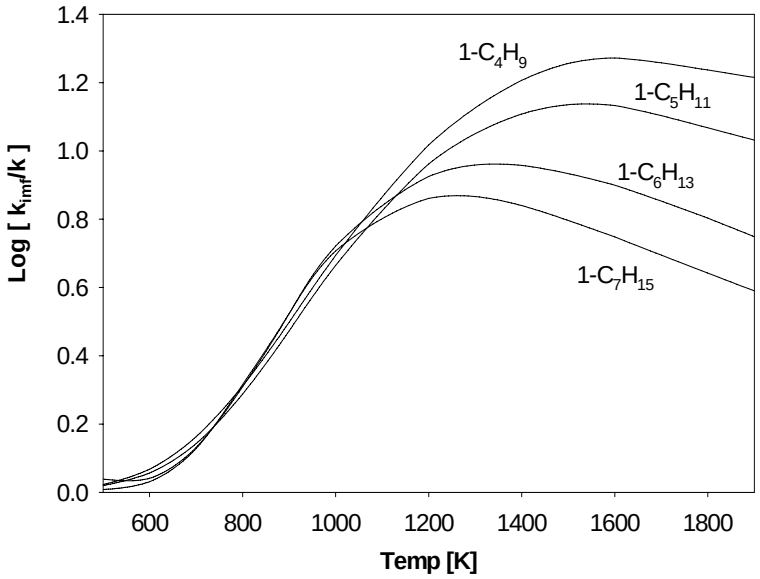

Figure 12: Departure from high pressure behavior for the beta bond scission reactions of various 1-alkyl radicals,

C: Molecular Decomposition : The stable molecules of interest are heptane and 1-olefins ranging from 1-hexene to 1-butene. The high pressure rate expressions for these processes are well established. Experimental data range from single pulse shock tube results in the 1100 K range and inferred rate constants for combination of the radicals formed from bond cleavage. For the 1-olefins there are also a retroene process leading to the production of two olefins. Here too earlier studies have led to correlations that permit the prediction of rate constants. The results are summarized in Table 21 . Due to the high reaction thresholds for these stable compounds fall-off behavior are only exhibited at temperatures much higher than that for the much less stable radicals described earlier. However, at the highest temperatures the fall-off is much more than the radicals since the reaction thresholds are always higher than the peak of the distribution functions.

General Observations: For all the unimolecular reactions treated here at sufficiently high temperatures fall-off effects must be taken into account. For the radicals that have been examined it is expected that at sufficiently high temperatures fall-off effects will become smaller as the size of the molecule becomes larger. From Figure 12, it appears that also there is a decrease in the deviation from the high pressure limit with molecular size at 1 bar. This decrease is very slow and unless the pressure is much higher it is probably not possible to ignore this effect for simulations. This is somewhat disappointing since it would be much simpler to be able to neglect the pressure dependence and use the high pressure rate expressions.

Reaction: Rate Expression A T^nexp(-E/RT) Log A, n, E/R	[P]	Temperature [K]						Rationale for assigments
		1000	1200	1400	1600	1800	2000	
nC_7H_{16} =nC_4H_9+C_3H_7 24.41, -2.21, 44149	0-1	-0.03	-0.20	-0.65	-1.31	-2.02	-2.69	Correlation of results from alkane decomposition. Rate constants for reverse combination. Geometric mean rule. Detailed balance.[25.26]
	1	0.00	-0.06	-0.30	-0.76	-1.34	-1.94	
	10	0.00	-0.01	-0.10	-0.35	-0.76	-1.25	
	100	0.00	0.00	-0.02	-0.11	-0.34	-0.68	
nC_7H_{16} =nC_5H_{11}+C_2H_5 24.84, -2.33, 44340	0-.1	-0.03	-0.21	-0.66	-1.32	-2.05	-2.72	Same as above
	1	0.00	-0.07	-0.30	-0.77	-1.36	-1.95	
	10	0.00	-0.01	-0.10	-0.35	-0.77	-1.27	
	100	0.00	0.00	-0.02	-0.12	-0.35	-0.69	
nC_7H_{16} =nC_6H_{13}+CH_3 23.19, -1.85, 45286	0-.1	-0.04	-0.25	-0.74	-1.44	-2.19	-2.89	Same as above
	1	-0.01	-0.08	-0.35	-0.84	-1.46	-2.08	
	10	0.00	-0.02	-0.12	-0.39	-0.84	-1.35	
	100	0.00	0.00	-0.03	-0.13	-0.38	-0.74	
1-C_6H_{12}=C_3H_5+nC_3H_7 23.03, -2.03, 37724	0-.1	-0.06	-0.26	-0.66	-1.18	-1.73	-2.23	Experimental results for single pulse shock tube studies. Rate constants for combination from geometric mean rule and detailed balance [25,26]
	1	-0.01	-0.08	-0.29	-0.64	-1.06	-1.49	
	10	0.00	-0.02	-0.09	-0.26	-0.53	-0.86	
	100	0.00	0.00	-0.02	-0.07	-0.19	-0.38	
1-C_6H_{12}=2C_3H_6 6.85, 165, 27052	0-.1	-0.01	-0.10	-0.36	-0.76	-1.20	-1.62	Experimental results from single pulse shock tube [25,26]
	1	0.00	-0.03	-0.15	-0.40	-0.74	-1.09	
	10	0.00	-0.01	-0.04	-0.16	-0.37	-0.63	
	100	0.00	0.00	-0.01	-0.04	-0.13	-0.28	
1-C_5H_{10}=C_3H_5+C_2H_5 22.86, -1.94, 37982	0-.1	-0.13	-0.41	-0.84	-1.38	-1.92	-2.42	Experimental results for single pulse shock tube studies. Rate constants for combination from geometric mean rule and detailed balance [25,26]
	1	-0.03	-0.15	-0.41	-0.79	-1.23	-1.66	
	10	-0.01	-0.04	-0.15	-0.36	-0.66	-1.00	
	100	0.00	-0.01	-0.03	-0.12	-0.27	-0.48	
1-C_5H_{10}=C_3H_6+C_2H_4 6.21, 1.81.26902	0-.1	-0.13	-0.41	-0.84	-1.38	-1.92	-2.42	Experimental results from single pulse shock tube
	1	-0.03	-0.15	-0.41	-0.79	-1.23	-1.66	
	10	-0.01	-0.04	-0.15	-0.36	-0.66	-1.00	
	100	0.00	-0.01	-0.03	-0.12	-0.27	-0.48	
1-C_4H_8=C_3H_5+nCH_3 21.53,-1.60,38894	0-.1	-0.25	-0.44	-0.95	-1.41	-1.89	-2.33	Correlation of results from alkene decomposition Rate constants for reverse combination. Geometric mean rule. Detailed balance.[25,26]
	1	-0.08	-0.24	-0.50	6.40	-1.21	-1.60	
	10	-0.02	-0.08	-0.20	-0.98	-0.66	-0.96	
	100	0.00	-0.01	-0.05	6.66	-0.28	-0.46	

Table 21: Rate constants and expressions for heptane and molecular products from heptane pyrolysis

Compounds	Threshold Soot Index	Compounds	Threshold Soot Index
ethane	0	Ethene	1.3
propane	0.6	Propene	4.8
butane	1.4	1-butene	4.4
isobutane	2.2	isobutene	4.8
pentane	1.3	1,3 butadiene	25
hexane	2.5	1-pentene	4.2
2-methypentane	2.9	1-hexene	4.4
heptane	2.7	1-heptene	4.6
octane	3.2	cyclohexene	5.7
cyclohexane	3.2		

Table 22: Propensity for forming soot for various organic compounds

The rate constants and expressions deduced in the manner described above is necessary for simulation purposes and also as a basis for estimates for related reactions. Note that the highest temperatures are above those from the experimental measurements. There is thus uncertainty regarding the proper extrapolation of the high pressure rate constants. This may be a source of uncertainty. However extrapolation from 1100K to 1900 K is comparatively small in 1/T space.

A very interesting consequence of the pyrolytic mechanism is the possibility of ranking various fuels in terms of soot formation propensities. This is of course an important practical issue.Table 22 contains a listing of threshold soot index. The important feature is the very large value for 1,3butadiene. Thus the propensity for 1,3-butadiene formation can be taken as a surrogate for soot formation. This in turn suggest that small hydrocarbon fuels will be less sooting than the larger hydrocarbon fuels, since only the decomposition of the latter can lead to butadiene formation. Also, larger olefinic fuels will be more likely to soot than the larger hydrocarbons. From this is follows that a fuel such as cyclohexane will have have similar soot forming propensities as the larger olefins. The overall scale of soot forming tendencies will be light alkanes< larger alkanes<larger oefins ~cyclohexane. This is in rather good agreement with the listings in Table 22. It suggests the great importance of pyrolysic processes and is dominated by butadiene formation. Note that along with butadiene formation resonance stabilized radicals are also formed. It would be extremely interesting to see how these qualitative insights can be fine tuned through the modeling of pyrolytic systems. The importance of such work is that they relate soot forming propensities to molecular properties and will be extremely important for mixtures.

References

1 Gilbert, R.S. and Smith S. C.,"Theory of Unimolecular and Recombination Reactions", Blackwell Scientific, London, 1990

2. Tsang, W., "A Pre-processor for the Generation of Chemical Kinetics Data for Simulations" AAIA-2001-0359, 39th AIAA Aerospace Sciences Meeting and Exhibit, Jamuary 8-11, 2001 Reno. NV

3. Tsang, W. and Lifshitz, A., "Single Pulse Shock Tube", in "***Part III Chemical Reactions in Shock Waves***," Academic Press ,New York (2001) 108-193 .

4. Tsang, W.,Awan,I., McGovern, S., Manion, J. A., "Soot Precursors from Real Fuels: The Unimolecular Reactions of Fuel Radicals" in "Combustion Generated Fine Carbon Particles" (A. Sarofim, ed) in press

5. Stull, D. R., Westrum, D. F., and Sinke, G. C. "***The Chemical Thermodynamics of Organic Compounds"***, John Wiley and Sons, New York, (1969)

6. Pitzer, K. S., J. Chem. Phys . 12, 310-314, 1944

7. Benson, S. W., "***Thermochemical Kinetics***", John Wiley and Sons, New York, (1974)

8.. Tsang, W, Walker, J. A. and Manion, J. A., Proc. Comb. Institute, 31, 141-148, 207

9. Knyazev, V. D. and Slagle, I. R., *J. Phys. Chem*., 100, (1996), 5318-5328

10. Kerr, J. A., and Parsonage, M. J., "Evaluated Kinetic Data on Gas Phase Addition Reactions, Reactions of Atoms and Radicals with Alkenes, Alkynes and Aromatic Compounds, CRC Press, 18901 Cranwood

11. Jitariu, L. C., Jones, L. D., Robertson, S. H., Pilling, M. J., and Hillier, I. H., *J. Phys. Chem*. A, 107 (2003) 8607-86178.

12. Watkins, K. M. , *J. Phys. Chem.,* 77 (1973) 2938-2941

13. Dobe, S., Berces, T., Reti, F. and Marta, F. *Int. J. Chem Kin.* , 19 (1987) 895-921

14. Curran, H. J., Gaffuri, P., Pitz, W. J., and Westbrook, C. K., Comb. and Flame., 114, 149, 1998

15. Stein, S. E. and Rabinovitch, B. S., J. Phys. Chem., 79, 191, 1975

16. Tsang, W., J. Phys. Chem. Ref. Data., 17 (2): 887-952 1988

17. Tsang, W., Walker, J. A. and Manion, J. A., 27th Int. Symp.on Comb., The Combustion Institute, Pittsburg, Pa., 2431-2439, (1999)

18. Tsang, W., J. Phys. ChemA.,110 (27): 8501-8509 JUL 13 2006

19. Carter, W. J., and Tardy, D., J. Phys. Chem., 1974, 78, 1245-1248

20**.** Tsang, W. , Walker, J. A., J. Phys. Chem., 1992, 96, 8378-8384

21. Handbury-Styring, S. M., Walker, R. W.,; J. Chem. Soc. Farad Trans., 1995, 91 1431-1438

22. Gordon, A. S., Can. J. Chem. 1965., 43, 570-581

23 Fahr, A. , Stein, S. E., Proc. Comb. Inst. 1988, 1023-1029

24. Shestov1, A. A., Popov, K. V., Slagle, I. R., and , Knyazev, V. D., Chem. Phys. Letters. Letters. 408 2005 339

25. Tsang, W. and Kiefer, J. H. "Unimolecular Reactions of Large Polyatomic Molecules" in "The Chemical Dynamics and Kinetics of Small Radicals, Vol 1, (K. Liu and A. Wagner,ed) World Scientific, Singapore, 1995, pg 58

26. Tsang, W., and Lifshitz, A. "Shock Tube Techniques in Chemical Kinetics" in 41th Ann. Rev. of Phys. Chem. (Strauss, H. L., ed.) Nnual Reviews, Inc. Palo Alto, 559-599,1990

27. Calcote, H. F. and Manos, D. M., Combustion and Flames, 49: 289-304 (1983)

Component: C4H7-3
Units: Joules

T	Cp	S	-(F°-H°)/T	H°-H°(298)	dH°	dF°	log Kp
0	0.000	0.000	inf	-15.594	160.501	160.501	inf
300	75.250	326.678	326.215	0.139	142.145	188.495	-32.820
400	96.569	351.247	329.419	8.731	136.475	204.819	-26.747
500	116.104	374.942	336.168	19.387	131.596	222.489	-23.243
600	132.792	397.625	344.535	31.854	127.499	241.064	-20.987
700	146.947	419.186	353.673	45.859	124.130	260.271	-19.422
800	159.051	439.617	363.150	61.174	121.425	279.908	-18.276
900	169.475	458.967	372.731	77.612	119.314	299.853	-17.403
1000	178.485	477.300	382.279	95.021	117.717	320.001	-16.715
1100	186.284	494.685	391.714	113.268	116.552	340.290	-16.159
1200	193.042	511.190	400.989	132.242	115.749	360.668	-15.699
1300	198.905	526.879	410.074	151.846	115.233	381.099	-15.313
1400	203.998	541.809	418.955	171.997	114.950	401.569	-14.983
1500	208.434	556.038	427.623	192.623	114.852	422.041	-14.697
1600	212.306	569.616	436.076	213.664	114.895	442.525	-14.447
1700	215.698	582.591	444.316	235.068	115.041	462.992	-14.226
1800	218.677	595.006	452.345	256.789	115.266	483.457	-14.030
1900	221.303	606.901	460.169	278.791	115.549	503.905	-13.853
2000	223.626	618.312	467.793	301.039	115.867	524.336	-13.694

Component: C4H7-4
Units: Joules

T	Cp	S	-(F°-H°)/T	H°-H°(298)	dH°	dF°	log Kp
300	80.576	319.915	319.419	0.149	200.731	249.109	-43.374
400	100.948	345.888	322.820	9.227	195.546	266.035	-34.741
500	119.547	370.454	329.911	20.272	191.057	284.193	-29.689
600	135.493	393.695	338.622	33.044	187.265	303.188	-26.395
700	149.090	415.627	348.071	47.289	184.136	322.768	-24.085
800	160.779	436.315	357.820	62.796	181.623	342.747	-22.379
900	170.891	455.849	367.637	79.391	179.669	363.013	-21.069
1000	179.663	474.318	377.389	96.928	178.200	383.466	-20.030
1100	187.277	491.806	387.003	115.283	177.143	404.049	-19.187
1200	193.890	508.391	396.433	134.349	176.431	424.710	-18.487
1300	199.635	524.142	405.656	154.031	175.994	445.418	-17.897
1400	204.634	539.123	414.658	174.250	175.779	466.160	-17.393
1500	208.992	553.393	423.435	194.936	175.740	486.898	-16.955
1600	212.801	567.004	431.986	216.029	175.835	507.645	-16.573
1700	216.138	580.007	440.314	237.479	176.028	528.372	-16.235
1800	219.071	592.446	448.422	259.242	176.295	549.094	-15.934
1900	221.658	604.361	456.318	281.281	176.615	569.797	-15.665
2000	223.947	615.789	464.008	303.563	176.966	590.481	-15.422

Component: C5H9-5
Units: Joules

T	Cp	S	-(F°-H°)/T	H°-H°(298)	dH°	dF°	log Kp
300	101.062	353.369	352.747	0.186	180.617	259.954	-45.262
400	128.698	386.251	357.041	11.684	173.923	287.437	-37.535
500	153.404	417.690	366.050	25.820	168.275	316.493	-33.064
600	174.273	447.555	377.167	42.233	163.617	346.590	-30.173
700	191.896	475.777	389.257	60.564	159.862	377.398	-28.162
800	206.953	502.407	401.752	80.524	156.929	408.679	-26.684
900	219.930	527.549	414.345	101.883	154.730	440.290	-25.554
1000	231.160	551.315	426.865	124.451	153.165	472.106	-24.660
1100	240.894	573.814	439.210	148.064	152.133	504.056	-23.936
1200	249.339	595.144	451.323	172.585	151.548	536.078	-23.335
1300	256.671	615.398	463.172	197.894	151.317	568.131	-22.828
1400	263.048	634.657	474.738	223.887	151.372	600.203	-22.394
1500	268.605	652.999	486.016	250.475	151.654	632.246	-22.017
1600	273.459	670.493	497.003	277.583	152.108	664.279	-21.687
1700	277.712	687.201	507.703	305.146	152.687	696.266	-21.394
1800	281.450	703.182	518.122	333.108	153.361	728.226	-21.133
1900	284.746	718.489	528.268	361.420	154.105	760.144	-20.898
2000	287.661	733.170	538.149	390.043	154.888	792.019	-20.685

Component: c-C5H9
Units: Joules

T	Cp	S	-(F°-H°)/T	H°-H°(298)	dH°	dF°	log Kp
300	91.721	302.094	301.530	0.169	117.839	212.559	-37.010
400	123.086	332.803	305.505	10.919	110.397	245.292	-32.032
500	151.395	363.389	314.031	24.679	104.374	279.742	-29.225
600	175.323	393.171	324.754	41.050	99.675	315.278	-27.447
700	195.387	421.749	336.585	59.615	96.153	351.508	-26.230
800	212.342	448.977	348.946	80.024	93.669	388.163	-25.344
900	226.776	474.843	361.510	101.999	92.086	425.081	-24.671
1000	239.122	499.392	374.082	125.310	91.264	462.129	-24.139
1100	249.714	522.692	386.542	149.765	91.074	499.231	-23.706
1200	258.820	544.820	398.818	175.203	91.406	536.324	-23.346
1300	266.668	565.855	410.864	201.487	92.150	573.370	-23.038
1400	273.450	585.871	422.656	228.501	93.226	610.359	-22.773
1500	279.328	604.942	434.178	256.147	94.566	647.243	-22.539
1600	284.439	623.137	445.423	284.341	96.106	684.047	-22.332
1700	288.900	640.518	456.392	313.013	97.795	720.735	-22.145
1800	292.808	657.144	467.087	342.103	99.596	757.331	-21.977
1900	296.244	673.069	477.512	371.559	101.484	793.820	-21.824
2000	299.275	688.343	487.674	401.338	103.423	830.208	-21.683

Component: C5H9-4
Units: Joules

T	Cp	S	-(F°-H°)/T	H°-H°(298)	dH°	dF°	log Kp
300	95.489	367.800	367.213	0.176	168.473	243.481	-42.394
400	123.139	399.070	371.288	11.113	161.218	269.605	-35.207
500	148.328	429.316	379.887	24.715	155.036	297.441	-31.073
600	169.847	458.314	390.560	40.653	149.903	326.421	-28.417
700	188.109	485.903	402.226	58.574	145.739	356.186	-26.579
800	203.731	512.067	414.335	78.185	142.457	386.479	-25.234
900	217.184	536.858	426.584	99.247	139.960	417.142	-24.210
1000	228.808	560.357	438.796	121.560	138.141	448.041	-23.403
1100	238.866	582.647	450.869	144.956	136.890	479.097	-22.750
1200	247.577	603.813	462.740	169.288	136.117	510.244	-22.210
1300	255.131	623.935	474.372	194.432	135.721	541.437	-21.755
1400	261.692	643.087	485.744	220.280	135.632	572.661	-21.366
1500	267.403	661.341	496.847	246.741	135.786	603.866	-21.028
1600	272.388	678.761	507.676	273.736	136.127	635.068	-20.733
1700	276.752	695.408	518.233	301.197	136.605	666.231	-20.471
1800	280.585	711.338	528.522	329.068	137.188	697.373	-20.237
1900	283.963	726.600	538.548	357.299	137.850	728.477	-20.027
2000	286.950	741.243	548.320	385.847	138.558	759.543	-19.837

Component: 3-CH2C4H7
Units: Joules

T	Cp	S	-(F°-H°)/T	H°-H°(298)	dH°	dF°	log Kp
300	104.691	350.078	349.434	0.193	172.465	252.790	-44.015
400	132.038	383.987	353.871	12.046	166.126	280.547	-36.636
500	156.123	416.109	363.136	26.486	160.783	309.792	-32.364
600	176.411	446.418	374.515	43.142	156.368	340.023	-29.602
700	193.562	474.935	386.844	61.663	152.803	370.928	-27.679
800	208.253	501.764	399.549	81.772	150.018	402.283	-26.266
900	220.950	527.043	412.324	103.247	147.935	433.951	-25.186
1000	231.967	550.905	425.000	125.905	146.461	465.812	-24.332
1100	241.538	573.473	437.481	149.591	145.501	497.799	-23.639
1200	249.858	594.854	449.712	174.170	144.974	529.852	-23.064
1300	257.094	615.146	461.664	199.526	144.791	561.932	-22.579
1400	263.396	634.434	473.322	225.557	144.884	594.028	-22.163
1500	268.894	652.798	484.680	252.178	145.198	626.092	-21.802
1600	273.701	670.309	495.738	279.313	145.679	658.144	-21.486
1700	277.917	687.031	506.503	306.898	146.281	690.148	-21.206
1800	281.625	703.023	516.979	334.879	146.974	722.125	-20.956
1900	284.896	718.339	527.177	363.208	147.734	754.058	-20.730
2000	287.792	733.028	537.105	391.845	148.531	785.948	-20.527

Component: 1-C6H11-6
Units: Joules

T	Cp	S	-(F°-H°)/T	H°-H°(298)	dH°	dF°	log Kp
300	124.041	395.443	394.680	0.229	160.506	268.217	-46.701
400	157.736	435.767	399.947	14.328	152.485	305.364	-39.877
500	187.930	474.291	410.993	31.649	145.773	344.390	-35.978
600	213.409	510.871	424.618	51.752	140.298	384.648	-33.487
700	234.895	545.424	439.431	74.195	135.945	425.736	-31.769
800	253.233	578.016	454.736	98.624	132.606	467.368	-30.516
900	269.026	608.776	470.159	124.755	130.170	509.372	-29.563
1000	282.687	637.843	485.487	152.356	128.512	551.598	-28.813
1100	294.525	665.354	500.599	181.230	127.507	593.962	-28.205
1200	304.792	691.431	515.424	211.208	127.049	636.391	-27.701
1300	313.706	716.187	529.923	242.142	127.025	678.837	-27.276
1400	321.457	739.724	544.075	273.909	127.349	721.286	-26.912
1500	328.210	762.138	557.871	306.399	127.952	763.681	-26.594
1600	334.110	783.512	571.311	339.522	128.763	806.047	-26.315
1700	339.278	803.925	584.398	373.196	129.729	848.339	-26.066
1800	343.820	823.449	597.140	407.355	130.809	890.585	-25.844
1900	347.824	842.147	609.547	441.941	131.975	932.764	-25.643
2000	351.367	860.080	621.628	476.904	133.189	974.878	-25.461

Component: c-C6H11
Units: Joules

T	Cp	S	-(F°-H°)/T	H°-H°(298)	dH°	dF°	log Kp
300	110.378	326.521	325.842	0.204	72.618	201.005	-34.998
400	149.080	363.609	330.637	13.189	63.482	245.225	-32.023
500	184.069	400.730	340.952	29.889	56.150	291.548	-30.458
600	213.742	436.991	353.953	49.823	50.506	339.183	-29.529
700	238.685	471.868	368.325	72.480	46.366	387.646	-28.927
800	259.773	505.155	383.365	97.432	43.550	436.601	-28.507
900	277.709	536.815	398.671	124.330	41.881	485.847	-28.198
1000	293.022	566.889	414.002	152.886	41.178	535.219	-27.957
1100	306.130	595.447	429.210	182.861	41.274	584.626	-27.762
1200	317.375	622.579	444.204	214.050	42.028	633.992	-27.597
1300	327.045	648.374	458.925	246.283	43.302	683.271	-27.454
1400	335.385	672.923	473.341	279.415	44.992	732.450	-27.328
1500	342.600	696.314	487.432	313.323	47.011	781.476	-27.213
1600	348.865	718.630	501.190	347.903	49.281	830.376	-27.109
1700	354.325	739.947	514.613	383.069	51.738	879.111	-27.012
1800	359.102	760.338	527.702	418.746	54.336	927.711	-26.921
1900	363.297	779.869	540.463	454.870	57.040	976.159	-26.836
2000	366.996	798.599	552.905	491.388	59.810	1024.460	-26.756

Component: 1-C6H11-5
Units: Joules

T	Cp	S	-(F°-H°)/T	H°-H°(298)	dH°	dF°	log Kp
300	118.607	404.559	403.830	0.219	152.129	257.104	-44.766
400	152.429	443.328	408.886	13.777	143.566	293.421	-38.317
500	183.156	480.723	419.537	30.593	136.349	331.751	-34.658
600	209.286	516.491	432.739	50.251	130.430	371.407	-32.334
700	231.390	550.458	447.151	72.314	125.696	411.964	-30.741
800	250.263	582.618	462.093	96.421	122.035	453.115	-29.585
900	266.503	613.055	477.191	122.278	119.326	494.675	-28.710
1000	280.530	641.877	492.231	149.647	117.434	536.486	-28.023
1100	292.668	669.197	507.088	178.321	116.229	578.457	-27.469
1200	303.181	695.124	521.686	208.125	115.599	620.509	-27.010
1300	312.298	719.759	535.983	238.909	115.424	662.592	-26.623
1400	320.218	743.200	549.954	270.544	115.617	704.688	-26.292
1500	327.113	765.533	563.587	302.918	116.103	746.740	-26.004
1600	333.133	786.840	576.880	335.937	116.811	788.769	-25.751
1700	338.402	807.198	589.833	369.519	117.684	830.732	-25.525
1800	343.031	826.674	602.454	403.596	118.682	872.653	-25.324
1900	347.111	845.332	614.749	438.107	119.773	914.511	-25.142
2000	350.719	863.230	626.729	473.002	120.919	956.308	-24.976

Component: cC5H9-CH2
Units: Joules

T	Cp	S	-(F°-H°)/T	H°-H°(298)	dH°	dF°	log Kp
300	104.910	354.495	353.850	0.193	95.620	215.614	-37.542
400	143.353	389.956	358.424	12.613	85.918	257.122	-33.577
500	178.194	425.786	368.317	28.735	78.007	300.877	-31.432
600	207.514	460.946	380.839	48.064	71.759	346.063	-30.127
700	232.004	494.828	394.720	70.076	66.974	392.181	-29.265
800	252.649	527.193	409.273	94.336	63.467	438.887	-28.656
900	270.207	557.992	424.100	120.502	61.066	485.973	-28.205
1000	285.220	587.258	438.965	148.293	59.596	533.268	-27.855
1100	298.100	615.062	453.721	177.475	58.900	580.677	-27.574
1200	309.177	641.487	468.276	207.852	58.843	628.117	-27.341
1300	318.727	666.620	482.575	239.259	59.290	675.539	-27.143
1400	326.981	690.550	496.582	271.554	60.143	722.924	-26.973
1500	334.138	713.359	510.280	304.619	61.319	770.217	-26.821
1600	340.364	735.127	523.658	338.351	62.741	817.441	-26.687
1700	345.799	755.928	536.713	372.665	64.346	864.552	-26.564
1800	350.561	775.831	549.449	407.488	66.090	911.579	-26.453
1900	354.749	794.899	561.869	442.758	67.940	958.500	-26.351
2000	358.445	813.191	573.981	478.421	69.854	1005.321	-26.256

Component: 1-CH3cC5H8-3
Units: Joules

T	Cp	S	-(F°-H°)/T	H°-H°(298)	dH°	dF°	log Kp
300	108.038	346.612	345.948	0.199	89.349	211.709	-36.862
400	147.379	383.134	350.662	12.989	80.018	253.951	-33.163
500	182.122	419.864	360.836	29.514	72.511	298.341	-31.168
600	211.006	455.705	373.679	49.216	66.635	344.084	-29.955
700	235.005	490.089	387.872	71.552	62.174	390.700	-29.154
800	255.203	522.826	402.712	96.091	58.945	437.859	-28.589
900	272.380	553.903	417.800	122.492	56.780	485.367	-28.170
1000	287.078	583.381	432.897	150.484	55.512	533.061	-27.844
1100	299.699	611.350	447.860	179.839	54.988	580.848	-27.582
1200	310.564	637.904	462.600	210.365	55.080	628.653	-27.365
1300	319.937	663.142	477.064	241.902	55.657	676.427	-27.179
1400	328.046	687.156	491.220	274.311	56.623	724.156	-27.019
1500	335.080	710.034	505.051	307.475	57.900	771.785	-26.876
1600	341.203	731.860	518.549	341.296	59.410	819.338	-26.749
1700	346.550	752.709	531.715	375.690	61.095	866.773	-26.633
1800	351.237	772.653	544.550	410.584	62.910	914.120	-26.527
1900	355.360	791.756	557.062	445.919	64.825	961.357	-26.430
2000	359.000	810.078	569.258	481.640	66.797	1008.491	-26.339

Component: 2-CH3-4-C5H8-1
Units: Joules

T	Cp	S	-(F°-H°)/T	H°-H°(298)	dH°	dF°	log Kp
300	120.474	379.048	378.307	0.222	157.990	270.619	-47.119
400	154.745	418.438	383.444	13.997	149.644	309.456	-40.411
500	185.357	456.343	394.260	31.042	142.656	350.247	-36.590
600	211.188	492.488	407.645	50.906	136.943	392.322	-34.155
700	232.964	526.723	422.233	73.143	132.383	435.264	-32.480
800	251.539	559.074	437.335	97.391	128.864	478.779	-31.261
900	267.528	589.647	452.576	123.364	126.269	522.687	-30.336
1000	281.353	618.566	467.742	150.824	124.470	566.833	-29.608
1100	293.330	645.957	482.709	179.572	123.339	611.131	-29.020
1200	303.717	671.935	497.405	209.437	122.768	655.504	-28.533
1300	312.735	696.610	511.787	240.269	122.642	699.904	-28.122
1400	320.577	720.080	525.834	271.944	122.874	744.314	-27.771
1500	327.410	742.435	539.535	304.351	123.393	788.676	-27.464
1600	333.381	763.760	552.888	337.397	124.129	833.015	-27.195
1700	338.611	784.132	565.895	371.002	125.025	877.284	-26.956
1800	343.208	803.619	578.565	405.097	126.041	921.511	-26.742
1900	347.262	822.286	590.904	439.625	127.149	965.674	-26.548
2000	350.849	840.191	602.924	474.534	128.309	1009.776	-26.373

Component: 1-C6H11-3
Units: Joules

T	Cp	S	-(F°-H°)/T	H°-H°(298)	dH°	dF°	log Kp
300	119.880	378.117	377.380	0.221	104.015	216.923	-37.770
400	154.400	417.384	382.500	13.953	95.627	255.860	-33.412
500	184.940	455.211	393.286	30.962	88.603	296.760	-31.002
600	210.630	491.268	406.638	50.778	82.841	338.952	-29.508
700	232.356	525.413	421.190	72.956	78.222	382.021	-28.507
800	251.008	557.688	436.254	97.147	74.646	425.670	-27.793
900	267.176	588.208	451.458	123.075	72.007	469.719	-27.262
1000	281.246	617.103	466.591	150.512	70.184	514.011	-26.849
1100	293.501	644.497	481.530	179.264	69.057	558.455	-26.519
1200	304.176	670.503	496.203	209.160	68.518	602.973	-26.247
1300	313.477	695.226	510.570	240.053	68.452	647.513	-26.017
1400	321.589	718.761	524.607	271.816	68.772	692.058	-25.821
1500	328.673	741.195	538.304	304.337	69.405	736.549	-25.649
1600	334.874	762.610	551.659	337.521	70.279	781.006	-25.497
1700	340.315	783.078	564.674	371.286	71.335	825.387	-25.361
1800	345.104	802.668	577.356	405.562	72.532	869.714	-25.238
1900	349.331	821.443	589.712	440.288	73.838	913.966	-25.127
2000	353.074	839.458	601.752	475.412	75.213	958.147	-25.024

Component: 4-C6H11-3
Units: Joules

T	Cp	S	-(F°-H°)/T	H°-H°(298)	dH°	dF°	log Kp
300	119.313	367.751	367.017	0.220	103.177	219.195	-38.165
400	154.639	406.966	372.125	13.936	94.773	259.173	-33.845
500	186.010	444.936	382.915	31.010	87.814	301.109	-31.457
600	212.466	481.258	396.303	50.973	82.199	344.316	-29.975
700	234.769	515.732	410.924	73.365	77.795	388.370	-28.981
800	253.780	548.355	426.083	97.817	74.479	432.970	-28.270
900	270.122	579.213	441.399	124.033	72.127	477.935	-27.739
1000	284.230	608.421	456.654	151.767	70.602	523.111	-27.325
1100	296.432	636.098	471.720	180.815	69.771	568.408	-26.991
1200	306.997	662.354	486.522	210.999	69.520	613.753	-26.716
1300	316.157	687.298	501.015	242.168	69.729	659.097	-26.483
1400	324.112	711.025	515.175	274.190	70.310	704.425	-26.282
1500	331.037	733.629	528.991	306.956	71.187	749.681	-26.106
1600	337.081	755.190	542.460	340.368	72.290	794.888	-25.950
1700	342.373	775.788	555.584	374.347	73.559	840.003	-25.810
1800	347.020	795.492	568.369	408.821	74.955	885.053	-25.684
1900	351.115	814.366	580.823	443.733	76.446	930.019	-25.568
2000	354.737	832.470	592.956	479.029	77.993	974.902	-25.462

Component: 1-C6H11-4
Units: Joules

T	Cp	S	-(F°-H°)/T	H°-H°(298)	dH°	dF°	log Kp
300	111.618	412.809	412.123	0.206	151.279	253.780	-44.187
400	145.552	449.593	416.909	13.074	142.026	289.375	-37.789
500	176.277	485.456	427.051	29.203	134.123	327.157	-34.178
600	202.448	519.975	439.683	48.175	127.518	366.404	-31.898
700	224.711	552.898	453.524	69.562	122.107	406.666	-30.346
800	243.859	584.185	467.918	93.014	117.792	447.618	-29.226
900	260.455	613.889	482.501	118.249	114.460	489.059	-28.384
1000	274.885	642.095	497.062	145.033	111.983	530.818	-27.727
1100	287.438	668.897	511.476	173.163	110.236	572.794	-27.200
1200	298.361	694.386	525.665	202.466	109.103	614.898	-26.766
1300	307.868	718.652	539.584	232.788	108.466	657.073	-26.402
1400	316.152	741.778	553.207	263.999	108.234	699.296	-26.091
1500	323.381	763.842	566.520	295.983	108.331	741.504	-25.821
1600	329.704	784.919	579.516	328.645	108.682	783.714	-25.586
1700	335.250	805.077	592.196	361.898	109.227	825.879	-25.376
1800	340.128	824.381	604.563	395.672	109.922	868.021	-25.189
1900	344.433	842.888	616.622	429.905	110.734	910.116	-25.021
2000	348.244	860.654	628.383	464.542	111.623	952.164	-24.868

Component: 3-CH2C5H9
Units: Joules

T	Cp	S	-(F°-H°)/T	H°-H°(298)	dH°	dF°	log Kp
300	130.790	387.665	386.860	0.241	155.080	265.124	-46.162
400	164.237	429.940	392.397	15.017	147.735	302.946	-39.561
500	193.401	469.811	403.931	32.940	141.625	342.482	-35.779
600	217.841	507.297	418.068	53.537	136.645	383.139	-33.355
700	238.456	542.467	433.353	76.380	132.690	424.551	-31.680
800	256.103	575.489	449.077	101.129	129.672	466.456	-30.456
900	271.358	606.555	464.866	127.520	127.496	508.697	-29.524
1000	284.601	635.846	480.513	155.333	126.049	551.133	-28.788
1100	296.112	663.524	495.904	184.382	125.220	593.688	-28.192
1200	306.123	689.728	510.974	214.505	124.908	636.293	-27.697
1300	314.833	714.582	525.688	245.562	125.006	678.904	-27.279
1400	322.421	738.198	540.031	277.434	125.435	721.509	-26.920
1500	329.043	760.673	553.997	310.014	126.127	764.053	-26.607
1600	334.835	782.098	567.589	343.214	127.017	806.563	-26.332
1700	339.914	802.553	580.814	376.957	128.051	848.995	-26.086
1800	344.382	822.111	593.680	411.176	129.191	891.376	-25.867
1900	348.325	840.838	606.199	445.815	130.410	933.687	-25.669
2000	351.815	858.795	618.383	480.826	131.672	975.930	-25.489

Component: C7H15-1
Units: Joules

T	Cp	S	-(F°-H°)/T	H°-H°(298)	dH°	dF°	log Kp
300	156.159	450.000	449.040	0.288	14.297	185.893	-32.367
400	202.477	501.352	455.726	18.251	3.303	244.807	-31.968
500	242.705	550.987	469.848	40.569	-5.582	306.255	-31.994
600	276.049	598.277	487.347	66.558	-12.607	369.311	-32.151
700	303.946	642.984	506.418	95.596	-18.015	433.417	-32.342
800	327.706	685.161	526.150	127.209	-21.997	498.187	-32.528
900	348.182	724.969	546.050	161.027	-24.728	563.390	-32.698
1000	365.919	762.593	565.840	196.753	-26.394	628.832	-32.847
1100	381.314	798.207	585.360	234.132	-27.165	694.400	-32.974
1200	394.685	831.972	604.516	272.947	-27.192	760.003	-33.082
1300	406.308	864.033	623.256	313.010	-26.630	825.580	-33.172
1400	416.424	894.522	641.553	354.158	-25.592	891.113	-33.248
1500	425.245	923.560	659.393	396.251	-24.177	956.532	-33.309
1600	432.955	951.256	676.775	439.169	-22.476	1021.871	-33.361
1700	439.713	977.711	693.705	482.810	-20.564	1087.073	-33.402
1800	445.655	1003.016	710.191	527.084	-18.494	1152.177	-33.435
1900	450.895	1027.254	726.245	571.917	-16.304	1217.154	-33.462
2000	455.532	1050.502	741.881	617.243	-14.046	1282.014	-33.483

Component: C7H15-2
Units: Joules

T	Cp	S	-(F°-H°)/T	H°-H°(298)	dH°	dF°	log Kp
0	0.000	0.000	inf	-26.797	48.874	48.874	inf
300	148.303	453.697	452.786	0.274	4.576	175.062	-30.481
400	195.438	502.897	459.173	17.490	-7.164	233.721	-30.521
500	236.616	551.063	472.759	39.152	-16.707	295.093	-30.828
600	270.893	597.326	489.695	64.579	-24.293	358.195	-31.184
700	299.612	641.302	508.239	93.144	-30.174	422.435	-31.522
800	324.059	682.946	527.498	124.358	-34.554	487.401	-31.824
900	345.096	722.359	546.980	157.841	-37.621	552.847	-32.086
1000	363.290	759.682	566.400	193.282	-39.572	618.565	-32.311
1100	379.056	795.064	585.594	230.417	-40.587	684.437	-32.501
1200	392.730	828.646	604.460	269.022	-40.824	750.363	-32.662
1300	404.602	860.560	622.943	308.902	-40.444	816.281	-32.799
1400	414.924	890.931	641.009	349.890	-39.566	882.167	-32.914
1500	423.918	919.871	658.643	391.842	-38.292	947.950	-33.011
1600	431.774	947.486	675.839	434.635	-36.716	1013.662	-33.093
1700	438.656	973.873	692.600	478.164	-34.917	1079.244	-33.161
1800	444.703	999.121	708.933	522.338	-32.947	1144.735	-33.219
1900	450.034	1023.310	724.847	567.080	-30.847	1210.105	-33.268
2000	454.750	1046.516	740.354	612.324	-28.672	1275.361	-33.309

Component: C7H15-3
Units: Joules

T	Cp	S	-(F°-H°)/T	H°-H°(298)	dH°	dF°	log Kp
300	153.633	448.511	447.567	0.283	4.585	176.628	-30.754
400	200.923	499.292	454.170	18.049	-6.605	235.722	-30.782
500	241.665	548.644	468.161	40.241	-15.617	297.392	-31.068
600	275.309	595.776	485.537	66.143	-22.729	360.690	-31.401
700	303.393	640.385	504.502	95.118	-28.200	425.051	-31.718
800	327.278	682.498	524.145	126.682	-32.230	490.084	-31.999
900	347.841	722.262	543.970	160.463	-34.999	555.556	-32.244
1000	365.641	759.854	563.696	196.159	-36.695	621.270	-32.452
1100	381.083	795.445	583.161	233.513	-37.491	687.113	-32.628
1200	394.490	829.192	602.269	272.307	-37.539	752.992	-32.777
1300	406.141	861.239	620.968	312.352	-36.994	818.848	-32.902
1400	416.280	891.717	639.228	353.485	-35.971	884.661	-33.007
1500	425.119	920.746	657.036	395.565	-34.569	950.361	-33.095
1600	432.844	948.434	674.390	438.472	-32.880	1015.981	-33.168
1700	439.615	974.883	691.294	482.102	-30.979	1081.466	-33.229
1800	445.567	1000.183	707.756	526.367	-28.917	1146.852	-33.281
1900	450.816	1024.417	723.790	571.192	-26.736	1212.113	-33.323
2000	455.461	1047.661	739.406	616.511	-24.485	1277.257	-33.359

Component: C7H15-4
Units: Joules

T	Cp	S	-(F°-H°)/T	H°-H°(298)	dH°	dF°	log Kp
300	153.633	448.508	447.564	0.283	4.585	176.629	-30.754
400	200.923	499.289	454.167	18.049	-6.605	235.723	-30.782
500	241.665	548.641	468.159	40.241	-15.617	297.393	-31.068
600	275.309	595.773	485.534	66.143	-22.729	360.691	-31.401
700	303.393	640.382	504.499	95.118	-28.200	425.053	-31.718
800	327.278	682.495	524.142	126.682	-32.230	490.087	-31.999
900	347.841	722.259	543.967	160.463	-34.999	555.558	-32.244
1000	365.641	759.851	563.693	196.159	-36.695	621.273	-32.452
1100	381.083	795.442	583.158	233.513	-37.491	687.116	-32.628
1200	394.490	829.189	602.267	272.307	-37.539	752.996	-32.777
1300	406.141	861.236	620.965	312.352	-36.994	818.852	-32.902
1400	416.280	891.714	639.225	353.485	-35.971	884.665	-33.007
1500	425.119	920.743	657.033	395.565	-34.569	950.365	-33.095
1600	432.844	948.432	674.387	438.472	-32.880	1015.986	-33.169
1700	439.615	974.880	691.291	482.102	-30.979	1081.471	-33.230
1800	445.567	1000.180	707.754	526.367	-28.917	1146.857	-33.281
1900	450.816	1024.414	723.787	571.192	-26.736	1212.119	-33.323
2000	455.461	1047.658	739.403	616.511	-24.485	1277.262	-33.359

Component: 1-C5H11
Units: Joules

T	Cp	S	-(F°-H°)/T	H°-H°(298)	dH°	dF°	log Kp
300	113.921	366.782	366.081	0.210	55.570	170.140	-29.624
400	145.081	403.832	370.919	13.165	47.427	209.595	-27.370
500	173.200	439.300	381.073	29.114	40.668	250.950	-26.217
600	196.982	473.038	393.613	47.655	35.211	293.540	-25.555
700	217.107	504.953	407.260	68.385	30.916	336.953	-25.144
800	234.361	535.095	421.372	90.978	27.663	380.901	-24.870
900	249.287	563.580	435.605	115.177	25.330	425.208	-24.678
1000	262.247	590.530	449.762	140.768	23.784	469.727	-24.536
1100	273.511	616.064	463.729	167.568	22.900	514.371	-24.425
1200	283.303	640.292	477.442	195.420	22.567	559.068	-24.336
1300	291.820	663.311	490.861	224.185	22.672	603.773	-24.260
1400	299.237	685.214	503.967	253.746	23.131	648.469	-24.195
1500	305.705	706.085	516.752	283.999	23.870	693.103	-24.136
1600	311.361	725.998	529.212	314.858	24.824	737.697	-24.083
1700	316.319	745.026	541.351	346.247	25.936	782.210	-24.034
1800	320.678	763.232	553.176	378.101	27.168	826.667	-23.989
1900	324.523	780.675	564.693	410.365	28.490	871.048	-23.947
2000	327.926	797.409	575.913	442.990	29.866	915.357	-23.907

Component: 2-C5H11
Units: Joules

T	Cp	S	-(F°-H°)/T	H°-H°(298)	dH°	dF°	log Kp
300	108.348	376.383	375.717	0.200	45.852	157.543	-27.431
400	139.520	411.822	380.336	12.594	37.149	196.121	-25.611
500	168.122	446.100	390.081	28.009	29.857	236.739	-24.732
600	192.554	478.971	402.177	46.076	23.924	278.694	-24.262
700	213.319	510.253	415.401	66.396	19.221	321.548	-23.994
800	231.138	539.929	429.128	88.640	15.619	364.990	-23.831
900	246.539	568.063	443.016	112.542	12.988	408.831	-23.728
1000	259.893	594.745	456.866	137.879	11.188	452.916	-23.658
1100	271.481	620.072	470.562	164.461	10.086	497.148	-23.608
1200	281.540	644.135	484.032	192.124	9.564	541.453	-23.569
1300	290.279	667.023	497.235	220.724	9.504	585.780	-23.537
1400	297.879	688.819	510.147	250.141	9.819	630.110	-23.510
1500	304.502	709.601	522.757	280.267	10.431	674.388	-23.484
1600	310.289	729.442	535.059	311.013	11.271	718.634	-23.461
1700	315.357	748.408	547.055	342.300	12.282	762.806	-23.438
1800	319.812	766.562	558.749	374.063	13.423	806.927	-23.416
1900	323.739	783.961	570.148	406.244	14.663	850.977	-23.395
2000	327.213	800.656	581.259	438.795	15.964	894.960	-23.374

Component: nC4H9
Units: Joules

T	Cp	S	-(F°-H°)/T	H°-H°(298)	dH°	dF°	log Kp
300	93.037	329.512	328.940	0.172	78.528	163.284	-28.430
400	118.135	359.741	332.891	10.740	71.928	192.561	-25.146
500	140.457	388.565	341.167	23.699	66.430	223.379	-23.336
600	159.231	415.881	351.364	38.711	61.948	255.206	-22.218
700	175.103	441.650	362.439	55.448	58.373	287.713	-21.469
800	188.739	465.943	373.873	73.656	55.608	320.669	-20.938
900	200.579	488.872	385.389	93.135	53.564	353.934	-20.542
1000	210.902	510.551	396.831	113.720	52.140	387.388	-20.235
1100	219.912	531.084	408.111	135.271	51.239	420.961	-19.990
1200	227.774	550.564	419.177	157.664	50.777	454.596	-19.788
1300	234.635	569.072	430.001	180.792	50.664	488.252	-19.618
1400	240.628	586.684	440.569	204.561	50.836	521.917	-19.473
1500	245.868	603.468	450.874	228.892	51.234	555.545	-19.346
1600	250.460	619.486	460.915	253.713	51.806	589.155	-19.234
1700	254.493	634.794	470.697	278.965	52.506	622.712	-19.134
1800	258.045	649.442	480.223	304.595	53.306	656.235	-19.043
1900	261.183	663.480	489.501	330.560	54.180	689.708	-18.961
2000	263.963	676.949	498.539	356.819	55.099	723.132	-18.886

Component: nC3H7
Units: Joules

T	Cp	S	-(F°-H°)/T	H°-H°(298)	dH°	dF°	log Kp
300	72.028	290.383	289.940	0.133	100.315	155.815	-27.130
400	90.177	313.602	292.982	8.248	95.191	175.108	-22.867
500	106.517	335.523	299.318	18.103	90.837	195.608	-20.435
600	120.415	356.205	307.092	29.468	87.216	216.914	-18.884
700	132.281	375.680	315.513	42.117	84.263	238.775	-17.818
800	142.558	394.029	324.192	55.870	81.918	261.011	-17.042
900	151.536	411.350	332.922	70.585	80.119	283.513	-16.455
1000	159.403	427.731	341.592	86.140	78.791	306.186	-15.994
1100	166.293	443.254	350.134	102.432	77.864	328.974	-15.622
1200	172.324	457.988	358.513	119.369	77.276	351.831	-15.315
1300	177.599	471.993	366.708	136.871	76.957	374.724	-15.057
1400	182.214	485.327	374.708	154.866	76.858	397.640	-14.836
1500	186.255	498.039	382.510	173.294	76.936	420.546	-14.645
1600	189.801	510.176	390.113	192.101	77.149	443.452	-14.477
1700	192.918	521.778	397.519	211.240	77.463	466.332	-14.329
1800	195.666	532.884	404.733	230.672	77.855	489.199	-14.196
1900	198.095	543.529	411.760	250.362	78.306	512.039	-14.077
2000	200.249	553.746	418.605	270.281	78.794	534.854	-13.969

D: Kinetic Modeling of Heptane Combustion and PAH Formation

A kinetic model for high temperature oxidation and pyrolysis of heptane has been developed. The model is based on new results for heptane decomposition, decomposition and isomerization of heptyl radicals, and decomposition of olefins and olefinic radicals. It is combined with kinetic data from Grimech-3.0 model on the reactions of C_1-C_2 species. The subset on C_3-C_4 chemistry is based on the works of Marinov et al (1998) and Laskin et al (2000). The database for PAH formation is based on results from kinetic models on heptane suitably modified from various soot formation models. The model was validated against experimental data on burning velocity, ignition delays, and OH time history during heptane ignition behind shock wave. The reactions determining burning velocity were established through sensitivity analysis. The main reactions determining burning velocity of heptane are similar to the reactions determining burning velocity of C_1-C_4 hydrocarbons. Influence of product distribution of heptyl radical decomposition on PAH production was analyzed.

I. Introduction.

The aim of this work was to develop a complete kinetic model of heptane combustion including new data on the cracking of heptane. This involves the kinetics of heptane decomposition, heptyl radical decomposition and isomerisation, and decomposition of olefins and olefinic radicals. The intention is to combine it with C_1-C_2 species reactions [1] from Grimech-3.0 mechanism and the reaction subset of C_3-C_4 chemistry based on the works of Marinov et al [2] and Laskin et al [3]. With the use of this model we will analyze reaction pathways for PAH formation during heptane combustion. The PAH reaction subset was assembled from the data bases of Marinov et al [2], Appel et al [4], Richter et al [5,6] and recent kinetic data on PAH formation from several sources [7-9]. The purpose of PAH formation modeling was to investigate in more detail the dependence of PAH formation on the product distribution from heptyl radical decomposition and the dependence of PAH production on equivalence ratio. The transition through the critical sooting equivalence ratio is of particular interest, since this is where changes in the reaction mechanism may be expected.

We will present two versions of the suggested kinetic model. First is the detailed kinetic model for high temperature heptane oxidation, mentioned above. Analysis of the decomposition kinetics of heptyl radicals and results of high temperature modeling of heptane oxidation demonstrates that reactions involving formation and consumption of heptyl radicals can be represented by overall processes due to the large reaction rates of their decomposition in comparison with other reaction processes. It was shown that temperature dependencies of branching ratios for decomposition of heptyl radicals can be represented by typical Arrhenius temperature dependence [10]. This leads to some simplification of the kinetic model and elimination of several species from the model through overall representation of heptane consumption reactions leading directly to C_1-C_6 products. Combination of these overall heptane consumption reactions with detailed kinetic model for C_1-C_6 species represents the second version of kinetic model.

We will begin with short review of kinetic models for heptane combustion and available data on the burning velocity. Next we will describe in detail the construction of a kinetic database for heptane combustion. Comparison of modeling results with experimental data on

burning velocity will be the specific target of this part. In the second part of paper, the results of kinetic modeling of PAH production during heptane combustion will be presented.

II. Background

Development of comprehensive kinetic models for the combustion of hydrocarbon fuels is of interest for detailed modeling of processes in engines, for studies of the emission of toxic combustion byproducts, soot formation and effects of different additives on the combustion process. Modeling of heptane combustion is of particular interest. Heptane is a reference fuel for the determination of a fuel's tendency to knock. It is a liquid fuel and can undergo many of the same type of reactions as larger alkanes. Heptane represents a model fuel for the alkane component of practical fuels. As was the case with smaller hydrocarbons there is a plethora of models with their individual databases.

A. Kinetic models of heptane combustion.

Earlier kinetics data bases for the modeling of heptane combustion are summarized in Table 1. (Note: Tables & Figures are at the end of this section) The first kinetic model of heptane combustion was developed by Coats and Williams [11]. Comprehensive kinetic models for heptane combustion were developed by Warnatz [12] and Westbrook et al [13]. These models served as a basis for further development and improvement of kinetic mechanisms of heptane oxidation [14-18].

More recent kinetics databases for heptane combustion of interest for the present work are discussed below. Curran et al [14] developed a comprehensive kinetic model which included reactions important to high and low temperature heptane oxidation. The model is based on previous kinetic models developed by Westbrook et al. [13]. Older data were brought up to date and new classes of reactions were added. Specific attention was paid to the low-temperature heptane oxidation. This is important for the modeling of NTC (negative temperature coefficient) phenomenon and cool flame oxidation. Under 900K, the primary reaction of alkyl radicals is the addition of oxygen due to the high activation energy of beta-scission of alkyl radicals. It was found that reactions of ketohydroperoxides are important for the modeling two-stage low temperature ignition. Recently, Westbrook et al [17,19] extended this model to combustion of different heptane isomers.

Seiser et al [18] simplified the model of Curran et al [14] for simulations of heptane ignition and combustion in counter-flow, non-premixed systems. Some modifications of rate constants (alkyl radical addition to oxygen and reactions of RO_2 radical) and thermodynamic parameters (peroxy radicals) were made. The model was validated against experimental data on ignition delays in the low temperature range and experimental data on heptane ignition in a counter-flow non-premixed system from author experiments.

Lindstedt and Maurice [15] assembled a n-heptane mechanism based on the works of Chakir et al [20-22], Dagaut et al [23-25], Foelsche et al [26], Tsang [27,28] and Westbrook et al [13,29]. The assembled model was optimized by comparisons with experimental data from diffusion flames, combustion in stirred reactors and premixed flames. The authors simulated the dependence of burning velocity on equivalence ratio. It was indicated that the modeling results agree with the experimental values determined by Gibbs and Calcote [30], but for rich flames,

the computed values of the burning velocity were too high in comparison with the experimental data.

Bakali et al [16] developed a heptane kinetic database for the analysis of heptane flame structure. The mechanism was based on a previously developed kinetic model for the combustion of rich acetylene-oxygen-argon flame. Simulated burning velocities of n-heptane-air mixtures at 298K were compared with experimental data of Gibbs and Calcote [30]. The authors indicated that the maximum burning velocity was in reasonable agreement. However, over-prediction for rich mixtures in comparison with experimental data was also observed.

B. Experimental data.

Experimental data on heptane combustion cover measurements of ignition delays, experiments in jet stirred, static and plug flow reactors, and measurements of concentration and temperature profiles for laminar premixed and opposed flow diffusion flames, burning velocity determinations, measurements in rapid compression machines and measurements in shock tubes. Data cover overall process characteristics (burning velocity, ignition delay, overall reaction rate, effective activation energy, extinction strain rate) and detailed characteristics of heptane oxidation (flame structure, concentrations for stirred and plug flow reactors). Table 1 contains a summary of the separate models and the various experimental data used for validation of these models.

There is a general tendency to cover only a limited set of experimental results. The earlier studies can be grouped in terms of two different types of applications. The first involves the simulation of high temperature behavior and is applicable to premixed and diffusion flames. A second group of studies cover the simulation of lower temperature behavior (cool flames, two-stage ignition, negative temperature coefficient) and the related phenomenon – engine knock. Division of models on high and low temperature models is limited. It is related to alkylperoxy radical kinetics, which is important for low and intermediate temperatures. Including of alkylperoxy radical reactions leads to substantial increase of kinetic models in the number of considered species and reactions. In general these reactions are not important for flame processes and high temperature ignition behind shock waves (temperatures more than 1200-1300K). Note that models developed for simulation of low temperature range phenomena contain reactions important for modeling of high temperature kinetics, e.g. recent kinetic model [14] with detailed description of alkylperoxy radical kinetics was validated against high temperature heptane ignition delays behind shock waves.

The first group of models (high temperature range) was validated against data on burning velocity, measurements for opposite diffusion flames, flame structure data, results obtained for jet stirred reactors and measurements in shock tubes. The basis for validation of the second group of models are measurements of auto-ignition delays, measurements in jet stirred reactors, rapid compression machines (ignition delay) and data obtained for plug and static reactors.

C. Burning velocity data.

Figure 1 contains available data on experimental measurements of equivalence ratio dependence of burning velocity. The early measurements of heptane burning velocity are those

of Gerstein et al [31], Heimel and Weast [32], and Gibbs and Calcote [30]. Recent measurements have been performed by Davis and Law [33] using the counter-flow twin flame procedure. In addition, Figure 1 contains experimental data of Takahashi et al [34]. Babkin et al [35] and Ryan and Leste [36] measured pressure and temperature dependencies of heptane burning velocity using a constant volume bomb procedure. Also included are the results on the calculated flame velocities [12,15,16,37]. It can be seen that there is rather large disagreement with the more recent and presumably more accurate determinations of Davis and Law [33]. The difference between measurements and results of modeling is as much as 10cm/s. This is particularly the case with rich mixtures. Clearly, there is a problem. Note that although the overall discrepancy may not appear to be large in an absolute sense, the difference is a suggestion that there is a problem with the kinetic model and (or perhaps) the experimental measurements. To some degree this disagreement reflects the continuous refinement of experimental measurements of heptane burning velocity and continuous refinement of kinetic data also. Thus the set of rate constants in older models was adjusted within the limits of their uncertainties to provide agreement with available experimental data that time.

D. Hierarchical structure of kinetic models of hydrocarbon combustion.

Due to the hierarchical structure of kinetic models of hydrocarbon combustion, kinetic models for oxidation of larger hydrocabons include models of oxidation of smaller hydrocarbons as sub-models. It is natural to assume that kinetics of C_1-C_2 hydrocarbons is well presented by the Grimech 3.0 mechanism, since this database was tested against numerous experimental results [1]. As a first step of model development, we consider the Grimech-3.0 mechanism as the main C_1-C_2 reaction subset of the heptane combustion kinetic model.

There exist alternative kinetic databases for C_1-C_2 hydrocarbon combustion, e.g. model [38]. This was developed by Hughes et al [38], and validated through comparisons with various experimental data on hydrogen, carbon monoxide, methane and ethane combustion. The principal difference between the databases [1,38] is that the set of rate constants from the Grimech 3.0 model is based on an optimization procedure that compared simulation and experimental data for different reaction systems while the Leeds version model is largely based on a set of recommended kinetic data [39].

In this work we will consider the sensitivity of global property - the flame velocity, to the reactions in the kinetic model. Of particular interest will be the modeling of freely propagating heptane flame and the dependence of burning velocity on the equivalence ratio,for which disagreement of modeling results with recent experimental measurements is observed. We will conclude with an analysis of PAH formation in heptane flames. Specific targets will be the influence of product distribution of heptyl radical decomposition on PAH production. We will analyze the reaction pathways leading to the formation of aromatic compounds.

III. Kinetic model of high temperature heptane combustion.

The first step in this project was to develop reaction pathways for the high temperature degradation of heptane to C_1-C_4 species. This will then serve as inputs to the Grimech-3.0 kinetic model and well tested kinetic models representing combustion of C_3-C_4 hydrocarbons. The construction of heptane kinetic models includes the following steps:

- determination of decomposition rates of heptane;
- consideration of heptyl radical formation through hydrogen atom abstraction by radicals;
- determination of decomposition and isomerization reaction rates of heptyl radicals;
- determination of rates of hydrogen atom abstraction from olefins, formed during heptyl radical decomposition;
- analysis of decomposition of olefins and olefinic radicals (C_6, C_5 and C_4);
- assembling of submodel for C3-C4 species based on the models of Marinov et al [2], Laskin et al [3], Curran et al [14] and Richter et al [5].
- including of Grimech 3.0 as submodel presenting C_1-C_2 species reactions.

Kinetic models used in this work are presented in Table 2. Heptane kinetic models analyzed here are the kinetic model of Curran et al [14], Seiser et al model [18], Lindstedt et al model [15], and model of Bakali et al [16]. Details of the model development are presented below.

A.. Decomposition rates of n-heptane.

Bakali et al [16] indicated that decomposition reactions of n-heptane affect the production of benzene, allene and propyne. They found that exclusion of decomposition channels involving C_2H_5 and 1-C_5H_{11} products leads to changes in the maximum concentrations of benzene and allene in flame zone by 20%. Similar conclusions concerning the effects of the decomposition reactions of heptane were made by Lindstedt and Maurice [15]. It was necessary to include both pyrolysis and radical attack reactions in order to accurately predict intermediate species profiles. Furthermore, the distribution of intermediate species is highly sensitive to the rates of pyrolysis steps. Our calculations of rich heptane combustion indicate that with increase of equivalence ratio contribution of heptane decomposition reactions to overall heptane consumption increases. Figure 2 contains dependencies of contributions of decomposition and radical abstraction reactions to heptane consumption on equivalence ratio. It can be seen that at equivalence ratio of 3 heptane consumption in decomposition reactions constitutes approximately 35% of overall consumption rate.

Table 3 contains results of calculations for C-C bond split in heptane. There are three types of C-C bonds in heptane. They are

$$C_7H_{16} = CH_3 + 1\text{-}C_6H_{13}$$
$$C_7H_{16} = C_2H_5 + 1\text{-}C_5H_{11}$$
$$C_7H_{16} = C_3H_7 + 1\text{-}C_4H_9$$

For calculations “Chemrate” program, that has been recently developed to determine energy transfer effects in unimolecular decompositions [41], was used. The calculations demonstrate that the three reactions all have pressure dependence even at 10 bar pressure. These results are based on single pulse shock tube studies on the decomposition of related hydrocarbons at 1100 K and analogous data for combination of alkyl radicals at room temperatures.

B. Hydrogen atom abstraction.

Analysis of reaction pathways for heptane consumption shows that the main mechanism for heptane consumption in the flame zone involves the formation of heptyl radicals through

hydrogen atom abstraction reactions with H and OH radicals for lean and near-stoichiometric mixtures. Increase of equivalence ratio leads to increasing contributions from heptane decomposition reactions. Recently, Westbrook et al [17] summarized data for H-atom abstraction from primary, secondary and tertiary sites in hydrocarbons by different radicals. Rates of hydrogen atom abstraction from heptane by radicals were assumed in accord with the data of this work.

C.. Heptyl radical isomerization and decomposition.

Decomposition of heptyl radicals in flame leads to a variety of products. The general mechanism is outlined in Figure 3. 1-C_7H_{15} radical decomposes with formation of C_2H_4 and 1-C_5H_{11}, mostly. 2-C_7H_{15} radical forms 1-C_4H_9 and C_3H_6 species. 3-C_7H_{15} radical has two decomposition channels: 1-C_4H_8+nC_3H_7 and 1-C_6H_{12}+CH_3. The main products of 4-C_7H_{15} radical decomposition are C_2H_5 and 1-C_5H_{10} species. The essential differences in the kinetic models [14-16] are the different reaction rates assigned to heptane reactions with radicals and decomposition reactions of heptyl radicals. Roughly, the different rates of heptane with radicals used in kinetic models lead to formation of different distributions of heptyl radicals in the flame zone. Different description of isomerization and decomposition reactions of heptyl radicals increases the differences in the concentrations of heptyl radicals and the products of its decomposition during heptane consumption. The rate constants assigned for these processes will dictate the branching ratio for the formation of the olefins that can be formed. The nature of the distribution of products can obviously have very strong effect on the subsequent decomposition process and may have impact on the initiation of soot formation.

We have recently obtained the following high pressure rate expressions for the relevant processes (Table 4). These data represent the first complete set of experimentally based rate expressions for these processes. They are important because they lead to a specific distribution of the smaller compounds that are the inputs to the other modules in the database. Furthermore the heptyl radical decomposition processes are competitive with their oxidation reactions (heptyl+O_2). The consequence is that at the lowest temperatures the oxidation process will predominate and the decomposition processes will not be important. At the highest temperatures decomposition will become the sole reaction and the distribution of products will be of key importance. This leads to possibility of lumping of decomposition and isomerization reactions of heptyl radicals and presentation of these reactions as the lumped hydrogen atom abstraction reactions for heptane with corresponding branching ratios. At the intermediate temperatures the differences between rate constants for oxidation and decomposition can play a key role in the subsequent behavior of the system. We estimate that this intermediate region range from 800 to 1000 K for a stoichiometric mixture. This is not an important temperature range for the present application. Thus the branching ratios are sufficient for most applications. Table 5 summarizes the calculated branching ratios.

D. Olefin kinetics.

The products of heptane and heptyl radical decomposition include olefins (1-C_6H_{12}, 1-C_5H_{10} and 1-C_4H_8) and olefinic radicals. Previous kinetic models of heptane combustion treated the formation of olefinic radicals from olefins in terms of lumped species (C_4H_7, C_5H_9, C_6H_{11}). We include reactions of hydrogen atom abstraction from olefins leading to the formation of the following radicals (1-C_4H_7-3, 1-C_4H_7-4, 1-C_5H_9-3, 1-C_5H_9-4, 1-C_5H_9-5, 1-C_6H_{11}-3, 1-C_6H_{11}-4,

1-C_6H_{11}-5, 1-C_6H_{11}-6). Rate constants for these processes are based on recent results of Simathi et al [45]. For H-atom abstraction from olefins by radicals different from hydrogen atom, the overall rate constants suggested by Curran et al [14] with branching coefficients for abstraction by hydrogen atom [45] are used as a first approximation. Kinetic data for decomposition of olefins and olefinic radicals were in accord with the results of Tsang [10]. The incorporation of this block of reactions into the model provides more accurate kinetic description of decomposition/oxidation pathways of olefins, which are important for PAH and soot formation modeling.

E. C1-C4 reaction block.

The sub-model of C_3-C_4 species reactions was mainly assembled from the models of Laskin et al [3], Marinov et al [2], Curran et al [14] and Richter et al [5]. The model includes the optimized C_1-C_3 kinetics database that was calibrated to fit the burning velocity dependencies of C_1-C_3 hydrocarbons on the equivalence ratio and temperature dependence of ignition delay [40]. This represents an extended version of the Grimech 3.0 mechanism [1] and constitutes the basic set of reactions of C_1-C_3 species in the heptane kinetic model. More detailed discussion concerning the modification of rates for some reactions of Grimech-3.0 model is given below in the section on laminar premixed flame modeling.

F. Kinetics of PAH growing process.

For modeling of PAH growing process, the kinetic sub-model was assembled using the kinetic databases of Marinov et al [2], Appel et al [4], and Richter et al [5,6]. Additional reactions and updates of rate constants were included from several recent sources [7-9]. The model was extended by analogy to include reactions of PAH formation up to ovalene. Additionally, calculations were conducted with the use of PAH formation database of Marinov et al [2] and Appel et al [4] as published for comparison purposes.

The overall kinetic database includes 1745 reactions with 347 species. Thermochemical data were from standard sources [14,15,1,2,4-6,8]. Where data were unavailable, they were estimated with the use of NIST Structures and Properties program [46] and through the use of the group additivity procedure [47,48]. The Chemkin-2 package was used for the simulation work [49].

IV. Comparison with experimental data.

Different parts of the database have been tested in the original investigations. For example, the optimized C3 mechanism [40], which is based on Grimech model [1], was tested against numerous experimental data for C_1-C_3 hydrocarbon systems. Marinov et al [2] tested their model of PAH formation against experimental data on flame structure for propane and butane flames. Comparison of modeling results on heptane combustion with experimental data was conducted for the following set of experimental data: dependence of burning velocity of heptane/air on equivalence ratio (next section), temperature dependence ignition delay of heptane/oxygen mixtures behind shock wave and OH time history during ignition of heptane/oxygene mixtures behind shock wave.

Vermeer et al [50] studied high temperature ignition of heptane/oxygen mixtures behind reflected shock waves for pressure range 1-4 atm and temperatures 1200-1700K. Results are summarized in Figure 4 and are in good agreement with the calculated temperature dependence of the ignition delay. The calculated ignition delay was taken as the time to achieve maximum concentration of the CH radical. The simulations show that heptane is decomposed before ignition. Thus ignition occurs in the presence of significant amount of the decomposition products (C_2H_4, C_3H_6, 1-C_4H_8, 1-C_6H_{12}, 1-C_5H_{10} and associated radicals). The ignition process can be characterized in terms of two-stage process, where the heptane decomposition is the first stage, and the second stage corresponds to ignition of decomposition products of heptane.

Horning et al [51] have studied ignition of n-heptane behind reflected shock waves over the temperature range of 1300-1700K and for 1-6 bar pressure range. Figure 5 contains comparisons of modeling results of temperature dependencies of ignition delays for lean, stoichiometric and rich heptane/oxygen mixtures at 1 bar. The ignition time was defined as before [51]. It can be seen that calculated ignition delays are about 20-30% shorter than experimentally determined ones for all three mixture compositions depending on the initial temperature.

Davidson et al [52] measured OH radical concentration evolution behind reflected shock waves in the oxidation of n-heptane. Initial conditions of these measurements were 1360-1780K and 2.02-3.8atm. Experiments were performed for equivalence ratios 0.8-1.2 and concentration of fuel in mixture 200-300 ppm. Figure 6 contains experimental and modeling results for three different temperatures and stoichiometric mixtures. There is reasonable agreement for OH evolutions measured at different temperatures.

V. Burning velocity of heptane combustion.

Figure 7 illustrates the dependence of the laminar burning velocity on equivalence ratio and demonstrates that detailed kinetic models [15,16] over-predict burning velocity in comparison with experimental data of Davis and Law [33]. Calculations were also conducted using a combination of Grimech 3.0 with the reduced Seiser et al model [18]. Reduction of Seiser et al model involved the exclusion of reactions with hydrocarbon peroxides and hydroperoxy-radicals. These reactions are important for low temperature range and conditions typical for NTC conditions. As before this combined model substantially over-predicts burning velocity in comparison with the data [33].

We have also made calculations using a combination of the Grimech-3.0 database [1] on C_1-C_2 species kinetics, with those of Lindstedt and Maurice [15] and Bakali et al [16] for the larger species. This is similar in spirit with the combined model of Seiser et al [18]. The calculated burning velocities (the range of equivalence ratio was 0.8-1.2) deviated from each other by less than 3-5%. This demonstrates that the main reactions contributing to the burning velocity correspond to reactions in the C_1-C_2 system, with the inclusion of some reactions of the C_3 species. As was the case with the combined Seiser et al data base [18], the burning velocity was over-predicted when compared with the latest experiments.

A. Sensitivity analysis.

Figures 8-10 contain results on the sensitivity of the flame velocity to the reactions in the combined reduced model of Seiser et al [8] with Grimech 3.0 [27], Bakali et al model [6] and Lindstedt and Maurice model [5]. In general, the models demonstrate that reactions controlling the heat release kinetics in heptane flames are similar to reactions of C_1-C_4 hydrocarbon flames [39]. Nevertheless, they have different patterns of sensitivity coefficients. For example the results of Lindstedt and Maurice [5] show that the flame velocity is more sensitive to the rate constant of HCO radical decomposition than those of the reactions $HCO+H=H_2+CO$ and $CH_3+CH_3=C_2H_5+H$. Calculations from the database in the work of Bakali et al [6] demonstrate that the flame velocity is equally dependent on the rate constants for the three reactions.

Sensitivity calculations reveal that the main reactions determining burning velocity are the reactions $H+O_2=H+OH$, $CO+OH=CO_2+O$, $H+O_2+M=HO_2+M$, $HCO+M=H+CO+M$, $H+HCO=CO+H_2$, $CH_3+CH_3=C_2H_5+H$, $C_2H_5=C_2H_4+H$ and $H+aC_3H_5=C_3H_6$. In all cases, the influence of reactions involving the C_5-C_7 species on burning velocity is small or less than 2-4% of the sensitivity level for the chain branching reaction $H+O_2=OH+O$. Within these small limits, the following reactions involving heptane make the most contributions: $C_7H_{16}+OH=2-C_7H_{15}+H_2O$, $C_7H_{16}+H=C_7H_{15}+H_2$, $C_7H_{16}+OH=3-C_7H_{15}+H_2O$ and heptyl radical decomposition $1-C_7H_{15}=aC_5H_{11}+C_2H_4$, $2-C_7H_{15}=aC_4H_9+C_3H_6$, $1-C_7H_{15}=2-C_7H_{15}$. OH attack is particularly important for lean and stoichiometric flames. It is of interest that the model of Seiser et al [18] show that the most important reactions of C7 species with respect to the flame velocity corresponds to the reactions of heptane with H and OH radicals. On the other hand the models of Lindstedt and Maurice [15] and Bakali et al [16] demonstrate some sensitivity to the rate constant for the decomposition of heptyl radical $1-C_7H_{15}=1-C_5H_{11}+C_2H_4$ and $2-C_7H_{15}=C_3H_6+p-C_4H_9$.

Table 6 contains calculated sensitivity coefficients of the main reactions for lean, stoichiometric and rich mixtures. In all cases the flame velocity was most sensitive to the reactions of C1-C2 hydrocarbon species. With increasing equivalence ratio, the sensitivity of burning velocity to the rate constant of $CH_3+H+M=CH_4+M$ reaction increases substantially. Burning velocity of lean mixture compositions is more sensitive to the reactions $H+O_2+M=HO_2+M$ and $CO+OH=CO_2+H$. Increase of equivalence ratio decreases sensitivity to these reactions. The sensitivity to rate constants of C3-C4 species reactions remains approximately at the same level with the change of equivalence ratio. It is of interest that most of reactions with positive sensitivities correspond to reactions, which produce hydrogen atom. Negative sensitivity coefficients correspond to reactions consuming hydrogen atom mainly. Thus reactions determining burning velocity are the reactions related to hydrogen atom, which concentration is important for contribution of chain branching reaction H+O2=OH+O.

B. Modification of Grimech-3.0 model.

The simulation results show that modification of the kinetic model for the reactions involving C1-C3 species is required if agreement is to be achieved between simulation and experimental results on the relation between burning velocity and equivalence ratio. Sensitivity analysis does not reveal reactions with the relatively large sensitivity coefficients from C5-C7 reaction sub-system. The main reactions influencing burning velocity are the reactions of C1-C3 hydrocarbon species and they are general part of the Grimech-3.0 model. Unfortunately this

means that some aspects of the well tested Grimech-3.0 [1] database dealing with the C1-C2 reaction subset must be adjusted.

Recently Qin et al [40] developed a kinetic database for propane combustion using Grimech 3.0 mechanism as a basis for the C1-C2 reaction subset. It was found that the first version of the mechanism substantially also over-predicts the burning velocity of propane. The authors [40] concluded that for fitting experimental data on burning velocities and ignition delay, modifications of the rate constants for the base model – methane combustion, is required. A reasonable match to experimental data on burning velocity and ignition delays for C1-C3 hydrocarbons was obtained by re-optimizing of 9 rate constants of the Grimech 3.0 kinetic model.

Table 7 contains the set of reactions whose rate constants were adjusted to fit calculations and experiments for propane combustion in the original publication [40]. Also included are the set of reactions modified in this work in such a manner as to provide agreement with the experimental data on burning velocity of Davis and Law [33]. This set is based on sensitivity analysis, effects arising from variations of rate constant and analysis of available data on rate constant for various processes. It includes 4 reactions from Grimech-3.0 kinetic model compared to 9 reactions suggested by Qin et al [40]. Two of these reactions correspond to the set of reactions of Qin et al [40]. Other suggested reactions correspond to C3 reaction sub-system. Most of these reactions involve the formation and consumption of allyl radical.

Propene is an important product from heptyl radical decomposition. It is also formed during the decomposition of olefins and olefinyl radicals. Allyl radicals are very stable and can therefore inhibit chain processes by combination with radicals. They are also an important precursor for aromatic formation. This is readily demonstrated from sensitivity calculations. Increasing the reaction rates of channels with allyl radical formation leads to burning velocity decreases, as a result of inhibition sequence of reactions involving allyl radical:

$C_3H_6 + H\ (O, OH) = aC_3H_5 + H_2\ (OH, H_2O)$
$aC_3H_5 + H + M = C_3H_6 + M$

Recombination of allyl radical with hydrogen leads to propene formation and permits through hydrogen atom attack some cycling and catalytical recombination of H atom, thus decreasing burning velocity.

As a first approach to developing of heptane combustion model we follow suggestions of Qin et al [40]. It is of interest to indicate that optimization of the C1-C3 model [40] was conducted without taking into account constraints determined by branching ratios, e.g. data for process $H+HO_2$=>products were modified without taking into account that there exist certain branching ratio for the channels of this reaction, which is important for modeling of self-ignition processes and ignition in intermediate temperature range. Also, data for reactions of formation aC_3H_5 in the radical reactions with C_3H_6 were modified without corresponding corrections for other channels of these processes. Thus, future additional justification of these modifications will be needed.

C. Effect of $C_2H_3+O_2$ reaction.

The reaction of vinyl and O_2 is another high sensitivity reaction. Reaction of vinyl radical with oxygen was analyzed in several works [54-58]. It is one of the main reactions that determine the level of conversion of C2 species into those with one carbon atom. The following channels were considered in the kinetic model for this multi-channel process:

$$C_2H_3 + O_2 = C_2H_2+HO_2 \qquad a$$
$$C_2H_3 + O_2 = HCO+CH_2O \qquad b$$
$$C_2H_3 + O_2 = O+CH_2CHO \qquad c$$

Calculations demonstrate that burning velocity is sensitive to the channel c with O+CH2CHO products, which is the chain branching process. It was noted, that the channel (b) leading to the formation of CH2O+HCO is most important at low temperatures. As the temperature is increased, channel (a) with $C_2H_2+HO_2$ formation becomes important [54,38,39]. It was indicated that in order to have reasonable prediction of ignition delays in ethane/O_2/Ar mixtures, it was necessary to have the $HO_2+C_2H_2$ channel despite the lack of experimental evidence for it [54,38]. The reaction of C_2H_3 with O_2 has to be assumed to have the products HO_2 and C_2H_2 at high temperature, in contrast to low temperature measurements where the products are HCO and CH_2O. Otherwise no reasonable results for ignition delay times and burning velocities are possible [38,39].

Mebel et al [56] have analyzed this reaction theoretically and computed rate constants for all three channels. They concluded that in the temperature range 500-900K, the channel (a) forming $CHO+CH_2O$ dominates. With increasing temperature (T>900K) the chain branching (c) process becomes more important. It is only at the highest temperatures (T>2500K), that the channel yielding $C_2H_2+HO_2$ products begin to make contributions [56]. These rate constants were used in Grimech 3.0 model. Marinov et al [2] used different ratio of rate constants, based on the work of Westmoreland [55] and calculations of Melius for reaction b [59]. The rate constant for chain branching channel c obtained by Wesmoreland [55] was increased by Marinov et al [2,59] due to the necessity to match experimental data for acetylene concentrations in rich flames. Recently Carriere et al [58] concluded that the channel with CH_2CHO+O products does not make contribution until ~2300K. Our results confirms the claim that the rate constant assigned in Grimech-3.0 model for this channel is too high if agreement between simulations and experimental data on burning velocity is to be achieved.

The overall rate constant was measured by Fahr and Laufer [60], and Knyazev and Slagle [61]. Based on these measurements, Baulch et al [39] recommended temperature independent value $5.42x10^{12}$ for overall rate constant. This value was used for channel a in the model [38] to represent the reaction C_2H_3+O2. Note that in the Grimech 3.1 model, reaction of vinyl radical with oxygen was represented by channel b, only. Qin et al [40] decreased the rate constant for chain branching channel by a factor of 0.4. The decreased rate constant coincides with the data used by Marinov et al [2] at temperature approximately 1380K, but the temperature dependencies are different.

VI. Influence of product distribution of heptyl radical decomposition on PAH formation.

The values of the rate constants assigned to the formation, isomerization and decomposition of heptyl radicals determine the level and distribution of the PAHs. The main

stable products from heptyl radicals are CH_4, C_2H_4, C_3H_6, 1,3-C_4H_6, 1-C_5H_{10}, 1-C_6H_{12}. Calculated distribution of hydrocarbon products from heptane oxidative decomposition at the maximum of C_3H_6 and 1,3-C_4H_6 concentration is CH_4:C_2H_2:C_2H_4:C_2H_6:C_3H_6:1,3-C_4H_6=2.4:1.3:12:1.2:2.6:1 for an equivalence ratio 2 in a jet stirred reactor. This ratio approximately coincides with the product distribution for stoichiometric mixtures at the position of maximum concentrations of C_3H_6 and 1,3-C_4H_6. Details of PAH growing processes at high temperatures were analyzed through the modeling of combustion process in jet stirred reactor. Calculations of freely propagating heptane flames with kinetic model including PAH formation processes require large times of computer processor. Figure 11 contains dependencies of intermediate products of high temperature heptane combustion on residence time in a jet stirred reactor. It shows the changes in the branching ratio of heptane products with the residence time during heptane consumption.

Figures 12 contains the results of calculations of PAH yields for the combustion of a variety of hydrocarbons (CH_4, C_2H_6, C_2H_4, C_2H_2, C_3H_8, C_3H_6, C_4H_{10}, 1-C_4H_8, 1,3-C_4H_6 and heptane) at the same equivalence ratio. The lowest production of C_6H_6, $C_{10}H_8$, phenanthrene and pyrene correspond to methane combustion. The maximum yield corresponds to 1,3-butadiene. In terms of propensity for PAH production the 1,3-butadiene is followed by propylene and 1-C_4H_8. Heptane is comparable with ethylene in the production of pyrene. Figure 12 demonstrates the increasing of PAH production with the number of carbon atoms in the alkanes. These results correlate with experimental data on critical sooting equivalence ratio for premixed hydrocarbon flames [62].

Figure 13 contains major reaction pathways of propargyl radical and benzene formation for ethylene combustion. Note that ethylene represents the main product of decomposition of heptyl radicals. Propargyl radicals are formed from the reactions of CH_2 and $^1CH_2$ with acetylene. Hydrogen atom abstraction from pC_3H_4 is a minor channel. Benzene formation is largely result of reactions of propargyl radical combination. Figure 14 contains reaction pathways of propargyl radical and benzene formation for propylene. Our mechanism highlights the route to propargyl radical formation through allyl radical and successive hydrogen atom abstraction. The reaction pathways of benzene formation in C_3H_6 combustion were discussed by Pope and Miller [63] and is in accord with our conclusions. Figure 15 presents reaction pathways of propargyl and benzene formation for combustion of 1,3-butadiene. For 1,3-butadiene the following reaction pathway provides additional contributions to the formation of propargyl radical and benzene: 1,3-C_4H_6+H(OH) = CH_2CHCCH_2+ H_2 (H_2O); CH_2CHCCH_2 = CH_3CCCH_2; CH_3CCCH_2+H =C_3H_3+ CH_3 and CH_3CCCH_2 +C_2H_2=C_6H_6 +H. Figure 16 contains simplified reaction pathways of propargyl and benzene formation for combustion of heptane in jet stirred reactor. It demonstrates that formation of ring compounds for heptane combustion represents some combination of reaction pathways of benzene and propargyl radical formation for ethylene and propylene combustion and analyzed conditions of reaction proceeding. Formation of ethylene, 1-C_4H_8, 1-C_5H_{10}, pC_4H_9, C_3H_6, nC_3H_7, C_2H_5 as the result of decomposition and isomerization reactions of heptyl radicals leads to two major reaction routes in the generation of propargyl radicals and benzene. First route includes formation aC_3H_5 radical which leads to formation of aC_3H_4/pC_3H_4 and C_2H_3 species. Reactions of aC_3H_4 and pC_3H_4 lead to the formation of C_3H_3. Second pathway incorporates formation of ethylene from C_2H_5 and nC_3H_7 radicals, which leads to propargyl radical through formation of C_2H_3 and C_2H_2.

VII. Conclusions

We have studied the kinetics of heptane combustion at high temperatures through numerical modeling. A kinetic model of high temperature heptane combustion was constructed. The model is based on new kinetic data for decomposition of heptane, olefins, heptyl and olefinic radicals. The model includes four main blocks of reactions: C1-C2 chemistry, which is based on Grimech-3.0 model [1,40]; block of C3-C4 reactions based on the models [2,3,5] and block of C4-C7 reactions, which is based on new results and previous heptane combustion models [10,14,18,15,17]. Block of reactions of PAH formation was assembled based on the models of Marinov et al [2], Richter [5] and ABF model [4]. The modeling of heptane combustion was concentrated on simulation of burning velocity dependence on equivalence ratio and temperature dependence of ignition delay at high temperatures. Comparison of modeling results with experimental data on burning velocity of Davis and Law [33], ignition delay of Vermeer et al [50] and Horning et al [51], OH kinetics behind shock waves [52] and branching ratio of olefin production during heptane decomposition at high temperatures [43] demonstrates reasonable agreement. Rate constants for heptane decomposition were calculated. It was demonstrated that for 1 and 10 atm pressures, decomposition of n-heptane proceeds in fall-of region, and rate constants are pressure dependent. The reactions determining burning velocity were established through sensitivity analysis. The main reactions determining burning velocity are similar to reactions determining burning velocity of C1-C4 hydrocarbons. Sensitivity of burning velocity to reactions of C5-C7 species is relatively small. Modeling of influence of product distribution of heptyl radical decomposition on PAH formation demonstrates that reaction pathway of formation of first aromatic compounds represents some combination of reaction pathways of benzene and propargyl radical formation in ethylene and propylene combustion.

Acknowledgement.

Authors would like to thank F.Dryer, N.Peters, H.Richter, R.Seiser and C.Vovelle for providing their kinetic models.

References

1. Smith, G. P., Golden, D. M., Frenklach, M., Moriarty, N. W., Eiteneer, B., Goldenberg, M., Bowman, C. T., Hanson, R. K., Song, S., Gardiner, Jr. W. C., Lissianski, V. V., and Qin, Z., "GRI-Mech 3.0," http://www.me.berkeley.edu/gri_mech, 2000.
2. Marinov, N.M., Pitz, W.J., Westbrook, C.K., Vincitore, A.M., Castaldi, M.J., Senkan, S.M., and Melius, C.F., "Aromatic and Polycyclic Aromatic Hydrocarbon Formation in a Laminar Premixed n-Butane Flame," Combust.Flame., vol. 114, 1998, pp.192-213.
3. Laskin, A., Wang, H., and Law, C.K., "Detailed Kinetic Modeling of 1,3-Butadiene Oxidation at High Temperatures," Int.J.Chem.Kinetics, vol. 32, 2000, pp.589-614.
4. Appel, J., Bockhorn, H., and Frenklach, M., "Kinetic Modeling of Soot Formation with Detailed Chemistry and Physics: Laminar Premixed Flames of C2 Hydrocarbons," Combust.Flame, vol.121, 2000, pp.122-136.
5. Richter H., Personal communication, 2002.
6. Richter, H., Grieco, W.J., and Howard, J.B., "Formation Mechanism of Polycyclic Aromatic Hydrocarbons and Fullerenes in Premixed Benzene Flames," Combust.Flame, vol.119, 1999, pp.1-22.
7. D'Anna, A., Violi, A., and D'Alessio, "Modeling the rich Combustion of Aliphatic Hydrocarbons", Combust.Flame, vol.121, 2000, pp.418-429.
8. Lindstedt, P., Maurice, L., and Meyer, M., "Thermodynamic and Kinetic Issues in the Formation and Oxidation of Aromatic Species," Faraday Discussions, vol.119, 2001, pp.409-432.
9. Bohm, H., and Jander, H., "PAH Formation in Acetylene-benzene pyrolysis," Phys.Chem.Chem.Phys., vol.1, No 16, 1999, pp.3775-3781.
10. Tsang, W., "Progress in the Development of a Kinetic Data Base for Heptane Combustion," AIAA Paper 2003-0063, Jan. 2003.
11. Coats, C.M., and Williams, A., "Investigation of the Ignition and Combustion of n-Heptane-Oxygen Mixtures," Proc.Combust.Inst., vol.17, 1978, pp.611-621.
12. Warnatz, J., "Chemistry of High Temperature Combustion of Alkanes up to Octane," Proc.Combust.Inst., vol.20, 1984, pp.845-856.
13. Westbrook, C.K., Warnatz, J., and Pitz, W.J., "A Detailed Chemical Kinetic Reaction Mechanism for the Oxidation of Iso-Octane and n-Heptane over an Extended Temperature Range and its Application to Analysis of Engine Knock," Proc.Combust.Inst., vol.22, 1988, p.893-901.
14. Curran, H.J., Gaffuri, P., Pitz, W.J., and Westbrook, C.K., "A Comprehensive modeling of n-Heptane Oxidation,", Combust.Flame, vol.114, 1998, pp.149-177.
15. Lindstedt, R.P., and Maurice, L.Q., "Detailed Kinetic Modeling of n-Heptane Combustion," Combust.Sci.Tech., vol.107, 1995, pp.317-353.
16. El. Bakali, A.E., Delfau, J-L., and Vovelle, C., "Kinetic Modeling of a Rich, Atmospheric Pressure, Premixed n-Heptane/O2/N2 Flame," Combust.Flame, vol.118, 1999, pp.381-389.
17. Westbrook, C.K., Pitz, W.J., Curran, H.C., Boercker, J., and Kunrath, E., "Chemical kinetic Modeling Study of Shock Tube Ignition of Heptane Isomers," Int.J.Chem.Kinet., vol.33, 2001, pp.868-877.
18. Seiser, R., Pitsch, H., Seshadri, K., Pitz, W.J., and Curran, H.J., "Extinction and Autoignition of n-Heptane in Counterflow configuration, Proc.Combust.Inst., vol.28, 2000, pp.2029-2037.

19. Westbrook, C.K., Pitz, W.J., Boercker, J.E., Curran, H.J., Griffiths, J.F., Mohamed, C., and Ribaucour, M., “Detailed Chemical Kinetic Reaction Mechanisms for Autoignition of Isomers of Heptane Under Rapid Compression,” Proc.Combust.Inst., vol.29, 2002.
20. Chakir, A., Cathonnet, M., Boettner, J.C., and Gaillard, F., "Kinetic Study of n-Butane Oxidation," Combust.Sci.Technol., vol.65, 1988, pp.207-230.
21. Chakir, A., Cathonnet, M., Boettner, J.C., and Gaillard, F., “Kinetic Study of 1-Butene Oxidation in a Jet-Stirred Flow Reactor,” Proc.Combust.Inst., vol.22, 1988, pp.873-881.
22. Chakir, A., Belliman, M., Boettner, J.C., and Cathonnet, M., "Kinetic Study of n-Heptane oxidation," Int.J.Chem.Kinet., vol.24, 1992, pp.385-410.
23. Dagaut, P., Boettner, J.C., Cathonnet, M., and Gaillard, F., "Kinetic Modeling of Propane Oxidation", Combust.Sci.Technol., vol.56, 1987, pp.23-63.
24. Dagaut, P., Cathonnet, M.,and Boettner, J.C., "Propyne Oxidation - A Kinetic Modeling Study", Combust.Sci.Technol., vol.71, 1990, pp.111-128.
25. Dagaut, P., Cathonnet, M., and Boettner, J.C., "Kinetics of Ethane Oxidation," Int.J.Chem.Kinet., vol.23, 1991, pp.437-455.
26. Foelshe, R.O., Keen, J.M., and Solomon, W.C. "A non-equilibrium computational method for predicting fuel rich gas generator performance and exhaust properties. Vol.2: Reaction kinetics and computational results." University of Illinois, Report No AAE9307, UIL93-0507, 1993.
27. Tsang, W., "Thermal Stability of Cyclohexane and 1-Hexene," Int.J.Chem.Kinet., vol.10, 1978, pp.1119-1138.
28. Tsang, W., “Thermal Decomposition of Cyclopentane and Related Compounds,” Int.J.Chem.Kinet., vol.10, 1978, pp.599-617.
29. Westbrook, C.K., Pitz, W.J., Thornton, M.M., and Malte, P.C., “A Kinetic Modeling Study of Normal Pentane Oxidation in a Well-Stirred Reactor”, Combust.Flame, vol.72, 1988, pp.45-62.
30. Gibbs, G.J., and Calcote, H.F., “Effect of Molecular Structure on Burning Velocity,” J.Chem.Eng.Data, vol.4, No 3, 1959, pp.226-237.
31. Gerstein, M., Levine, O., and Wong, E.L., “Flame Propagation. 2. The Determination of Fundamental Burning Velocities of Hydrocarbons by a Revised Tube Method,” J.Am.Chem.Soc., vol.73, 1951, pp.418-422.
32. Heimel, S., and Weast, R.C., “Effect of Initial Mixture Temperature on the Burning Velocity of Benzene-Air, n-Heptane-Air and Isooctane-Air Mixtures,” Proc.Combust.Inst., vol.6, 1956, pp.296-302.
33. Davis, S.G., and Law, C.K., “Determination of and Fuel Structure Effects on Laminar Flame Speeds of C1-C8 Hydrocarbons,” Combust.Sci.Technol., vol.140, 1998, pp.427-449.
34. Takahashi, K., Inomata, T., Abe, T., Fukaya, H., Hayashi, E., and Ono, T., “Inhibition of Combustion by Bromine-free Polyfluorocarbons. 2. Burning Velocities of Methane and n-Heptane Flames with Polyfluorocarbons containing Oxygen, Nitrogen, or Sulfur,” Combust. Sci.Technol., vol.131, 1998, 187-191.
35. Babkin, V.S., V’yun, A.V., and Kozachenko, L.S., “Determination of Burning Velocity from Pressure Record in a Constant Volume Bomb,” Combust.Expl.Shock Waves, vol.3, No 3, 1967, p.221..
36. Ryan, T.W., and Lestz, S.S., “The Laminar Burning Velocityu of Isooctane, n-Heptane, Methanol, Methane, and Propane at Elevated Temperature and Pressures in the Presence of a Diluent," SAE International Congress and Exposition, SAE Paper No. 800103, SAE Transactions, Vol. 89, Detroit, Michigan, February 1980.

37. Held, T.J., Marchese, A.J., and Dryer, F.L., “A Semi-empirical Reaction Mechanism for n-Heptane Oxidation and Pyrolysis,” Combust.Sci.Technol., vol.123, 1997, pp.107-146.
38. Hughes, K.J., Turani, T., Clague, A.R., and Pilling, M.J., “Development and Testing of a Comprehensive Chemical Mechanism for the Oxidation of Methane,” Int.J.Chem.Kinet., vol.33, 2001, pp.513-538, (http://www.chem.leeds.ac.uk/Combustion.html).
39. Baulch, D.L., Cobos, C.J., Cox, R.A., Frank, P., Hayman, J., Just, T., Kerr, J.a., Murrells, T., Pilling, M.J., Troe, J., Walker, R.W., and Warnatz, J., “Evaluated Kinetic Data for Combustion Modeling. Supplement 1,” J.Phys.Chem.Ref.Data, vol.23, 1994, pp.847-1033.
40. Qin, Z., Lissianski, V.V., Yang, H., Gardiner, W.C., Jr., Davis, S.G., and Wang, H., “Combustion Chemistry of Propane: A Case Study of Detailed Reaction Mechanism Optimization,” Proc.Inst.Combustion, vol.28, 2000, pp.1663-1669.
41. Mokrushin, V., and Tsang, W., “A Calculational Data Base for Unimolecular Reactions,” Abstracts of Work-in-Progress, 27th Int.Symp.Combustion, 1998, p.439.
42. Allison T.C., and Tsang, W. Proceedings of the Second Joint Meeting of the US Sections of the Combustion Institute, Oakland, CA, 2001.
43. Babushok, V., Tsang, W., Awan, I., and Manion, J.A., "Initial Stages of Heptane Decomposition," Proceedings of 2001 Fall Technical Meeting Eastern States Section of the Combustion Institute, 2001.
44. Tsang, W., Walker, J.A., and Manion, J.A., "Single-Pulse Shock-Tube Study on the Decomposition 1-Pentyl Radicals," Proc.Combust.Inst., vol.27, 1998, pp.135-142.
45. Sumathi, R., Carstensen, H.-H., and Green, W.H. Jr., “Reaction Rate Prediction via Group Additivity. Part 2: H-Abstraction from Alkenes, Alkynes, Alcohols, Aldehydes, and Acids by H Atoms,” J.Phys.Chem., A, vol.105, 2001, pp.8969-8984.
46. Stein, S.E., Rukkers, J.M., and Brown, R.L. "NIST Structures&Properties Database and Estimation Program," NIST, Gaithersburg, MD, 1991.
47. Stein, S.E., and Fahr, A., “High-Temperature Stabilities of Hydrocarbons,” J.Phys.Chem, vol.89, 1985, pp.3714-3725.
48. Wang, H., and Frenklach, M., "Enthalpies of Formation of Benzenoid Aromatic Molecules and Radicals," J.Phys.Chem, vol.97, 1993, pp.3867-3874.
49. Kee, R. J., Rupley, F. M., and Miller, J. A., "CHEMKIN-II: A Fortran Chemical Kinetics Package for the Analysis of Gas Phase Chemical Kinetics," Sandia National Laboratory, SAND89-8009B, 1989.
50. Vermeer, D.J., Meyer, J.W., and Oppenheim, A.K., “Auto-Ignition of Hydrocarbons behind Reflected Shock Waves,” Combust.Flame, vol.18, 1972, p.327.
51. Horning, D.C., Davidson, D.E., and Hanson, R.K., "Study of the High-Temperature Autoignition of n-Alkane/O2/Ar Mixtures," J.Propul.Power, vol.18, 2002, pp.363-371.
52. Davidson, D.F., Herbon, J.T., Horning, D.C., and Hanson, R.K., “OH Concentration Time Histories in n-Alkane Oxidation,” Int.J.Chem.Kinet., vol.33, 2001, pp.775-783.
53. Babushok, V.,and Tsang, W., “Inhibitor Rankings for Alkane Combustion,” Combust.Flame, vol.123, 2000, pp.488-506.
54. Warnatz, J., “Resolution of Gas Phase and Surface Combustion Chemistry into Elementary Reactions,” Proc.Combust.Inst., vol.24, 1992, pp.553-579.
55. Westmoreland, P.R., "Thermochemistry and Kinetics of C2H3+O2 Reactions," Combust.Sci. Technol., vol.82, 1992, pp.151-168.
56. Mebel, A.M., Diau, E.W.G., Lin, M.C., and Morokuma, K., “Ab Initio and RRKM Calculations for Multichannel Rate Constants of the C2H3+O2 Reaction,” J. Am. Chem. Soc., vol.118, 1996, pp.9759-9771.

57. Bozzelli, J.W., and Dean, A.M., “Hydrocarbon Radical Reactions with O2 – Comparison of Allyl, Formyl, and Vinyl to Ethyl,” J. Phys. Chem., vol.97, 1993, pp.4427-4441.
58. Carriere, T., Westmoreland, P.R., Kazakov, A., Stein, Y.S., and Dryer, F.L., "Modeling Ethylene Combustion from Low to High Pressure," Proc.Combust.Inst., vol.29, 2002.
59. Marinov, N.M. Personal Communication, 2001.
60. Fahr, A., and Laufer, A.H., “Ultraviolet Absorption of the Vinyl Radical and Reaction with Oxygen,” J. Phys. Chem., vol.92, 1988, pp.7229-7232.
61. Knyazev,V.D. and Slagle, I.R., “Kinetics of the Reaction of Vinyl Radical with Molecular Oxygen,” J. Phys. Chem., vol.99, 1995, pp.2247-2249.
62. Glassmann, I., "Combustion," Academic Press, San Diego, CA, 1996.
63. Pope, C.J., and Miller, J.A., “Exploring Old and New Benzene Formation Pathways in Low-Pressure Premixed Flames of Aliphatic Fuels,” Proc.Combust.Inst., vol.28, 2000, pp.1519-1527.
64. Bohm, H., Jander, H., and Tanke, D., "PAH Growth and Soot Formation in the Pyrolysis of Acetylene and Benzene at High Temperatures and Pressures: Modeling and Experiment," Proc.Combust.Inst., vol.27, 1998, pp.1605-1612.
65. D’Anna, and Violi, A., "A Kinetic Model for the Formation of Aromatic Hydrocarbons in Premixed Laminar Flames," Proc.Combust.Inst., vol.27, 1998, pp.425-433.
66. Street, J.C., and Thomas, A., "Carbon Formation in Premixed Flames," Fuel, vol.34, 1955, pp.4-36.

Figure Captions:

Fig.1. Burning velocity dependence on equivalence ratio of heptane/air mixtures. Symbols – experimental data [30,31,33,34]; lines – modeling results [12,15,16,37].

Fig.2. Contributions of decomposition reactions and radical reactions to heptane consumption (jet stirred reactor, 1650K, 1 atm, residence time 0.0057s).

Fig3. Reaction pathways of decomposition of heptyl radicals

Fig.4. Temperature dependence of heptane ignition delay behind shock wave (2.5% heptane, 27.5%O_2, 70%Ar); symbols – experimental data [50], 1.9-2.6 atm; line- this work, 2.3 atm.

Fig.5. Temperature dependence of heptane ignition delay for different equivalence ratios (0.5, 1, 2; 0.4% heptane), pressure 1 atm; symbols – experimental data [51]; lines- this work.

Fig.6. OH concentration for different temperatures. Lines – experimental data [52]; symbols – this work (300 ppm C_7H_{16}, heptane/O2/Ar, equivalence ratio 1; 1551 K (2.14 atm); 1640 K (2.04 atm), 1784K (2.12 atm)).

Fig.7. Dependence of heptane burning velocity on equivalence ratio; symbols – experimental data [33]; lines – results of calculations [15,16, present work].

Fig.8. Sensitivity coefficients for heptane/air flame, kinetic model of Bakali et al [16].

Fig.9. Sensitivity coefficients for heptane/air flame, Grimech 3.0 and reduced kinetic model of Seiser et al [18].

Fig.10. Sensitivity coefficients for heptane/air flame, kinetic model of Lindstedt et al [15].

Fig.11. Dependence of intermediate products of heptane combustion on residence time (equivalence ratio 2, 1650K, 1 atm).

Fig.12. Concentrations of naphthalene and pyrene for combustion of different hydrocarbons (equivalence ratio 2; 1650K, 0.0057s, 1 atm).

Fig 13. Consumption pathways of ethylene (equivalence ratios 1 and 2.5, 1650K, residence time 0.0057s, 1 atm).

Fig.14. Major reaction routes of propargyl radical and benzene formation for propylene combustion (equivalence ratio 2; 1650K, 0.0057s, 1 atm).

Fig.15. Major reaction routes of propargyl radical and benzene formation for 1,3-butadiene combustion (equivalence ratio 2; 1650K, 0.0057s, 1 atm).

Fig.16. Major reaction routes of propargyl radical and benzene formation for heptane combustion (equivalence ratio 2; 1650K, 0.0057s, 1 atm).

Fig. 17. Dependence of H, OH,C_3H_3,C_2H_2, benzene and naphthalene concentrations on equivalence ratio for ethylene combustion (1650K, 1 atm).

Fig. 18. Dependence of H, OH,C_3H_3,C_2H_2, benzene and naphthalene concentrations on equivalence ratio for heptane combustion (1650K, 1 atm).

Table 1. Comparison of modeling results on heptane combustion with experimental data*.

Model	Ignition delay	Burning velocity	Opposite diffusion flame	Flame structure	Stirred reactor	Flow reactor	Static reactor	Rapid compression machine
Warnatz [1] Nehse et al [2]	[26,27]	[24, 25]						
Westbrook et al [3] Chevalier et al [4] Curran et al [5] Seiser et al [6]	[28,29, 26,23] [26]		[6]		[45,46]	[18,49]	[50]	[18,51-55]
Lindstedt et al [7]		[25]	[37-40]		[16]			
Fournet et al [8] Come et al [9] Glaude et al [10]					[16,45,47,48]			
Bakali et al [11] Doute et al [12]		[25]		[11,43] [44]				
Muller et al [13] Bui-Pham et al [14] Bollig et al [15]	[26]		[38,41,42]					
Chakir et al [16]	[23,30,31]				[16]			
Ranzi et al [17] Callahan et al [18]	[26]				[45,46]	[18]		[18,56]
Darabiha et al [19]			[19]					
Held et al [20] Ingermasson et al [21]	[28]	[24,25]		[21]	[16]	[20]		
Basevich et al [22]	[31-36]							
Coats et al [23]	[23]							

* References to Table 1: 1. Warnatz, J., 20-th Symp.(Int.) on Combustion, 1984, pp.845-856; 2. Nehse, M., Warnatz, J., Chevalier, C., 26th Symp.Int. on Combustion, Combustion Institute, 1996, pp.773-780; 3. Westbrook, C.K., Warnatz, J., Pitz, W.J., 22-th Symp.(Int.) on Combustion, The Combustion Inst., 1988, p.893-901; 4. Chevalier, C., Pitz, W.J., Warnatz, J., Westbrook, C.K., Melenk, H., 24th Symp.Int. on Combustion, The Combustion Institute, 1992, pp.93-101; 5. Curran, H.J., Gaffuri, P., Pitz, W.J., Westbrook, C.K. Combust.Flame, 114:149-177 (1998); 6. Seiser, R., Pitsch, H., Seshadri, K., Pitz, W.J., Curran, H.J., 28th Symp.Int. on Combustion, 2000; 7. Lindstedt, R.P., Maurice, L.Q., Combust.Sci.Tech., 1995, 107: 317-353; 8. Fournet, R., Warth, V., Glaude, P.A., Battin-Leclerc, F., Scacchi, G., Come, G.M., Int.J.Chem.Kinet., 2000, 32:36-51; 9. Come, G.M., Warth, V., Glaude, P.A., Fournet, R., Battin-Leclerc, F., Scacchi, G., 26th Symp.(Int.) on Combustion, 1996, pp.755-762; 10. Glaude, P.A., Warth, V., Fournet, R., Battin-Leclerc, F., Come, G.M., Scacchi, G., Bull.Soc.Chim.Belg., 1997, 106:343; 11. Bakali, A.E., Delfau, J-L., Vovelle, C., Combust.Flame, 1999, 118:381-389; 12. Doute, C., Delfau, J.-L., Vovelle, C., Combust.Sci.Technol., 1999, 147:61-109; 13. Muller, U.C., Peters, N., Linan, A., 24-th Symp.(Int) on Combustion, 1992, pp.777-784; 14. Bui-Pham, M., Seshadri, K., Combust.Sci.Technol., 1991, 79:293-310; 15. Bollig, M., Pitsch, H., Hewson, J.C., Seshadri, K., 26th Symp.Int. on Combustion, 1996, pp.729-737; 16. Chakir, A., Belliman, M., Boettner, J.C., Cathonnet, M., 1992, 24:385-410; 17. Ranzi, E., Gaffuri, P., Faravelli, T., Dagaut, P., Combust.Flame, 1995, 103:91-106; 18. Callahan, C.V., Held, T.J., Dryer, F.L., Minetti, R., Ribaucour, M., Sochet, L.R., Faravelli, T., Gaffuri, P., Ranzi, E. 26th Symp.Int. on Combustion, 1996, pp.739-746; 19. Darabiha, N., Lacas, F., Rolon, J.C., Candel, S. Combust.Flame, 1993, 95:261-275; 20. Held, T.J., Marchese, A.J., Dryer, F.L., Combust.Sci.Technol., 1997, 123:107-146; 21. Ingermasson, A.T., Pedersen, J.R., Olsson, J.O., Combust.Flame, 1999, 103:8222-8230; 22. Basevich, V.Ya., Belyaev, A.A., Brandshteter, V., Neigauz, M.G., Tashl, R., Frolov, S.M., Combustion, Explosion, and Shock Waves, 1994, 30(6):737-745; 23. Coats, C.M., Williams, A., 17-th Symp.(Int.) Combustion, 1978, pp.611-621; 24. Gerstein, M., Levine, O., Wong, E.L., J.AM.Chem.Soc., 1951, 73:418; 25. Gibbs, G.J., Calcote, H.F., J.Chem.Eng.Data, 1959, 4:3; 26. Ciezki, H., Adomeit, G., Combust.Flame, 1993, 93:421-433; 27. Fieweger, K., Pfahl, U., Blumenthal, R., Adomeit, G., Kolloquium des Sonderforshungsbereich 224, "Motorische Verbrennung", (Pishing, F., Ed.), March 19-20, 1996, RWTH Aachen, 1996; 28. Vermeer, D.J., Meyer, J.W., Oppenheim, A.K. Comb.Flame, 1972, 18:327; 29. Adomeit, G., 1989; 30. Burcat, A, Farmer, R.F., Matula, R.A., 13th Int.Symp. on Shock Tubes and Waves (Ch.E.Treanor, J.G.Hall, Eds), 1981, pp.826-833; 31. Ciezki, H., Adomeit, G., 16th Int.Symp. on Shock Tubes and Waves, 1987, pp.481-486; 32. Poppe, C., Schreber, M., Griffiths, J.F., Proc.Joint Meeting of the Soviet and German Sections of the Combustion Institute, Cambridge, 1993, pp.360; 33. Teichmann, H., Z.Elektrochem.Angew.Phys.Chem., 47, 297 (1941); 34. Scheuermeyer, M., Steigerwald, H. Motortech. Z., 5:229 (1943); 35. Rogener, H., Z.Elektrochem.Angew.Phys.Chem., 53:389 (1949); 36. Taylor, C.F., Taylor, E.S., Livengood, J.C. et al., SAE Quart.Trans., 4:232 (1950); 37. Hamins, A., Diffusion Flame Studies, PhD Thesis, University of California, San Diego, 1985; 38. Hamins, A., Seshadri, K, Combust.Flame, 1987, 68:295; 39. Abdel-Khalic, S.I., Tamaru, T., El-Wakie, M., 15-th Symp.(Int.) on Combustion, The Combustion Inst.,

1968, p.389; 40. Abdel-Khalic, S.I., An Investigation of the Diffusion Flame Surrounding a Simulated Liquid Fuel Droplet, PhD Thesis, 1973, University of Wisconsin-Madison; 41. Kent, J.H., Williams, F.A., 15th Symp.Int. on Combustion, The Combustion Institute, Pittsburgh, 1974, pp.315-325; 42. Seshadri, K., Ph.D. Thesis, University of California, San Diego, 1977; 43. Bakali, A.E., Delfau, J.-L., Vovelle, C., Combust.Sci.Technol., 1998, 140:69-91; 44. Doute, C., Delfau, J.-L., Vovelle, C., Combust.Sci.Technol., 1997, 124: (1-6) 249-276; 45. Dagaut, P., Reuillon, M., Cathonnet, M., Combust.Sci.Technol., 1994, 95:233-260; 46. Dagaut, P., Reuillon, M., Cathonnet, M., Combust.Flame, 1995, 101:132-140; 47. Dagaut, P., Boettner, J.C., Cathonnet, M., Combust.Sci.Technol., 1994, 95:233; 48. Dagaut, P., Koch, R., Cathonet, M., Comb.Sci.Technol., 122:345, (1997); 49. Vermeersch, M.L., Held, T.J., Stein, Y.S., Dryer, F.L., SAE Trans. 1991, 100:645; 50. Barnard, J.A., Harwood, B.A., Combust.Flame, 1973, 21:141; 51. Minetti, R., Carlier, M., Ribaucour, M., Therssen, E., Sochet, L.r., Combust.Flame, 102:298-309, 1995; 52. Minetti, R., Carlier, M., Ribaucour, M., Therssen, E., Sochet, L.r., 26th Symp.(Int.) Combustion, 1996, pp.747-753; 53. Griffiths, J.F., Halford-Maw, P.A., Rose, D.J., Combust.Flame, 95:291-306, 1993; 54. Griffiths, J.F., Hughes, K.J., Schreiber, M., Poppe, C., Combust.Flame, 1994, 99:533-540; 55. Cox, A., Griffiths, J.F., Mohamed, C., Curran, H., Pitz, W.J., Westbrook, C.K. 26th Int.Symp. on Combustion, The Combustion Institute, Pittsburgh, 1996; 56. Leppard, W.R., 1988, reference in [3].

Table 2. Kinetic models used in this work

Kinetic model	Year	Hydrocarbon
Curran et al [14]	1998	C_7H_{16}
Seiser et al model [18]	2000	C_7H_{16}
Reduced Seiser et al model [18], present work		C_7H_{16}
Lindstedt and Maurice model [15]	1995	C_7H_{16}
Bakali et al [16]	1999	C_7H_{16}
Model based on Grimech-3.0 [1], present work		C_7H_{16}
Kinetic model of heptane combustion, present work		C_7H_{16}
Kinetic model of heptane combustion, including PAH formation reactions, present work		C_7H_{16}, PAH
Kinetic model of heptane combustion with lumped heptyl radical kinetics, present work		C_7H_{16}
Grimech 3.0 [1]	2000	CH_4 (C1-C2)
Optimized C1-C3 model of Qin et al [40]	2000	C1-C3
1,3-butadiene oxidation model of Laskin et al [3]	2000	1,3-butadiene oxidation
Marinov et al [2]	1998	Butane, PAH
ABF model [4]	2000	C1-C2, PAH, soot
PAH formation model of Richter et al [5,6]	1999, 2002	PAH

Table 3. Rate constants of heptane decomposition reactions (mol,s,cm,cal)

Reaction	logA	n	E
$nC_7H_{16}=C_2H_5+C_5H_{11}$			
P=1 atm	130.877	-32.851	154719
P=10 atm	106.605	-25.7163	141639
K_{inf}	25.9353	-2.64065	88876
$nC_7H_{16}=C_6H_{13}+CH_3$			
P=1 atm	132.618	-33.37	158270
P=10 atm	108.604	-26.284	145.691
K_{inf}	24.6292	-2.24889	91008
$nC_7H_{16}=nC_3H_7+nC_4H_9$			
P=1 atm	129.502	-32.451	153300
P=10 atm	105.229	-25.3215	140150
K_{inf}	25.885	-2.623	88319

Table 4. High pressure rate expressions for the decomposition of heptyl radicals.

Reactions:	Log A	n	E/R
C_7H_{15}-1 = C_2H_4 + nC_5H_{11}	11.07	0.614	13358
C_7H_{15}-2 = C_3H_6 + nC_4H_9	11.94	0.431	13702
C_7H_{15}-3 = 1-C_4H_8 + nC_3H_7	11.91	0.434	13674
C_7H_{15}-3 = CH_3 + 1-C_6H_{12}	11.94	0.44	14748
C_7H_{15}-4 = 1-C_5H_{10} + C_2H_5	11.35	0.68	13397
C_7H_{15}-2 = C_7H_{15}-1	2.721	2.429	8599.3
C_7H_{15}-3 = C_7H_{15}-1	3.647	2.362	8862.6
C_7H_{15}-4 = C_7H_{15}-1	5.805	1.961	12509.7
C_7H_{15}-2 = C_7H_{15}-3	5.291	2.117	10854.8
C_7H_{15}-1 = C_7H_{15}-2	3.473	2.205	7185.3
C_7H_{15}-1 = C_7H_{15}-3	4.26	2.211	7504.9
C_7H_{15}-1 = C_7H_{15}-4	6.592	1.734	11136.3
C_7H_{15}-3 = C_7H_{15}-2	5.438	2.042	10841.2

Table 5. Branching ratios for decomposition of heptyl radical*

Initial Radical	Decomposition Reactions	Log A	n	E/R (K)
C_7H_{15}-1	C_7H_{15} -1 => C_2H_4 + nC_5H_{11}	-1.09	-.345	1824
	C_7H_{15} – 2 => C_3H_6 + nC_4H_9	9.82	3.195	1988
	C_7H_{15} – 3 => 1-C_4H_8 + nC_3H_7	9.05	2.83	2183
	C_7H_{15} -3 => CH_3 + 1-C_6H_{12}	5.62	1.869	2069
	C_7H_{15} –4 => 1-C_5H_{10} + C_2H_5	-3.66	.935	291
C_7H_{15}-2	C_7H_{15} -1 => C_2H_4 + nC_5H_{11}	3.128	1.384	1274
	C_7H_{15} – 2 => C_3H_6 + nC_4H_9	.364	.121	399
	C_7H_{15} – 3 => 1-C_4H_8 + nC_3H_7	.277	.375	-392.8
	C_7H_{15} -3 => CH_3 + 1-C_6H_{12}	-2.93	-.523	-452
	C_7H_{15} –4 => 1-C_5H_{10} + C_2H_5	1.458	1.045	69,7
C_7H_{15}-3	C_7H_{15} -1 => C_2H_4 + nC_5H_{11}	4.36	1.646	1838
	C_7H_{15} – 2 => C_3H_6 + nC_4H_9	1.33	.724	-287.2
	C_7H_{15} – 3 => 1-C_4H_8 + nC_3H_7	1.2	.415	482.1
	C_7H_{15} -3 => CH_3 + 1-C_6H_{12}	-2.875	-.733	187.8
	C_7H_{15} –4 => 1-C_5H_{10} + C_2H_5	2.98	1.375	785.6
C_7H_{15}-4	C_7H_{15} -1 => C_2H_4 + nC_5H_{11}	-7.86	-1.91	153.5
	C_7H_{15} – 2 => C_3H_6 + nC_4H_9	2.56	1.46	493.5
	C_7H_{15} – 3 => 1-C_4H_8 + nC_3H_7	3.28	1.52	1154
	C_7H_{15} -3 => CH_3 + 1-C_6H_{12}	.1148	.632	1100.4
	C_7H_{15} –4 => 1-C_5H_{10} + C_2H_5	.124	.0413	38.1

Expressions in the form of A(1/T)^n*exp(-E/RT)

Table 6. Normalized sensitivity coefficients for heptane/air flame (dependence on equivalence ratio).

Reaction/equiv.ratio	0.8	1	1.4
$H+O_2=OH+O$	0.205	0.23	0.703
$CH_3+H+M=CH_4+M$	-0.0198	-0.0249	-0.262
$HCO+M=H+CO+M$	0.0435	0.042	0.0846
$OH+CO=CO_2+H$	0.143	0.0857	0.032
$H+O_2+M=HO_2+M$	-0.0838	-0.040	-0.019
$H+aC_3H_5+M=C_3H_6+M$	-0.053	-0.043	-0.11
$H+C_2H_4+M=C_2H_5+M$	0.00971	0.00965	0.03

Table 7.

Set of reactions used for optimization by Qin et al [40]	Set of reactions determined in this work
$C_2H_4+OH=C_2H_3+H_2O$ [1]	
$C_2H_4+O=H+CH_2CHO$ [1]	
$C_2H_4+O=CH_3+HCO$ [1]	
$H+C_2H_4+M=C_2H_5+M$ [1]	$H+C_2H_4+M=C_2H_5+M$ [1]
$C_2H_3+O_2==O+CH_2CHO$ [1]	$C_2H_3 + O_2 =>$ [1]
$C_2H_3+H=H_2+C_2H_2$ [1]	
$CH_3+HO_2=CH_3O+OH$ [1]	
$HO_2+H=OH+OH$ [1]	
$HO_2+H=H_2+O_2$ [1]	
	$H+CH_3+M=CH_4+M$ [1]
	$HCO+M=H+CO+M$ [1]
$C_3H_6+H=aC_3H_5+H_2$	$C_3H_6+H=aC_3H_5+H2$
$C_3H_6+OH=aC_3H_5+H_2O$	$C_3H_6+OH=aC_3H_5+H_2O$
$C_3H_6+H=C_2H_4+CH_3$	
$aC_3H_5+H+M=C_3H_6+M$	$aC_3H_5+H+M=C_3H_6+M$
	$aC_3H_5+O =>$
	$C_3H_6+O=aC_3H_5+OH$
	$aC_3H_4+H+M=aC_3H_5+M.$
	$CH_3+C_2H_2+M=a\text{-}C_3H_5+M$

Figure 1

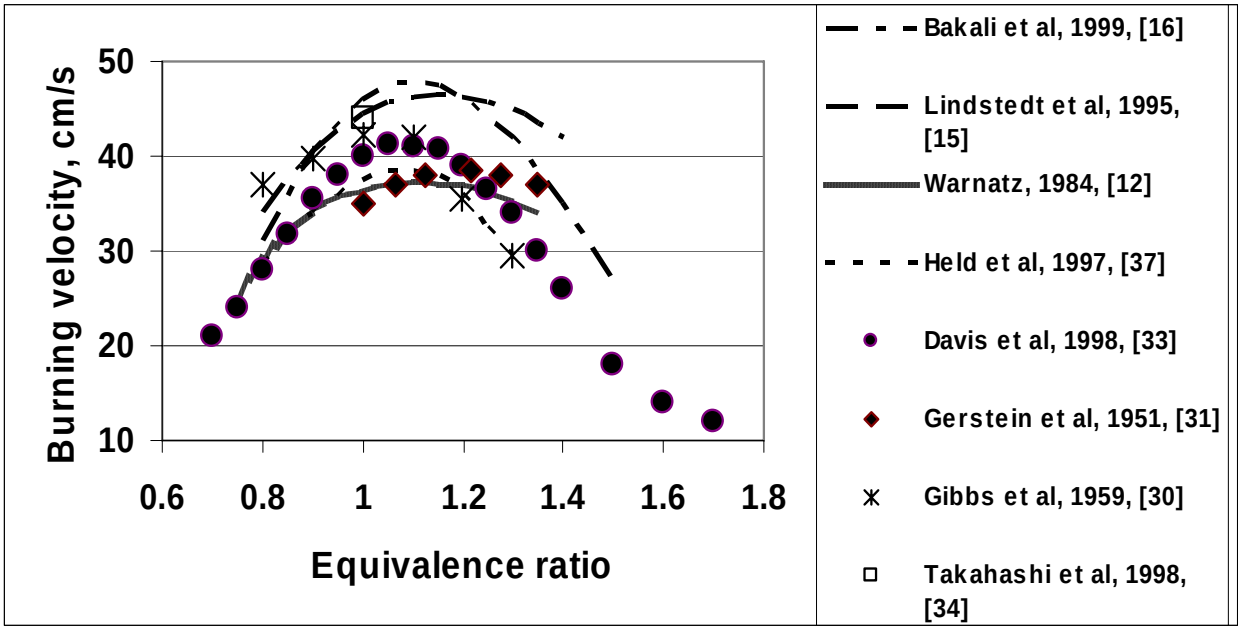

Figure 2.

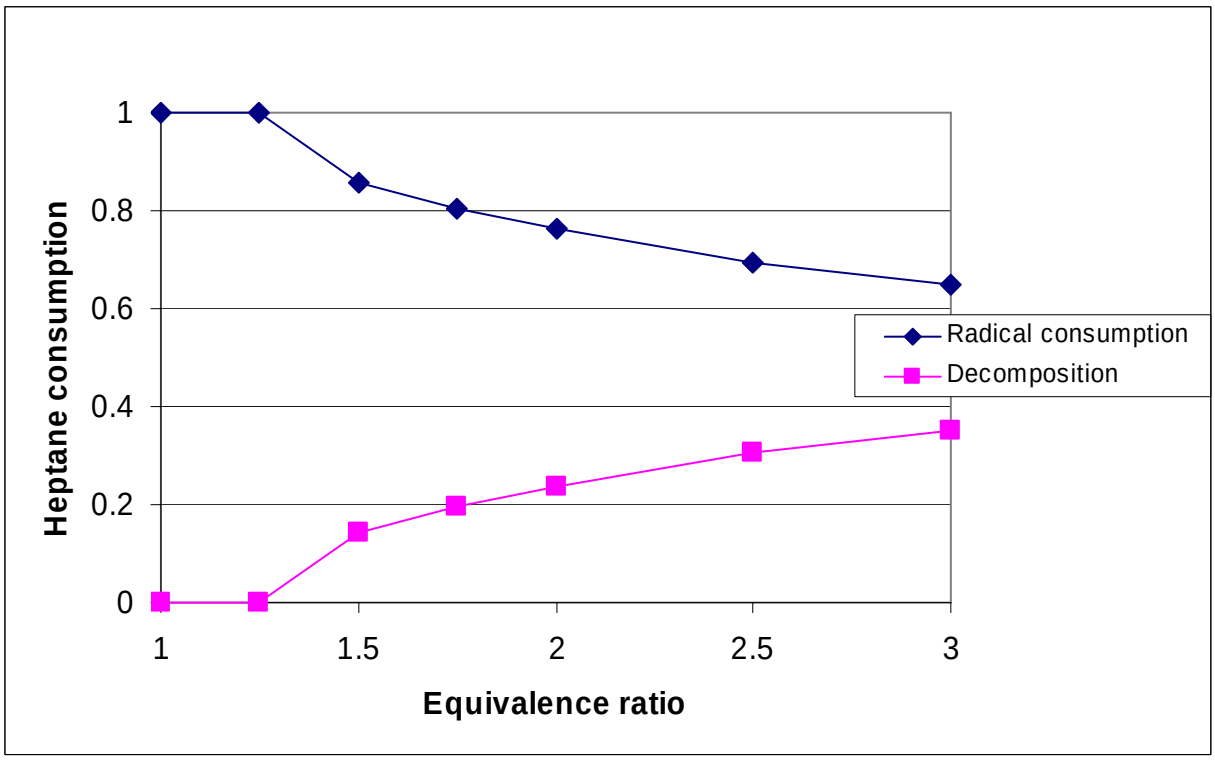

Figure 3

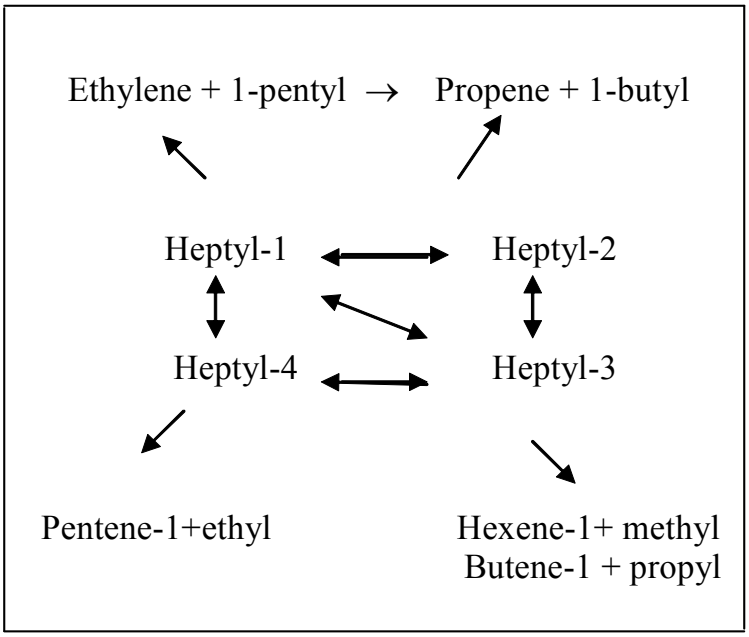

Figure 4

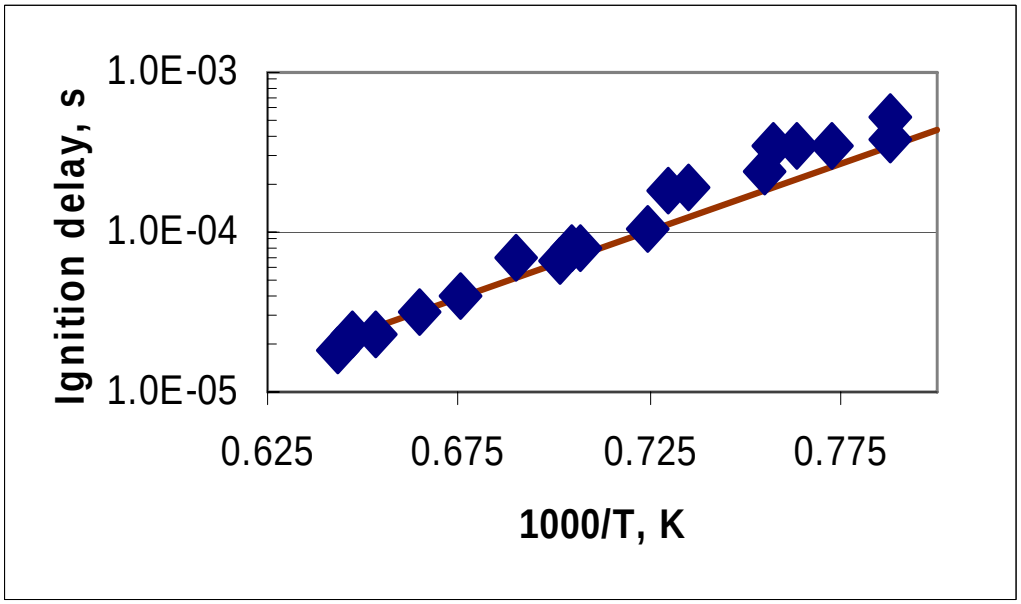

Figure 5

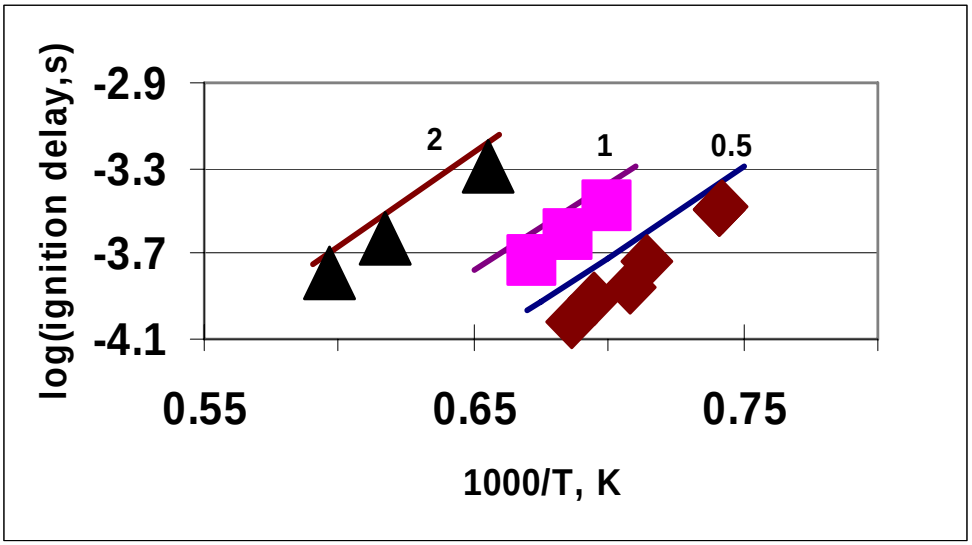

Figure 6

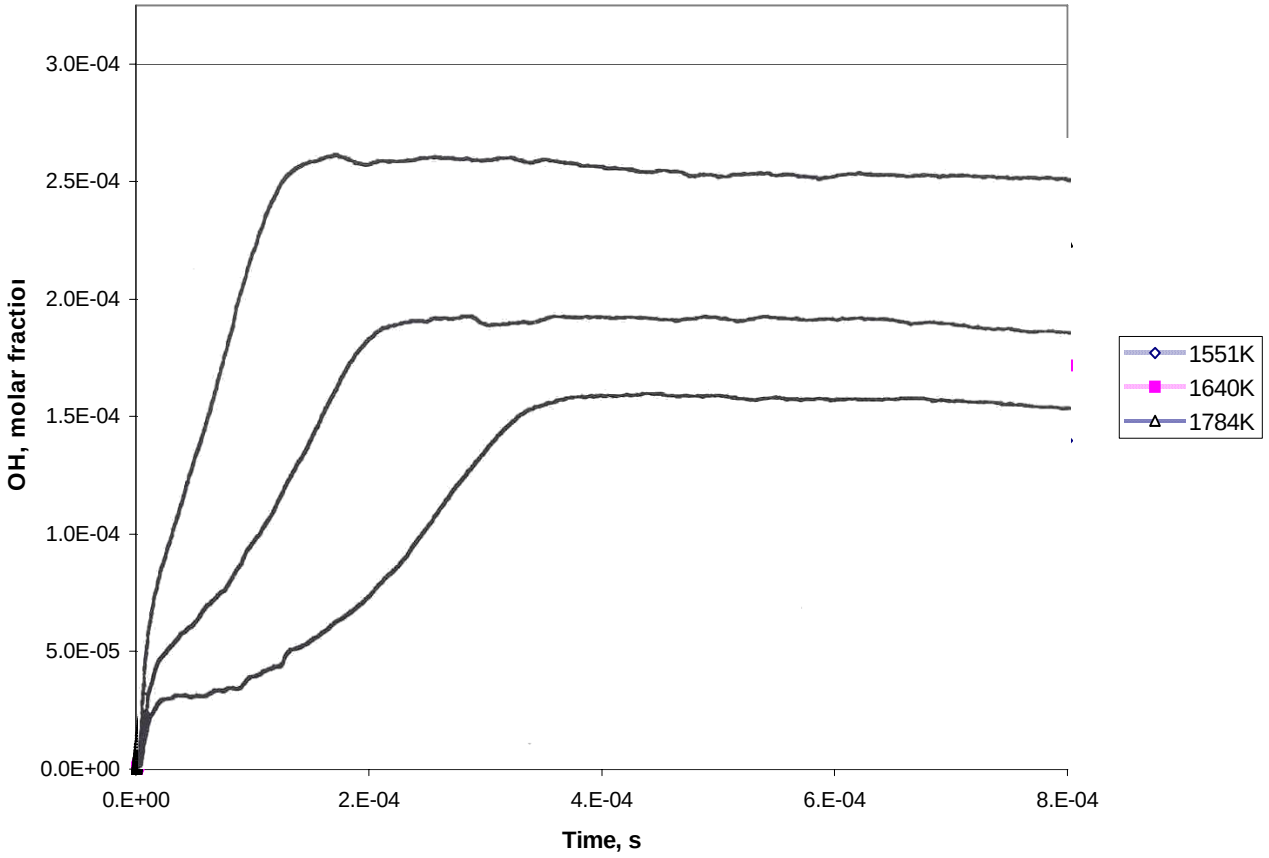

Figure 7

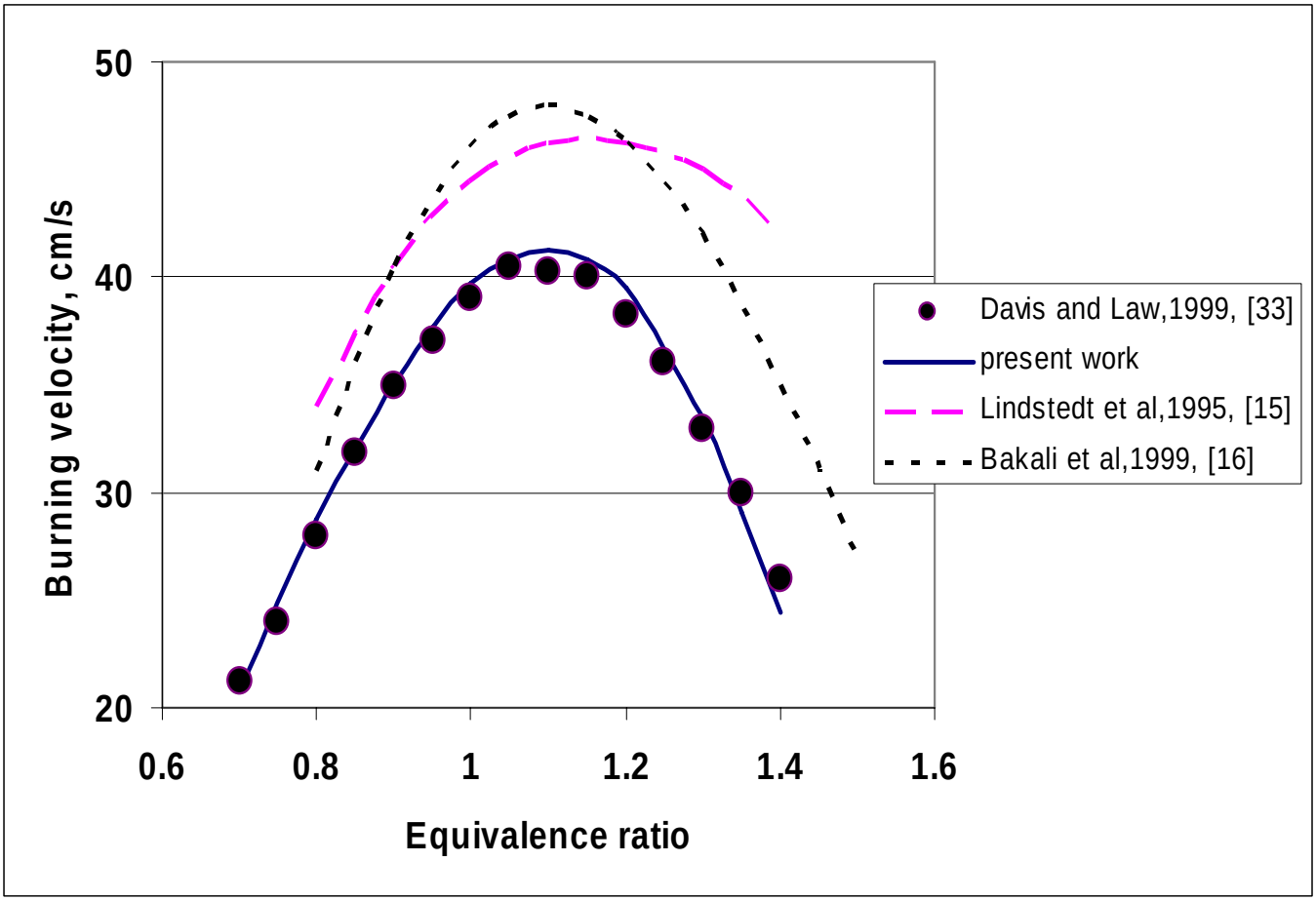
50
40
30
20
Burning velocity, cm/s
0.6
0.8
1
1.2
1.4
1.6
Equivalence ratio
Davis and Law,1999, [33]
present work
Lindstedt et al,1995, [15]
Bakali et al,1999, [16]

Figure 8.

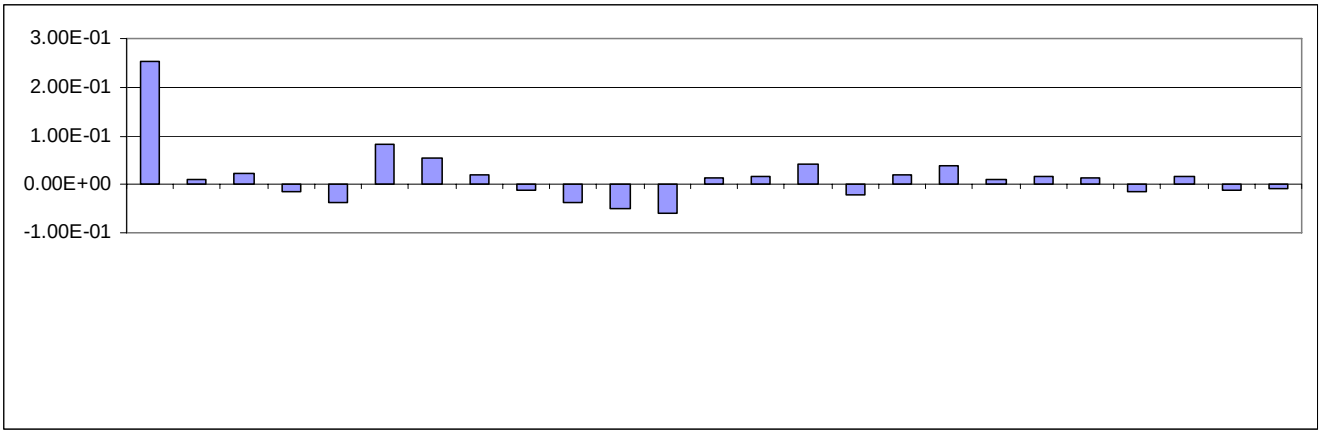

Figure 9

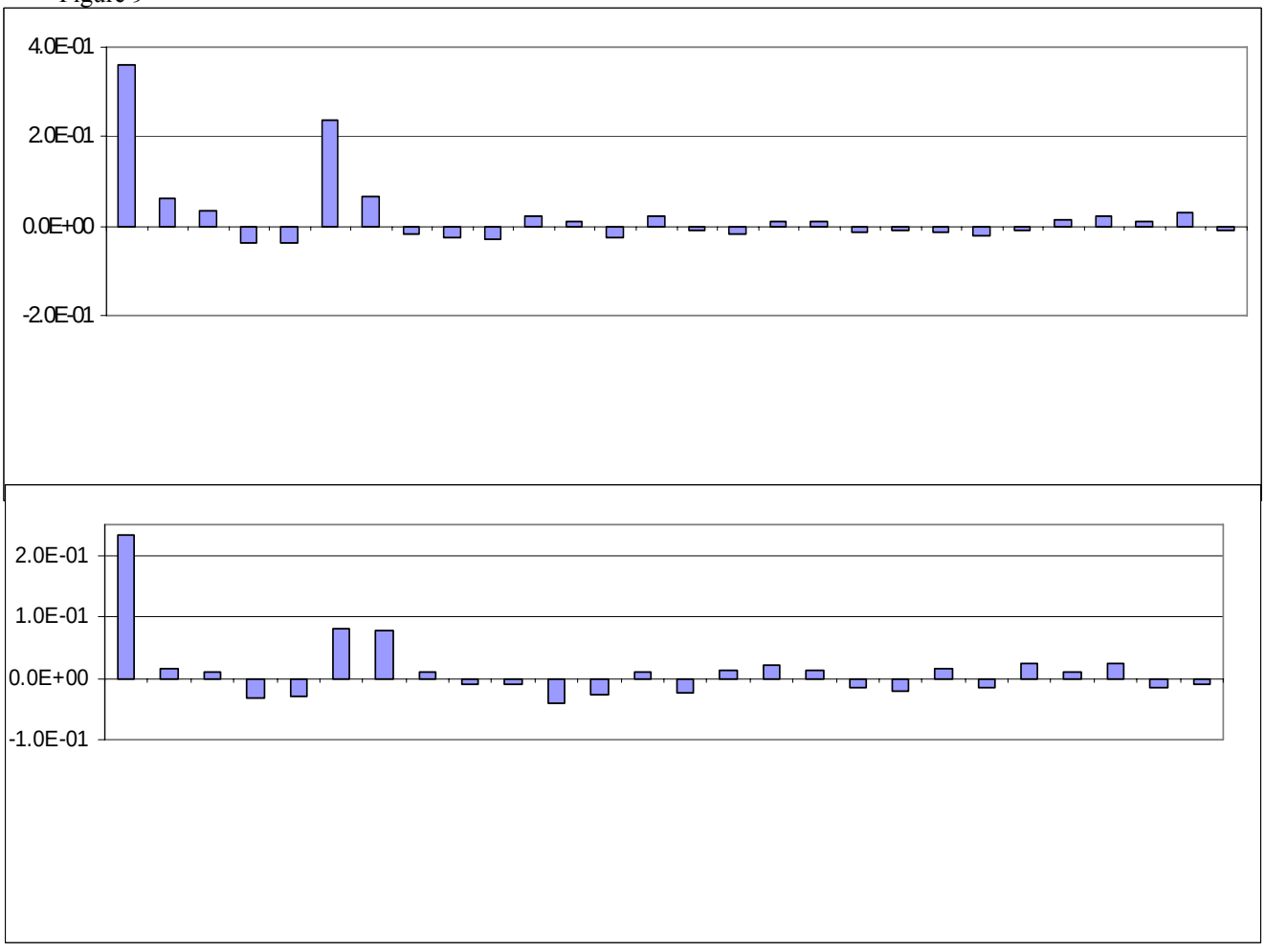

Figure 11.

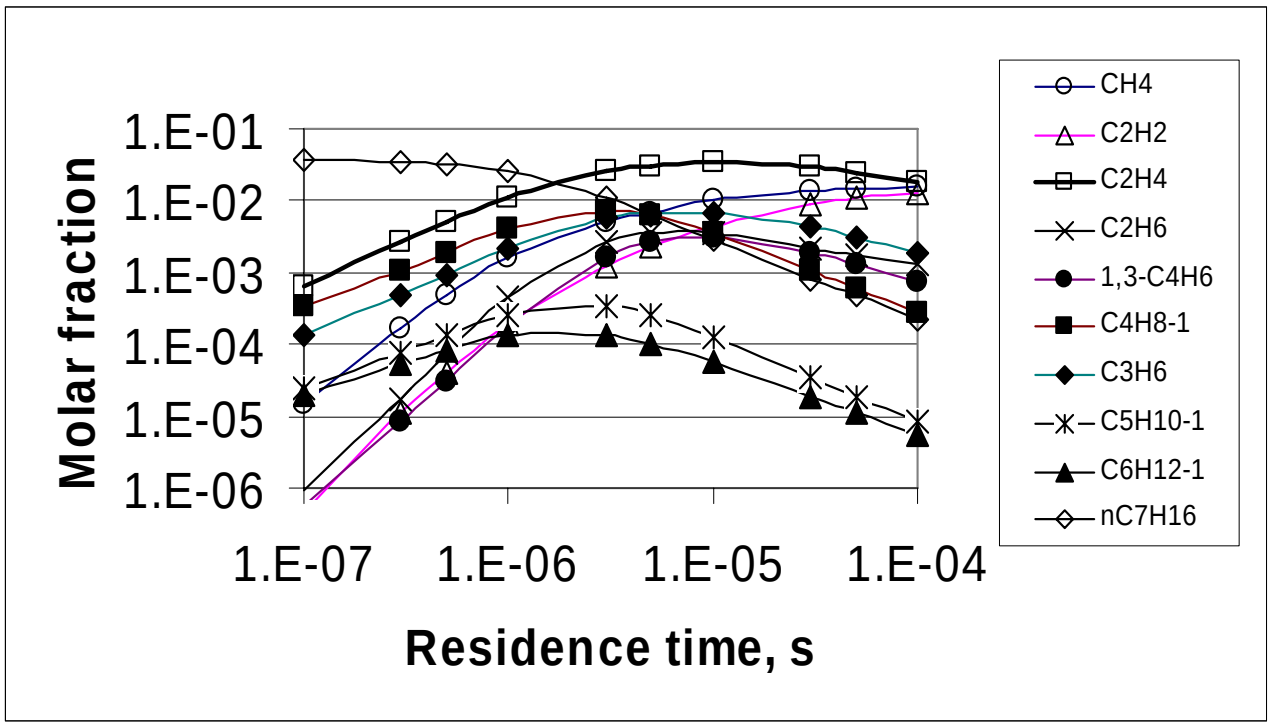

Figure 12

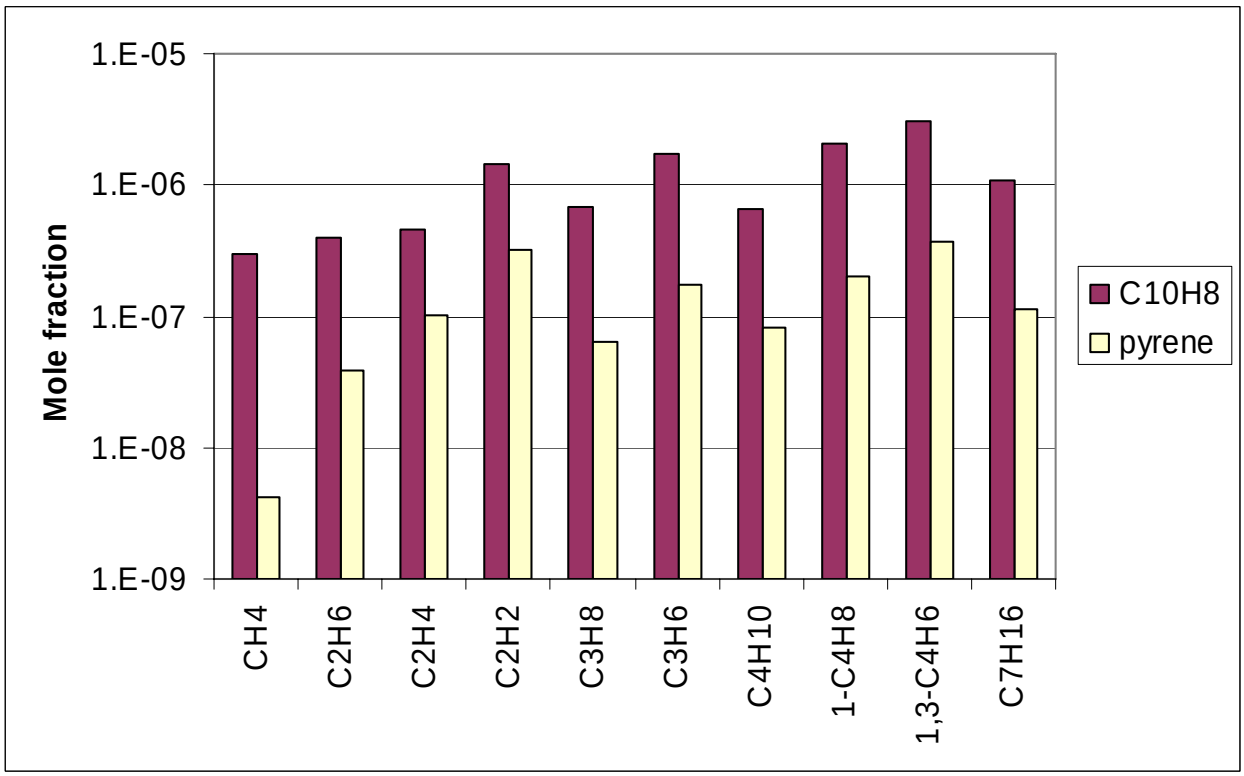

Figure 13

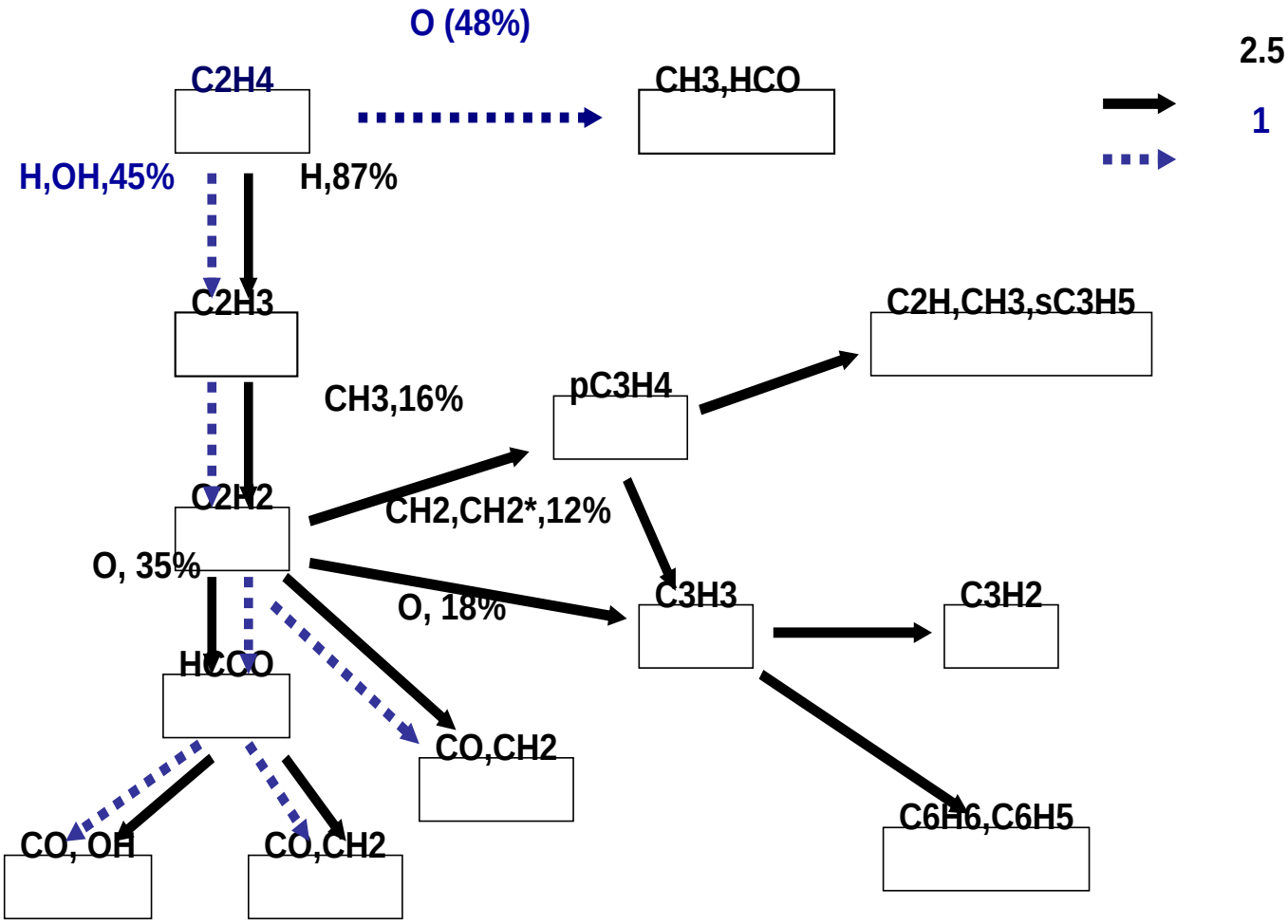
O (48%)
2.5
C2H4
CH3,HCO
1
H,OH,45%
H,87%
C2H3
C2H,CH3,sC3H5
CH3,16%
pC3H4
C2H2
CH2,CH2*,12%
O, 35%
O, 18%
C3H3
C3H2
HCCO
CO,CH2
C6H6,C6H5
CO,OH
CO,CH2

Figure 14

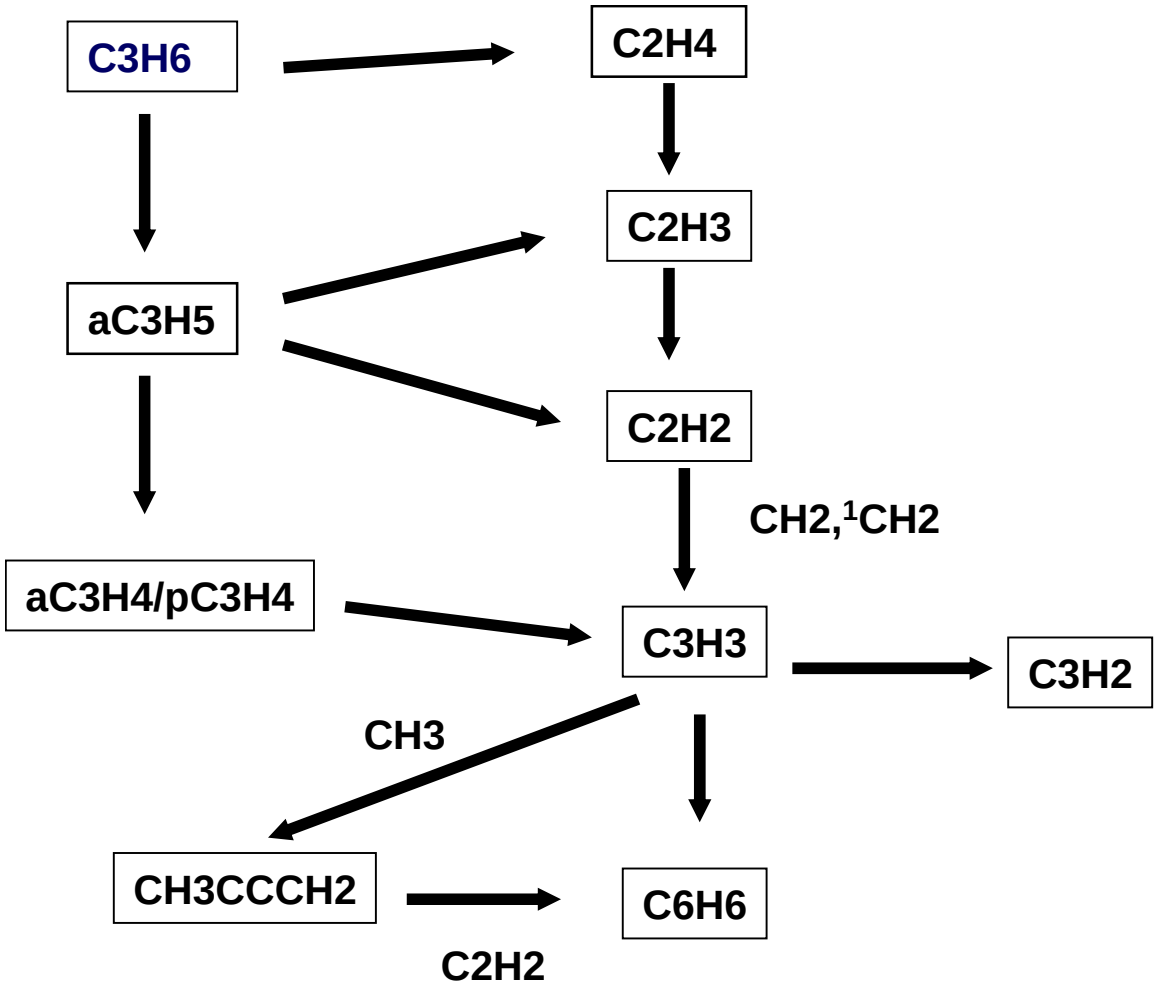
C3H6
C2H4
C2H3
aC3H5
C2H2
CH2,1CH2
aC3H4/pC3H4
C3H3
C3H2
CH3
CH3CCCH2
C6H6
C2H2

Figure 15

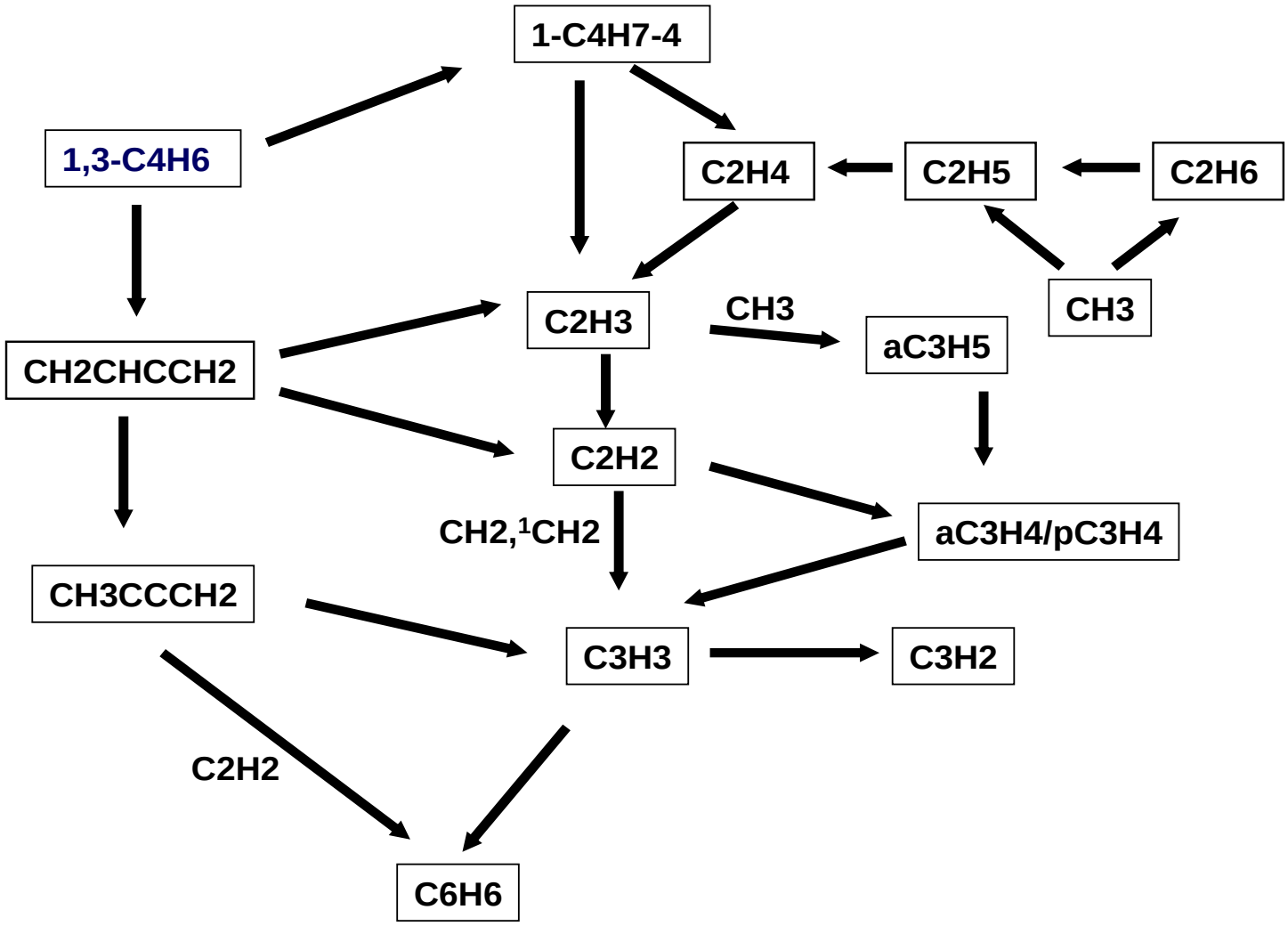
1-C4H7-4
1,3-C4H6
C2H4
C2H5
C2H6
CH3
C2H3
CH3
aC3H5
CH2CHCCH2
C2H2
CH2,1CH2
aC3H4/pC3H4
CH3CCCH2
C3H3
C3H2
C2H2
C6H6

Figure 16

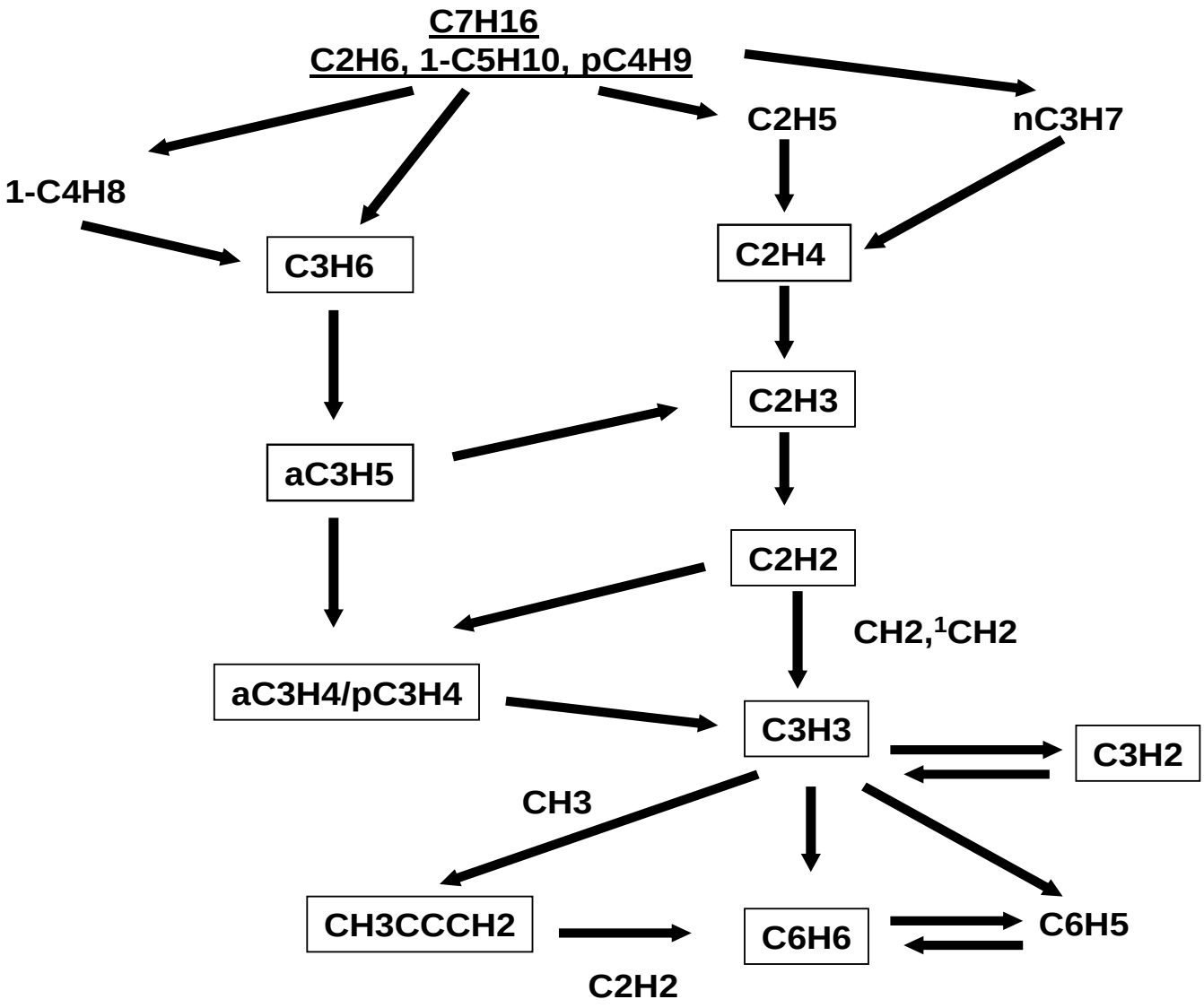
C7H16
C2H6, 1-C5H10, pC4H9
C2H5
nC3H7
1-C4H8
C3H6
C2H4
C2H3
aC3H5
C2H2
CH2,1CH2
aC3H4/pC3H4
C3H3
C3H2
CH3
CH3CCCH2
C6H6
C6H5
C2H2

Figure 17

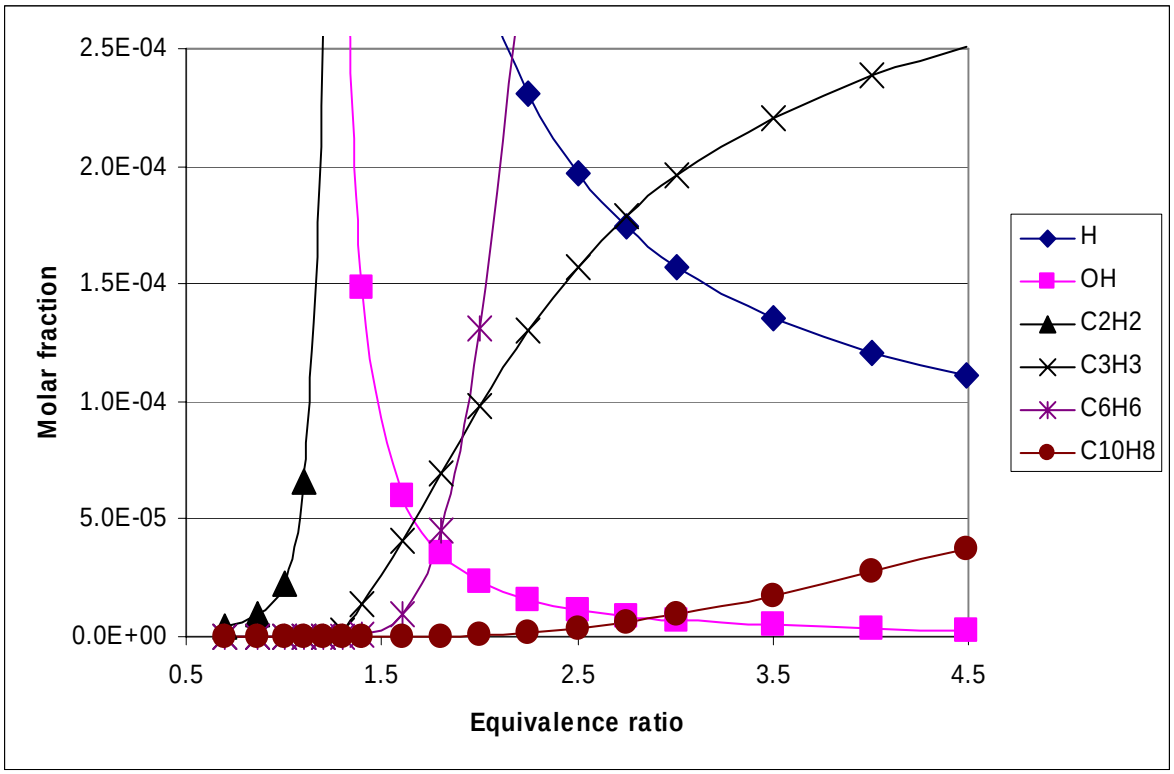

Figure 18.

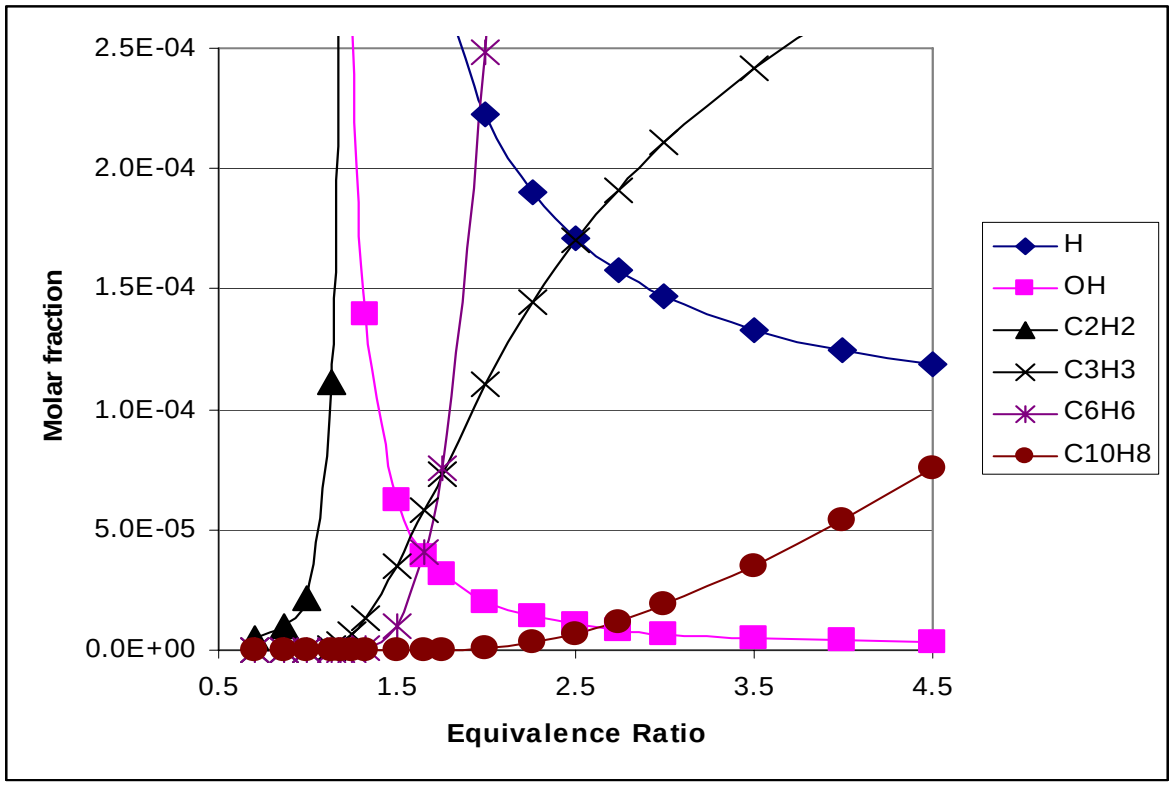

E. Ring Expansion Reactions in the Thermal Decomposition of *t*-Butyl-1,3-Cyclopentadiene

Abstract

The thermal decomposition of *t*-butyl-1,3-cyclopentadiene has been investigated in single pulse shock tube studies at shock pressures of (182 to 260) kPa and temperatures of (996 to 1127) K. Isobutene (2-methylpropene), 1,3-cyclopentadiene, and toluene are observed as the major stable products in the thermolysis of dilute mixtures of the substrate in the presence of a free radical scavenger. Hydrogen atoms were also inferred to be a primary product of the decomposition and could be quantitatively determined on the basis of products derived from the free radical scavenger. Of particular interest is the formation of toluene, which involves the expansion of the ring from a five to a six-membered system. The overall reaction mechanism is suggested to include isomerization of the starting material, a molecular elimination channel, and C–C bond fission reactions, with toluene formation occurring via radical intermediates formed in the latter pathway. These radical intermediates are analogous to those believed to be important in soot formation reactions occurring during combustion. Molecular and thermodynamic properties of key species have been calculated from G3MP2B3 quantum chemistry calculations and are reported. The temperature dependence of the product spectrum has been fit with a detailed chemical kinetic model and best-fit kinetic parameters have been derived using a Nelder-Mead simplex minimization algorithm. Our mechanism and rate constants are consistent with and provide experimental support for the H-atom assisted routes to the conversion of fulvene to benzene that have been proposed in the literature on the basis of theoretical investigations.

Introduction

The formation of soot in combustion processes[1] is typically initiated by the creation of aromatic ring species. Small unsaturated radicals add to the aromatic species to form polycyclic aromatic hydrocarbons (PAH). These PAH compounds act as building blocks for subsequent growth pathways, ultimately leading to particulate soot. An understanding of the early stages in the soot formation process is thus useful for controlling and restricting growth of large particulates in combustion exhaust.

A significant pathway for the formation of aromatic species in pyrolytic environments is via recombination of propargyl (C_3H_3) radicals to form benzene molecules. Recent theoretical studies by Miller and Klippenstein [2,3] have proposed several mechanistic pathways to the formation of benzene. Important among these is the rearrangement of fulvene, formed from propargyl radical recombination reactions, to benzene. In the absence of other radical species, this reaction occurs through multiple pathways, including those involving carbene or tricyclic benzvalene intermediates. Additional pathways for the rearrangement of fulvene to benzene in the presence of H atoms have been proposed by Melius, *et al.[4]* with final energetics determined using bond-additivity corrected fourth-order Moller-Plesset (BAC-MP4) methods. A more detailed computational study, including rates of reaction and evaluation of alternative mechanistic pathways has been performed by Dubnikova and Lifshitz.[5] A simplified mechanism for the formation of benzene from five-membered rings in the presence of H is shown in Figure 1. Addition of H to fulvene or loss of H from one of the methyl-cyclopentadienyl adducts shown in the figure produces resonantly stabilized radicals that rapidly interconvert. Subsequent reaction of the (1,3-cyclopentadienyl)-5-methyl radical (**V** in Figure **1.**) produces benzene + H.

Experimentally, there have been previous attempts to study the ring expansion reactions of methyl-(1,3-cyclopentadiene) (MeCp) at high temperatures. Ikeda, *et al.* examined the pyrolysis of MeCp in a shock tube from (1000 to 2000) K over a pressure range of (7.8 to 78) kPa using laser schlieren techniques to examine the time-dependence of the gas density with time-of-flight mass-spectrometric examination of products from a smaller subset of temperatures and pressures.[6] Qualitative observation of a wide range of aromatic species was observed for shocks of 4.5 % mixtures of MeCp, including benzene, toluene, styrene, indene, methylindene, dihydronaphthalene, napthalene, and several larger species. Notably, the mass balance in that study was poor, which was attributed by those authors to the formation of soot. A later shock-tube study of lower-concentration mixtures was undertaken by Lifshitz and coworkers at temperatures ranging from (1070 to 1270) K in which the product spectrum was examined using gas chromatography with mass spectrometric detection.[7] These studies were performed with 0.3 % mixtures of MeCp, significantly decreasing the extent of bimolecular reactions relative to that in the conditions used by Ikeda, *et al*. As in the previous shock tube study, larger aromatic hydrocarbons were observed, including indene and naphthalene, and a large (105 elementary reactions) mechanism was used to model the pyrolysis. In this model, ring expansion from the five-membered ring system to six-membered was assumed to occur via radical intermediates (Figure 1). The model fit the temperature-dependent data reasonably well, especially for the observed aromatic products.

The previous studies have been complicated by the lack of a clean source of the intermediate believed to be responsible for the ring expansion. In particular, the ring expansion reactions in

the MeCp isomers in these previous experimental studies are likely initiated by bimolecular reactions of the reactant species with H or CH_3 to form RH• (1,3-cyclopentadienyl)-methyl radical isomers (**I**, **II**, and **V** in Figure **1**). The radicals present in these studies undergo numerous reactions in addition to those involving the MeCp species. These chain processes complicate the analysis of the product spectrum and may mask some salient features of the ring-expansion reactions.

In the present study, we examine the thermal decomposition of *t*-butyl cyclopentadiene (TBCP). The unimolecular decomposition of TBCP provides an experimentally convenient means to probe a ring expansion analogous to that shown in Figure 1 by the direct formation of radical s pecies analogous to **I**, **II**, and **V**. The lack of radicals in a system initiated by unimolecular decomposition, especially when radical-radical reactions are inhibited by the presence of a radical scavenger, provides a much clearer window into the ring expansion mechanism for these fulvene systems than the previous studies of MeCp.

TBCP exists as three isomers, which rapidly interconvert via 1,5 sigmatropic shifts of the H atom around the cyclopentadienyl ring as illustrated in Scheme I.

.

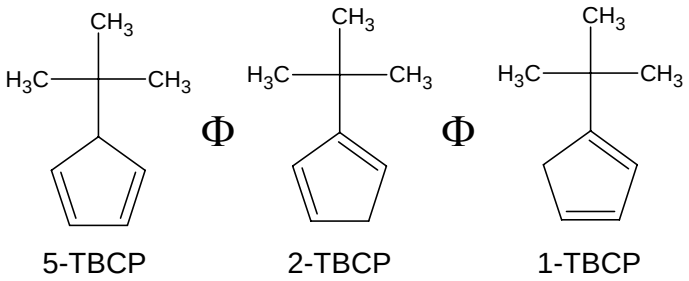

Scheme I. Isomerization of *t*-butyl cyclopentadiene.

In this work, the isomers will be named in terms of the location of the *t*-butyl moiety on the cyclopentadienyl ring as shown in Scheme I. As shown subsequently, thermal decomposition of TBCP in the temperature range 1000 K to 1100 K results in formation of *t*-butyl radicals, cyclopentadienyl radicals, H atoms, methyl radicals, isobutene, cyclopentadiene, and toluene. We propose a reaction mechanism that involves the rapid isomerization of the reactant species and the radical intermediates in the system. Although the complexity, especially with regard to the initial product distribution, precludes a unique quantitative determination of many of the rate parameters, we are able to demonstrate the expansion of a five-membered ring to a six-membered aromatic species in this system. We further establish the plausibility of the proposed mechanism by fitting the temperature dependence of the major product spectrum to a thermodynamically and kinetically self-consistent model that describes the decomposition and ring expansion processes.

Experiment[8]

Experiments were performed in a heated single pulse shock tube, and details of the experimental apparatus and procedures have been given previously.[9,10] Briefly, a shock wave is created in a sample gas mixture by bursting a diaphragm separating a low pressure (20.0 kPa) sample mixture from a higher pressure driver gas (130 kPa to 320 kPa H_2). The shock wave

passes through the sample gas, resulting in a substantial temperature and pressure increase behind the shock front. Subsequent interaction with the rarefaction wave results in cooling of the gas back to the initial temperature. In this apparatus, the heating is equivalent to a 500 μs pulse heater.

Temperatures were determined using an internal standard reaction. The decomposition of *n*-propyl acetate to form propene and acetic acid was used as a reference with an Arrhenius expression[11] $\log k = 12.4 - 24000/T$. Product distributions are determined using gas chromatography coupled with simultaneous flame ionization detection and mass spectrometry (Aglient 6890N, 5873*inert* with capillary splitter).

All studies were performed on dilute mixtures of TBCP, the temperature standard *n*-propyl acetate, and a free radical scavenger (mesitylene), in a bath gas of argon (99.999 %, Praxair). Samples of TBCP (a mixture of isomers) were obtained from Aldrich. Mixtures prepared by direct injection of the unpurified liquid TBCP into the sample bulb were found by GC/MS analysis to contain significant gas-phase concentrations of TBCP dimers. The presence of these species significantly affected product distributions and results from these studies were not used in the analysis. Sample mixtures were instead made by collecting the head gas over cold liquid samples of TBCP that had undergone several freeze-pump-thaw cycles. In this case no dimers were observed in 100 parts per million (ppm) mixtures down to the detection limit of the GC.

To ensure that chain processes did not affect the product distributions, mesitylene (1,3,5-trimethylbenzene, 99 %, Acros Organics) was used as a radical scavenger by addition to the sample mixtures in large excess. Mesitylene reacts with hydrogen atoms to form either (H_2 + 3,5-dimethylbenzyl radicals) or (*m*-xylene + methyl radicals). This latter reaction is the only source of *m*-xylene in this system, providing a means to determine H atom concentrations, using the known[12] ratio of methyl displacement to H abstraction, $k_d/k_a = \exp(-1086/T)$. Methyl radicals may also abstract hydrogen from mesitylene to form (CH_4 + 3,5-dimethylbenzyl radicals). The resonantly stabilized dimethylbenzyl radicals do not undergo significant further reaction during the heating pulse, effectively preventing H and CH_3 radicals from reacting with the reactant or reference species. A summary of the mixtures utilized in the present study is given in Table 1.

Results

Major products observed from the decomposition of the mixture of TBCP isomers were isobutene (2-methylpropene), 1,3-cyclopentadiene, toluene, and H atoms, the last of which was inferred from the formation of *m*-xylene. Additional minor products were observed that are the result of various recombinations involving 3,5-dimethyl-1-benzyl (C_9H_{11}) and cyclopentadienyl (C_5H_5) radicals. Two distinct $C_{10}H_{10}$ isomers were observed, though no definitive structural identification has been made. Also found were a $C_{14}H_{16}$ compound, assigned to the recombination of the dimethylbenzyl and cyclopentadienyl radicals, and a $C_{18}H_{22}$ species from the recombination of the dimethylbenzyl radicals. No naphthalene was observed. Further experiments on the recombination products are underway and will be the subject of a future publication. Presently, we focus on the origins of the isobutene, 1,3-cyclopentadiene, toluene, and H, which are all derived from decomposition of the TBCP isomeric mixture.

Relative concentrations of the reaction products derived from decomposition are shown as a function of temperature in Figure **2**. Circles, triangles, diamonds, and squares represent the

concentrations of isobutene, toluene, 1,3-cyclopentadiene, and *m*-xylene (indicative of H-atoms), respectively. The concentrations of *m*-xylene have been scaled by a factor of 0.5 for separation from the 1,3-cyclopentadiene curves. The closed symbols represent runs using mixture A (Table 1), and open symbols are runs with mixture B. Error bounds were determined by parameterizing measured standard deviations from repeated runs of mixtures containing compounds over a range of different concentrations. The reported error bars represent random errors in the concentration measurements to two standard deviations and do not include possible systematic errors. The lines represent the results of a simultaneous fit using a kinetics model described below. The solid and dashed lines represent fits to data derived from mixtures B and A, respectively. The solid lines thus correspond to fits to the open symbols and the dashed lines to the closed symbols.

The TBCP isomer mixture undergoes several competing reactions at the temperatures of the present study. These will be discussed in turn with an emphasis on the origins of the observed products. A radical product channel, shown in Scheme IIfor the decomposition of 5-TBCP, results in the formation of cyclopentadienyl and *t*-butyl radicals. Under these experimental conditions, the *t*-butyl radical will rapidly decompose to form H and isobutene.[13] Similar cracking of the ring/*t*-butyl bond is expected to occur for 1-TBCP and 2-TBCP, though these reactions are energetically less favorable since they involve fission of a vinylic C–C bond. Our data do not permit us to distinguish the reactive isomer(s) since any vinylic C_5H_5 radicals formed from 1-TBCP and 2-TBCP are expected to rapidly isomerize to cyclopentadienyl radicals. The resonantly stabilized cyclopentadienyl radicals will be generally unreactive toward other molecules in the system, though as discussed above, products of both self-recombination and recombination with 3,5-dimethyl-1-benzyl radicals have been observed. Cyclopentadienyl radicals may also combine with H atoms in the system to form 1,3-cyclopentadiene.

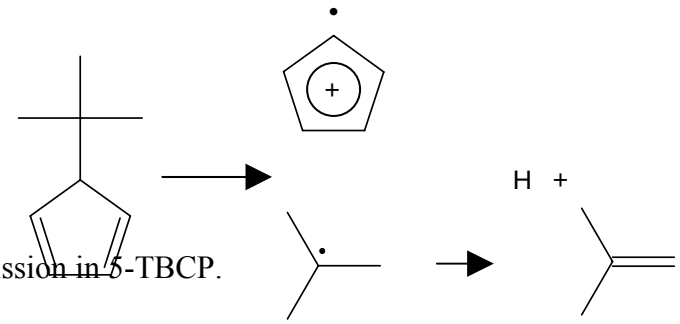

Scheme II. Bond scission in 5-TBCP.

A molecular pathway to isobutene and cyclopentadiene is also present and occurs via a retro-ene reaction as shown in Scheme III. Unlike the bond scission, this reaction does not occur in 1-TBCP or 2-TBCP because no six-membered transition state for the hydrogen atom transfer is present.

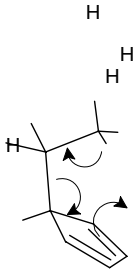

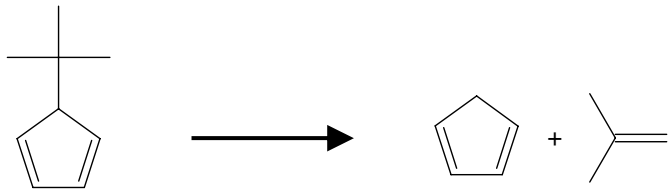

Scheme III. Retro-ene reaction in 5-TBCP.

While Scheme II and Scheme III provide the origins of the 1,3-cyclopentadiene, isobutene, and H-atom products, the ring expansion reactions that result in the formation of toluene are more complex. The proposed mechanism for the ring expansion closely follows that proposed by Melius, *et al.* for the H-assisted rearrangement of fulvene to benzene. As shown in Scheme IV, the initial step in the ring expansion mechanism is suggested to be CH_3 bond fission in 1-TBCP and 2-TBCP to form resonantly-stabilized radicals, identified as isopropyl-1-Cp and isopropyl-2-Cp radicals for the remainder of this paper. Facile H migration in the Cp ring leads to formation of all three possible isopropyl-Cp isomers, including isopropyl-5-Cp. This latter species is proposed to be the key intermediate in the ring expansion. Note that 1-TBCP and 2-TBCP are the primary sources of isopropyl-Cp radicals, since methyl loss in 5-TBCP does not lead to a resonantly stabilized product and is therefore a much higher energy process. The energetics of these processes and resulting distributions are further discussed below.

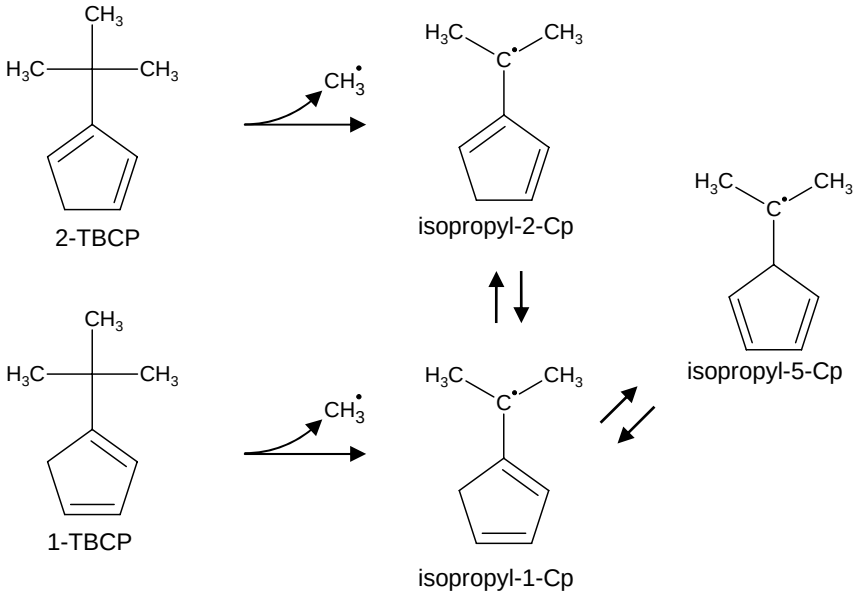

Scheme IV. CH_3-loss channels and subsequent isomerization of 1-TBCP and 2-TBCP.

While isopropyl-1-Cp and isopropyl-2-Cp radicals are more stable than isopropyl-5-Cp, the former have no obvious pathways to major product formation while the latter undergoes a further fast reaction (see Scheme V). The bicyclic cyclopropyl structure proposed therein is formed by an internal radical addition to one of the double bonds and is similar to that postulated by Melius, *et al. [4]* in the decomposition of the analogous (1,3-cyclopentadienyl)-5-methyl radical.

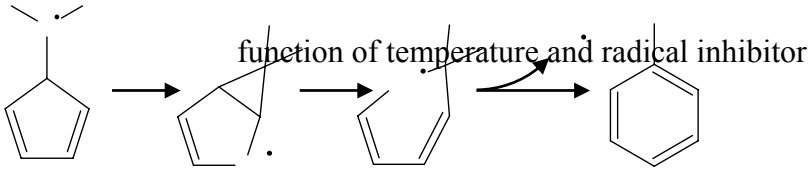

Scheme V. Ring expansion of isopropyl-5-Cp radical.

The isopropyl-1-Cp and isopropyl-2-Cp radicals may undergo additional H-loss reactions to form conjugated trienes (Scheme VI. These species may subsequently rearrange to form dimethylfulvene and *o*-xylene from isopropyl-1Cp and isopropyl-2Cp radicals, respectively. Minor quantities (less than 2 % of reaction) of both products were observed.

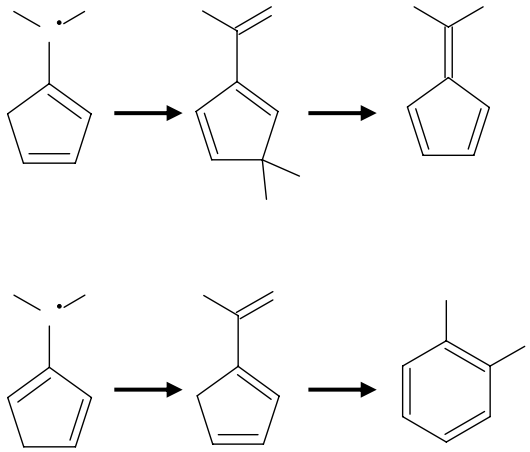

Scheme VI. Alkene formation and subsequent rearrangement from isopropyl-1Cp and isopropyl-2Cp radicals.

Discussion

The plausibility of the above mechanism was evaluated by fitting the measured product spectra using a kinetics model that includes all of the reactions presented in Schemes I–VI. The reactions of primary interest are those that result in the formation of the products with concentrations shown in Figure 2. Additional bimolecular reactions were included to account for reactions of the radical scavenger as well as that of cyclopentadienyl radicals with H. Tables and 2 and 3 show the reactions used in the kinetics model. Due to the large number of isomers of both the reactants and the reactive intermediates expected in this system, we have employed a series of constraints to the rate constants in the kinetics model, and the implications and validity of these constraints are discussed below.

The set of differential equations resulting from this kinetics model was solved using the ODEPACK suite of differential equation solvers implemented through a Python interface.[14,15] Product concentrations for all of the major products (those shown in Figure **2**) were calculated as a

function of temperature and radical inhibitor concentration and compared to the data. A Nelder-Mead simplex algorithm**[16]** was utilized to determine the best-fit parameters, which are shown in Table 3. The figure of merit in the simplex minimization was the sum of the χ^2 values of the fits relative to the four major product channels and both mesitylene concentrations as shown in Table **3**. This provides for a simultaneous fit to all available data and should result in a robust means for determining appropriate Arrhenius parameters for the relevant reactions in the present system.

Rate constants that were not permitted to vary during the fitting procedure are shown in Table 2. These reactions were chosen to remain nonvarying either because they had well-established rate parameters or the model required only that they be fast on the reaction timescale. Parameters for the decomposition of *t*-butyl radical to form isobutene and H were taken from the literature review of Tsang. The decomposition of *t*-butyl radical to form propene and methyl radical was previously found to represent a ≈3 % channel in our temperature range.[17] The ratio of propene to isobutene derived from the decomposition of *t*-butyl radicals, $k_{C_3H_6}/k_{i-C_4H_8}$, was presented in [18]relative to the rate of decomposition of cyclohexene to form ethene and 1,3-butadiene. We have renormalized this ratio to thecurrently recommended Arrhenius expression for the decomposition of cyclohexene to provide the following expression for the ratio of propene to isobutene:

$$k_{C_3H_6}/k_{i-C_4H_8} = 0.120\exp(-1535/T).$$

The reactions of H with mesitylene, including the displacement of methyl radicals from the ring and the abstraction of H from a terminal methyl group have been studied previously in this laboratory. The reaction of H with cyclopentadienyl radical was recently studied at (1150 to 1500) K using the shock tube/atomic atomic resonance absorption spectroscopy technique and found to have a rate constant of 4.32×10^{-10} cm^3 molecule^{-1} s^{-1} independent of temperature.[18] We have chosen to use this rate constant in the present work without change. The isomerization reactions of the reactant TBCP isomers (1–4 in Table 2),are required only to be fast and consistent with the relative thermodynamics of these species. They are discussed more fully the following section. The rate constant for the reaction isopropyl-5-Cp → toluene + CH_3 will be justified subsequently, but has no effect on the results as long as it is fast.

Arrhenius parameters for the reactions shown in Table 3 were allowed to vary in the simplex minimization. Initial guesses were typically derived from thermodynamics of similar reactions that had well-established rate parameters. Constraints to the variable Arrhenius parameters have been implemented and are utilized to describe isomerization reactions and reactions in which similar isomeric reactants and products are involved. These constraints are shown as parenthetical entries in the table. Since these similar isomers ultimately produce a small number of major products, we have elected to constrain these fits in order to evaluate the overall plausiblity of the mechanism rather than allow them to vary in an attempt to determine quantitative rate parameters.

Isomerization Reactions

The isomerization reactions of both the reactant 1-TBCP, 2-TBCP, and 5-TBCP molecules and the intermediate isopropyl-1Cp, -2Cp, -5Cp radicals have a significant effect on the final product distributions. We have elected to treat the reactant species differently from the radical intermediates in the kinetic model. As discussed and justified below, the reactant species are assumed to be in equilibrium throughout the reaction, and *ab initio* thermodynamics calculations were used to determine the equilibrium reactant concentrations. For the intermediate radical species the equilibrium assumption is not valid according to our model, and these Arrhenius parameters are allowed to vary in the minimization procedure subject to constraints detailed below.

Reactant Isomers. Isomerization of the reactant isomers is assumed to be fast on the timescale of the experiment, meaning that the distributions are thermodynamically controlled throughout the reaction. While isomerization of TBCP has not been studied to our knowledge, several experimental and theoretical studies on close analogues of the reactant molecules have been reported. The isomerization of 5-H-perdeutero-1,3-cyclopentadiene was found by nuclear magnetic resonance (NMR) spectroscopy to have an Arrhenius expression[19]

$$k = 1.3\times10^{12}\exp\left[(-102\pm2)\ \text{kJ mol}^{-1}/RT\right]\ \text{s}^{-1}$$

in the temperature range (318 to 338) K in CCl_4. In that study, the isomerization rate was found to be a factor of 0.32 lower in the gas phase at 323 K. Extrapolation to the reaction temperatures utilized in this study, while not expected to provide a quantitatively accurate rate constant, can provide some insight into the relevant isomerization rates. At 1000 K, the rate of isomerization is calculated to be $6.1 \times 10^6\ \text{s}^{-1}$, entailing a half-life of 0.11 μs. Similar NMR studies by McLean and Haynes of the isomerization of 5-methyl-1,3-cyclopentadiene both neat and in CCl_4 solutions yielded the following Arrhenius expression in the temperature range (278 to 313) K:[20]

$$k = 2.9\times10^{11}\exp\left[(-85.4\pm1.2)\ \text{kJ mol}^{-1}/RT\right]\ \text{s}^{-1}.$$

Extrapolation to 1000 K yields a reaction rate of $1.0 \times 10^7\ \text{s}^{-1}$. In addition, Bachrach has calculated *ab initio* potential energy surfaces for the [1,5] sigmatropic hydrogen shift in 1,3-cyclopentadiene.[21] The barrier to rearrangement was found to be 110 kJ mol^{-1} at the MP2/6-31G*//HF/6-31G* level of theory. Melius, *et al.* have calculated isomerization barriers for all of the methyl cyclopentadiene isomers using a bond-additivity corrected MP4 (BAC-MP4) method and found they ranged from (115 to 130) kJ mol^{-1}. However, those authors noted that the BAC-MP4 calculated [1,5] sigmatropic H-shift isomerization barriers in various cyclopentadienyl derivatives overestimate experimental values by (18 to 25) kJ mol^{-1}. All of the above data are consistent with our assumption that isomerization of TBCP is fast relative to the 500 μs timescale of the shock pulse. We have arbitrarily chosen to use the following rate expression for both the 5$\rightarrow$1 and

1$\rightarrow$2 (exothermic) isomerizations:

$$= 2.0\times10^{11}\exp(-85.4\ \text{kJ mol}^{-1}/RT)\ \text{s}^{-1}.$$

The reverse reaction rate expressions were derived from calculations of thermodynamic parameters as discussed below.

Thermodynamic properties of 1-, 2-, and 5-TBCP. To our knowledge, the thermodynamic properties of the TBCP isomers have not been experimentally determined. We have derived these from G3MP2B3 quantum chemistry calculations[22] and checked our computational method by comparing the results of analogous calculations on the methylcyclopentadienes, for

which experimental data are available. Calculations were performed on the Biowulf PC/Linux cluster at the National Institutes of Health in Bethesda, MD and a Pentium 4 PC at NIST using the Gaussian 03 software package.[23] G3MP2B3 calculations were performed on the ground states of 1-TBCP, 2-TBCP, and 5-TBCP molecules. Thermodynamic functions were derived with the NIST ChemRate program.[24,25] Over our experimental temperature range the relative entropies and enthalpies are essentially linear with respect to temperature. Hence the equilibrium constants can be represented as ratios of simple Arrhenius rate expressions for the forward and reverse reactions. Appropriate ratios of *A*-factors and differences in activation energies for the forward and backward isomerization reactions were derived for 1050 K, the approximate midpoint temperature of our studies. The resulting parameters are shown as parenthetical expressions in Table 3. The frequencies and rotors used to derive the entropies and enthalpies used in the calculation of the *A*-factor ratios and activation energy differences are shown in Table 4. Tables of temperature-dependent thermodynamic parameters for all species for which G3MP2B3 thermodynamics were calculated are provided as supplementary data. The calculated G3MP2B3 thermodynamic parameters and relative equilibrium concentrations are shown in Table 5 for the reactant species at 1050 K.

To evaluate the validity of the G3MP2B3 computational method to the present system, we have additionally calculated thermodynamic parameters of the 1-, 2-, and 5-methyl-1,3-cyclopentadiene (MeCp) molecules, for which experimental equilibrium data are available. These parameters were then used to calculate the expected equilibrium distribution of isomers as a function of temperature. At 239 K, McLean and Haynes found an equilibrium distribution of 0.80:1:0.02 for the 1:2:5 isomers of MeCp in liquid ammonia.[20]Calculation of the gas-phase equilibrium distribution from the G3MP2B3 thermodynamics at this temperature yields 0.50:1:0.0008 for 1:2:5 isomers. Additional equilibrium experiments by McLean and Haynes [20] yielded 0.82:1 and 0.86:1 for the ratio of the 1:2 MeCp isomers in various solvents at room temperature. The calculated G3MP2B3 gas-phase ratio for room temperature equilibrium is 0.59:1. The calculated values show good qualitative agreement with the experimental values, and the differences may likely be attributed to both solvent effects and experimental error. In particular, the relatively large differences between the calculated and measured equilibrium concentrations of 5-MeCp (0.0008 vs 0.02, respectively) may be due to a small amount of unreacted material present in the solution study, since 5-MeCp was used as a reactant.

Previous theoretical studies have also evaluated the relative energies of the MeCp isomers. Melius, *et al.* found 0:0:9 kJ mol^{-1} for the relative enthalpies of the 1:2:5 MeCp isomers at the BAC-MP4 level. [4] Dubnikova and Lifshitz calculated 0.9:0:12.8 kJ mol^{-1} for the relative energies of 1:2:5 MeCp at the QCISD(T)/cc-pVDZ//B3LYP/cc-pVDZ level of theory. Though these calculated values are not enthalpies, corrections to the relative heats of formation are expected to be no larger than 1 kJ mol^{-1}. Relative thermodynamics from G3MP2B3 calculations may be found in Table 5. The relative enthalpies at 298 K were found to be 1.3:0:13.5 kJ mol^{-1} for 1:2:5 MeCp. The good agreement between the calculated G3MP2B3 parameters and the previous experimental and theoretical work gives us confidence that the quantum chemistry calculations on the reactant TBCP isomers will provide reasonable thermodynamic parameters for the calculation of the equilibrium distributions.

Intermediate Radical Isomers. Unlike the closed-shell reactant species, the isomerization of the radical isomers isopropyl-1Cp, -2Cp, and -5Cp may not be treated as a simple equilibrium problem. The enthalpies of formation of the three isomers differ markedly because of allylic resonance stabilization in both the -1Cp and -2Cp isomers that is not present in the -5Cp isomer. This large difference in stabilization implies that an *a priori* assumption that the isomers are in equilibrium is inappropriate. Dubnikova and Lifshitz calculated rate expressions for isomerization from the QCISD(T) thermochemistry. The calculated Arrhenius expression for the exoergic isomerization of the 2-(1,3-cyclopentadienyl)-methyl radical to the 1-(1,3-cyclopentadienyl)-methyl radical is

$$k_\infty = 3.7\times10^{13}\exp\left[-131.8\ \text{kJ mol}^{-1}/RT\right]\ \text{s}^{-1},$$

which corresponds to a reaction rate of $1.0 \times 10^7\ \text{s}^{-1}$ at 1050 K. This is similar to the isomerization rates observed for the reactants and is fast on the timescale of reaction in the present system. However, due to the large differences in relative stabilities expected for these radicals, the reverse isomerization reactions are likely comparable to the reaction timescale and the Arrhenius parameters for these reactions are explicitly allowed to vary in the present system (Table 3).

As in the case of the reactant molecules, we have fixed the ratios of the *A*-factors and differences in the activation energies for the forward and reverse reactions. We have attempted to utilize G3MP2B3 calculations to obtain the thermodynamics of the radical intermediates to use as constraints. The results are shown in Table 5. The allylic stabilization in isopropyl-2Cp was found to provide 59.7 kJ mol^{-1} of resonance energy, and the additional conjugation via the cyclopentadienyl ring in isopropyl-1Cp provides another 21.9 kJ mol^{-1} stabilization. These may be compared to previous calculations of the radical energetics in MeCp. Dubnikova and Lifshitz have performed quantum chemistry calculations on 1:2:5-(1,3-cyclopentadienyl)methyl radicals at the QCISD(T)/cc-pVdz//B3LYP/cc-pVdz level of theory. As expected, the 1-(1,3-cyclopentadienyl)methyl radical isomer (analogous to isopropyl-1Cp) was most stable followed by the 2-(1,3-cyclopentadienyl)methyl radical. The 5-(1,3-cyclopentadienyl)methyl radical is the highest energy isomer with no allylic stabilization of the radical. Those authors calculated relative energies for the 1:2:5-(1,3-cyclopentadienyl)-methyl radicals to be 0:21.1:85.6 kJ mol^{-1}. Melius, *et al.* have also performed quantum chemistry calculations the methyl cyclopentadiene radical intermediates [4] and found relative enthalpies (298 K) of 0:27:114 kJ mol^{-1} for the 1:2:5-(1,3-cyclopentadienyl)methyl radical intermediates. The present G3MP2B3 calculated enthalpies of 0:21.9:81.6 kJ mol^{-1} for the 1:2:5 isomers of isopropyl-*n*Cp are similar to the QCISD(T) calculations of Dubnikova and Lifshitz for the (1,3-cyclopentadienyl)methyl radical species.

Based on these computational results, we have attempted to fix the relative differences in activation energies to the calculated G3MP2B3 enthalpy values at 1050 K. Similarly, we have fixed the ratios of Arrhenius *A*-factors for the radical isomerization reactions to correspond to the calculated values of the reaction entropy change at 1050 K. The Arrhenius parameters for the energetically uphill reactions (i.e. isopropyl-1Cp→isopropyl-5Cp and isopropyl-1Cp→isopropyl-2Cp) were then allowed to vary during the simplex minimization. When the G3MP2B3 values were used to generate the *A*-factor and activation energy constraints, the model was unable to reproduce the measured toluene concentrations for any reasonable values of the remaining Arrhenius parameters. Therefore, we have assumed that the G3MP2B3 calculations have overestimated the relative enthalpies for the radical isomer species. We have

instead elected to use an approximate value of 46.1 kJ mol^{-1} for the resonance energy of the allylic radical moiety in the isopropyl-1Cp and isopropyl-2Cp isomers. This energy should represent a good estimate of the relative energy difference between the isopropyl-2Cp and isopropyl-5Cp isomers. The additional resonance energy gained from the addition of a second conjugated double bond in the cyclopentadienyl ring, as is found in isopropyl-1Cp but is absent in isopropyl-2Cp, was assumed to be approximately 16.7 kJ mol^{-1}. The relative enthalpies of the isopropyl-*n*Cp radical isomers were thus chosen to be 1:2:5 = 0:16.7:62.8 kJ mol^{-1}. Using these values, we obtained a good fit to all of the measured concentrations; the final values for the varied Arrhenius parameters are shown in Table 3.

Other Reactions

In the decomposition of the methyl-1,3-cyclopentadiene molecules, Dubnikova and Lifshitz proposed pathways for "direct" ring expansion from (1,3-cyclopentadienyl)-1-methyl and (1,3-cyclopentadienyl)-2-methyl radicals to cyclohexadienyl radical. One set of pathways involves a carbene intermediate, while the other set undergoes ring-opening of the cyclopentadienyl ring. These two pathways were calculated to proceed in parallel. However, in their study, the calculated overall rate of the "direct" expansion of these two isomers, despite the vastly larger concentrations of the 1 and 2 isomers than that of the 5 isomer, was dwarfed by the calculated rate of ring-opening via the (1,3-cyclopentadienyl)-5-methyl radical. In the TBCP system, the analogous reactions would be of the isopropyl-1Cp and isopropyl-2Cp radicals forming toluene and methyl radicals directly. We attempted to incorporate these reactions into the model by providing a direct pathway for the formation of toluene from isopropyl-1Cp. However, irrespective of the initial guess, the Arrhenius parameters in the simplex minimization consistently produced negligible reaction rates, suggesting that these pathways are unimportant. This is indicated in Table 3 by an asterisked entry.

The molecular elimination channel for the TBCP-5 isomer (Scheme III) occurs via a retro-ene reaction involving the transfer of a terminal methyl H-atom to the cyclopentadienyl moiety.

The simplex minimization resulted in a rate expression of

$$k = 1.54\times10^{13}\exp\left(-194.7\text{ kJ mol}^{-1}/RT\right)\text{ s}^{-1}$$

for this reaction. The activation energy of 194.7 kJ mol^{-1} is lower than that typically observed for hydrocarbon systems.[26] The presently reported activation energy compares favorably to that in the decomposition of 1,6-heptadiene reported initially by Eggers and Vitin[27] and extended to a wider temperature range by King.[28] The measured Arrhenius expression in the decomposition of 1,6-heptadiene was found to be

$$k = 2.0\times10^{11}\exp\left(-197\text{ kJ mol}^{-1}/RT\right)\text{ s}^{-1}.$$

As noted by Eggers and Vitin, resonance stabilization of the forming double bond within the cyclic six-membered transition state caused a decreased activation energy relative to that in 1-heptene. Similarly, in the present system, the double bond in the cyclopentadienyl moiety that is not directly participating in the reaction resonantly stabilizes the forming double bond in the transition state. As expected, the activation energy for the retro-ene reaction in 5-TBCP is similar to that for 1,6-heptadiene. The *A*-factor is also higher for the retro-ene decomposition of 5-TBCP than in typical hydrocarbon retro-ene reactions.[27]This difference is due to the presence of nine labile hydrogen atoms in the *t*-butyl moiety that react with two equivalent double bonds in the cyclopentadienyl ring.

The H loss reactions shown in Scheme IV are relatively minor channels, and no attempt to fit the final products was made. However, because these reactions have the effect of removing isopropyl-1Cp and isopropyl-2Cp from the system, we have modeled the H-loss reactions from both species. The Arrhenius parameters from the reaction of isopropyl-1Cp were allowed to float, and those of the isopropyl-2Cp H-loss channel were fixed relative it based on G3MP2B3 calculations as described above. These values are shown in Table 4.

Application to Fulvene Systems

While the present system is not expected to play a role in the sooting or PAH-forming reactions in the combustion of typical hydrocarbon fuels, it provides an experimentally convenient means to probe radical assisted ring-expansion reactions that likely play a role in such systems. The mechanism proposed in Schemes I-IVis analogous to that initially proposed by Melius, *et al*. for the H-assisted ring expansion of fulvene to benzene.[4] In that mechanism, H adds to fulvene, producing 1-, 2-, and 5-(1,3-cyclopentadienyl)methyl radicals, which are analogous to the isopropyl-(1,2, and 5)-Cp radicals. As is the case with isopropyl-5Cp, the 5-(1,3-cyclopentadienyl) methyl radicals are significantly higher energy; however, ring expansion occurs only from that isomer. The ring expansion from the 5-(1,3-cyclopentadienyl)methyl radical has been predicted to occur analogously to the reaction shown in Scheme V, where the radical site reacts with one of the double bonds in the cyclopentadienyl ring, forming a three-centered intermediate species. The expansion of the five-membered ring then occurs by the opening of the three-centered moiety, followed by subsequent ejection of an H atom to form benzene.

While the energetics of the reactions in the fulvene+H system differ from the present system (which is equivalent to a dimethylfulvene+H reaction), the general features of the mechanism appear to be identical. As illustrated in Figure **3**, the formation of the six-membered product in the fulvene+H reaction is rate-limited by the formation of the 5-(1,3-cyclopentadienyl)methyl radical. Melius, *et al.* calculated a barrier to isomerization of the 1→5 isomers of (1,3-cyclopentadienyl)methyl radicals of 179 kJ mol^{-1}, and Dubnikova and Lifshitz found an activation energy from QCISD(T)/cc-pVdz calculations of 176 kJ mol^{-1} for the same reaction. A value of 148 kJ mol^{-1} for the activation energy of the isopropyl-1Cp → isopropyl-5Cp reaction was found to provide a good to fit to our experimental product distributions. The predicted activation barriers for the two reactions are similar, and it is expected that the ring expansions occur along these similar pathways. In addition, Dubnikova and Lifshitz calculated Arrhenius parameters for the 5-(1,3-cyclopentadienyl)methyl radical conversion to cyclohexadienyl radical and found that the *A*-factor was 1.4×10^{13} s^{-1} and the activation energy was 72.8 kJ mol^{-1}. At 1050 K, this yields a rate constant of 3.3×10^{9} s^{-1}, which is substantially faster than the calculated 1→5 isomerization rate constant in the (1,3-cyclopentadienyl)methyl species of 1.3×10^{5} s^{-1} at the same temperature. The present mechanism includes this assumption and is consistent with the measured data. We conclude that the rate-limiting step in the H-assisted expansion of fulvene to benzene is the isomerization to form 5-(1,3-cyclopentadienyl)methyl radicals.

Conclusion

Overall, the proposed mechanism for the decomposition of the isomers of *t*-butyl cyclopentadiene is consistent with that proposed by Melius, *et al.* for the H-assisted ring opening reactions of fulvene. Previous studies of the pyrolysis of methyl-(1,3-cyclopentadienes) have been hampered by the requirement that large radical concentrations be present to allow bimolecular initiation of the ring expansion reactions.In the present study, the use of *t*-butyl-(1,3-cyclopentadiene) in lieu of methyl-(1,3-cyclopentadiene) produced radicals similar to those found in the H+fulvene ring-opening reactions (namely the isopropyl-*n*Cp) without the need for bimolecular reactions. The use of a radical scavenger served both to eliminate chain process interference as well as providing a means to further probe the mechanism by monitoring H-atom concentrations. We have observed the expansion of the five-membered rings system to a six membered aromatic ring system in a shock tube in the temperature range (1000 to 1100) K. We find that the ring expansion reactions are rate-limited by the formation of isopropyl-5Cp radicals, which subsequently undergo rapid ring expansion followed by loss of methyl radical to form toluene. This mechanism is fully consistent with previously proposed mechanisms for the H+fulvene reaction, in which the isomerization to form 5-(1,3-cyclopentadienyl)methyl radicals is the rate-limiting step in the formation of the six-membered ring.

Supplementary Information

Results of the G3MP2B3 calculations, calculated thermochemical tables for the species shown in Table 5, and measured product concentrations as a function of temperature are provided as supplementary material.

Tables

Table 1. Sample mixtures used in the present study.

Identifier	Component	Concentration	Units[a]
A	TBCP isomers	100	ppm
	propyl acetate	100	ppm
	mesitylene	0.44	%
B	TBCP isomers	100	ppm
	Propyl acetate	100	ppm
	Mesitylene	1.10	%

[a]ppm = parts per million, mole %.

Table 2. Arrhenius parameters used in fitting procedure for reactions which were not allowed to vary. Values were taken from the literature or are justified in the text.

No.	Reaction	A^a	E_a (kJ mol^{-1})	Ref.
1	TBCP-1 → TBCP-5	1.68×10^{12}	97.4	This work
2	TBCP-5 → TBCP-1	2.00×10^{12}	85.4	This work
3	TBCP-2 → TBCP-1	1.03×10^{12}	86.5	This work
4	TBCP-1 → TBCP-2	2.00×10^{12}	85.4	This work
5	isopropyl-5-Cp → toluene + CH_3	8.30×10^{13}	159.6	This work
6	*t*-butyl → isobutene + H	2.00×10^{13}	62.8	This work
7	*t*-butyl → propene + CH_3	9.96×10^{12}	172.4	
8	H + mesitylene → 3,5-dimethyl-1-benzyl + H_2	6.56×10^{-10} *b*	36.1	
9	H + mesitylene → *m*-xylene + CH_3	1.11×10^{-10} *b*	27.1	
10	H + *c*-C_5H_5 → *c*-C_5H_6	4.32×10^{-10} *b*	0.0	

Table 3. Best-fit Arrhenius parameters for reactions allowed to vary in fitting procedure.

No.	Reaction	A (s^{-1})	E_a (kJ mol^{-1})
11	TBCP-5 → *c*-C_5H_6 + isobutene	1.54×10^{13}	194.7
12	TBCP-5 → *c*-C_5H_5 + *t*-butyl	6.40×10^{15}	243.3
13	TBCP-2 → isopropyl-2Cp + CH_3	1.93×10^{15}	252.5
14	TBCP-1 → isopropyl-1Cp + CH_3	1.93×10^{15} [a]	277.6[b]
15	isopropyl-1Cp → toluene + CH_3	** [c]	**[c]
16	isopropyl-2Cp → propenyl-2Cp + H	2.85×10^{13}	183.6
17	isopropyl-1Cp → propenyl-1Cp + H	2.85×10^{13} [a]	164.8[b]
19	isopropyl-2Cp → isopropyl-1Cp	2.11×10^{13}	89.2
20	isopropyl-1Cp → isopropyl-2Cp	1.73×10^{13} [a]	72.5[b]
21	isopropyl-1Cp → isopropyl-5Cp	7.88×10^{13}	159.1
22	isopropyl-5Cp → isopropyl-1Cp	3.18×10^{14} [a]	96.3[b]

[a]The *A*-factor for reactions with numbers in parentheses has been fixed relative to that of the previous reaction in the table in the fitting procedure.

[b]The activation energy for reactions with numbers in parentheses has been fixed relative to that of the previous reaction in the table in the fitting procedure.

[c]This rate constant for this reaction consistently became negligible during the fitting procedure, and it was not used in the final fits.

Table 4. Molecular properties derived from G3MP2B3 calculations used for determination of relative thermodynamic parameters.

Species	Property	
TBCP-1	Frequencies (cm^{-1})	143.7, 292.5, 305.1, 330.3, 343.5, 367.5, 462.4, 466.2, 555.3, 573.0, 698.5, 809.8, 820.5, 885.0, 889.5, 932.8, 938.5, 946.0, 950.5, 970.5, 971.8, 1032.1, 1055.8, 1057.3, 1107.7, 1134.3, 1152.3, 1236.4, 1236.9, 1278.3, 1298.8, 1333.3, 1399.0, 1421.6, 1425.5, 1450.3, 1453.6, 1510.7, 1516.6, 1521.0, 1532.1, 1534.5, 1548.8, 1595.4, 1671.2, 3032.5, 3038.5, 3041.9, 3049.7, 3058.1, 3103.7, 3107.2, 3114.1, 3115.3, 3118.2, 3118.6, 3209.8, 3229.0, 3240.6
	Moments of inertia (amu·$Å^2$)	External[a]: 493.5, 437.4 (466.0, inactive), 170.8
		Internal Rotors[b]: 38.9 (3, 6.3 kJ mol^{-1}), 3.1 (3, 17.2 kJ mol^{-1}) ×3
TBCP-2	Frequencies (cm^{-1})	141.0, 209.1, 229.8, 328.8, 337.7, 369.2, 420.2, 464.7, 573.7, 646.6, 719.9, 781.1, 812.4, 820.1, 908.6, 935.8, 939.6, 945.6, 949.0, 951.6, 970.4, 1001.8, 1051.3, 1058.6, 1106.0, 1132.5, 1152.3, 1236.5, 1239.8, 1282.3, 1288.2, 1329.6, 1402.3, 1423.0, 1423.2, 1452.8, 1454.8, 1509.5, 1516.9, 1519.3, 1532.8, 1532.8,

		1548.3, 1596.2, 1680.7, 3023.5, 3040.8, 3041.4, 3046.2, 3049.3, 3106.4, 3107.6, 3113.4, 3114.9, 3118.2, 3119.6, 3209.3, 3236.8, 3240.4
	Moments of inertia (amu·Å^2)	External: 492.5, 435.6 (463.2, inactive), 171.9 Internal Rotors: 39.3 (3, 7.9 kJ mol^{-1}), 3.1 (3, 17.2 kJ mol^{-1}) ×3
TBCP-5	Frequencies (cm^{-1})	128.3, 204.1, 234.5, 334.9, 357.4, 406.6, 435.3, 546.8, 564.7, 694.1, 719.5, 800.7, 812.7, 838.7, 886.0, 943.5, 944.5, 953.0, 953.5, 975.6, 990.6, 1026.2, 1026.3, 1057.1, 1078.3, 1131.0, 1142.2, 1194.2, 1225.3, 1270.0, 1276.7, 1314.3, 1332.0, 1422.7, 1428.5, 1430.3, 1459.1, 1511.4, 1518.4, 1518.8, 1534.0, 1538.8, 1548.0, 1576.3, 1662.6, 2973.8, 3039.1, 3042.7, 3050.6, 3099.7, 3105.1, 3111.8, 3117.1, 3120.0, 3125.7, 3207.3, 3218.8, 3240.2, 3245.2
	Moments of inertia (amu·Å^2)	External: 457.9, 404.0 (430.1, inactive), 176.0 Internal: 48.1 (3, 23.8 kJ mol^{-1}), 3.1 (3, 17.2 kJ mol^{-1}) ×3
Isopropyl-1Cp	Frequencies (cm^{-1})	165.0, 226.1, 330.5, 351.5, 448.4, 476.5, 550.1, 555.5, 655.7, 760.8, 810.0, 825.7, 929.1, 933.2, 949.4, 970.5, 979.0, 993.7, 1063.0, 1092.5, 1120.3, 1137.6, 1161.3, 1190.1, 1289.1, 1297.7, 1339.9, 1412.0, 1438.5, 1447.3, 1474.0, 1500.6, 1502.4, 1514.7, 1517.9, 1535.4, 1600.3, 3010.6, 3017.9, 3022.2, 3044.6, 3046.9, 3051.9, 3137.5, 3143.7, 3209.3, 3233.4, 3242.3
	Moments of inertia (amu·Å^2)	External: 453.4, 342.7 (394.2, inactive), 120.0 Internal: 30.0 (2, 62.7 kJ mol^{-1}), 3.1 (3) ×2
Isopropyl-2Cp	Frequencies (cm^{-1})	172.2, 239.7, 339.2, 358.9, 402.8, 469.0, 555.8, 581.7, 629.8, 751.1, 792.5, 859.9, 930.5, 943.0, 950.9, 964.3, 975.6, 986.8, 1010.0, 1080.1, 1109.5, 1130.8, 1152.4, 1199.1, 1288.6, 1307.5, 1364.3, 1412.4, 1435.6, 1448.1, 1467.9, 1478.3, 1497.5, 1513.6, 1514.5, 1555.4, 1651.6, 2996.0, 3006.0, 3008.9, 3013.6, 3039.2, 3045.3, 3144.5, 3145.1, 3215.1, 3237.4, 3240.1
	Moments of inertia (amu·Å^2)	External: 458.3, 348.2 (399.5, inactive), 119.4 Internal: 29.8 (2, 46.0 kJ mol^{-1}), 3.1 (3) ×2
Isopropyl-5Cp	Frequencies (cm^{-1})	122.5, 177.7, 332.2, 334.9, 368.9, 525.9, 562.3, 706.1, 725.4, 805.8, 833.7, 844.2, 913.4, 948.6, 954.3, 960.9, 992.7, 1007.9, 1012.9, 1038.0, 1066.7, 1122.3, 1134.7, 1183.1, 1217.7, 1298.9, 1320.0, 1339.3, 1414.1, 1428.1, 1444.8, 1498.7, 1506.7, 1511.1, 1525.0, 1570.0, 1658.3, 2948.7, 2971.5, 2993.8, 3041.6, 3047.9, 3094.8, 3120.1, 3206.2, 3217.2, 3236.6, 3242.3
	Moments of inertia (amu·Å^2)	External: 371.6, 355.9 (363.7, inactive), 126.1 Internal: 35.4 (2), 3.1 (3) ×2
1-methyl-Cp	Frequencies (cm^{-1})	150.6, 229.0, 370.4, 525.1, 616.6, 693.2, 818.6, 854.7, 882.0,

		929.7, 950.1, 958.2, 1007.0, 1037.6, 1063.1, 1134.3, 1152.1, 1200.5, 1281.3, 1332.6, 1402.1, 1443.3, 1450.3, 1509.5, 1518.7, 1604.4, 1685.8, 3022.2, 3027.9, 3049.2, 3067.2, 3116.1, 3205.2, 3217.9, 3240.8
	Moments of inertia (amu·Å^2)	External: 213.8, 157.1 (183.2, inactive), 63.0
		Internal: 3.0 (3, 5.9 kJ mol^{-1})
2-methyl-Cp	Frequencies (cm^{-1})	158.1, 233.2, 369.0, 577.4, 617.7, 706.8, 753.8, 819.6, 915.0, 936.4, 943.2, 949.8, 983.7, 1029.5, 1081.0, 1118.4, 1132.9, 1222.1, 1279.1, 1310.2, 1406.9, 1443.5, 1453.4, 1511.1, 1521.6, 1599.3, 1697.0, 3024.5, 3034.0, 3047.3, 3080.2, 3122.6, 3204.7, 3223.6, 3236.7
	Moments of inertia (amu·Å^2)	External: 214.0, 156.3 (182.9, inactive), 63.9
		Internal: 3.0 (3, 6.3 kJ mol^{-1})
5-methyl-Cp	Frequencies (cm^{-1})	167.6, 293.1, 542.1, 561.6, 717.3, 721.0, 785.3, 809.7, 874.4, 950.9, 952.8, 960.0, 1004.4, 1031.6, 1088.1, 1104.4, 1124.4, 1152.9, 1278.0, 1300.0, 1332.9, 1417.2, 1438.2, 1530.0, 1530.1, 1577.6, 1663.2, 2994.2, 3050.6, 3115.4, 3128.8, 3205.8, 3215.1, 3231.5, 3238.8
	Moments of inertia (amu·Å^2)	External: 193.6, 142.9 (166.3, inactive), 72.2
		Internal: 3.0 (3, 16.3 kJ mol^{-1})

[a]The molecules were treated as a symmetric top with the moment of inertia around the non-unique axes taken to be the geometric mean of the two largest moments of inertia in the molecule. This value is shown in parentheses. The moment of inertia about the unique axis of the symmetric top was taken to be the smallest molecular moment of inertia.

[b]The symmetry number of the internal rotor is shown in parentheses. If a hindered rotor was used to model the rotation, the barrier to hindrance is given in kJ mol^{-1}. Multiple identical rotors (such as the methyl rotors in the TBCP isomers) are denoted by $\times n$ after the given moment of inertia, where n is the number of rotors.

Table 5. Summary of thermodynamic parameters derived from G3MP2B3 calculations.

	Relative $\Delta_f H$(298 K), kJ mol^{-1}	**Entropy (298K) J mol^{-1} K^{-1}**	**Relative $\Delta_f H$(1050 K) kJ mol^{-1}**	**Entropy (1050K) J mol^{-1} K^{-1}**	**Relative equilibrium concentrations at 1050 K**
1-TBCP	2.06	394.7	1.12	753.4	0.44
2-TBCP	0	398.6	0	759.1	1
5-TBCP	11.06	391.5	13.16	754.9	0.13
isopropyl-1Cp	0	401.7	0	694.1	1
isopropyl-2Cp	21.93	402.7	22.36	695.8	0.095
isopropyl-5Cp	81.61	419.4	78.23	706.2	0.00055
1-methyl-Cp	1.57	320.1	1.34	533.9	0.90
2-methyl-Cp	0	319.3	0	533.4	1
5-methyl-Cp	11.90	309.7	13.46	526.1	0.089

Figures

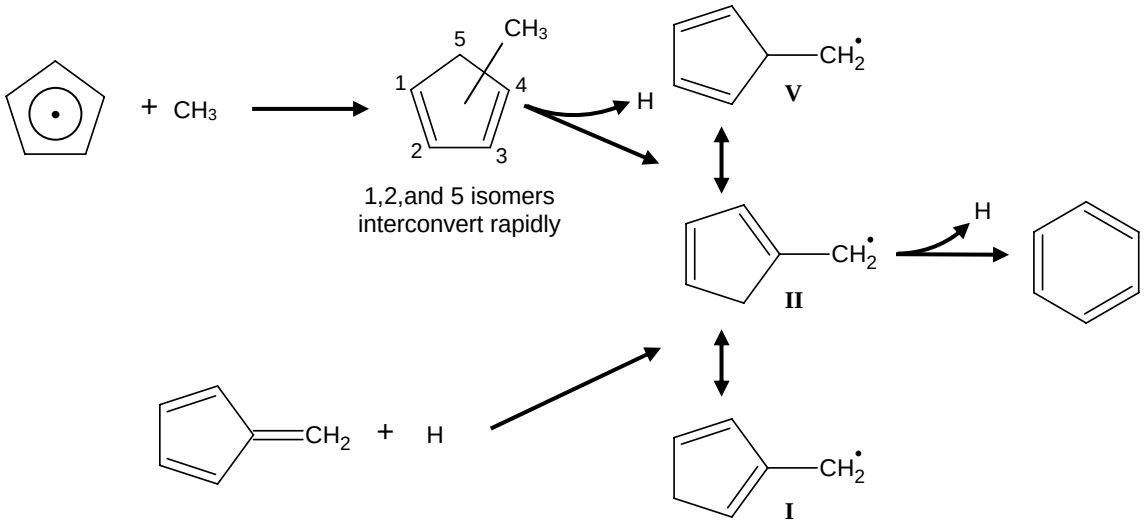

Figure 1. Ring expansion reactions of cyclopentadienyl systems.

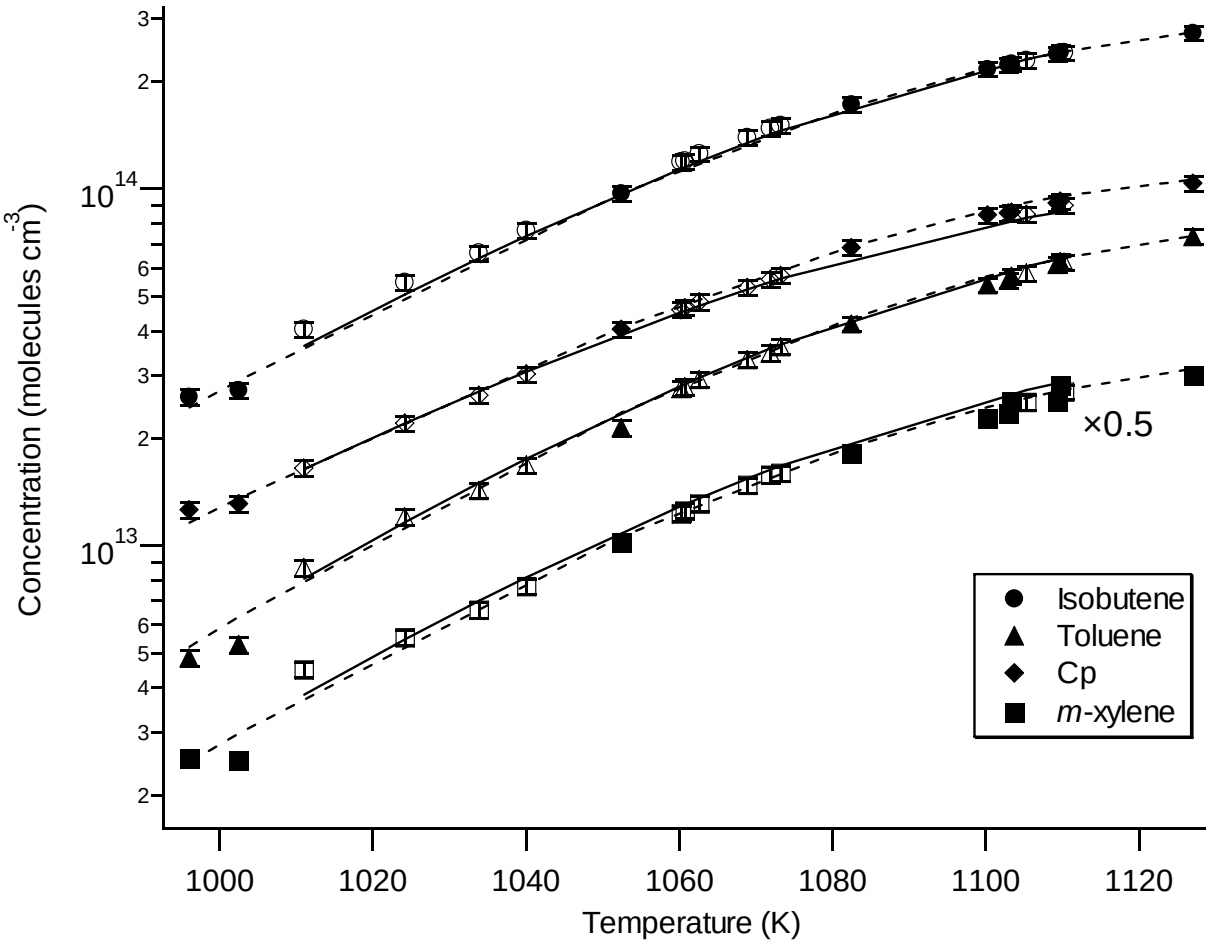

Figure 2. Relative concentration data for major products in the decomposition of TBCP. Circles, triangles, diamonds, and squares represent the concentrations of isobutene, toluene, 1,3-cyclopentadiene (Cp), toluene, and *m*-xylene (indicative of H-atoms). The concentrations of *m*-xylene have been scaled by 0.5 for clarity. Closed and open symbols are for mixtures A and B, respectively. Dashed and solid lines show the fits of the final model to the data from mixtures A and B, respectively. Error bars are 2σ uncertainties derived from a parameterization of estimated random measurement errors vs. peak area in the GC analyses (see text).

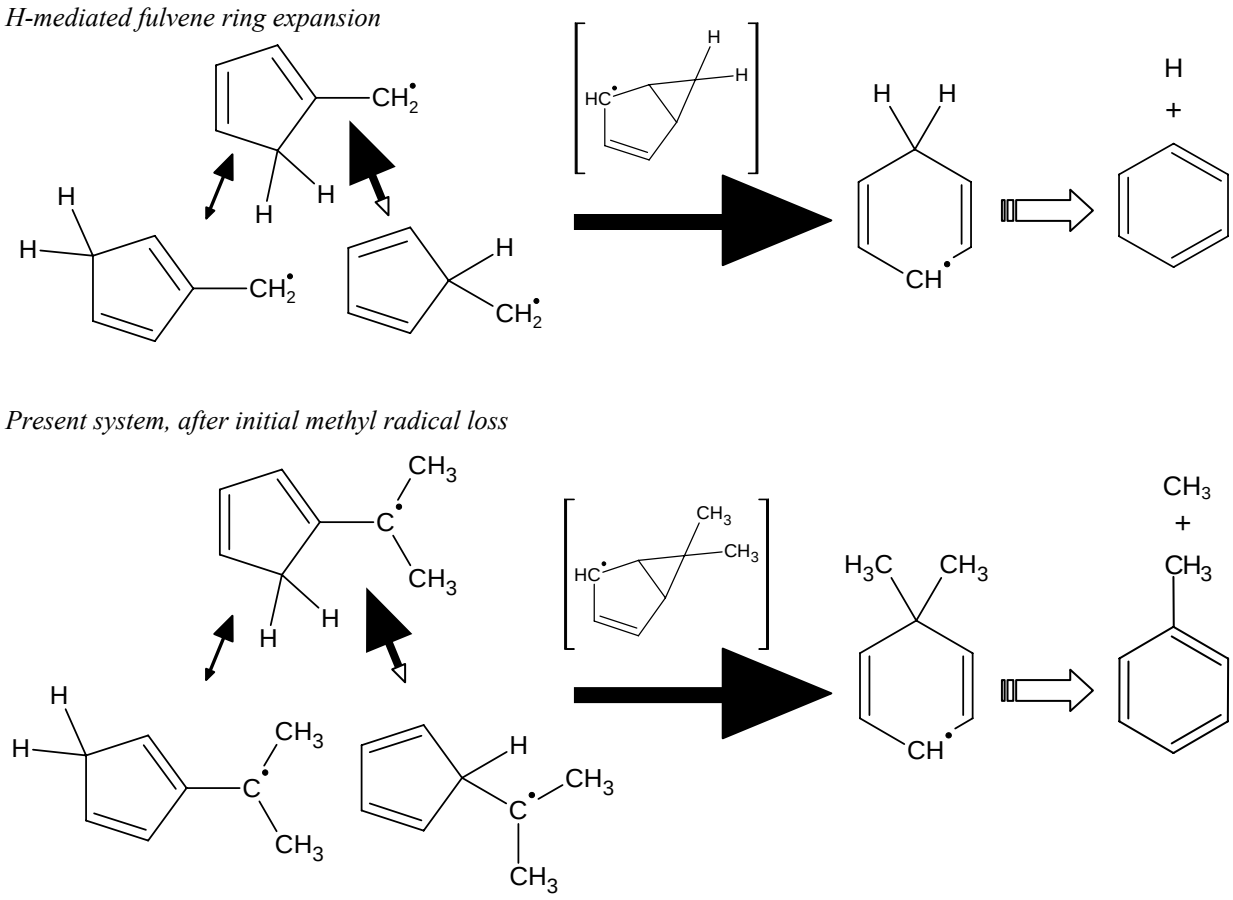

Figure 3. Parallels between proposed mechanism for H-mediated fulvene expansion to form benzene and presently proposed mechanism. The areas of the solid arrowheads provide a pictorial representation of the reaction rates for each step. The area of the hollow arrowheads has been scaled by 1000×. The present experiment is not sensitive to the rate of the final step and is indicated with a stylized arrow that carries no information on the rate constant.

References

[1] Richter H.; Howard, J. B. Prog. Energy and Comb. Sci, 2000, 26, 565–608.
[2] Miller, J. A.; Klippenstein, S. J. J. Phys. Chem. A 2001, 105, 7254–7266.
[3] Miller, J. A.; Klippenstein, S. J. J. Phys. Chem. A 2003, 107, 7783–7799.
[4] Melius, C. F.; Colvin, M. E.; Marinov, N. M.; Pitz, W. J.; Senkan, S. M. Proc. Combust. Inst. 1996, 26, 685–692.
[5] Dubnikova, F.; Lifshitz, A. J. Phys. Chem. A 2002, 106, 8173–8183.
[6] Ikeda, E.; Tranter, R. S.; Kiefer, J. H.; Kern, R. D.; Singh, H. J.; Zhang, Q. Proc. Combustion Inst. 2000, 28, 1725–1732.
[7] Lifshitz, A.; Tamburu, C.; Suslensky, A.; Dubnikova, F. Proc. Combusion Inst. 2005, 30, 1039–1047.
[8] Certain commercial materials and equipment are identified in this paper in order to specify adequately the experimental procedure. In no case does such identification imply recommendation or endorsement by the National Institute of Standards and Technology, nor does it imply that the material or equipment is necessarily the best available for the purpose.
[9] Tsang, W. In Shock Waves in Chemistry; Lifshitz, A.; Ed.; Marcel Dekker, New York, 1981, pp. 59–129.
[10] Herzler, J.; Manion, J. A.; Tsang, W. Int. J. Chem. Kin. 2001, 33, 755–767.
[11] Benson, S. W.; O'Neal, H. E. Kinetic Data on Gas Phase Unimolecular Reactions, National Standard Reference Data Series, National Bureau of Standards (United States), Washington, DC, 1970; Vol. 21, p. 159.
[12] Manion, J. A.; Tsang, W. J. Phys. Chem. 1996, 100, 7060–7065.
[13] Tsang, W. J. Phys. Chem. Ref. Data 1990, 19, 1–68.
[14] Radhakrishnan, K.; Hindmarsh, A. C., Description and Use of LSODE, the Livermore Solver for Ordinary Differential Equations; UCRL-ID-113855; Lawrence Livermore National Laboratory, Livermore, CA, 1993
[15]Jones, E.; Oliphant, T.; Peterson, P. Scipy: Open Source Tools for Python, http://www.scipy.org.
[16] Press, W. H.; Flannery, B. P.; Teukolsky, S. A.; Vetterling, W. T. Numerical Recipes in C: The Art of Scientific Computing; Cambridge University Press: Cambridge, 1992, Chapter 10.
[17] Tsang, W. J. Chem. Phys. 1966, 44, 4283–4295.
[18] Roy, K.; Braun-Unkhoff, M.; Frank, P.; Just. Th. Int. J. Chem. Kin. 2001, 33, 821–833.
[19] Roth, W. R. Tetrahedron Lett. 1964, 17, 1009–1013.
[20] McLean, S.; Haynes, P. Tetrahedron 1965, 21, 2329–2342.
[21] Bachrach, S. M. J. Org. Chem. 1993, 58, 5414–5421.
[22] Baboul, A. G.; Curtiss, L. A.; Redfern, P. C.; Raghavachari, K. J. Chem. Phys. 1999, 110, 7650–7657.
[23] Gaussian 03, Revision C.02, Frisch, M. J.; Trucks, G. W.; Schlegel, H. B.; Scuseria, G. E.; Robb, M. A.; Cheeseman, J. R.; Montgomery, Jr., J. A.; Vreven, T.; Kudin, K. N.; Burant, J. C.; Millam, J. M.; Iyengar, S. S.; Tomasi, J.; Barone, V.; Mennucci, B.; Cossi, M.; Scalmani, G.; Rega, N.; Petersson, G. A.; Nakatsuji, H.; Hada, M.; Ehara, M.; Toyota, K.; Fukuda, R.; Hasegawa, J.; Ishida, M.; Nakajima, T.; Honda, Y.; Kitao, O.; Nakai, H.; Klene, M.; Li, X.; Knox, J. E.; Hratchian, H. P.; Cross, J. B.; Bakken, V.; Adamo, C.; Jaramillo, J.; Gomperts, R.; Stratmann, R. E.; Yazyev, O.; Austin, A. J.; Cammi, R.; Pomelli, C.; Ochterski, J. W.; Ayala, P. Y.; Morokuma, K.; Voth, G. A.; Salvador, P.; Dannenberg, J. J.; Zakrzewski, V. G.; Dapprich, S.; Daniels, A. D.; Strain, M. C.; Farkas, O.; Malick, D. K.; Rabuck, A. D.; Raghavachari, K.; Foresman, J. B.; Ortiz, J. V.; Cui, Q.; Baboul, A. G.; Clifford, S.; Cioslowski, J.; Stefanov, B. B.; Liu, G.; Liashenko, A.; Piskorz, P.; Komaromi, I.; Martin, R. L.; Fox, D. J.; Keith, T.; Al-Laham, M. A.; Peng, C. Y.; Nanayakkara, A.; Challacombe, M.; Gill, P. M. W.; Johnson, B.; Chen, W.; Wong, M. W.; Gonzalez, C.; and Pople, J. A.; Gaussian, Inc., Wallingford CT, 2004.
[24] Tsang, W.,"A Pre-processor for the Generation of Chemical Kinetics Data for Simulations" AAIA-2001-0359, 39th AIAA Aerospace Sciences Meeting and Exhibit, January 8–11, 2001 Reno. NV
[25] Tsang, W.; Bedanov, V.; Zachariah, M. R. J. Phys. Chem. 1996, 100, 4011–4018.
[26] Tsang, W.; Lifshitz, A. In Handbook of Shock Waves; Ben-Dor, G; Igra, E.; Elperin, T; Lifshitz, A., Eds.; Academic Press; San Diego, 2001; Vol. 3, pp. 107–210.
[27] Eggers, K. W.; Vitins, P. J. Am. Chem. Soc. 1974, 96, 2714–2719.
[28] King, K. D. J. Phys. Chem. 1980, 84, 2517–2521.

F: NIST Well Stirred Reactor/Plug Flow Reactor Facility (WSR/PFR)

Under SERDP funding, the NIST Well-stirred Reactor/Plug Flow Reactor (WSR/PFR) was designed and constructed to examine soot inception of rich ethylene/air oxidation (equivalence ratio, Φ = 1.8 and 2.0) in the high temperature regime (≈1700 K) at atmospheric pressure. The reactor is comprised of four parts, namely the WSR, the PFR, the afterburner, and the exhaust cooling sections (see **Figure 1**). In addition to the unique facility developed under SERDP funding, several innovative diagnostic methods were developed to quantify soot particle size distributions as well as gas phase species.

The NIST WSR reactor was based on the design currently implemented by Stouffer *et al*. [**1**]. The WSR consists of a 250 ml toroidal chamber 32 mm in diameter made by an upper and lower section of silicon carbide (SiC) and an inconel jet ring inserted between the two SiC sections. The jet ring consisted of 48 nozzles (1 mm diameter) which injected a premixed fuel/air mixture at near sonic velocities. The resulting jets of fuel/air mixture caused rapid macroscopic and microscopic mixing of reactants, intermediates, and products within the WSR, approximating a highly turbulent combustion environment. Figure 1 shows a cross section of the WSR, including the jet ring. To minimize leaks, ceramic gaskets were placed between the SiC and jet ring sections and the assembly was compressed together using steel plates. The assembly was further housed in a steel casing which was purged with nitrogen (≈50 SLPM) to maintain safe jet ring temperatures and to minimize the hazards of possible leaks. Access to the toroidal chamber for ignition and instrumentation was achieved using four holes cast into the lower SiC section.

The air, nitrogen, and gaseous fuel flow rates were controlled using Brooks Instruments[1] mass flow controllers. The pressure drop across the mass flow controllers was maintained at 20 psi with regulators to maximize the accuracy of the flow. The mass flow controllers were sized such that the residence times of the WSR could be varied between 5 ms and 12 ms. The air system utilized house compressed air that was filtered and dried prior to use. The air system was designed to accommodate flow rates up to 400 SLPM. A surge tank (750 liter) was installed inline after the air dryer and prior to the mass flow controller to minimize the effects of pressure perturbations during the recycling/regeneration of the air drying system. The dew point of the dried air was continuously monitored to ensure "dry" air for the combustion process. Nominally, the air was dried to dew point less than -60 °C. A 1 kW heater was placed inline after the mass flow controller to allow preheating temperatures up to 473 K. The preheating was necessary to allow rapid and stable ignition of the reactor. The fuel system utilized a series of high pressure cylinders of ultra high purity ethylene (99.95%). Chemical analysis confirmed that the major impurities in the fuel were ethane and propylene. The cylinder pressure was reduced to 860 kPa though a series of regulators to minimize the potential of regulator freezing. The fuel system was designed to provide a steady flow of up to 75 SLPM. To control the temperature and reaction conditions, nitrogen dilution can be added to the gas streams. The nitrogen system utilized a series of high purity liquid nitrogen tanks. The tank pressure was maintained near 1300 kPa using pressure building valves and was reduced to 790 kPa prior to the mass flow controllers. The nitrogen system was designed to accommodate flow rates up to 100 SLPM. Prior to injection of the gas stream into the WSR

[1] Certain commercial equipment is identified in this paper to accurately describe the experimental procedure, this in no way implies endorsement by NIST

and jet ring, the air, nitrogen, and fuel streams are combined and pass through a turbulent mixing section to ensure the system is fully premixed. To reduce the risk of catastrophic failure due to autoignition and potential flashback from the jet ring, a porous metal flash arrestor was installed after the turbulent mixing section.

The exhaust gases from the WSR exit the toroidal chamber through 8 channels into a transition region which contains a silicon carbide flow straightener to remove any rotational flow and direct the flow to the entrance of the PFR section. The PFR section includes an inner Halsic-I (silicon carbide) tube surrounded by an outer alumina insulating sleeve, all of which is encased in a steel vessel. The inner Halsic tube is 70 cm long and has an inner diameter of 5.1 cm. Four sampling ports are spaced every 15.2 cm (6.0 in) along the length of the PFR section. The gas velocity in the PFR section is a function of flow conditions into the WSR. Under the flow conditions in the present study, the velocity is on the order of 10 m/s.

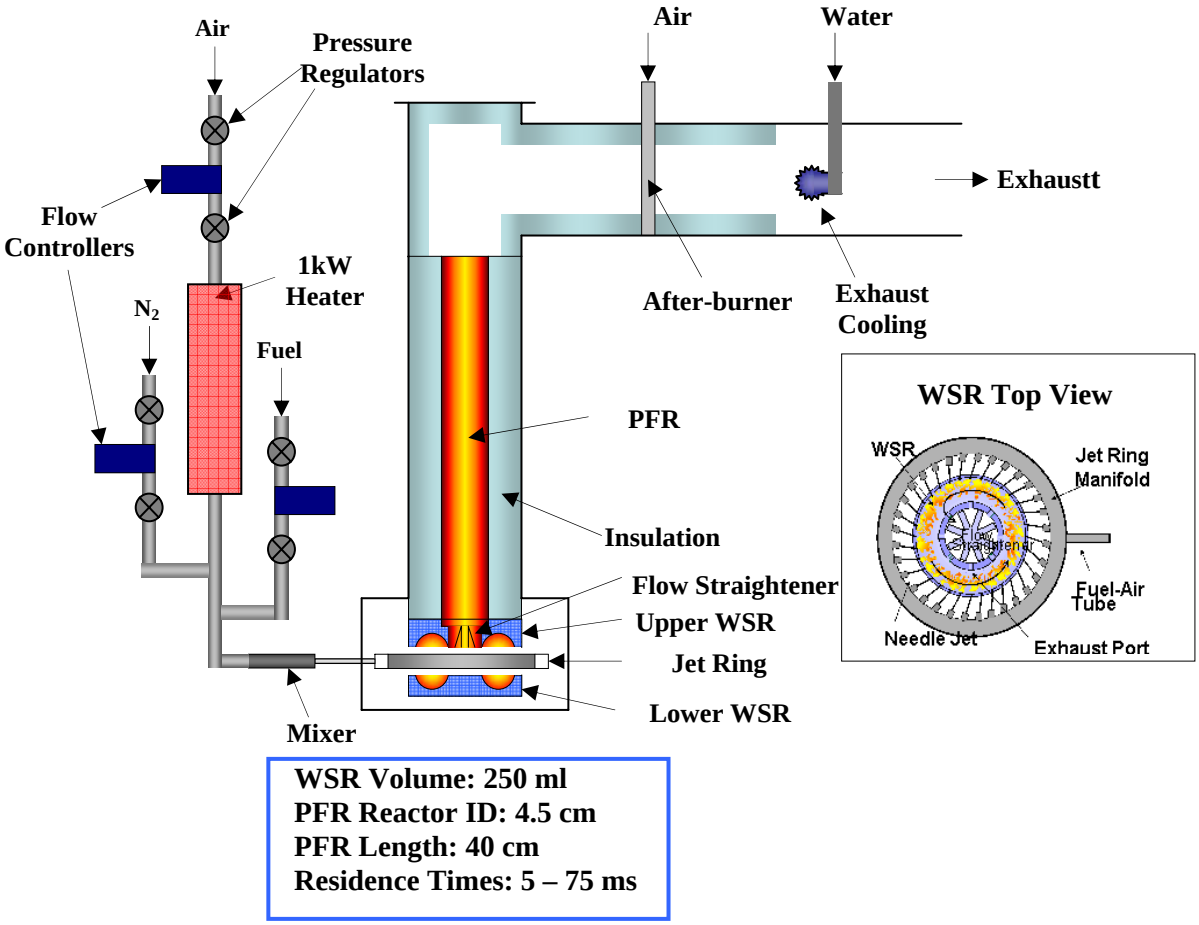

Figure 1 NIST Well Stirred Reactor/Plug Flow Reactor (WSR/PFR)

The fuel rich conditions necessary for soot inception resulted in volume fractions of carbon monoxide (CO) in excess of 14% volume (dry). As this is a serious safety concern, an afterburner was installed after the PFR section to burn out most of the CO. The afterburner consisted of an Inconel 601 tube fitted perpendicular to the flow and had slits for air to pass through it. The Inconel tube acted as a bluff body to stabilize the flame. Air was metered into the afterburner using a mass flow controller once the exhaust stream had reached sufficient temperature to autoignite the CO/air mixture, typically 670ºC. The products were then cooled

using a water spray nozzle prior to being released to ambient. **Figures 2-3** show the fuel and air handling system; a picture of the NIST WSR/PFR is shown in **Figure 4**.

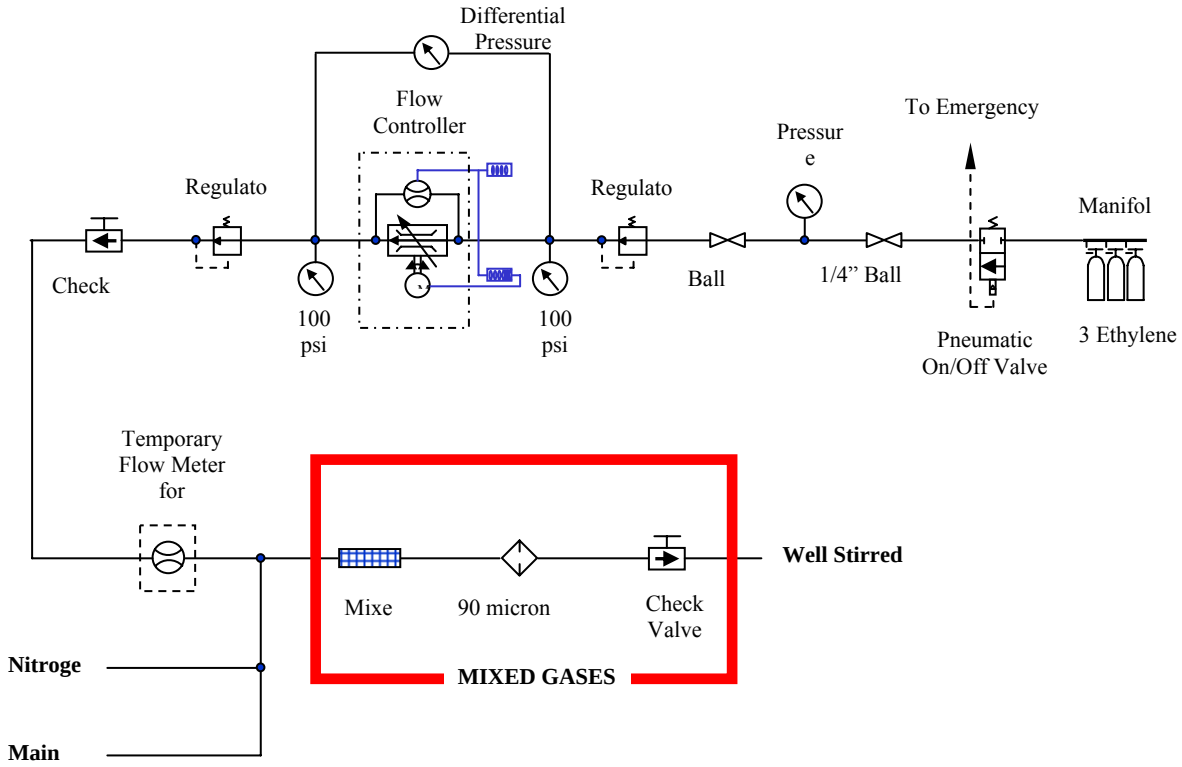

Figure 2 NIST WSR/PFR Main Fuel System

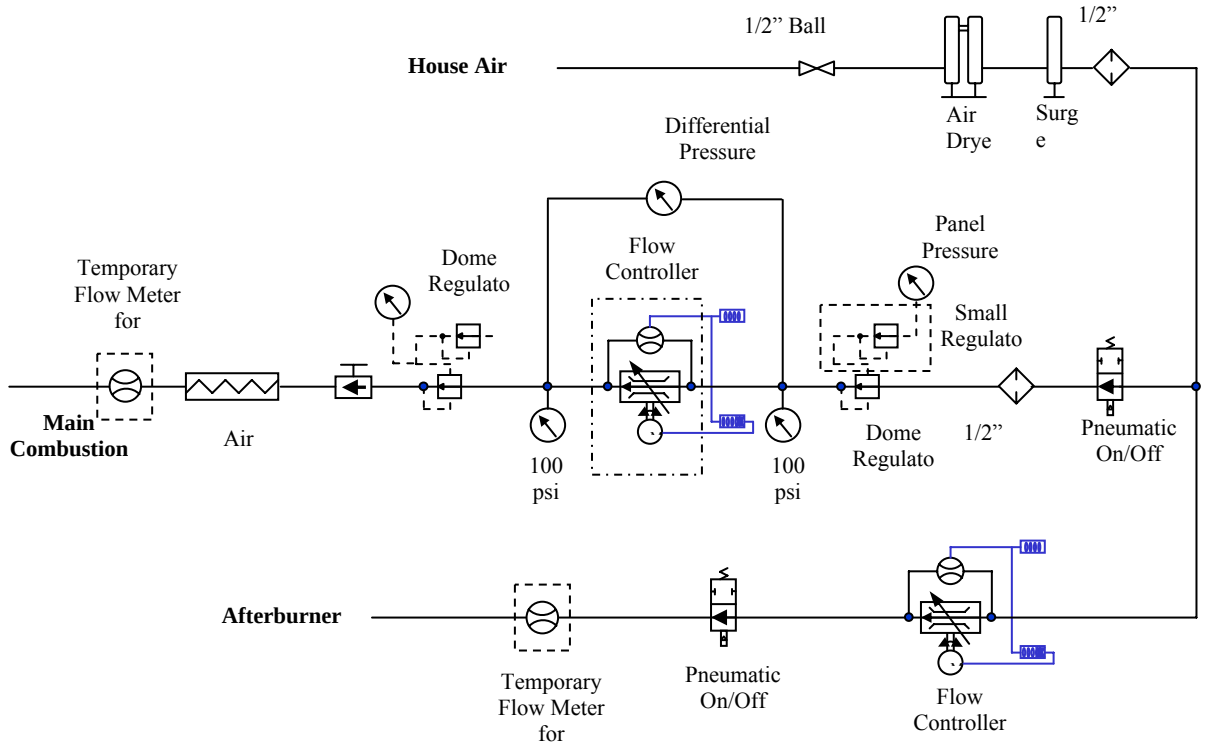

Figure 3 NIST WSR/PFR Air Flow System

Figure 4 Picture of NIST WSR/PFR

Soot Sampling and Dilution

Under this project, two different dilution probe designs were utilized during these experiments to obtain soot size distributions. The first dilution probe, based upon the design of Zhao *et al*. [**2]**, was utilized in the PFR section. **Figure 5** shows a schematic of the diluter. It is important to recognize that the dilution probe used in the present study was gas cooled, as opposed to a water cooled dilution probed used by Zhao *et al*. [**2**]. It was simpler to use a gas cooled probe in our WSR/PFR, as it avoids a hazardous condition if water leaked or over-heated and gas cooling provided less thermal gradients. The dilution probe was made from a 400 mm long Inconel 601 tube (6.15 mm OD, 5.15 mm ID) with a single 0.50 mm orifice in the side wall for sampling the particulate and other combustion products. Nitrogen flow through the tube was controlled by a mass flow controller, which was held constant at 30 SLPM. To insulate the Inconel from the reactor stream, two zirconia ceramic sleeves (9.53 mm OD, 6.35 mm ID, 63.5 mm long) were bonded to the Inconel tube starting approximately 2.0 mm from each side of the orifice. The resulting gap was partially covered with a ceramic paste to help reduce the temperature of the Inconel tube. Using this technique resulted in a dilution exhaust temperature of 160 ºC. An ejector pump was used to adjust the pressure drop across the orifice to vary the dilution ratio from 10^2 to 10^4.

The second dilution probe was designed specifically to enable soot size distributions measurements in the WSR toroidal chamber. As such, design required a coannular design of

limited diameter. **Figure 6** shows a schematic of the diluter. The dilution probe was made from a 250 mm long Inconel 601 tube (9.5 mm OD, 7.75 mm ID). An endcap was welded to one end of the tube and a single 0.50 mm orifice was placed in the center of the endcap. A second 350 mm long Inconel 601 tube (6.25 mm OD, 5.15 mm ID) was inserted into the center of the large tube. A gap of 2.5 mm was left between the end of the smaller central tube and the endcap. Nitrogen flow (30 SLPM) was used as a diluent and was directed through the gap between larger and smaller inconel tubes prior to entrainment and quenching of the particles from the orifice. The exterior of the probe was coated with thermal barrier coating to reduce the heat transfer to the probe. Using this probe, temperature of the dilution exhaust ranged from 200 – 300 ºC depending on sampling location in the cross-section of the torriod. Although higher than the first dilution probe, additional insulation was not possible due to the constraints in the port sizes of the torriod chamber.

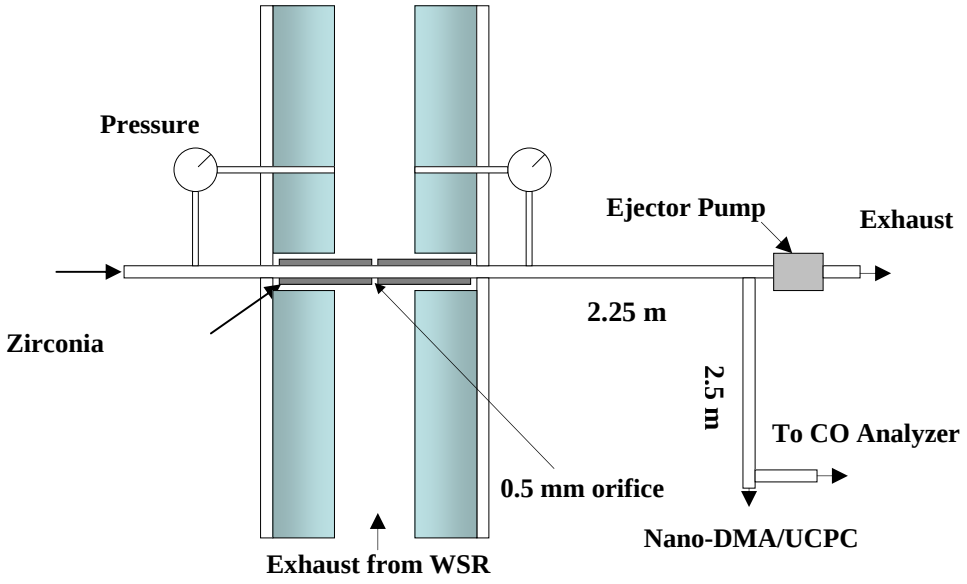

Figure 5Diluter used in the PFR section of NIST WSR/PFR.

In either probe design, an ejector pump was used to adjust the pressure drop across the orifice to vary the dilution ratio from 10^2 to 10^4. Copper tubing, 9.35 mm OD, 2.1 m long, was used to connect the diluter with the ejector pump. A portion of the diluted flow immediately prior to the ejector pump was directed to a nano-DMA for particle size and concentration measurements and a non-dispersive infrared (NDIR) analyzer for CO measurements (Horiba Model VIA-510). Copper tubing, 6.25 mm OD, 0.55 m long, was used to direct the particles to a nano-DMA. To determine the dilution ratio, a second CO measurement was made of the undiluted PFR stream at the top most port. The undiluted CO measurement was dried through a combination of wet and dry ice baths. Unlike laminar flame studies, the orifice cannot be cleaned between nano-DMA scans in the WSR/PFR facility and small quantities of soot deposits around the orifice can degrade the quality of the size distributions. To mitigate the formation of such growths, the diluters were over pressurized to exhaust nitrogen into the reactor between nano-DMA scans.

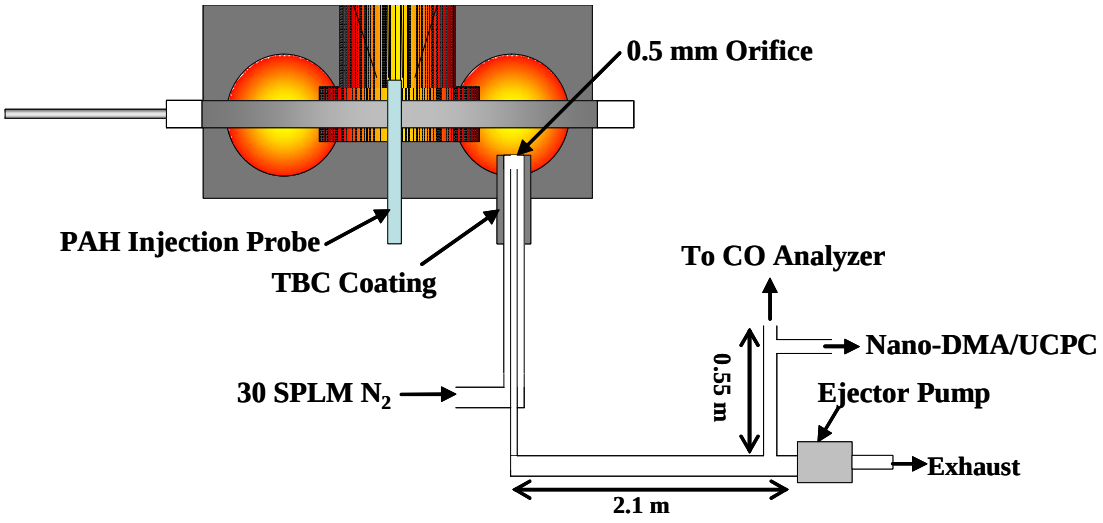

Figure 6 Diluter used in the PFR section of NIST WSR/PFR.

Nano-Differential mobility analyzer (Nano-DMA)

The particle measurement system consisted of a Nano-DMA (TSI Model 3085) and a UCPC (TSI Model 3025A). The diluted soot first passes through a radioactive ionizing source (Po^{210}) which is installed prior to the Nano-DMA. An equilibrium charge distribution develops as the particles flow through the neutralizer with $P(D_p)$, the probability that a particle with diameter D_p carries one elementary unit of charge. The charge distribution obtained is in good agreement with the Boltzmann charge distribution [**3**]. In the size range examined in this study, the Boltzmann equilibrium contains only small fractions of +1 and −1 particles, nominally ≈1% at 3 nm and ≈17% at 50 nm. Wiedensohler has [**4**] developed an approximation of the bipolar charge distribution.

The positively charged aerosol particles enter at the outer annular tube of the DMA and moves toward the central rod under the influence of the electric field. A small flow of particles exit through a slit in the central rod of the DMA and are counted by a UCPC. The number concentration of particles exiting from the DMA, $N(V)$, at voltage V, is related to the integral of the product of the DMA transfer function, Ω, and the size distribution function $G(D_p)=dN/dD_p$, where $G(D_p)dD_p$ is equal to the number of particles per cm^3 with diameter between D_p and D_p+dD_p:

$$N(V) = \int_0^\infty \Omega(Z_p, V) \cdot G(D_p) \cdot P(D_p) \cdot \left| \frac{dD_p}{dZ_p} \right| dZ_p \qquad (1)$$

This explicit form of the equation was derived by Mulholland *et al*. [**5**]. The transfer function Ω for the DMA operating at voltage V is defined as the probability that a charged particle entering the DMA with electric mobility Z_p will leave through the sampling slit. The transfer function was assumed to have a triangular shape with a peak value of 1, and for a perfectly monodisperse aerosol, all the aerosol entering the DMA exits through the slit in the center electrode.

The electric mobility corresponding to the peak in the transfer function for a voltage is given by the following equation:

$$Z_p = \frac{Q_c}{2\pi VL} \ln\left(r_2 / r_1\right) \tag{2}$$

where Q_c *is* the flow of the sheath gas (10 SLPM), r_1 and r_2 are the inner and outer diameters of the classifying region, and L is the length of the classifying region. This equation is valid provided the sheath air flow is equal to the excess flow, Q_m , leaving the classifier.

In general, an expression for the electric mobility of a singly charged particle involving the particle diameter is obtained by equating the electric field force with the Stokes drag force:

$$Z_p = \frac{eC_c(D_p)}{3\pi\mu D_p} \tag{3}$$

where μ is the air viscosity, e is the electron charge, and $C_c(D_p)$, the Cunningham slip correction factor, which corrects for the non-continuum gas behavior on the motion of small particles.

The concentration of the monodisperse aerosol leaving the Nano-DMA is monitored using the UCPC. The number concentration is measured as a function of voltage as the voltage is stepped up from about 10 volts to 5000 volts, corresponding to particle diameters of approximately 3 nm to 60 nm, using 30 bins. A typical experiment consisted of setting the voltage constant for 10 seconds and recording number concentration data from the UCPC for 5 seconds (1 sample per second) at each bin. Initially a rapid scanning procedure was used, but there were problems with lack of repeatability between the upward and downward scans. The number concentration reported by the UCPC, the CO concentrations of the diluter and PFR section, and voltage was recorded with using a custom data analysis program.

In general, the determination of the size distribution requires the inversion of Eq. (1). For the case where the size distribution is broad and changing slowly with diameter in comparison with the transfer function, an approximate expression can be obtained for the size distribution function:

$$\frac{dN}{d\log(D_p)} = \frac{Q_c\left[2C_c(D_p) - 1 + \gamma\beta e^{\left(-\frac{\gamma D_p}{2\lambda}\right)}\right] N_{cpc}\eta_{para}\eta_{Dil}}{Q_a C_c(D_p) P(D_p)\eta_{cpc}\eta_{loss}} \tag{4}$$

where N_{cpc} is the output of the condensation particle counter, λ is the mean free path in air, and α, β, γ, are constants taken from Kim *et al*. [**6**]. Several correction factors are applied to correct the UCPC measurement for probe dilution ratio, η_{dil}, diffusion losses during transport, η_{loss}, UCPC detection efficiency, η_{cpc}, and coincidence effects, η_{para} [**7**]. The diffusion losses were estimated through the two transfer lines using the procedure of Zhao *et al.* [**2**] for the turbulent section and that of Hinds [**8**] for the laminar section. The transfer efficiency through the turbulent section was defined as:

$$\eta_{turbulent} = e^{-\frac{D(D_p)\sigma_s}{\delta}\tau} \tag{5}$$

where D is the diffusion coefficient, σ_s is the surface to volume ratio, τ is the transfer time, and δ is the thickness of the laminar sublayer. The laminar sublayer thickness was estimated based

on a smooth pipe [**9**] and the diffusion coefficient was obtained from Hinds [**8**]. The transfer efficiency throughout the turbulent section ranged from 0.47 at 3 nm to 0.94 at 10 nm and approached unity at larger particles sizes. The transfer efficiency though the laminar section was defined as [**10**]:

$$\eta_{laminar} = 0.819e^{-3.657\mu} + 0.097e^{-22.3\mu} + 0.032e^{-57\mu} \quad (6)$$

where μ is the deposition parameter ($\mu = DL/Q$ where D is the diffusion coefficient of the particles, L the length of tube, and Q the volume rate of flow through the tube) through the laminar section, the transfer efficiency ranged from 0.70 at 3 nm to 0.91 at 10 nm and approached 0.95 at larger particles sizes. The multiplication of the two efficiencies was used determine the total transfer efficiency, η_{loss}. An uncertainty analysis was performed to define the expanded uncertainty (95 % confidence level) for the particle diameters and particle concentrations [**11**]. Based on this analysis, the expanded uncertainty in the reported particle diameter was ± 5 % and ± 22 % in the reported concentration. The two main sources of uncertainty in the particle diameter resulted from voltage and Cunningham slip correction factor, while the main sources for the particle concentration resulted from the UCPC measurement uncertainty and particle loss estimations.

Additive Injection Probe

An injection system was designed and fabricated to inject fuel additives into the WSR/PFR. Fuel additives of interest included aromatics and PAH species thought to be important in the soot formation process. The additives were injected as a vapor just below the flow-straightener, between the WSR and PFR sections of the reactor. As most species of interest are in the solid phase, the additives were designed to be dissolved in a solvent, such as methanol. The liquid additive (PAH species dissolved in methanol or a liquid aromatic) was controlled and vaporized using a peristaltic pump and a heated nebulizer. Liquid flow rates from the peristaltic pump can range from 0.3 to 2.5 ml/min. Argon gas was used to drive the nebulizer, which creates droplets ranging in size from 10 to 30 μm. The jet of nebulized additive was sprayed into a heated quartz mixing chamber. A stream of heated argon gas vaporizes the liquid droplets and carries the vaporized additive to the reactor. Flow of both argon gas streams are controlled by rotameters, and the total flow of argon is approximately 4 lpm (1 lpm through the nebulizer and 3 lpm as a carrier gas). The heated quartz mixing chamber, argon gas, and transfer lines were all heated to nominally 100 °C to 200 °C, depending on fuel additive, to completely vaporize the additive and prevent condensation.

The injection probe was partially based upon the design of Marr [**12**]. The injection probe in the present was inconel and used three concentric tubes to minimize heat transfer to the fuel additive, as opposed to a single ceramic injector used by Maas. A schematic of the injector probe is shown in **Figure 7**. The tubes of the injector probe were made from Inconel 600 tubing, the outer tube was made from 200 mm long 6.35 mm OD with 0.40 mm wall thickness, the middle tube was made from 300 mm long 4.75 mm OD with 0.40 mm wall thickness, and the inner most tube was made from 400 mm long 3.18 mm OD with 0.25 mm wall thickness. A small endcap was welded onto the center most tube and eight 0.63 mm holes were evenly spaced along the circumference of the tube. The probe used by Marr [**12**] also used 8 evenly spaced holes around the circumference of the ceramic probe, however the holes were 0.8 mm.

These holes were aligned with the gap between the flow straighteners to ensure uniform mixing of the additive.

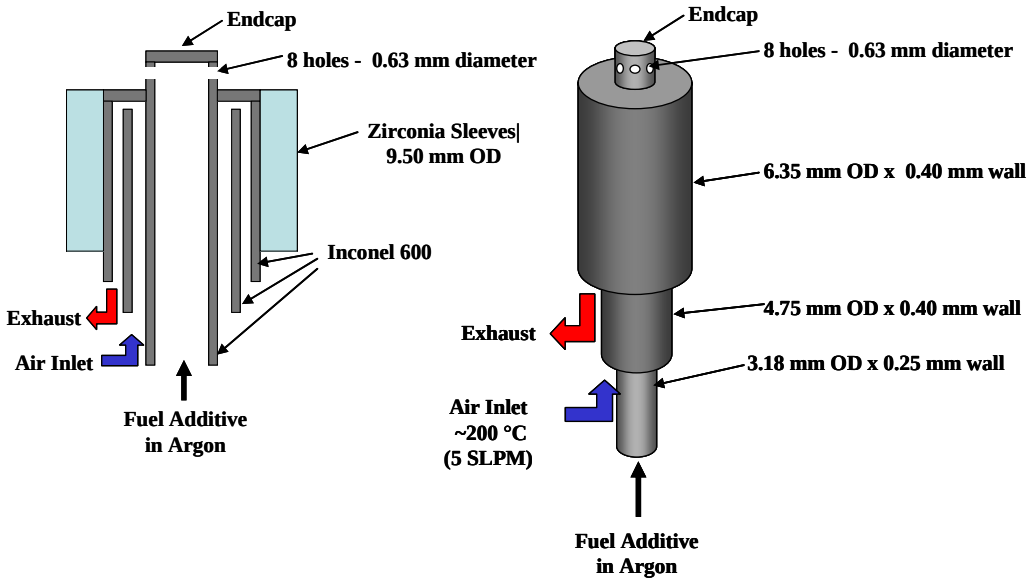

Figure 7 Diluter used in the PFR section of NIST WSR/PFR.

References

[1] Stouffer, S. D., R. C. Striebich, C. W. Frayne and J. Zelina (2002). Combustion Particulates Mitigation Investigation Using a Well-Stirred Reactor. AIAA 38th Joint Propulsion Conference & Exhibit, Paper Number: 2002-37, Indianapolis, Indiana, July 7-10, 2002.

[2] Zhao, B., Yang, Z., Wang, J., Johnston, M.V., and Wang, H., *Aerosol Sci. Tech*. 37:611 620 (2003).

[3] Kim, S.H., Liu, B.Y.H., and Zachariah, M.R., *J. Coll. Interface Sci*. 282:46-57 (2005).

[4] Wiedensohler, A., *J. Aerosol Sci*., 19:387-289 (1988).

[5] Mulholland, GW., Donnelly, M.K., Hagwood, C., Kukuck, S.R., Hackley, R., and Pui, D.Y.H., accepted for publication in *J. Res. NIST*, in press (2005).

[6] Kim, J.H., Mulholland, G.W., Kukuck, S.R., Pui, D.Y.H., *J.Res. NIST* 110: 31-54 (2005).

[7] Kesten, J., Reinking, A., and Porstendorfer, *Aerosol Sci. Technol*. 15:107-111 (2005).

[8] Hinds, W.C., Aerosol Technology: Properties, Behavior, and Measurement of Airborne Particles, John Wiley and Sons, New York, 483, 1998.

[9] Benedict, R.P. Fundamentals of Pipe Flow, John Wiley and Sons, New York, 531, 1980.

[10] Friedlander, S.K. Smoke, Dust, and Haze: Fundamentals of Aerosol Dynamics, Oxford University Press, New York, 432, 2000.

[11] Taylor, B.N. and Kuyatt, C.E., "Guidelines for Evaluating and Expressing the Uncertainty of NIST Measurement Results," NIST TN 1297, September, 1994.

[12] Marr, J.A., PAH Chemistry in a Jet-Stirred Reactor/Plug Flow Reactor, PhD Thesis, MIT, 1993.

G: Soot Particle Size Distributions in the PFR Section-No Additives Present

For the present experiments, ethylene was used as the fuel. The air flow rate was kept constant at 175 SLPM and the ethylene fuel flow rate was varied near the soot inception point. Under these flow conditions, the residence time in the WSR was on the order of 11 ms. Data was collected at four equivalence ratios near the soot inception point, namely Φ = 1.8, 1.9, 2.0, and 2.1. The expanded uncertainty in the reported equivalence ratios was ± 3 %. The two main sources of uncertainty in the equivalence ratio resulted from the calibration uncertainty of the fuel and repeatability in the calibrations.

The soot size distribution results are plotted in **Figure 1** for four values of the equivalence ratio. For reasons discussed below, all soot size distributions reported in **Figure 1** were obtained at a nominal dilution ratio of 1000. The CO measurement technique enabled dilution measurements with an expanded uncertainty of ± 9 %. Lognormal fits were applied to the particle size distributions. As can be seen in Figure 8, the particle size distribution data is well represented by the lognormal fits. At Φ = 1.8, there was no indication of flame generated particles. The actual particle concentration obtained by the UCPC for this condition was less than 1 particle/cm^3 and the nominal value of 10^5 cm^{-3} for the size distribution function was primarily a result of the 1000 fold dilution and the low charging probability of nanometer size particles. The peak in the size distribution at Φ = 1.9 was a couple orders of magnitude larger than the background, but also a couple of orders of magnitude less than the values observed at

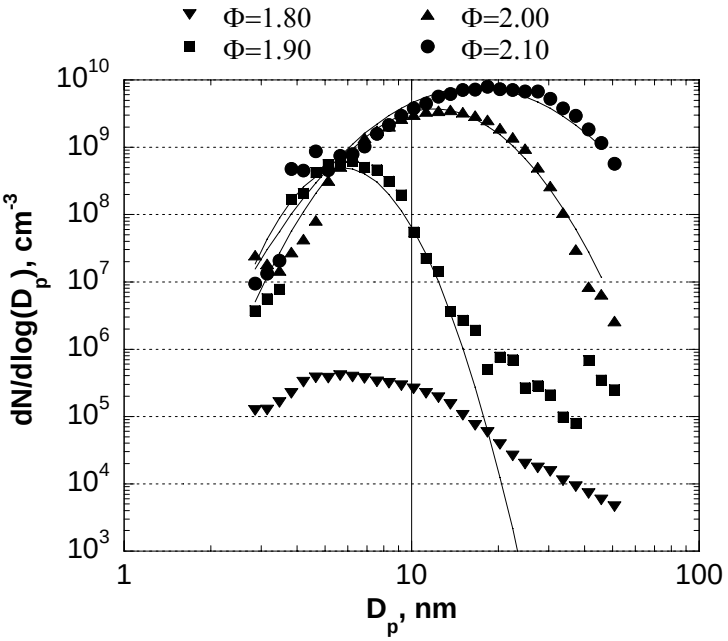

Fig.1 Soot size distributions obtained with the Nano-DMA are plotted for the WSR operating at four equivalence ratios close to the point of soot inception. At Φ = 1.8, there was no indication of flame generated particles. Lognormal fits are applied to the distributions.

the higher equivalence ratios. The peak in the size distribution at Φ = 1.9 occurred at a particle size of 5 nm to 8 nm compared to 15 nm to 16 nm for Φ = 2.0, and a broad peak extending from about 15 nm to 22 nm for Φ = 2.1. The size distribution at Φ = 2.1 was significantly broader

than the other two. These results demonstrate that soot size distributions obtained using our WSR/PFR were sensitive to equivalence ratio.

Soot size distribution measurements were made as a function of dilution ratio. As demonstrated in **Figure 2**, the soot size distributions were not affected by the increased dilution. A critical dilution ratio on the order of 1000 was necessary to mitigate coagulation growth in the sampling line [**1**]. If coagulation were taking place during the dilution process, the size distribution of the more concentrated soot would be shifted to larger particle sizes. This behavior was observed as the dilution ratio was stepped down, from 1000, at a fixed equivalence ratio.

Figure 3 displays the influence of temperature on the measured soot size distributions in the PFR. Temperature measurements were made in the WSR section by two type-B thermocouples of differing bead sizes, 0.81 mm, and 1.08 mm. Due to the very high velocity field in the WSR section, convective heat transfer to the thermocouples dominates the radiative losses to the walls of the WSR. Consequently, the temperatures reported for the WSR have not been corrected for radiative losses. Temperature measurements in the PFR section had to be corrected for radiative losses due the significantly slower velocity field. Three type-B thermocouples of differing bead sizes, 0.38 mm, 0.78 mm, and 1.07 mm, were use to estimate the gas temperature. Each bead was corrected for radiative losses, assuming spherical beads. Iteration of the energy balance of the beads was used to determine the wall temperature, emissivity, and gas temperature. Under sooting conditions (Φ = 2.0), the procedure is complicated by the possibility of soot accumulation on the beads. The effects of the accumulation were estimated by varying the emissivity and bead sizes. Using reasonable changes in these properties only increased the calculated gas temperature by less than 50 °C. Based on this analysis, the expanded uncertainty in the temperature measurements was ± 10 %.

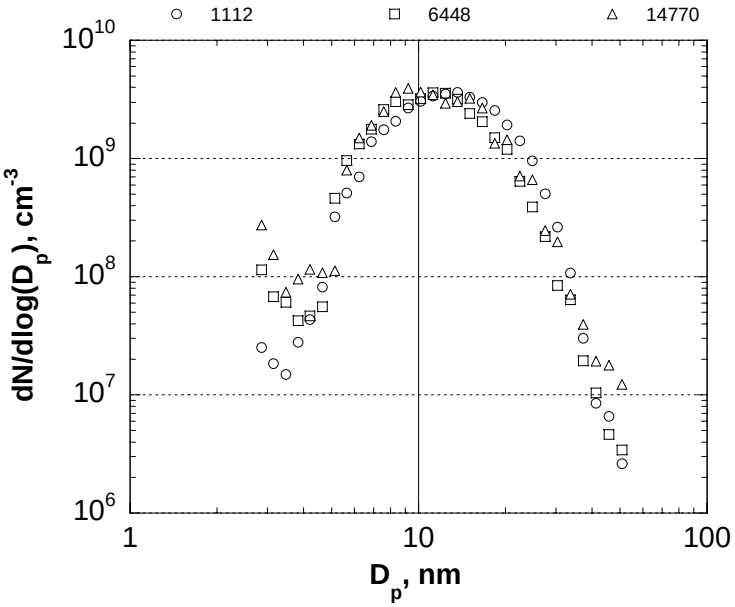

Figure 2 The effect of the dilution ratio on the measured soot size distribution. Experimental conditions: equivalence ratio, Φ = 2.0, dilution ratio varied from 1112 to 14770.

The temperature of the WSR section was altered by adjusting the flow of nitrogen, from 0 SLPM to 30 SPLM. All of the soot size distributions reported in **Figure 3** were obtained at a fixed equivalence ratio of Φ = 2.0. From the figure, an addition of 20 SLPM of nitrogen resulted in a decrease of the measured WSR from 1450 °C to 1340 °C. Under these conditions, the soot size distributions measured in the PFR section did not change significantly. Specifically, the peak particle size was reduced from 10 nm to about 8 nm. When the nitrogen flow was increased to 30 SLPM in the WSR section, the temperature measured in the WSR section decreased to 1285 °C (from 1450 °C under 0 SLPM nitrogen flow). Soot particles were no longer detected within the PFR section under these conditions. The effects of temperature and dilution on soot inception have been well characterized for other flames. A critical temperature for soot inception in diffusion flames has been observed to occur around 1375 °C **[2**]. From our results, at Φ = 2.0, it was observed that soot formation was suspended when the WSR section was reduced to 1285 °C.

TEM Analysis

It was desired to view the particles characterized by the Nano-DMA/UCPC using an independent method. As a result, the particles were sampled using the rapid insertion probe at the same height as the dilution probe (**Figure 4)**. Multiple insertions were required to obtain a high enough particle density to image the particles using the TEM. **Figure 5** displays characteristic images for particles collected at Φ = 1.9, 2.0, and 2.1. It is important to note that the higher magnifications were required to images particles at Φ = 1.9 as compared to Φ = 2.0, and Φ = 2.1. The soot particles observed under the TEM were droplet-like at the soot inception

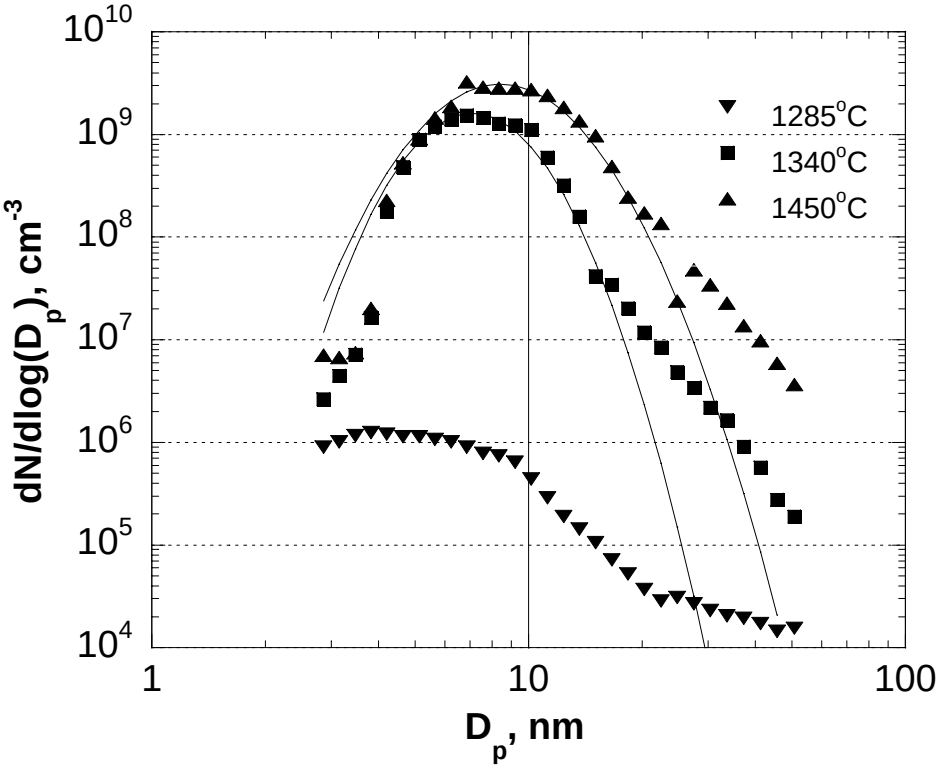

Figure 3 The effect of temperature on the measured soot size distribution. Experimental conditions: dilution ratio 1000, equivalence ratio, Φ = 2.0. Lognormal fits are applied to the distributions.

These observations of soot particle morphology agree qualitatively with the soot inception study of Dobbins *et al.* [**3**]. It is important to note that no particles were observed under the TEM at Φ = 1.8. An image processing technique was used to measure the sizes of the soot particles. Notable differences were observed in the size distribution of the particles measured using the Nano-DMA method as compare to the TEM. In a previous report, we reported on some sizing analysis conducted. However, presently, a far more extensive analysis was performed. This included equipping our TEM with a new, state of the art, digital camera. Our previous work has a larger uncertainty since we were using a film system and this required more intricate calibration to quantify the particle sizes. In any event, differences were observed between the Nano-DMA and TEM sizes.

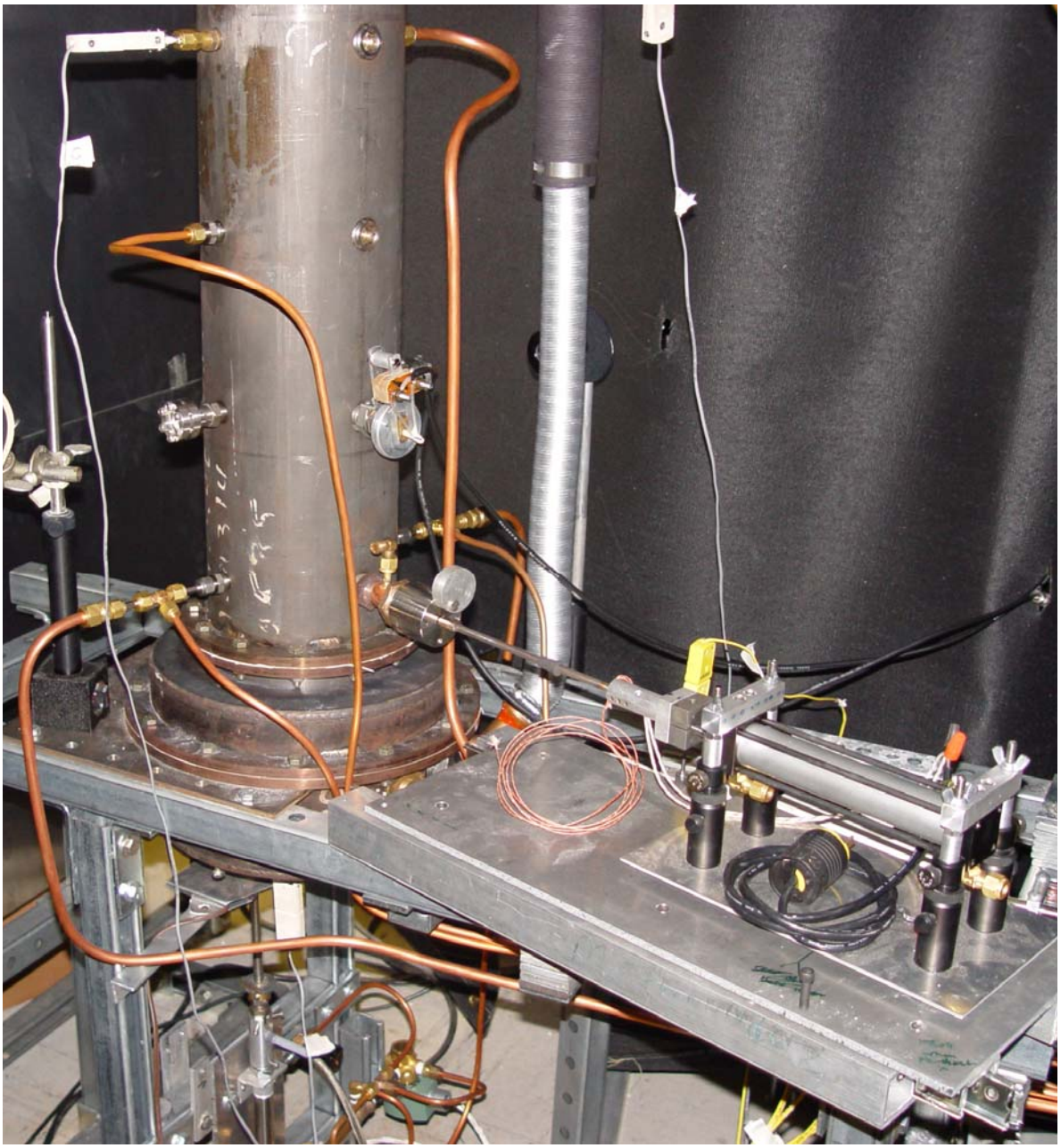

Figure 4 Picture of the TEM sampling probe. The PFR section is shown.

Recently, Zhao *et al*. **[4]** found large differences between the particle sizing from TEM analysis and Nano-DMA analyses as well. In their study, soot was extracted from a premixed ethylene-oxygen-argon flame operated Φ = 2.5. They attributed their differences to the liquid-like structure of the incipient particles and as the nano-particles are extracted from the flame and deposited on the TEM grid, they do not retain their sphericity and spread out onto the grid. Results of our measurements also suggest difficulty in comparing the size quantitatively from the TEM and Nano-DMA analysis. At present, this issue is debated extensively in the combustion literature and these issues cannot be addressed in this report.

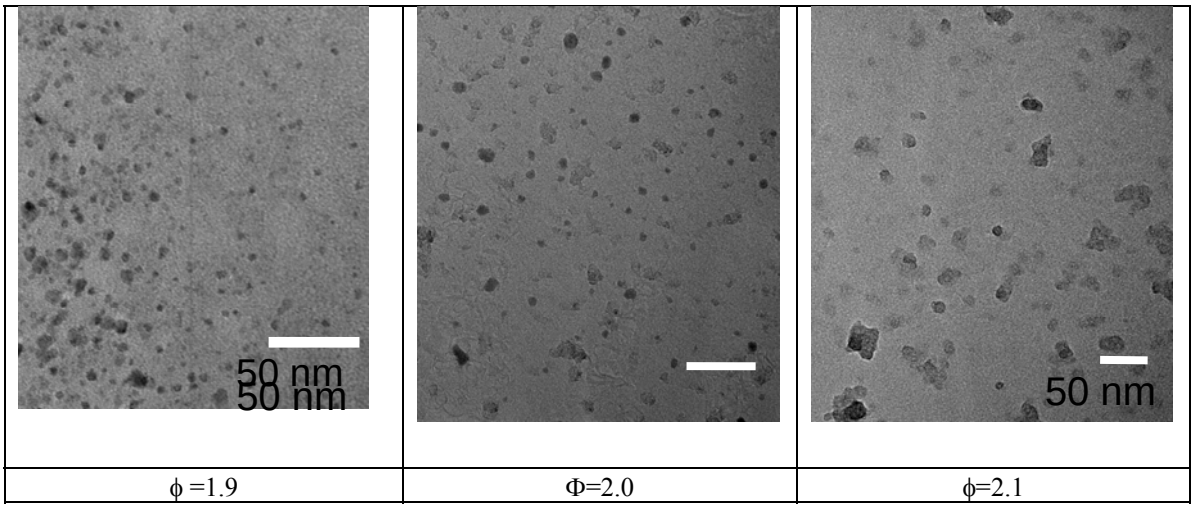

ϕ =1.9	Φ=2.0	ϕ=2.1

Figure 5 TEM Images of Soot Particles Collect for Ethylene/Air Combustion

The soot size distributions obtained from our WSR/PFR were sensitive to equivalence ratio. During particle growth, the particle size distribution changes as a function of time. For coagulation in the continuum regime, the self-preserving distribution (SPD) was obtained for the first time by Friedlander and Wang [**5**] using a similarity transform to the size distribution function, which is independent of the initial conditions. Subsequently, it was shown that the SPD was also valid in the free molecular regime. Vemury and Pratnisis [**6**] studied the self-preserving distributions in the free-molecular and continuum regimes for agglomerates of various fractal dimensions using their coagulation model. The similarity solutions of Vermury and Pratsinis **[6]** have been applied to a wide variety of problems including the calculation of SPD for coagulation in sooting flames [**7**].

Self preserving size distributions corresponding to the particle size distributions measured at $\Phi =$ 1.9, 2.0 and 2.1 were calculated by applying the similarity solutions of Vermury and Pratnisis [**7**]. **Figure 6** shows the soot particle size distribution for equivalence ratios $\Phi =$ 1.9, 2.0, and 2.1 with the calculated SPD's. The width of the lognormal distribution for Φ=1.9 is σ_g=1.31 and this value increases to σ_g=1.48 for $\Phi =$ 2.0, and σ_g=1.65 for Φ=2.1. Vemury *et al*. **[8]** computed σ_g = 1.46 for SPD in the free molecular regime. The particle size distribution obtained at $\Phi =$ 2.0 was closest to the SPD for coagulation in the free molecular regime. In the present experiments, Φ =1.9 was observed to be the soot inception point for the WSR/PFR. Particle coagulation is not expected to be the dominant mechanism of particle growth at particle inception. Therefore, the width of the lognormal distribution was expected to be smaller than the SPD at $\Phi =$ 1.9.

It is crucial to compare the soot size distribution obtained in a WSR/PFR to those measured in laminar flames. As mentioned, particle size distributions measured in a WSR/PFR are expected to be closer to those in actual combustors. Maricq *et al.* **[7**] and Zhao *et al*. **[9]** reported size distribution measurements for soot collected from a pre-mixed ethylene-air flame generated by a 6 cm diameter, water cooled, McKenna burner. The authors used a Nano-DMA similar to the one here and a high dilution probe, also similar to the one reported presently. The size distribution obtained by Maricq *et al.* **[7**] for Φ = 2.06 had a peak at the smallest size measured, independent of the sampling height. This was qualitatively different from our

findings. The reason for the difference may be the different combustion environment for a WSR compared to a premixed burner. In the WSR, the incoming fuel and air are rapidly mixed with the products of combustion including incipient soot, CO, PAHs, and free radicals; whereas, in a premixed burner, the combustion products are not back mixed into the fuel and air. The difference in mixing may also affect the size distribution. The soot inception region may terminate within the WSR so that only particle growth is occurring in the PFR section where the particles were sampled. The very low particle number concentrations observed at Φ = 1.9 might be a result of the WSR/PFR being operated so close to the soot inception point. This issue is addressed in section 2.6 using additives coupled with the coannular probe.

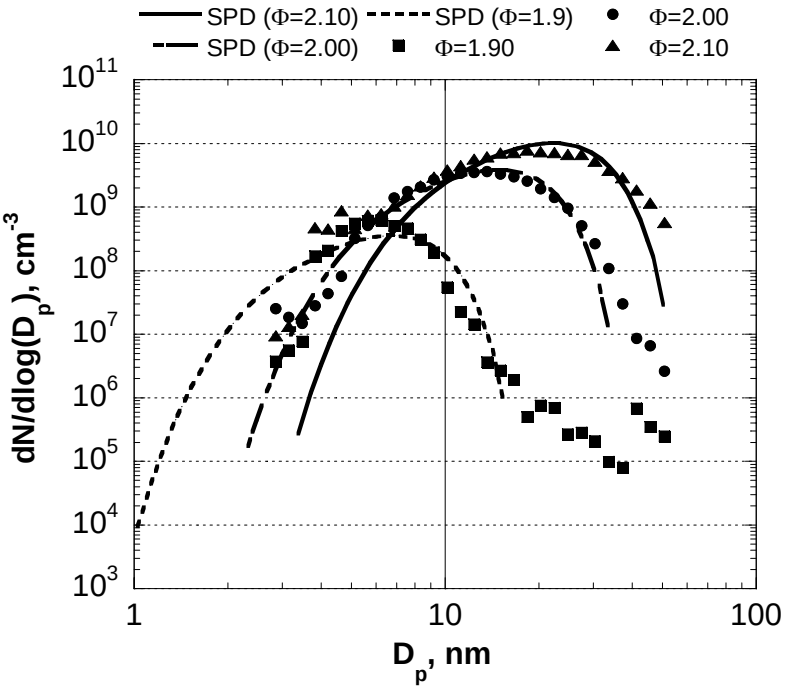

Figure 6 Comparison to self preserving size distribution at free molecular regime for three equivalence ratios.

Soot Particle Size Distributions in the WSR/PFR Section-Additives Present

Ethylene was used as the fuel and the air flow rate was kept constant at 175 SLPM and the ethylene fuel flow rate was varied near the soot inception point. Under these flow conditions, the residence time in the WSR was on the order of 11 ms. Data was collected at equivalence ratios near the soot inception point, namely Φ = 1.8 and 2.0, at different residence times in the PFR and WSR sections. Under the flow conditions of this study, the temperature of the WSR was nominally 1680 K for Φ = 2.0 and 1635 K for Φ = 1.8 with 30 SLPM of nitrogen. Under non-sooting conditions (Φ = 1.8 with 30 SLPM of nitrogen), the gas temperatures were determined to be 1420 K at the bottom most port (closest to the WSR section, Port #1) and 1340 K at Port #3 (305 mm, 12" above the bottom most port). The expanded uncertainty (95 % confidence level) in the temperature measurements was ± 10 %.

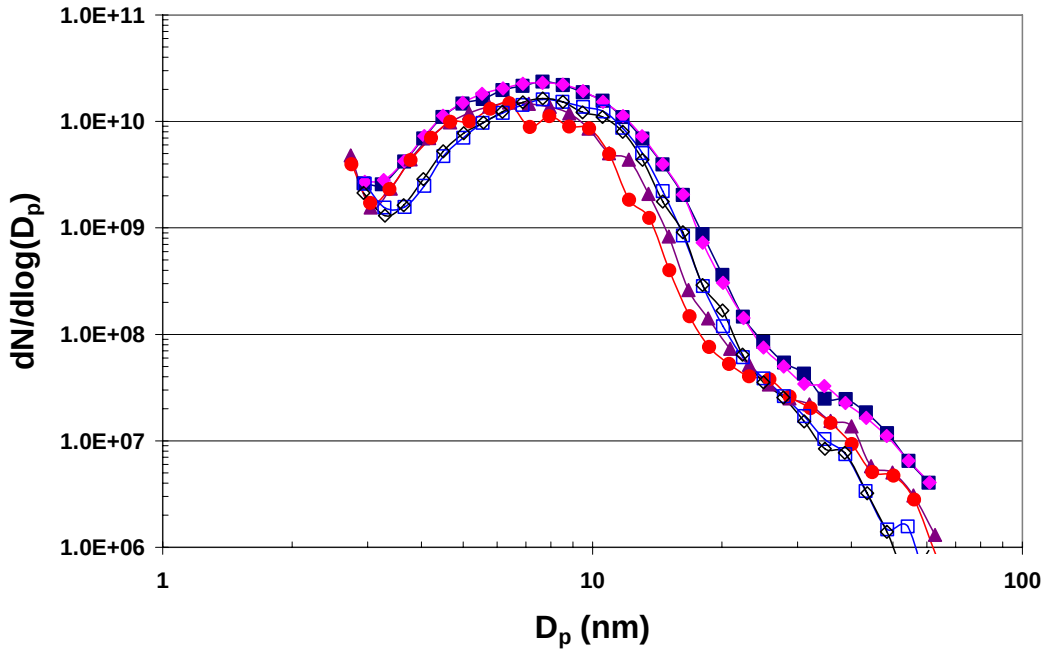

Figure 7 Soot particle size distribution in the PFR section of the WSR/PFR at two different residence times and two different probe designs for ethylene/air (Φ = 2.0, 175 SLPM air): (■) Linear probe, Port #1, Scan #1; (◆) Linear probe, Port #1, Scan #2; (▲) Coannular probe, Port #1, Scan #1; (●) Coannular probe, Port #1, Scan #2; (□) Linear probe, Port #3, Scan #1; (◇) Linear probe, Port #3, Scan #2.

The soot size distribution results are plotted in **Figure 7** for two different residence times and the two different probe configurations for Φ = 2.0. All of the soot size distributions reported were obtained at a nominal dilution ratio of 1000. The CO measurement technique enabled dilution measurements with an expanded uncertainty (95 % confidence level) of ± 9 %. Multiple size distributions were measured for each residence time and probe configuration. Two representative scans are shown in each figure to illustrate the stability and repeatability of the measurements. Two different resident times were examined with the linear diluter in the PFR section of the reactor using the bottom most port (closest to the WSR section, Port #1) and Port #3 (305 mm, 12" above the bottom most port). Under the flow conditions, the residence time difference between the two ports was on the order of 28 ms. The peak in the size distribution at the bottom port was nearly identical to that of the longer residence time port. The peak in the size distribution for both residence times occurred at a particle size of 7 nm. One notable difference was the net decrease in the number of particles associated with the longer residence times. Radial temperature measurements in the PFR section showed an approximate temperature decrease of 100 °C near the wall surface, indicating that thermophoretic losses may be the cause of the net decrease in particle concentrations. Using the correlation of Romay *et al.* **[10]**, the thermophoretic losses were estimated to be 10%. This was significantly smaller than the observed differences; the correlation was made at lower temperatures and for fully turbulent flow and the losses are sensitive to these parameters.

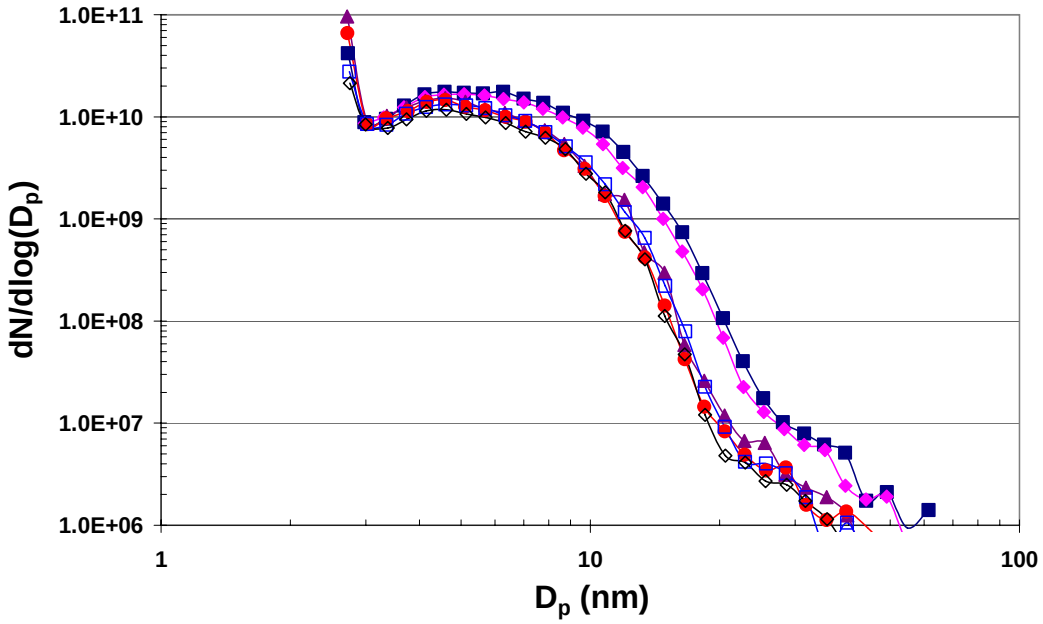

Figure 8 Soot size size distribution in the WSR section of the WSR/PFR at different cross section radii for ethylene/air (Φ = 2.0, 175 SLPM air) using the coannular dilution probe: (■) WSR surface, Scan #1; (◆) WSR surface, Scan #2; (▲) WSR half radius, Scan #1; (●) WSR half radius, Scan #2; (□) WSR centerline, Scan #1; (◇) WSR centerline, Scan #2.

It was desirable to examine the how the design constraints of the coannular dilution probe effected the soot particle size distribution. The soot particle size distribution was measured at the bottom most port using the coannular probe. The coannular soot particle size distribution begins to diverge from the linear diluter at particle sizes above 6 nm. Above 6 nm, the differences were on the order of 60%. It is important to note that the orifice in the coannular probe was perpendicular to the flow field of the PFR. As the coannular probe is not sampling isokinetically in this configuration, it is reasonable that some loss of larger particles would occur. This limitation in the highly turbulent environment of the WSR should not impose a significant problem. These results demonstrate that soot size distributions obtained using our WSR/PFR at Φ = 2.0 were not sensitive to residence time in the PFR section and the coannular nano-DMA dilution probe is an acceptable design for sampling in the WSR section of the WSR/PFR.

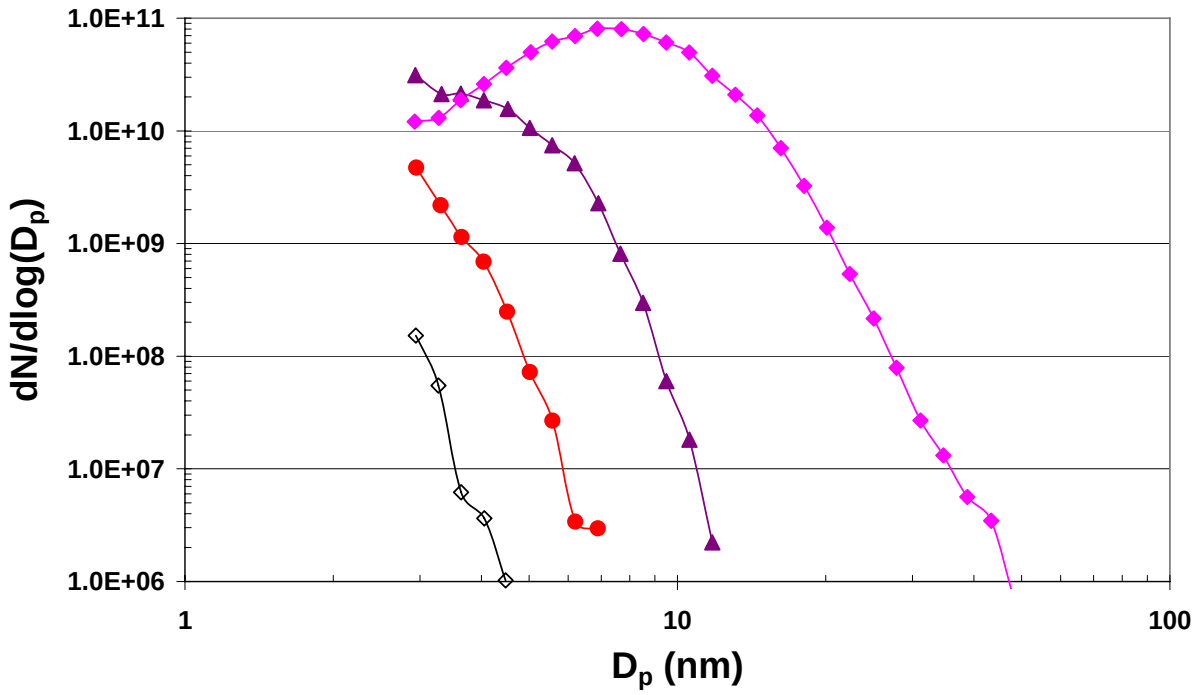

Figure 9 Soot particle size distribution using the linear probe in the PFR section of the WSR/PFR at two different residence times for ethylene/air/nitrogen with benzene injection(Φ = 1.8, 175 SLPM air, 30 SLPM nitrogen): (■) no Benzene injection, Port #3; (●) 0.52 ml/min Benzene injection, Port #3; (▲) 0.75 ml/min Benzene injection, Port #3; (◆) 1.23 ml/min Benzene injection, Port #3; (◇) 1.23 ml/min Benzene injection, Port #1.

Figure 8 displays the soot size distribution results for different WSR torriod cross section radii of the flow reactor. Measurements were made at three radii: the centerline of the WSR torriod (r = 0 mm), the half radius of the torroid (r = 8 mm), and the bottom surface of the torriod (r = 16 mm). At each of the different cross section radii, the soot size distributions showed a significant increase in the smaller particle sizes resulting in a peak in the size distribution at a particle size smaller than that observed for the bottom most port in the PFR section. The soot size distributions at the half radius and centerline are nearly identical, indicating the efficiency of the mixing processes of the WSR reactor. The peak in the size distribution for the centerline and half radius occurred at a particle size of 4.5 nm, and approximately 5 nm at the surface. These results showed that soot inception process is occurring in the WSR section of the reactor and that the WSR is creating a well mixed environment.

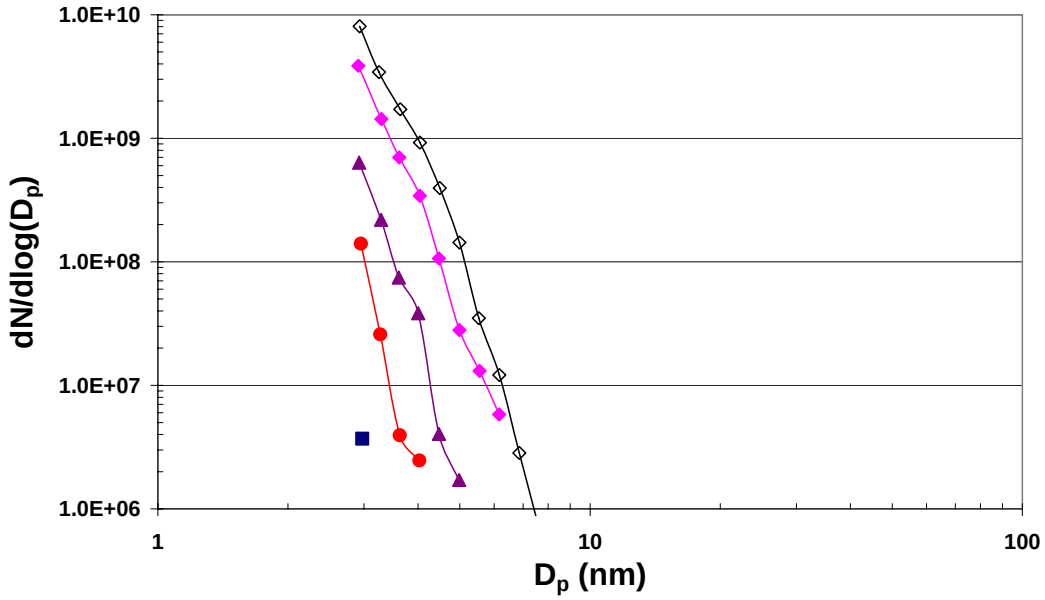

Figure 10 Soot size size distribution using the linear probe in the PFR section of the WSR/PFR for ethylene/air/nitrogen with naphthalene/methanol injection (Φ = 1.8, 175 SLPM air, 30 SLPM nitrogen): (■) 1.90 ml/min Methanol injection, Port #3; (●) 0.96 ml/min Naphthalene/Methanol injection, Port #3; (▲) 1.41 ml/min Naphthalene/Methanol injection, Port #3; (◆) 1.90 ml/min Naphthalene/Methanol injection, Port #3; (◇) 2.47 ml/min Naphthalene/Methanol injection, Port #3.

As mentioned earlier in Section 2.6, in the WSR and PFR section, the soot size distributions did not show the pronounced initiation peaks observed by Maricq *et al.* **[8]** and Zhao *et al.* **[2]** in pre-mixed ethylene-air flames generated by a 6 cm diameter, water cooled, McKenna burners. To determine if the lack of an inception peak was the result of the mixing characteristics of the WSR and to begin to investigate the importance of aromatic and PAH species thought to be important in the soot inception process, the fuel additive probe was installed in the transition region between the WSR and PFR. Although the transition region is difficult to characterize, the additive injector could not be inserted through the flow straightener without significant modification to the flow straightener. For the aromatic seeding, the flow WSR was operated under non-sooting conditions, specifically, $\Phi = 1.8$. Nitrogen (30 SLPM) was added as a diluent to enable long-term operation of the reactor within safe operating temperatures. Benzene and naphthalene were selected as the additives of choice as they are the smallest aromatics, and have relatively low boiling points. **Figure 9** displays the soot size distribution measurements for the benzene injection at two different residence times in the PFR section. At benzene flow rates less than 0.3 ml/min, no particle inception was observed at the longest residence times investigated. Appreciable formation of incipient particles was observed once benzene flow was increased to above 0.52 ml/min. As the flow rate was increased further, the peak in the size distribution shifted away from the smallest particle size. At this highest flow rate, the nano-DMA dilution probe was translated to the bottom most port. The soot size distribution changed significantly, the peak in the distribution shifted to the smallest particle sizes and significantly fewer particles were detected. Obviously, the addition of benzene would result in a shift in the global equivalence ratio of the mixture. At 0.52 ml/min, approximately 575 ppm of benzene was being injected into the reactor, which resulted in an increase of the global equivalence ratio to approximately 1.82. At 0.75 ml/min and 1.23 ml/min, the global

equivalence ratio increased to 1.84 and 1.86 respectively. However, if the ethylene flow rate was increased into the WSR to these equivalence ratios, no particle formation was observed.

In order to allow injection of naphthalene into the PFR, naphthalene had to be dissolved in a solvent. Methanol was selected at the solvent since naphthalene is relatively soluble in methanol, methanol would not significantly alter the global equivalence ratio, and was not likely to cause soot inception. **Figure 10** displays the soot size distribution measurements for two different solutions, a naphthalene/methanol solution (90.2 %mass methanol, 9.8%mass naphthalene) and neat methanol at Port #3 in the PFR section. For neat methanol, no particle inception was observed for flow rates up to 1.90 ml/min, a global equivalence ratio of 1.84. For the naphthalene/methanol solution, particle inception was observed to start at a flow rate of 0.96 ml/min. As the flow rate was increased further, the total concentration of particles increased, however, the peak in the size distribution always remained with the smallest particle size. The addition of the naphthalene/methanol solution would result in a shift in the global equivalence ratio of the mixture. At 0.96 ml/min, approximately 46 ppm of naphthalene was being injected into the reactor, which resulted in an increase of the global equivalence ratio to approximately 1.82. At 1.90 ml/min (≈125 ppm of naphthalene) and 2.47 ml/min (≈155 ppm of naphthalene), the global equivalence ratio increased to 1.85 and 1.86 respectively. These results clearly demonstrate that soot inception process can be initiated though the seeding of aromatic species into the WSR/PFR

To begin to elucidate the effects of benzene and naphthalene seeding on sooting inception, the sooting tendencies of the two were compared. At 0.3 ml/min of benzene seeding (≈310 ppm), no particle inception was observed, however, at significantly lower seeding levels of naphthalene, 0.47 ml/min (≈155 ppm of naphthalene) particle inception was observed. Furthermore, the particle inception process is more sensitive to naphthalene and benzene addition than ethylene. This suggests that naphthalene and benzene have a stronger chemical effect than ethylene. Specifically, the radicals and intermediate species responsible for the formation of benzene are the more rate limiting than the pathways from benzene to soot inception. Similarly, the radicals and intermediate species responsible for the formation of naphthalene are even more rate limiting than those for benzene, as the sooting process is more sensitive to the naphthalene injection.

In summary, coupling the soot size distribution measurements in the PFR section with those measured in the WSR section showed that soot inception process is occurring in the WSR section of the reactor and that the WSR is creating a well mixed environment. The results demonstrate for the first time the sensitivity of the sooting process and size distribution to the seeding of aromatic species in a WSR/PFR.

References

[1] Manzello, S.L., Mulholland, G.W., Donovan, M.T., Park, K., Zachariah, M.R., ans Stouffer, S., "On the use of a well stirred reactor to study soot inception," 4th Joint Meeting of the US Sections of the Combustion Institute, Philadelphia, PA, March 2005.

[2] Glassman, I., *Proc. Comb. Inst.* 22: 295-311(1988).

[3] Dobbins, R.A., Fletcher, R.A., and Chang, H.C., *Combust. Flame* 115: 285-298 (1998).

[4] Zhao, B., Uchikawa K., and Wang, H. Proc. Combust. Inst. 31:851-860 (2007).

[5] Friedlander, S.K. and Wang, C.S., *J. Coll. Interface Sci*. 22:126-135 (1966).

[6] Vermury, S. and Pratsinis, S.E., *J. Aerosol Science* 26:175-185 (1995).

[7] Maricq, M.M., Harris, S.J., and Szente, J.J.,*Combust. Flame* 132: 328-324 (2003).

[8] Vermury, S., Kusters, K.A., and Pratsinis, S.E., *J Coll. Interface Sci*. 165:53-59 (1994).

[9] Zhao, B., Yang, Z., Wang, J., Johnston, M.V., and Wang, H., *Aerosol Sci. Tech*. 37:611 620 (2003).

[10] Romay, F. J., S. S. Takagaki, D. Y. H. Pui and B. Y. H. Liu. (1998) *J. Aerosol Sci, 29*(8), 943-959.

H Gas-Phase Analysis

Over the final year, our GC/MS techniques were refined to quantify the gas-phase species with and without the presence of additive introduced into the transition regime between the well stirred reactor and plug flow reactor sections (WSR/PFR). GC/MS analysis, using a 30 m x 0.32 mm ID Agilent J&W DB-1 column with a 3 μm film thickness, was performed on combustion samples extracted from the NIST WSR/PFR sections for a given equivalence ratio and known residence time. Four diagnostic ports were used, numbered 1 to 4, with a residence time increase of ~10-15 ms between ports. Port 1 was closest to the exit of the WSR section. Each effluent gas sample was introduced onto the GC column for separation and then the sample stream was split and directed to both the MS and GC flame-ionization detector (FID) for simultaneous analysis. The MS was used to identify and the FID was used to quantify all individual species. Gas standards of known concentrations were used to calibrate the system, establishing expected GC column retention times for known species and to calculate the GC FID response factors used to quantify the species based on an effective carbon-atom number basis [**1-2]**. Where calibration standards were not available, heptane was the reference material used for quantification of the lighter hydrocarbon species (up to C_5). Benzene was used as the reference material for the aromatic hydrocarbon species (C_6 and larger).

When sampling hot combustion gas, there is the need to quench the sample to capture the species concentrations at the point of extraction, but there is also a concern with cooling the sample gases to the point that certain species are condensed out. Initially, a ceramic sampling probe was designed but the quenching times were determined to be inadequate as the combustion reactions were continuing to occur within the sampling lines upstream of the GC versus being quenched at the sampling point. A water cooled probe was also tested but the probe temperatures were too cold causing the condensation of water and other species within the sampling line.

To mitigate these problems, an oil cooled probe was designed, shown in **Figure 1**, which quenched and maintained the sample gases at a temperature of 150 °C, addressing both concerns. Three concentric stainless steel (SS) tubes were used to create a coolant circulation path, cooling the sample gases in the centermost SS 1/8" OD tube to 150 ° C. This inner 0.016", 1/8" OD tube was secured by an inconel cap welded to the outer SS 3/8" OD tube. The coolant was maintained at temperature by a recirculating heated bath. The oil cooled design allowed for adequate quenching times of less than 3 ms **[3**]. With the oil cooled probe, the gases were maintained at 150 °C throughout the sampling system up to the point of introduction into the GC. A valving system consisting of twelve 1 ml sample loops was employed to aid in sample storage and processing efficiency, enabling the analysis of multiple samples at varying conditions during a single reactor run. The GC analysis temperature profile ranged from -60 °C up to 280 °C, allowing for the quantification of light hydrocarbons and heavier polycyclic aromatic hydrocarbons with a single effluent gas sample. The deviation in the measured concentrations was less than ±10% for the lighter hydrocarbons and less than ±30% for most of the heavier hydrocarbons (C_6 and above).

Aromatic additives were introduced into the WSR/PFR system through an injector probe. The liquid additive was introduced at varying flowrates (0.3 to 2.5 ml/min) into the heated nebulizer through the use of a peristaltic pump. Argon gas was used to drive the nebulizer, creating droplets ranging in size from 10 to 30 μm. The jet of the nebulized additive

was sprayed into and vaporized in a quartz mixing chamber heated to 200 °C. From there, the vaporized additive is introduced into the WSR/PFR system.

The additive injection probe was installed in the transition regime between the WSR and the PFR, allowing the additive to participate in the combustion product reactions taking place in the PFR section. For the aromatic seeding, the flow reactor was operated under non-sooting conditions; specifically, Φ = 1.8. At these operating conditions, benzene and ethylbenzene were introduced into the system to study the subsequent additive effects on the gas phase species concentration and soot size distributions. In all cases, the controlled introduction of the aromatic additive induced the formation of soot particles.

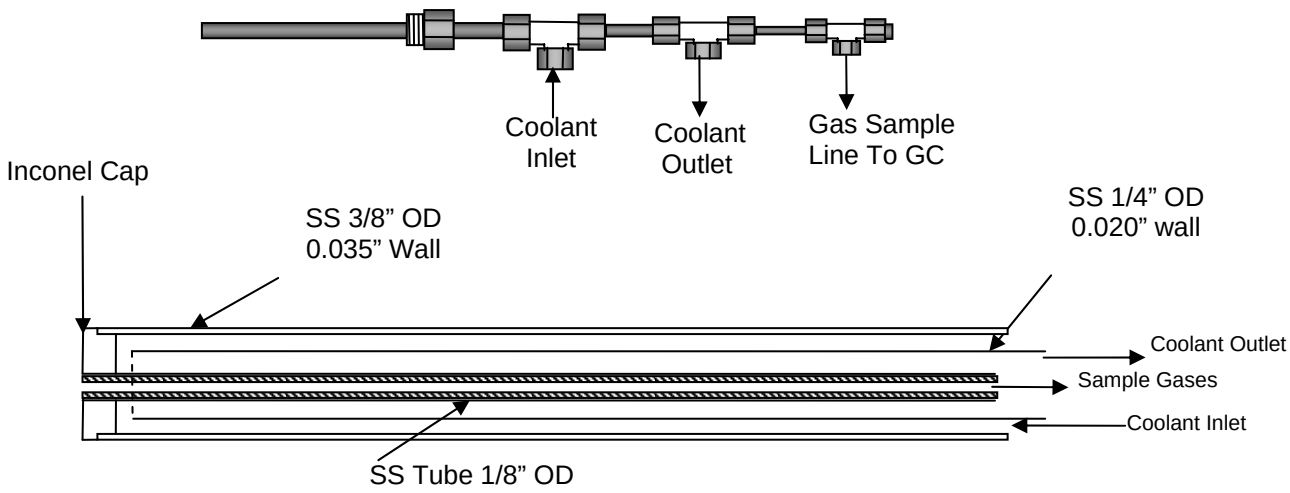

Figure 1 Schematic of oil cooled gas sampling probe

Table 1 provides the data depicting the change in gas phase species concentration with increasing residence time (WSR ~ 0-11 ms, Port 1 ~ 15 ms, Port 4 ~ 60 ms) and equivalence ratio (Φ = 1.8-2.1) for a representative range of combustion products found in the PFR effluent gas. An equivalence ratio of 1.8 is considered a non-sooting condition within the reactor, whereas Φ = 1.9 is considered the equivalence ratio at which soot inception starts to occur under normal reactor operating conditions, utilizing an ethylene-air flame. At Φ = 2.0 and 2.1, the reactor is considered to be operating under fully sooting conditions.

In general, the overall trends to note are the expected increases in lighter hydrocarbons (C_1-C_5) as the fuel concentration increases with increasing equivalence ratio. Along with this, there is a significant increase in the heavier hydrocarbons (>C_5) as residence time increases under sooting conditions (Φ = 2.0 – 2.1), similar to what has been noted by previous researchers [4-6]. Some of the lighter hydrocarbons exhibit a slight decrease in concentration as the measurement moves from the WSR portion to Port 1 of the PFR portion of the apparatus. Although, the decreases are not especially significant, the behavior can be attributed to slight

temperature losses that occur when transitioning from the well-stirred to the plug flow section of the apparatus. Finally, while the heavier hydrocarbons increase in concentration with increasing residence times, certain lighter hydrocarbon such as acetylene decrease in concentration due to their consumption during the formation of the heavier species.

Species Name	Φ = 1.8 Concentrations (ppm)			Φ = 1.9 Concentrations (ppm)			Φ = 2.0 Concentrations (ppm)			Φ = 2.1 Concentrations (ppm)		
	WSR	Port 1	Port 4	WSR	Port 1	Port 4	WSR	Port 1	Port 4	WSR	Port 1	Port 4
Methane	4180	3670	3940	4140	3860	4660	5500	5440	5710	7190	6940	7260
Ethylene	162	79	131	82	90	111	138	150	194	289	175	465
Acetylene	12960	8800	8250	13750	9350	8670	18730	14700	12380	23280	17850	10710
Propyne	98	61	36	91	39	39	147	76	64	288	117	52
Vinylacetylene	65	25	24	54	27	20	75	46	40	109	57	100
Diacetylene	518	294	245	689	268	223	1072	608	438	1330	873	308
Benzene	18	22	27	13	18	35	29	56	96	54	108	164
Naphthalene	1.6	2.9	6.0	1.0	1.8	4.6	2.9	9.4	19	7.3	23	41
Acenaphthelene	1.6	4.1	8.9	0.89	2.3	7.8	4.0	14	32	10	38	54
Fluorene	0.09	0.29	0.38	0.05	0.07	0.31	0.17	0.35	0.75	0.46	0.95	2.3
Anthracene	0.11	1.8	2.4	0.04	0.36	1.6	0.15	1.4	3.4	0.44	2.9	7.8
Fluoranthene	0.17	0.23	0.65	0.04	0.11	0.38	0.13	0.67	1.8	0.41	2.5	13
Pyrene	0.28	0.27	0.94	0.11	0.13	0.42	0.39	1.1	2.9	1.1	4.2	21

Table 1: GC/MS Baseline Data

Figure 2 shows the change in gas phase species concentration with increase in residence time with the addition of 725 ppm (0.66 ml/min) of benzene for a representative range of combustion products found in the PFR effluent gases. The introduction of benzene increases the global equivalence ratio to approximately 1.82 which is still a non-sooting condition for the ethylene-air flame. If the ethylene flow rate was increased into the WSR to these equivalence ratios, no particle formation is observed. The additive data are normalized relative to the baseline data of Φ = 1.8 with no additive. **Table 2** provides the measured gas phase species concentrations (ppm) at these conditions.

The results from benzene addition appear to be illustrative of a continual formation of ring structures. As residence times increase, higher molecular weight molecules are being formed at higher concentrations. Particularly impressive is the precipitant increase of the fluoranthene and pyrene structures between the 3rd and 4th ports. In contrast, the smaller non-aromatic compounds appear to relatively unaffected by the introduction of the additives. This response is similar to the behavior reported by Anderson, *et al.* in their study of flames doped with alkylbenzenes **[4]**. From a mass balance consideration it would appear that a significant quantity of the benzene is being recovered in the larger ring compounds, their respective rings remaining intact [**5**].

Ethylbenzene was another liquid aromatic that was introduced into the reactor at a flowrate of 0.66 ml/min (526 ppm) and an ethylene-air equivalence ratio of 1.8. Once again the aromatic seeding triggered the formation of soot particles under typically non-sooting conditions. These findings, normalized relative to the baseline data of Φ = 1.8 with no additive, are presented in **Figure 2** along with the tabulated data in **Table 3**.

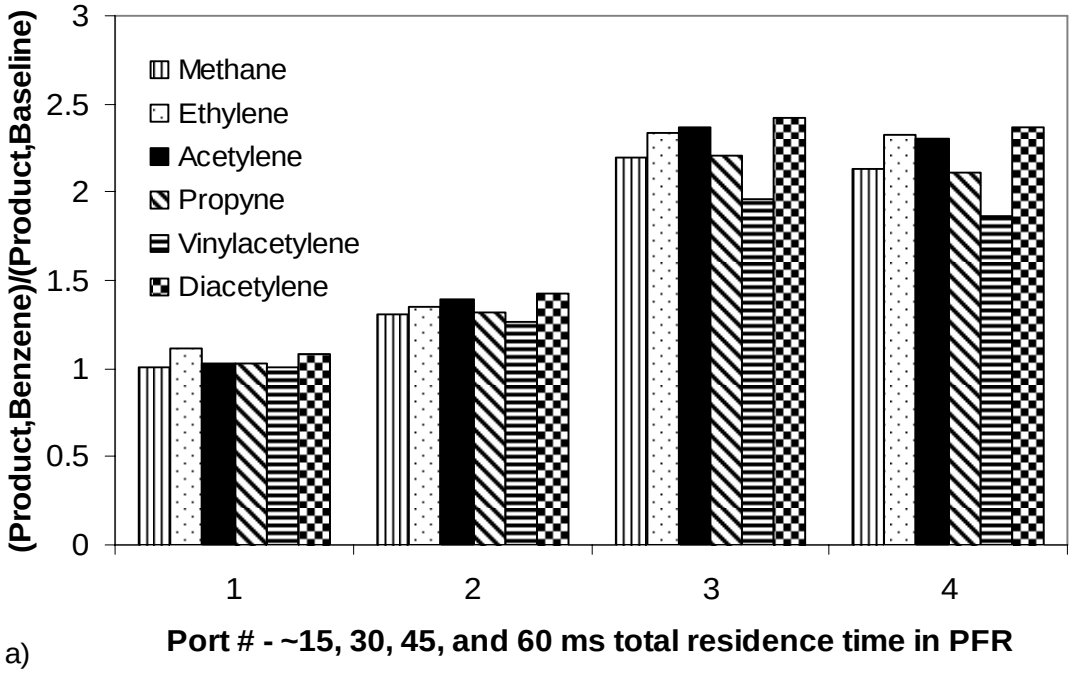

a)

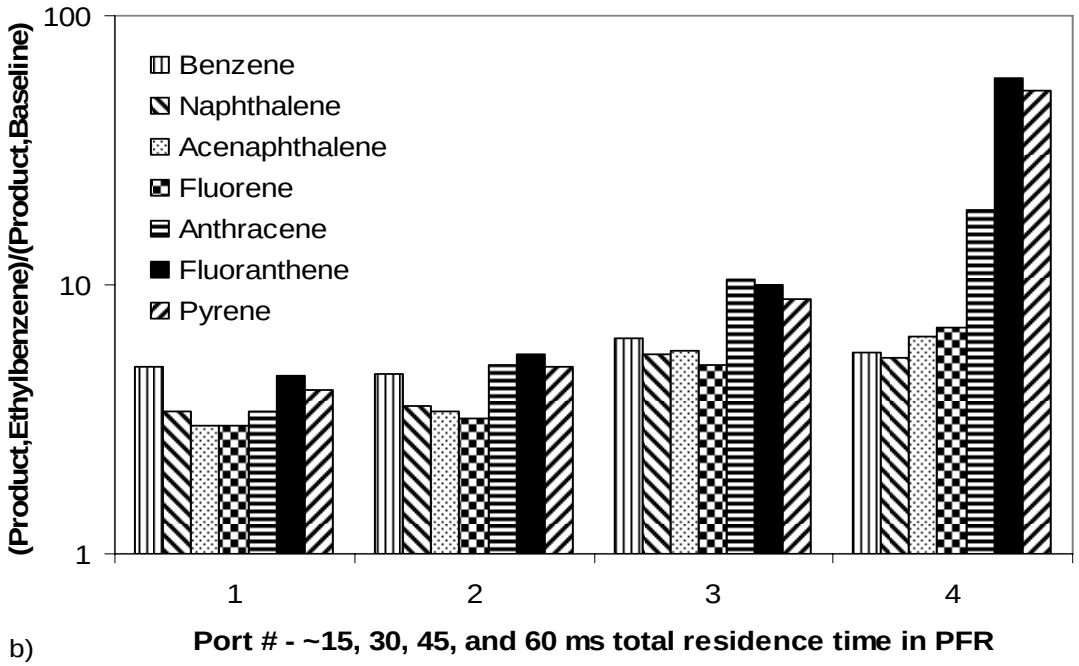

b)

Figure 2 Comparison of changes in gas phase species concentration as a function of increasing residence time with the addition of 725 ppm of benzene at ~1300 K and 1 bar. a) lighter hydrocarbons (less than C_6) b) heavier hydrocarbons (C_6 or greater)

Species Name	Port 1 Concentration (ppm)	Port 2 Concentration (ppm)	Port 3 Concentration (ppm)	Port 4 Concentration (ppm)
Methane	5000	5157	5127	5179
Ethylene	172	168	172	188
Acetylene	14227	14106	13525	13189
Vinylacetylene	45	41	39	38
Diacetylene	551	520	482	462
Benzene	287	265	250	260
Naphthalene	43	50	56	63
Acenaphthalene	50	71	87	99
Fluorene	2.6	3.0	2.8	3.0
Anthracene	4.1	7.1	9.0	16
Fluoranthene	1.7	3.3	5.0	26
Pyrene	2.4	5.0	7.6	40

Table 2: Φ = 1.8, 725 ppm Benzene Additive

Species Name	Port 1 Concentration (ppm)	Port 2 Concentration (ppm)	Port 3 Concentration (ppm)	Port 4 Concentration (ppm)
Methane	4253	4473	4579	4684
Ethylene	104	108	118	122
Acetylene	10147	10006	13525	13189
Vinylacetylene	29	27	26	26
Diacetylene	384	360	348	323
Benzene	92	93	97	99
Ethylbenzene	0.37	0.29	0.26	0.16
Naphthalene	21	21	22	22
Acenaphthalene	29	34	38	38
Fluorene	1.1	0.85	0.84	0.82
Anthracene	2.9	2.9	3.4	3.5
Fluoranthene	1.7	1.5	1.9	2.4
Pyrene	2.4	2.4	3.0	3.9

Table 3: Φ = 1.8, 526 ppm Ethylbenzene Additive

The linear species exhibit a similar response to that with benzene addition and show little change in concentration. The difference between the two additive conditions occurs when observing the formation of the heavier aromatic species. It appears that there are products formed from benzene decomposition which lead to larger aromatic ring formation, that are not present in ethylbenzene decomposition. This is evident due to the less than impressive perturbation of the heavier aromatic species. While an increase their respective concentration is noted, the effects are much less impressive in comparison that exhibited with benzene addition. Additionally, the largest concentration increases are seen at the shortest residence times (Port 1) with the ethylbenzene addition in comparison to that of the benzene addition where the sharpest increases are noted at Ports 3 and 4.

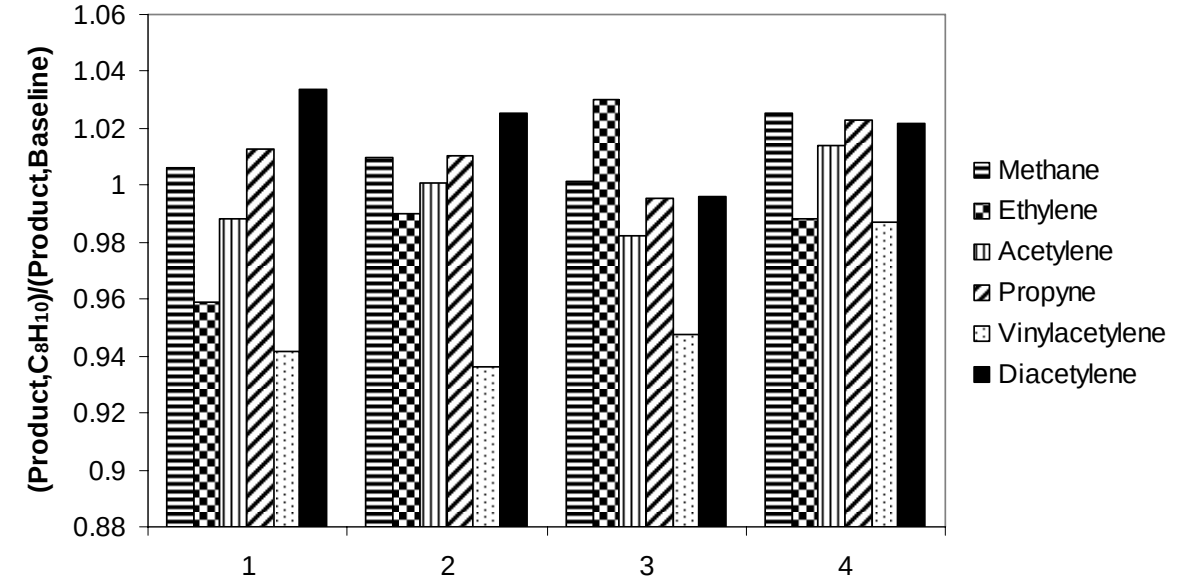

a)

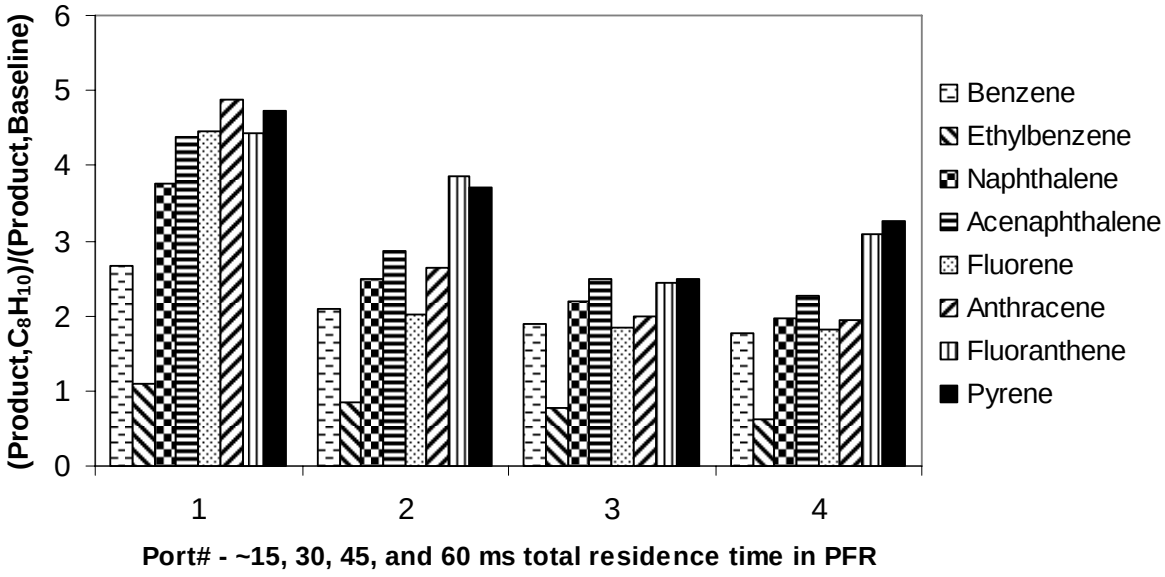

b)

Figure 3 Comparison of changes in gas phase species concentration as a function of increasing residence time with the addition of 526 ppm of ethylbenzene at ~1300 K and 1 bar. a) lighter hydrocarbons (less than C_6) b) heavier hydrocarbons (C_6 or greater)

The most likely breakdown product from ethylbenzene is the benzyl radical. It would appear that under the present conditions of 1300 K, 1 bar pressure and residence times increasing from 15 to 60 ms, the condensation products of benzyl and other reactive radicals do not contribute to the significant formation of larger aromatic rings. Furthermore, the breakdown of benzyl leads to concentrations of benzene or its breakdown products that are much smaller in comparison to those formed when benzene is directly introduced. A possible

mechanism addressing the ethylbenzene additive behavior could involve the rapid breakdown of the benzyl radical, formed from ethylbenzene decomposition, to smaller precursors and direct contributions from the phenyl radical in benzene decomposition. Under these conditions, it appears that the benzyl radical decomposition favors ring opening, contrasting the benzene additive condition where the integrity of the ring is maintained.

In addition to gas-phase analysis, a detailed analysis was performed for the soot collected on the filter samples. Particulate material is removed from the gas stream using quartz fiber filters. Removal of the particulates is also necessary to protect the sensitive components of the sample collection system and the gas chromatograph. In prior work, some preliminary analysis was completed for filter samples without the presence of additive species. This year, a detailed analysis was completed for soot samples collected with and without the presence of benzene additives.

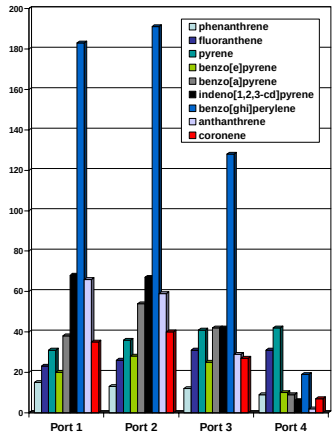

Figure 4Selected PAHs on Top Filters-No Benzene

Triplicate sets of filters (**see figure 5**) were collected at increasing residence times, from Port 1 to Port 4, (correlating to an increase of 10 to 15 ms between ports). Gas chromatography/mass spectrometry (GC/MS) analysis of filters for PAHs was performed. A pressurized fluid extraction and sep-pak clean-up was completed prior to GC/MS analysis. PAH concentrations were higher on particles collected in presence of benzene additive, particularly for higher molecular PAHs such as anthanthrene and coronene **(see figure 2 as compared to figure 3**).

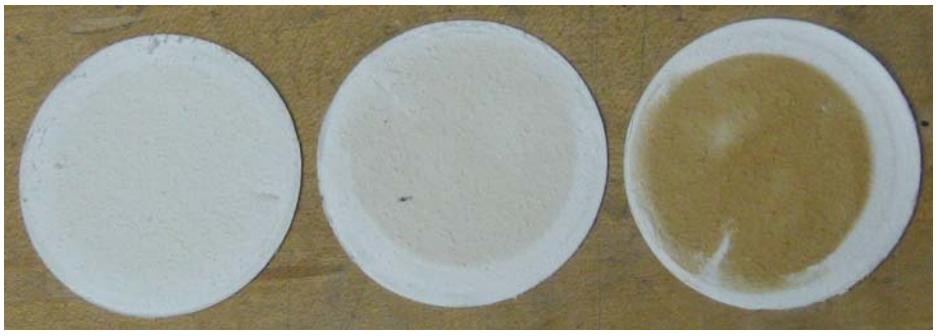

Figure 5 Filter used for analysis. From left to right- Port 1; Port 2; Port 3

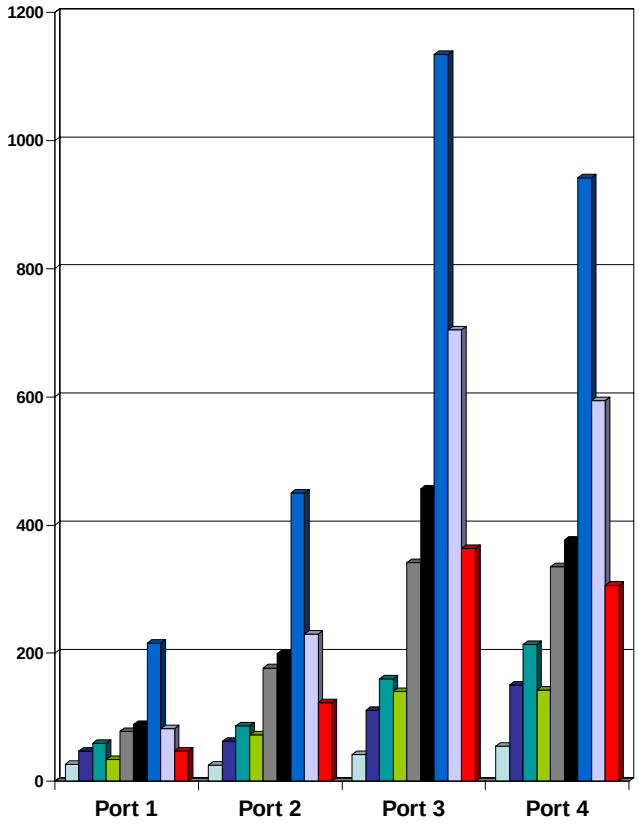

Figure 6 Selected PAHs on Top Filters-Benzene Addition

References

[1] Scanlon, J.T. and Willis, D.E., Journal of Chromatographic Science 23 (1985) 333-340.
[2] Kallai M. and Balla J.,, Chromotographia 56 (2002) 357-360.
[3] Vaughn, C.B., Howard, J.B., and Longwell, J.P., Combust. Flame 87 (1991) 278-288.
[4] Anderson, H.. McEnally, C.S., and L. D. Pfefferle, L.D., Proc. Combust. Inst. 28 (2000) 2577-2583.
[5 Lam, F.W., Longwell, J.P., and Howard, J.B., Proc Comb. Inst. 23 (1991) 1477-1484.
[6] Smyth K.C. and Mallard, W.G., Comb. Sci. and Tech. 26, 35-41(1981).

I: Use of Laser Diagnostics to Determine Soot Inception in WSR/PFR

Various laser based diagnostics have been used to study soot formation in flames such as laser-induced incandescence (LII), laser induced fluorescence (LIF), laser extinction, laser scattering, and laser-induced ionization. Laser-induced ionization is an attractive diagnostic for soot inception studies since it is a technique that has been used to detect small soot particles (≈ 2 nm) and atomic ions in premixed flames **[1-2]**. The advantage of the laser-induced ionization technique is that a sampling line is not required to detect soot inception in premixed flames. Recent work **[3,4]** has employed a dilution probe coupled with a nano-differential mobility analyzer (nano-DMA) to measure incipient soot particle size distributions in premixed flames. These studies have clearly shown that the magnitude of the dilution process can influence the particle size distributions.

For the laser-induced ionization diagnostic, signals are produced upon pulsed laser ionization in an electric field generated by a biased electrode. The electrons and ions move in opposite directions in the applied electric field, inducing a current that can be detected **[5]**. The electron signal is observed first with the subsequent ion signal detected later in time. From mobility measurements of the ions produced, it was shown that the molecular weight of the ions was estimated to be ≈ 2300-6000 amu. Spherical particles were assumed, resulting in a soot particle size of 1.6 to 2.2 nm. It is important to note that for the laser-induced ionization diagnostic, the ionization signals were observed right at the soot inception point. At these equivalence ratios, only very small particles exist**[6,7]**. Accordingly, based upon the laser energies used and corresponding beam diameters, such conditions were more than sufficient to raise a 1.6 to 2.2 nm particle well above the temperature required for thermal ionization. Thus, the ionization signals reported were thought to arise from laser-induced heating of 2 nm particles followed by thermal ionization[5].

Previously published studies have used a single biased electrode to generate the electric field, with the burner head serving as the path to ground **[1].** In the WSR/PFR, as well as many other practical combustion systems, a path to ground is not readily available. Accordingly, to apply the laser-induced ionization diagnostic to these geometries, a dual electrode geometry must be employed. In the dual electrode geometry, one electrode is biased and other is grounded. Such geometry has been used to measure H and C atom concentration in flames **[8]**.

The laser-induced ionization technique has not received a great deal of attention in the literature. One reason for this may be the application of the technique to limited geometries. This is unfortunate since this technique is a unique method for detecting incipient soot particles with a diameter of about 2 nm. The method has not been applied to the study of soot inception even though it has superior potential.

Therefore, the goal was to perform laser-induced ionization measurements in the post-flame region of a premixed flame using both the single and dual electrode configuration. The single electrode geometry coupled with the premixed flame was selected for comparison to previously published laser-induced ionization measurements. The premixed burner was used as a surrogate for other combustion systems, including the WSR/PFR. Finally, a dual electrode geometry was employed to gauge the ability of the laser-induced ionization diagnostic to determine the soot inception point in a premixed flame.

The pulsed laser source was a Continuum Nd:YAG system (≈ 5 ns pulse width) operating at a frequency doubled wavelength of 532 nm (certain commercial equipment are identified in this paper in order to accurately describe the experimental procedure–this in no way implies recommendation by NIST.) The laser beam was aligned parallel to the burner slot and was focused in the center of the flame using a 200 mm convex lens. An iris was located in front of the focusing lens to block reflections and the beam was terminated using a beam stop.

Premixed ethene/air flames were generated on a Perkin-Elmer slot burner with a slit length of 5 cm. This burner type has often been used for atomic absorption measurements. The venturi orifice was set to allow no flow into the burner. Ethene was selected as the fuel since it is the fuel to be used for the NIST WSR experiments. The air flow rate was fixed and the fuel flow rate was varied near the soot inception point for all experiments. All flow rates were controlled by mass flow controllers with an uncertainty of 5 %. The equivalence ratio reported corresponds to the fuel/air mixture *into* the burner. Under these conditions, the equivalence ratio at the sooting threshold was 2.5. This corresponds to a C/O ratio of 0.83. The burner was not equipped with a co-flow system of inert gas, thus the entrainment and diffusion of ambient air should be considered to know the exact composition of flame gases. The visible flame height was observed to be ≈ 10 cm above the burner head. The primary reaction zone, due to blue-green emission from C_2, was observed to be ≈ 4 mm above the burner head. For both single and dual electrode configurations, all measurements were performed downstream of the primary reaction zone.

For the single electrode configuration experiments, laser-induced ionization signals were collected using a 1 mm diameter (6 cm length) tungsten electrode that was inserted into the flame above the laser beam. The electrode was mounted parallel to the laser beam and the flame, at a location within 1 mm to 2 mm above the laser beam. This geometry is known to produce the strongest ionization signals because the signal is collected over the entire length of the flame[5-6]. The electrode voltage was varied from -300 V to -900 V.

The dual electrode configuration consisted of two electrodes (each 0.56 mm in diameter, 6 cm length) spaced 0.5 mm apart using a ceramic thermocouple insulator. For the dual electrode-laser beam geometry, the following positions were used: (1) parallel, laser beam below electrodes (2) perpendicular, laser beam below electrodes (3) parallel, laser beam between the electrodes (inclined). One electrode was biased and other was grounded. The biased electrode voltage was varied from -300 V to -900 V.

In both the single and dual electrode configurations, the current through the electrode was converted to voltage using a capacitively coupled amplifier, which was the identical device used in previous experiments **[1]**. Ionization signals were monitored using both digital and analog oscilloscopes, with time resolutions of 275-300 MHz. The ion signal intensity and arrival time were measured using the digital oscilloscope, where the trigger signal was synchronized to that of the laser. One hundred (100) waveforms were averaged to reduce noise.

Three peaks were visible in the oscilloscope trace using the 532 nm laser source. The electron peak, which was quickest to arrive at the electrode, was produced soon after the trigger signal. The second peak, with an arrival time of 22 μs, was smaller in magnitude than the electron signal. The third peak, with an arrival time of 90 μs, had the broadest range of ion arrival times.

The measured arrival times of the second and third peak were observed to vary with electric field strength and laser beam-to-electrode separation distance. These signals were only observed under fuel rich conditions and in those locations where soot was present. Therefore, one of these peaks was assigned as arising from ionized soot particles.

The presence of three peaks in the oscilloscope trace was different than two peaks previously published in laser-induced ionization experiments **[9]**. To quantitatively assign the second and third peak in the oscilloscope trace, the arrival times of ions were compared to previous experiments**[9]**. From kinetic theory, the ion mobility, *K*, can be expressed as follows **[10]**:

$$K = \frac{3e}{16N}\sqrt{\frac{1}{m}+\frac{1}{M}}\sqrt{\frac{2\pi}{kT}}\frac{1}{\Omega_D} \qquad (7)$$

where *m* is the ion mass, *M* is the mass of the neutral carrier, *N* is the number concentration, *T* is temperature, and Ω_D is the average collision cross section. From this expression, the ion mobility is a function of ion mass and the average collision cross section. The average collision cross section is dependent upon an effective ion size parameter. Unfortunately, it is difficult to determine an effective ion size parameter for most ions. As a result, many investigators have assumed that the volume of the ion is proportional to its mass and have introduced mass-mobility correlations to assign various ions from mobility data **[11]**. This assumption is known to be valid for various hydrocarbon ions but breaks down for heavy polyatomic ions, as the mass dependence on ion mobility becomes weaker as *m* is much larger than *M*.

Compared to previous laser-induced ionization experiments [**1**], the laser wavelength and laser energy per pulse were different. It has already been established in the literature that C_2 and C_3 fragments are produced upon irradiation of soot particles [**12-14**]. It was observed that the second peak had a similar arrival time to that of sodium ions, Na^+. Details of the sodium ion arrival experiments are available elsehwhere[5]. Therefore, based on the mass-mobility correlations[6], the second peak was assigned as arising from C_2^+ ions, since the mobility was expected to be close to sodium ions. The atomic weight of sodium is 23, versus 24 for C_2^+. With the Swan system of C_2 overlapping at 532 nm [**15**], C_2 was easily ionized during the laser pulse.

Figure 1 displays the electron signal as a function of laser energy (energy/pulse) for both sooting and non-sooting ethene/air flames. The data were generated using the single electrode configuration for comparison to previous work. Clearly, the electron signal was dependent upon laser energy up to ≈ 1mJ/pulse. For laser energy greater than 1 mJ/pulse, the electron signal was observed to saturate. A similar dependence on electron signal with laser energy was observed in previous experiments **[1]**. The influence of laser energy on the arrival time of ions was also investigated. As expected, the arrival times of C_2^+ and soot ions were observed to be independent of laser energy over the range of 0.15 mJ/pulse to 3.6 mJ/pulse.

Under non-sooting conditions, the influence of the flame on the electron signal was minimal. The magnitude of the electron signal was, at maximum, 1 % of the electron signal for the sooty flame. The influence of the flame was negligible on the measured electron signal and did not depend upon laser energy (see **Figure 3**).The ion mobility can be characterized using

low-field behavior, which implies that the mobility is independent of electric field **[1-2]**. The average velocity of an ion in a gas is called the drift velocity, v_d , and is directly proportional to the electric field intensity, E , provided that $v_d = KE$. The proportionality coefficient, K, is defined as ion mobility. Measurements of ion arrival times can be used to deduce ion mobilities **[1-2]**.

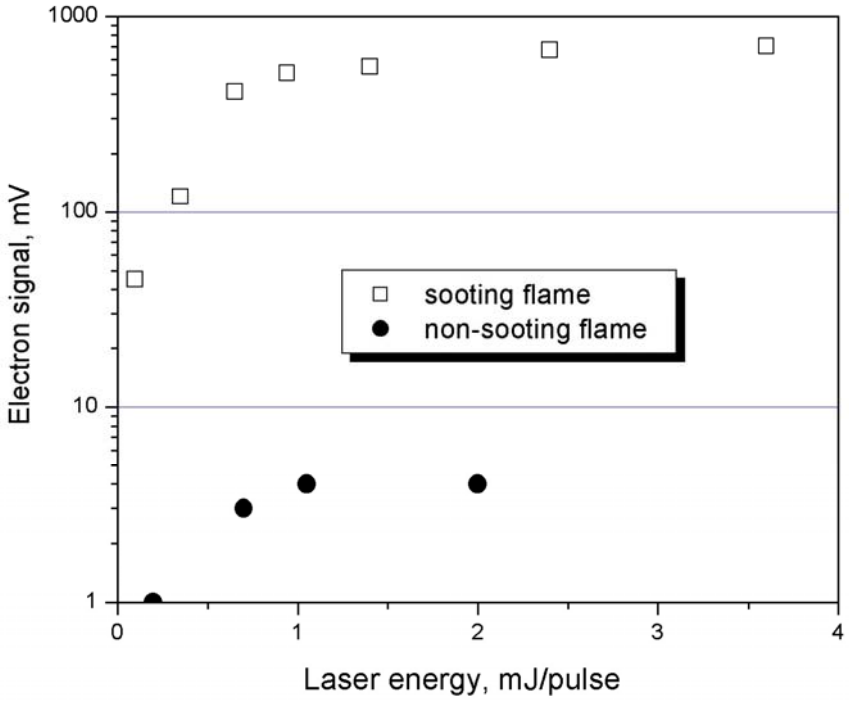

Figure 1 Electron signal (the first peak) as a function of laser energy for both sooting (ϕ = 2.7) and non-sooting (ϕ = 2.3) flame stoichiometry. Single electrode configuration.

Figure 2displays the ratio of soot ion arrival time to C_2^+ ion arrival time as a function of laser beam to burner head distance for three different equivalence ratios. The electrode-laser beam distance was fixed. The data were obtained using the single electrode configuration with the electrode biased at -700 V. As the laser beam to burner head distance was increased to 1 cm, the arrival times of soot ions was observed to increase while the arrival time of C_2^+ ions remained relatively constant. This trend suggests that as measurements are made higher in the flame, for a fixed equivalence ratio, the mass of soot ions increased, resulting in increased soot ion arrival time. This would be expected, since soot particles are known to increase in size as one moves to greater heights (away from the soot inception point) in a premixed flame. Eventually, as the measurements were made higher in the flame (1 cm from burner head), significant soot was observed to deposit on the electrodes, producing difficulties in detection of ionization signals.

When the dual electrode geometry was employed, the optical setup was identical to the single electrode experiments. The following three electrode geometries were considered: (1) parallel, laser beam below electrodes (2) perpendicular, laser beam below electrodes (3) parallel, laser beam between the electrodes (inclined). The inclined parallel electrode configuration was considered so that the laser beam could be placed close to the electrodes

without striking the electrode holder. All three of these configurations are illustrated in figure 1. To determine the optimum configuration to detect the ionization signals, the performance of these geometries was considered individually.

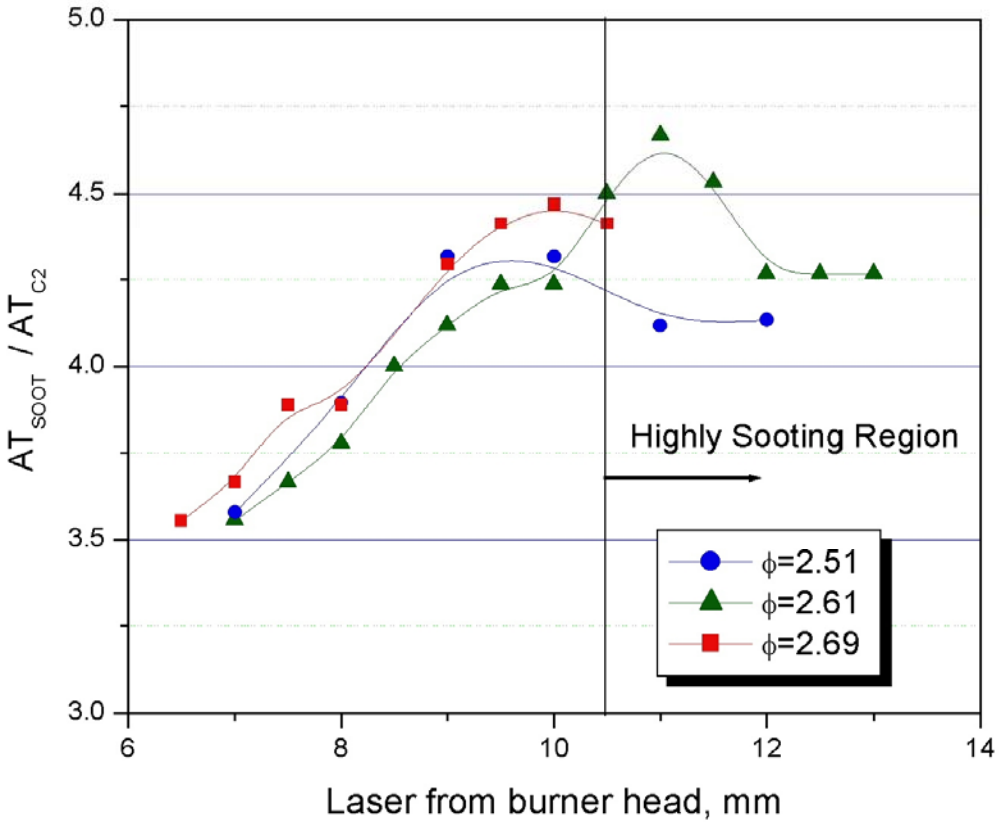

Figure 2 The ratio of soot ion arrival time to C_2^+ ion arrival time as a function of laser beam to burner head distance for three different equivalence ratios. The electrode-laser beam distance was fixed. The data were obtained using the single electrode configuration with the electrode biased at -700 V.

The influence of laser energy and biased electrode voltage on the electron signal intensity was investigated for the dual electrode geometries and is displayed in **Figure 3(a)-(c)**. In the figure, the acronyms SF and NSF denote sooting flame and non-sooting flame, respectively. It was observed that the lower the biased electrode voltage, the faster the electron signal was observed to saturate. The electron signal intensity had the following order: parallel > inclined > perpendicular. From the figure, the influence of the flame was deduced as function of electrode geometry. The effect of biased electrode voltage on background noise was negligible compared to the influence of laser energy. The maximum signal-to-noise ratios were different for each electrode configuration and were observed to be the following: perpendicular (33), parallel (17), inclined (5). Thus, the electrode configuration oriented perpendicular to the laser beam produced the best signal-to-noise ratio of the three geometries.

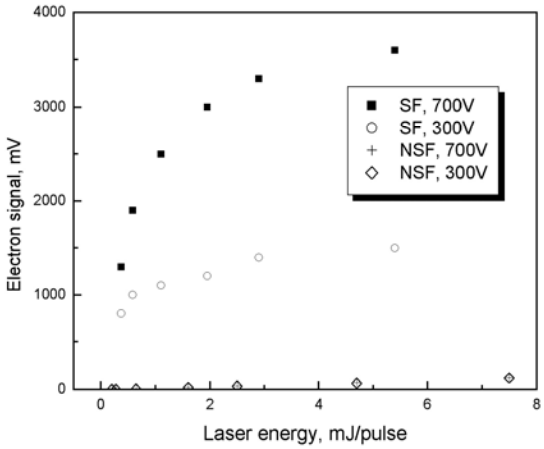

(a)

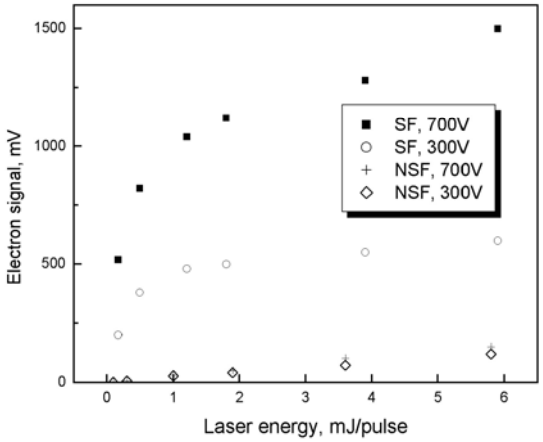

(b)

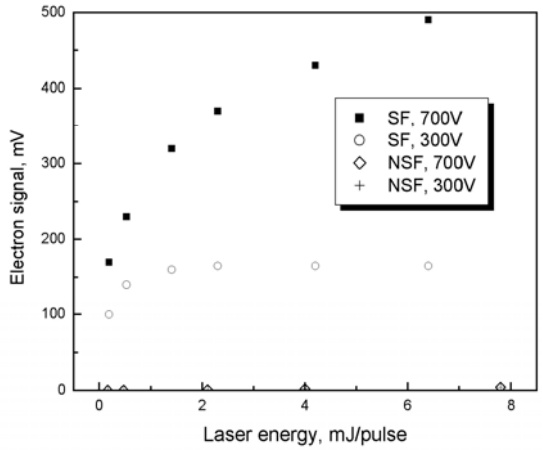

(c)

Figure 3 The influence of laser energy and biased electrode voltage on the electron signal intensity for three different dual electrode configurations (a) parallel (b) inclined (c) perpendicular. SF - sooting flame, NSF - non-sooting flame.

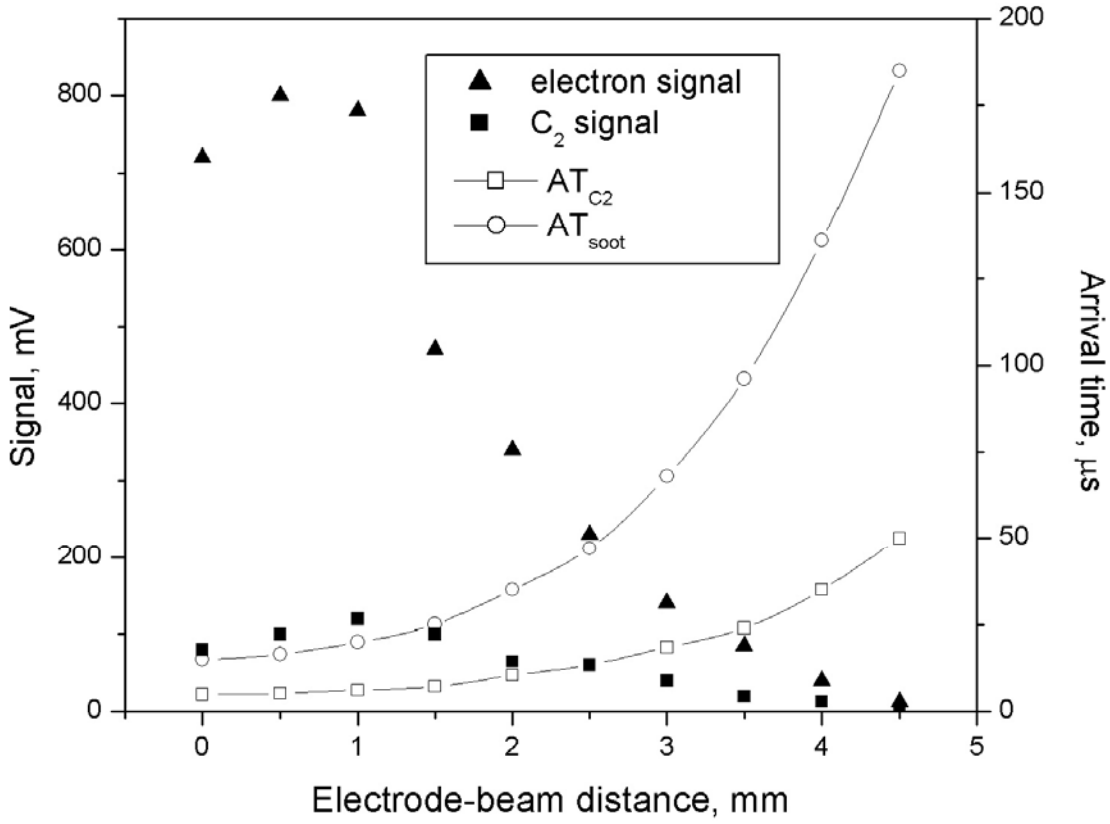

Figure 4 The effect of electrode laser-beam distance on the peak amplitude and arrival time of ions. The experimental conditions: ϕ = 2.69, laser energy = 0.6mJ/pulse, electrode biased at -500V, laser beam 1 cm above burner head.

It was observed that the arrival times of the soot and C_2^+ ionization signals varied depending on the different dual electrode configurations tested. The reason for this is that the ion arrival time depends on the local electric field and laser beam to electrode distance. Altering the electrode configuration alters the electric field. The parallel electrode configuration provided the broadest range in time of the appearance of C_2^+ and soot ion signals amongst the three configurations.

Figure 4 displays the electron and C_2^+ ionization signal magnitude and arrival time of soot and C_2^+ ions as a function of laser beam to electrode distance for fixed stoichiometry into the burner. The data were obtained using a dual electrode configuration oriented parallel to laser beam. The electrode was biased at -500V. As the electrode was moved further away from laser beam, the strength of the electron and C_2^+ ionization signals decreased. In addition, the time for soot and C_2^+ ions to arrive at the electrode increased with a further separation of the laser beam to the electrode distance. In these experiments, a negative voltage was applied to the electrode. The soot and C_2^+ ions were generated at the location where the laser beam passed through the premixed flame. Therefore, if the laser beam-burner head distance was fixed and the distance from the laser beam-electrode was increased, if the ions were positive, it would be expected that the time for the ions to arrive at the electrode would increase with further laser beam-electrode

separation. These observations were confirmed in figure 6 and this suggests that these are indeed positive ions.

Based on the parametric investigation, the electron signal should be used as an indication for soot inception using the dual electrode geometry. The electron signal was detected as rapidly as the electronics would allow and did not vary as a function of time for different electrode voltage and laser beam-to-electrode distance. Furthermore, the electron signal displayed the largest magnitude of the detected ionization signals. The electrode geometry oriented parallel to the laser beam provided the strongest electron signals. The perpendicular configuration provided electron signals as well, albeit weaker in magnitude than the parallel geometry. However, of the configurations investigated, the perpendicular configuration electrode configuration provided the best: (1) spatial resolution (2) signal to noise ratio. In addition, the perpendicular electrode configuration provided the simplest setup for use in practical combustion systems, such as the WSR. For the configuration with the laser beam placed in between the electrodes, careful alignment was required to obtain strong signals. This may result in difficulties when applying this configuration to combustion systems, such as the WSR, since small alignment modifications would result in large signal fluctuations.

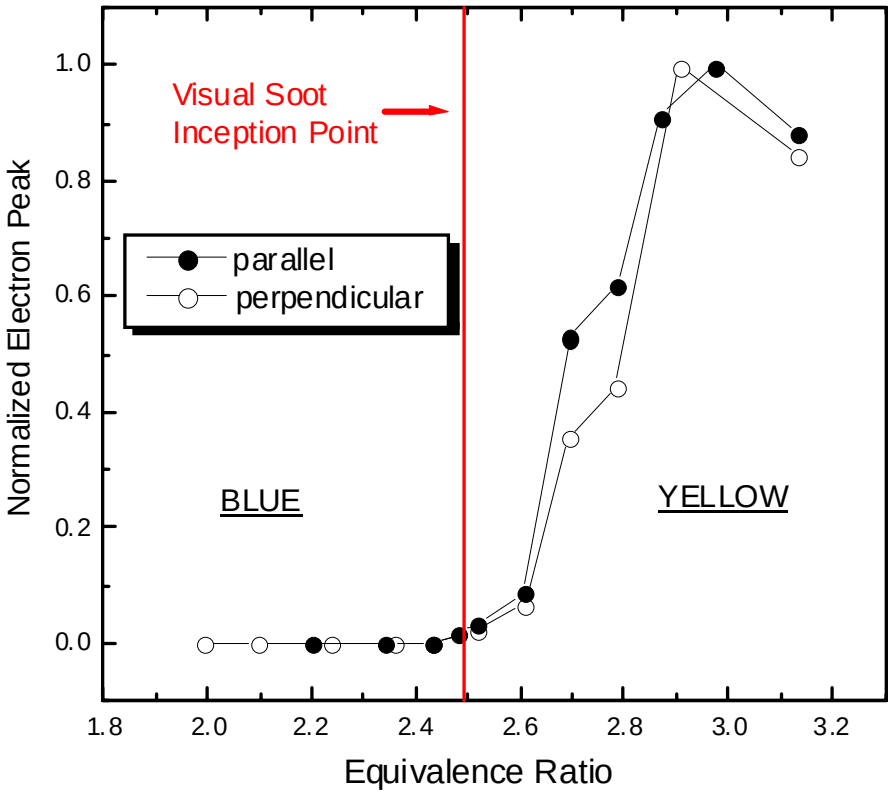

Figure 5 The variation of normalized electron signal intensity as a function of equivalence ratio for parallel and perpendicular electrode configurations. Electrode biased at -700 V.

To gauge the ability of the laser-induced ionization diagnostic to detect the onset of sooting in a premixed flame, the normalized electron signal was plotted as a function of

equivalence ratio and is shown in **Figure 5**. The following experimental procedure was adopted for the perpendicular electrode configuration. The electrode-laser beam distance was fixed (2 mm), and the burner head was varied until a signal was detected at the visual soot inception point. The visual soot inception point was defined as the first visible observation of yellow luminosity just above the reaction zone. The reaction zone was characterized by blue-green emission from C_2. The fuel flow rate was then increased and the electron signal was recorded as a function of equivalence ratio. A similar procedure was performed for the parallel electrode configuration. The biased electrode voltage was fixed at -700 V for each electrode configuration.

The parallel electrode configuration was the most sensitive in determining the soot inception point. For certain applications, the parallel electrode configuration may not be possible. The perpendicular electrode configuration may still provide quantitative information on the soot inception point in a premixed flame. These results demonstrate that the laser-induced ionization diagnostic can be used to detect the onset of soot inception in a premixed flame.

Accordingly, based on the success of applying a dual electrode geometry in a premixed burner, the technique was applied to the PFR section of the NIST WSR/PFR facility. Large fluctuations were observed in the quality of the signals when the electrodes were inserted into the PFR section. A variety of techniques were used to attempt to stabilize the electrodes in the flow field of the PFR section. What was observed is that in the PFR section, under the conditions used to operate the WSR, the corresponding velocity inside the PFR section was on the order of 10 m/s. This is considerably higher than the velocity in the premixed flame above and precluded the use of the diagnostic in the WSR/PPR. However, the parametric investigation performed is still of value to the combustion community.

References

[1] Smyth K.C. and Mallard, W.G., Comb. Sci. and Tech. 26, 35-41(1981).

[2] Mallard, W.G., and Smyth, K.C., Combust. Flame 44, 61-70 (1982).

[3] Stouffer, S. D., R. C. Striebich, C. W. Frayne and J. Zelina (2002). Combustion Particulates Mitigation Investigation Using a Well-Stirred Reactor. AIAA 38th Joint Propulsion Conference & Exhibit, Paper Number: 2002-37, Indianapolis, Indiana, July 7-10, 2002.

[4] Maricq, M.M., Harris, S.J., and Szente, J.J.,*Combust. Flame* 132: 328-324 (2003).

[5] Travis, J.C. and Turk, G.C., "Laser-Enhanced Ionization Spectrometry," John Wiley & Sons, New York (1996).

[6] D'Alessio, A., Di Lorenzo, A., Borghese, A., and Beretta, F., and S. Masi, Proc. Combust. Inst. 16, 695-703 (1977).

[7] Haynes, B.S., and Wagner, H.Gg., Ber. Bun. Phys. Chem. 84, 585-610 (1980).

[8] Smyth, K.C. and Tjossem, P.J.H..,Proc. Comb. Inst. 23, 1829-1837(1990).

[9] Mulholland, GW., Donnelly, M.K., Hagwood, C., Kukuck, S.R., Hackley, R., and Pui, D.Y.H., accepted for publication in *J. Res. NIST*, in press (2005).

[10] Griffin, G.W., Dzidic, I., Carroll, D.I., Stilwell, R.N., and Horning, E.C, Anal. Chem. 45, 1204-1209 (1973).

[11] Lin, S.N., Griffin, G.W., Horning, E.C., and Wentworth, W.E., J. Chem. Phys. 60, 4994 4999 (1974).

[12] Shaddix, C.R. and Smyth, K.C., Combust. Flame 107, 418-452 (1996).

[13] Bengtsson, P. and Aldén, M., Combust. Flame 80, 322-328 (1990).

[14] Eckbreth, A.C. and R.J. Hall, R.J., Combust. Flame 36, 87-98 (1979).

[15] Pearse, R.W.B. and Gaydon, A.G., "The Identification of Molecular Spectra," Fourth Edition, Chapman and Hall, London, 1976.

Publications and Presentations

Publications Resulting From SERDP Support:

Archival Journal:

D.B. Lenhert and S.L. Manzello, Effects of Benzene and Napthalene on Soot Particle Size Distributions in a Well Stirred Reactor/Plug Flow Reactor, *Proc. Combust. Inst*., submit.

S.L. Manzello, D.B. Lenhert, A. Yozgatligl, G.W. Mulholland, M.R. Zachariah, and W. Tsang, Soot Size Distributions in a Well Stirred Reactor / Plug Flow Reactor, *Proc. Combust. Inst.* 31:675-683, 2007.

S.L. Manzello, E.J. Lee, and G.W. Mulholland, On the Use of Laser-Induced Ionization to Detect Soot Inception in Premixed Flames, *Applied Optics* 44: 5105-5111, 2005.

Tsang W., "Energy transfer effects during the multichannel decompositionof ethanol" Int. J. Chem.. Kin.,36 (8): 456-465, 2004

Babushok VI, Tsang W "Kinetic modeling of heptane combustion and PAH formation ", J. Prop. Power. 20 (3): 403-414 MAY-JUN 2004

Baulch, D. L., Bowman, C. T., Cobos, R. A., Just, T.., Kerr, J. A., Pilling, M. J., Stocker, D., Tsang, W., Walker, R. W., and Warnatz, J., "Evaluated Kinetic Data for Combustion Modeling" Supplement II, Journal Of Phys. Chem. Ref. Data. 4(3) 757-1397) 2005

Colket M., Edward, C. T., Williams, S., Cernansky, N. P., Miller, D. L., Egolfopoulos, F., Lindstedt, P., Seshadri, K., Dryer F. L., Law, C. K., Friend, D., Lenhart, D. B., Pitsc, H., Sarofim, A, Smooke, M., Tsang, W., "Development of an Experimental Database and Kinetic Models for Surrogate Fuels", 45th AIAAAerospace Sciences Meeting and Exhibit, Reno, Nevada, January 9, 2007

Tsang, W., "Mechanism and Rate Constants for the Decomposition of 1-Pentenyl Radicals", J. Phys. Chem., A 110 27: 8501-8509 2006

Tsang, W., Walker, J. A., and Manion, J. A., "The Decomposition of n-Hexyl Radicals", Proc. Comb. Inst. 158, 2006

McGivern, S., Manion, J. A., and Tsang, W., "Kinetics and Thermal Decomposition of t-butyl-1,3, cyclpentaidene, J. Phys. Chem.., A110(47) 12822-12831, 2006

Tsang, W., Awan, I. A. McGivern, W. S. and Manion, J, A.,"Formation of Soot Precusors for Real Fuels: The Unimolecular Decomposition of Fuel Radicals"in "Proceedingsof the International Workshop on Combustion-Geenrated Fine Carbon Particles " (A. Sarofim , ed.) (in press)

Conference Proceedings:

D. Poster, C.B. Stroud, S.L. Manzello, and W. Tsang, Determination of PAHs in Particulates Generatedfrom Fuel Rich Flame in the Presence of an Aromatic Fuel Additive, 21st International Polycyclic Aromatic Compounds, Trondheim, Norway, 2007.

C.B. Stroud, W. Tsang, and S.L. Manzello, Detailed Modeling and Analysis of Aromatic Additive Effects in Ethylene-Air Flames, *5th Joint Meeting of the US Sections of the Combustion Institute*, San Diego, CA, 2007.

S.L. Manzello, D.B. Lenhert, C.B. Stroud, and W. Tsang, The Effects of Benzene and Napthalene on Soot Particle Size Distribution and Species Concentration in a Well Stirred Reactor/ Plug Flow Reactor, *5th Joint Meeting of the US Sections of the Combustion Institute*, San Diego, CA, 2007.

D. Lenhert, S.L. Manzello, and G.W. Mulholland, The Use of Laser Induced Ionization Measurements to Detect Soot Inception in a Well Stirred Reactor – Plug Flow Reactor, *24thAmerican Association of Aerosol Research (AAAR) Conference*, Austin, TX, 2005.

S.L. Manzello, D. Lenhert, M. Donovan, G.W. Mulholland, A. Yozgatligil, and M. Zachariah,Measurement of Particle Size Distributions from a Well Stirred Reactor – Plug Flow Reactor, *24th American Association of Aerosol Research (AAAR) Conference*, Austin, TX, 2005.

M. Donovan, S.L. Manzello, D. Lenhert, and W. Tsang, Modeling Soot Inception and PAHFormation in Rich Ethylene/Air Combustion, *6th International Conference on Chemical Kinetics*, Gaithersburg, MD, 2005. S.L. Manzello, G.W. Mulholland, M. Donovan, W. Tsang, K. Park, and M.R. Zachariah, On the Use of a Well-Stirred Reactor to Study Soot Inception, *4th Joint Meeting U.S. Sections of the Combustion Institute*, Philadelphia, PA, 2005.

S.L. Manzello, E.J. Lee, and G.W. Mulholland, On the Use of Laser-Induced Ionization to Detect Soot Inception in Premixed Flames, *23rd American Association of Aerosol Research (AAAR) Conference*, Atlanta, GA, 2004.

E.J. Lee, S.L. Manzello, K.C. Smyth, and G.W. Mulholland, Development of Laser-Induced Ion Mobility for Soot Inception, *4thAsia-Pacific Conference on Combustion*, Nanjing, China, 2003.

G. W. Mulholland, S.L. Manzello, E.J. Lee, S. Stouffer, L.G. Blevins, Size and Chemistry of Incipient Soot in a Well Stirred Reactor, *22nd American Association of Aerosol Research (AAAR) Conference*, Annaheim, CA, 2003.

Tsang , W. "Soot Precursor Formation from Real Fuels" 45th AIAA Aerospaces Dcience and Exhibit Meeting Reno, Nevada, January 7-10, 2008

Tsang, W., Chemically Activated Oxidation of n-Propyl Radicals " *2007 Fall Technical Meeting Eastern States Section of the Combustion Institute,University of VirginiaOctober 21-24, 2007*

Iftikhar Iwan, W. Sean McGivern, Jeffrey A. Manion and Wing Tsang "The Decomposition and Isomerization of Cyclohexyl and 1-Hexenyl Radical" *5th US Combustion Institute MeetingSan Diego, California March 26-28th, 2007*

Tsang, W., Awan, I. A. McGivern, W. S. amd manion, J, A., "Formation of Soot Precusors for Real Fuels: The Unimolecular Decomposition of Fuel Radicals" International Workshop on Combustion-Geenrated Fine Carbon Particles, Capril , April 2007

Tsang, W. "Butylbenzene Combustion Kinetics Ddatabase" 42nd. AIAA Aerospaces Dcience and Exhibit Meeting Reno, Nevada, January 2006

Tsang, W.,"Chemical Activation Reactions om Heptane Combustion Kinetics Database 42nd. AIAA Aerospaces Dcience and Exhibit Meeting Reno, Nevada, January 2006

Tsang, W., "Kinetic Database Development foro Combustion Simulation" National Energy and Technology

Tsang, W., "Present State of Combstion Kinetics"in JASON Briefing SnadDiego, June 2004

Tsang, W., "Progress in the Development of a Kinetic Database for Heptane Combustion, 39th AIAA Aerospaces Dcience and Exhibit Meeting Reno, Nevada, January 2003